THE HONG KONG POLYTECHNIC UNIVERSITY

Navigation of an Autonomous Outdoor Vehicle on a Road Surface with Changing Geometry

A Thesis

Submitted for the degree of Master of Philosophy

by

Chan, Fu Man Alick

Department of Mechanical Engineering

The Hong Kong Polytechnic University

September 1999

DECLARATION

I hereby declare that, apart from the source quoted, this thesis represents my own work under the supervision of Dr. H. K. Fung. The material of this thesis has not been submitted to The Hong Kong Polytechnic University or any other institution in an application for admission to a degree, diploma or any other qualifications.

CHAN, FU MAN ALICK

Department of Mechanical Engineering

The Hong Kong Polytechnic University

September 1999

ACKNOWLEDGEMENTS

I would like to thank my supervisor, Dr. H. K. Fung, for his guidance and encouragement throughout this research.

I would also like to thank Mr. K. L. Li and Mr. W. C. Cheng for their assistance in conducting the experimental work, Dr. X. Q. Wang for his recommendations on the vehicle model, and Dr. Y. Y. Li for his recommendations on the control system.

The financial support of The Hong Kong Polytechnic University is gratefully acknowledged.

Finally, special thanks go to my family and friends for their support, encouragement and patience throughout this research.

ABSTRACT

In this study, a truth vehicle model, a reference path model and a road model are developed. Three H_∞ control systems, K_{nom}, K_{mod} and K_{blk}, are designed based on three design models—1) nominal model (Velnom), 2) multiplicative uncertainty model (Velmod) and 3) system parameters uncertainty model (Velblk)—respectively. The simulations on general real 3-dimensional road surface were conducted. The results show that the H_∞ controller (K_{blk}) developed based on the system parameters uncertainty model has the best performance out of the three controllers. The H_∞ controller keeps the lateral off-path distance to less than 20cm and the off-path heading angle to less than 5 degrees, in the presence of system parameters variations, external disturbances and unmodeled dynamics, when a vehicle is running on a path of arc with radius of 183m on a road surface with road bank angle of 5.7 degrees.

This research emphasizes the importance of road geometry parameters and shows that the effectiveness of a steering tracking control system is greatly dependent on the road geometry parameters. The present research studies the vehicle control on a general real 3-dimensional road surface. The mathematical model is developed for the dynamics of a four-wheeled vehicle, with front wheel steering, running on a 3-dimensional road surface. The equations of motion are derived are put into state space form to investigate the vehicle-environment system's dynamic characteristics. The truth vehicle model contains 14 states variables. Two design vehicle models (Velmod & Velblk) also involve the steering mechanism.

Sensitivity analysis methods and μ-analysis are used to examine the effect of the

parameters' variation on vehicle system dynamics and vehicle handling performance. The sensitivity matrices in the frequency domain are calculated as the derivatives of the transfer function matrices with respect to the vehicle-environment system parameters, such as road banking angle and lateral forces. The unmodeled high-order dynamics and the potential modeling imperfection are both taken into account in frequency domain with μ-analysis. A procedure to convert the variations in model parameters onto a structured block matrix is developed in this research. This comes in handy if control engineers wish to use μ-analysis in the development of a robust controller.

μ-synthesized optimal H_∞ control methods are employed in this research. H_∞ controller is designed based on a linearized model for automatic lane changing and path tracking of a vehicle running on a road surface with a constant road bank angle. The yaw angle and lateral distance are the system parameters to be tracked by the steering controller. Satisfactory simulation results are obtained for different banked roads, and a simulation on the general 3-dimensional road surface is also performed. The effectiveness of the controller can be extended to control a vehicle on a general 3-dimensional surface, with time-varying profile. The last Section of Chapter 7 shows that a path on the general 3-dimensional road surface can be constructed in the simulation by joining all the landscapes along the path.

With the signals from different system sensors, such as Global Positioning System (GPS), Digital Magnetic Compass (DMC), gyros, accelerator and inclinometer, the actual position and orientation information of the vehicle can be determined on line using the methodology developed in this research.

CONTENTS

LIST OF FIGURES

LIST OF TABLES

NOMENCLATURE

Vehicle Model

L_i	Lateral force on ith tire
F_{xi}, f_{xi}	Longitudinal force (in x-direction) on ith tire
F_{yi}, f_{yi}	Lateral force (in y-direction) on ith tire
F_{si}, i=f,b	Lateral forces acting on the front/rear wheels
F_{li}, i=l,r	Longitudinal forces acting on the left/right wheels
F_{Ni}	Normal force on ith tire due to static load
F_{Dni}	Normal force on ith tire due to pitch and roll dynamics
F_{Dpi}	Normal force on ith tire due to pith dynamics
F_{Dri}	Normal force on ith tire due to roll dynamics
R_{toti}	Total reaction force on ith tire
R_i	Reaction force on ith tire
R_v	Vertical reaction force
R_l	Horizontal reaction force
a	Distance between the vehicle front and c.g.
b	Distance between the vehicle rear and c.g.
t_r	Base length at the vehicle rear
t_f	Base length at the vehicle front
h_{um}	Mean height of the rolling axis
h_f	Height of the front unsprung mass
h_b	Height of the rear unsprung mass
$\bar{x}, \bar{y}, \bar{z}$	Rectangular coordinate frame fixed at rolling axis
x_G, y_G, z_G	Rectangular coordinate frame fixed at sprung mass
X,Y,Z	Rectangular coordinate frame fixed at landscape
θ_x, θ_r	Roll angle of the vehicle
θ_y, θ_p	Pitch angle of the vehicle
θ_z	Yaw angle of the vehicle
$\hat{\theta}_s$, η	Road bank angle (steepest angle in a landscape)
l	Height of sprung mass from the rolling axis
m, m_s	Mass of the sprung mass
M_{tot}	Total mass of the vehicle
$M_{f,b}$	Total mass in the front/rear part of the vehicle
M_R	Moment acting on the sprung mass at the rolling axis
M_R'	Moment acting on the unsprung mass at the rolling axis
K_{roll}	Resultant angular stiffness in rolling
K_{pitch}	Resultant angular stiffness in rolling
k_{ij}, i=r,p; j=f,b,l,r	Angular stiffness at j due to roll/pitch dynamics
B_{roll}	Resultant angular damping coefficient in rolling
B_{pitch}	Resultant angular damping coefficient in rolling
β_{ij}, i=r,p; j=f,b,l,r	Angular stiffness at j due to roll/pitch dynamics
Γ_z	Total torque generated in z axis
ε_i	Deflection of the spring at ith tire
η, ζ	Vehicle banking angle and inclination angle
α_i	Slip angle at the ith tire

δ, δ_f	Steering angle at front wheels
$C_{\alpha i}$	Cornering Stiffness at ith tire
μ	The road coefficient of adhesion
y_r	The lateral displacement of the vehicle with respect to the reference path
ε_r	The angular displacement of the vehicle with respect to the reference path
ε_v	The road adhesion reduction factor
U	Vehicle's longitudinal speed
λ_s	Longitudinal wheel slip
C_x	The tires' longitudinal stiffness
f(S), F(S)	Reduction factor on lateral forces

Control System

ω	Frequency [rad/sec]
$d(s)$, $\delta(s)$	Disturbance
$d'(s)$, $\delta'(s)$	Normalized disturbance ($d(s) = W_{p1}(s)d'(s)$)
$e(s)$	Control error ($e(s) = r(s) - y(s)$)
$e_0(s)$	Measured control error ($e_0(s) = r(s) - y_m(s)$)
$e'(s)$	Weighted control error ($e'(s) = W_{p2}(s)e(s)$)
$m(s)$	Model output ($m(s) = G(s)u(s)$)
$n(s)$	Sensor noise
$r(s)$	Reference
$u(s)$	Input
$w(s)$	Perturbation
$y(s)$	Output
$z(s)$	Input to perturbation structure ($w(s) = \Delta(s)z(s)$)
$P(s)$	Generalized closed loop system
$S_o(s)/S_i(s)$	Sensitivity evaluated at plant output and input
$T_o(s)/T_i(s)$	Complementary sensitivity evaluated at plant output and input
$W_{p1}(s)$	Disturbance weight
$W_{p2}(s)$	Control error weight
$W_{u1}(s)$	Perturbation input weight
$W_{u2}(s)$	Perturbation output weight
$\tilde{\Delta}(s)$	Perturbation, $\bar{\sigma}(\Delta) \leq 1$
Δ(s)	Normalized perturbation, $\bar{\sigma}(\Delta) \leq 1$
Δ_p(s)	Performance block
$F_l(N(s), K(s))$	Lower LFT, $F_l(N(s), K(s)) = N_{11} + N_{12}K(I - N_{21}K)^{-1}N_{21}$
$F_u(P(s), \Delta(s))$	Upper LFT, $F_u(P(s), \Delta(s)) = P_{22} + P_{21}\Delta(I - P_{11}\Delta)^{-1}P_{12}$
A, B, C, D	State space matrices
I_n	n x n identity matrix
J_{np}	Nominal performance cost function
J_u	Robust stability cost function
J_{rp}	Robust performance cost function
$\Delta_{\arg}$	Change in argument as s traverses the Nyquist D contour
det(A)	Determinant of complex matrix A
A^T	Transpose of A

A^*	Complex conjugate transpose of A
A_{ij}	The (i, j) element of A
$\mathrm{tr}\{A\}$	Trace of A
$\lambda_i(A)$	The i'th eigenvalue of A
$\rho(A)$	The spectral radius of A
$\rho_R(A)$	The real spectral radius of A
$\mu_\Delta(A)$	The structured singular value of A
$\overline{\mu}_\Delta(A)$	Upper bound for $\mu_\Delta(A)$
Ric(H)	The Ricatti solution
$\|\cdot\|$	Norm
$<\cdot>$	Scalar product
$A = Y\Sigma U^*$	Singular value decomposition of A
$\overline{\sigma}(A)$	Maximum singular value of A, $\overline{\sigma}(A) = \sigma_1(A) = \|A\|_2$
$\underline{\sigma}(A)$	Minimum singular value of A, $\underline{\sigma}(A) = \sigma_k(A)$
$\sigma_i(A)$	The i'th singular value of A
$K(A)$	Condition number of A, $K(A) = \overline{\sigma}(A)/\underline{\sigma}(A)$
$\|G(s)\|_{H2}$	Transfer function 2-norm, $\|G(s)\|_{H2} = \sqrt{\frac{1}{2\pi}\int_{-\infty}^{\infty} \mathrm{tr}\{G(j\omega)^H G(j\omega)\}d\omega}$
$\|G(s)\|_{H\infty}$	Transfer function ∞-norm, $\|G(s)\|_{H\infty} = \sup_\omega \overline{\sigma}(G(j\omega))$
$\mathbf{K}$	Field of real or complex numbers
$\mathbf{H}$	A linear space
$\mathbf{C}^{n\times m}$	Set of complex n x m matrices
$\mathbf{R}^{n\times m}$	Set of real n x m matrices
L	Lebesque spaces
H	Hardy spaces
K_S	Set of all stabilizing controllers
D^f	Set of normalized generic disturbances, $\|\delta^f\|_2 \le 1$
D	Set of generic disturbances, $\delta(s) = W_{pl}(s)\delta^f(s)$
$\mathbf{\Delta}$	Block diagonal perturbation structure used with μ
$\mathbf{\Delta}_c$	Corresponding complex perturbation set
$\mathbf{B\Delta}$	Bounded subset of perturbations, $\mathbf{B\Delta} = \{\Delta(s) \in \mathbf{\Delta} \mid \overline{\sigma}(\Delta(j\omega)) < 1\}$
$\mathbf{Q}$, $\mathbf{D}$, $\mathbf{G}$, $\hat{\mathrm{D}}, \hat{\mathrm{G}}$	Sets of scaling matrices used for μ upper and lower bounds

1. INTRODUCTION

1.1 Background and Motivation

This research is related to the development of the autonomous road vehicle. The development of the autonomous road vehicle has two motivations: 1) reduction of accidents caused by lack of alertness, inattentiveness of driver and in situations where the driver cannot react in time [1] and 2) efficient usage of the roadway network in which construction of new roadways is no longer a solution for traffic congestion [2].

In Hong Kong, there are nearly 15,500 crashes each year, of which 4350 crashes involved casualties [3]. In the U.S., nearly 15,000 people die each year in single vehicle roadway departure crashes [4]. These crashes are directly caused by the driver's overconfidence, misjudgment of curvature and other careless mistakes.

From the engineering point of view, these accidents could be avoided by installing an advanced control system in the vehicle that can be self-controlled or controlled by a decentralized control system. Such researches on the development of the vehicle control system have been proposed in the U.S. and Europe. The Intelligent Vehicle Highway System (IVHS) in the U.S. and Road Transport Information (RTI) in Europe are good examples of the combination of traffic control system and vehicle control system. The core idea of IVHS and RTI is to transfer the control over the car from the driver to a decentralized control system. The ultimate goal of IVHS and RTI is to provide a safe and comfortable driving condition with no traffic jams or other difficulties and/or to provide intelligent guidance for the driver to determine the way the driver should accelerate, brake and steer.

Extensive research studies [5-8] on the development of autonomous road vehicle have been conducted, welcoming the epoch of IVHS and RTI. These studies mainly focused on the research of maneuvers in automatic steering and accelerating, lane changing, keep-on-lane, car following, collision avoidance, path planning (routing), etc. This study mainly concentrates on the steering, and keep-on-lane, which are the basic components of the unmanned road vehicle running automatically on urban road.

With these basic components, the unmanned road vehicle can run in an unstructured environment with or without a driver in a safe manner. However, the reliability of the control system is frequently dependent on the following design criteria:

1. Controller should react to actual command signals even though disturbance and/or noise are incorporated into the actual signals.
2. Controller should have an appropriate and fast response to those unpredictable changes or unstructured disturbances, since only little and/or no prior knowledge is available about those perturbations that are inserted into the system.
3. Control system should not be corrupted when operating a little bit, say 2%, out of its designed operating frequency range.
4. Controller should meet the design performance specification which is either described in frequency domain or time domain.
5. Controller should be nominal and robustly stable.

The criteria 2-5 are common for the robust control system, while criterion 1 is fulfilled either by the rejection of unwanted signals and/or disturbances or by the collection and input of perfect information in the control system. In the control of a highly dynamic and highly nonlinear system, the performance of a control system is very demanding in terms of the robustness to the disturbance and/or system modeling

error, nature of nonlinear control action and response time. Some of the advanced control methods have shown great success in the highly nonlinear system. However, the control problem in a highly dynamic system is still a challenging problem for control engineers [17]. The application of these advance control methods is usually targeted at high-ended, high-cost and extra-precision product or system, such as the control systems in aircraft or military submarine vehicle. For civilian products, the control systems are designed in a task-orientated and low-cost manner, such as the steering controller in some passenger cars.

When a vehicle is running at high speed, say 40 m/s, the control system of the vehicle becomes highly dynamic and depends very much on the system model preciseness. Apart from the fact that it is quite laborious to have a very precise model for the control system, the control system developed becomes system dependent on the model and hence cannot be easily applied to other systems or understood explicitly by control engineers. This increases the overall development cost of the control system.

A control system, with feedback or feed-forward path, contains the measuring device used to receive the interested states of the system for the system controller. In some cases, several of the sensors are also installed for the collection of environmental data to prepare a local map for the system, which defines the sensible region of the system.

In order to provide precise information to the system, multi-sensors are integrated, and each is characterized in a frequency domain. Thereafter, a sensor model is built along with the development of the control system, termed a multisensor system throughout the study. Recall Luo's definition on multisensor integration and

multisensor fusion [9]: multisensor integration refers to the synergistic use of the information provided by multiple sensory devices to assist in the accomplishment of a task by a system; multisensor fusion refers to any stage in the integration process where there is an actual combination (or fusion) of different sources of sensory information into one representational format. The relationship between the multisensor system and the control system is shown as follows (Figure 1.1):

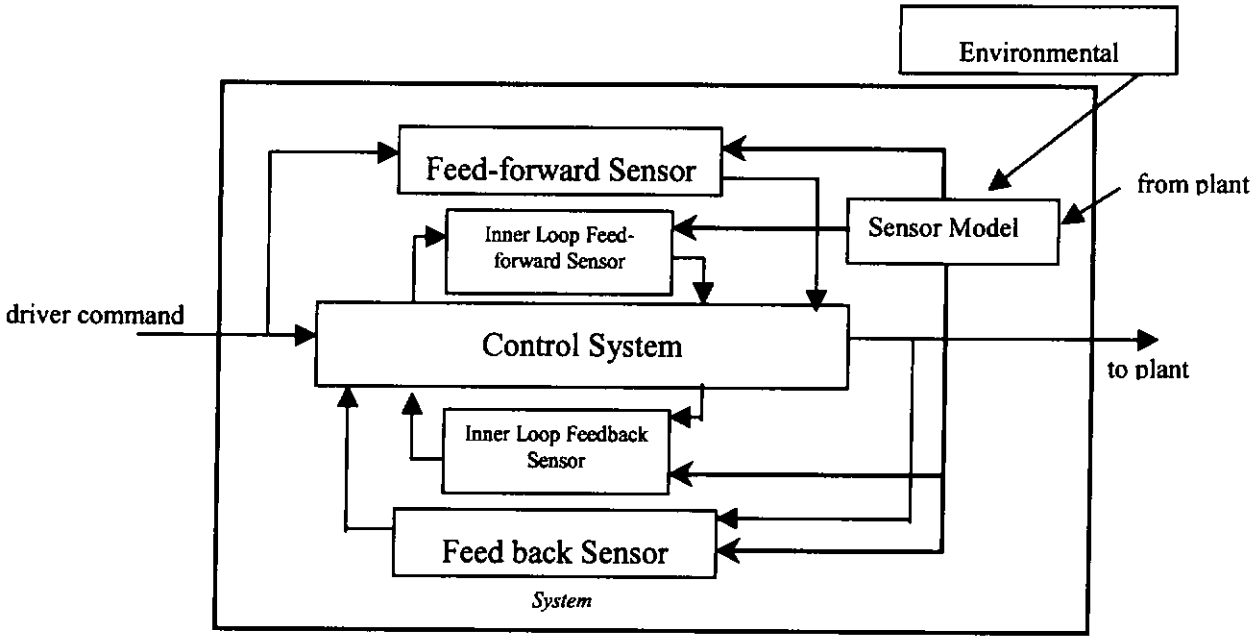

Figure 1.1 Multisensor System and Control System

Information available to the system in a highly dynamic condition is time varying and nonlinear. This makes the signal-processing filter unreliable and unstable, especially in the case of the filter output divergence in recursive type filter. Most of the low-cost sensors also suffer from time-dependent error and shifted initial error [74]. Integration and fusion are necessary for the sensors with these kinds of errors in order to give meaningful information to the control system that is otherwise unavailable. With the integration and/or fusion techniques, the redundancy and the accuracy of the multisensor system are both enhanced.

With the aforementioned control system and multi-sensor system, an autonomous navigation system (ANS) is structured. It is termed ANS, since it is a system specially designed for the navigation of the land vehicle.

Chapter 2 of this thesis surveys all the research works on the development of control methodologies and sensor integration methodologies in the field of autonomous vehicles, and the trend in system configuration of multi-sensor system. Chapter 3 covers the development of the complex and design vehicle models. The complex vehicle model contains 8 degrees of freedom (*Dof*) describing the motions of the mass center of the vehicle. Six of the *Dofs* include 3 translational and 3 rotational orientation, which are the vehicle fundamental orientations to describe a rigid body in three-dimensional space. The other two *Dofs* describe the pitching and rolling of the vehicle body about the principal axis on the vehicle base. Chapter 4 is devoted to the navigation scheme used in this study. The navigation algorithm is developed and makes possible the navigation of a vehicle on a 3-dimensional road surface with time varying profile. Chapter 5 describes the methodology used in control synthesis. This involves the methodology used to describe the perturbation model with the structured μ framework. The optimal H_∞ design is illustrated as well. Based on the design vehicle model built in Chapter 3 and the control system design algorithm developed in Chapter 5. The vehicle design model is verified by comparing it with the complex (truth) vehicle model in Chapter 6. Six types of input signals are used for the verification. The effects of lateral forces and the road parameters on the vehicle dynamics are also investigated.. Based on the design vehicle model built in Chapter 3 and the control system algorithm developed in Chapter 5, three ad hoc optimal $H\infty$

controllers are built for the vehicle lateral control in Chapter 7. Two of them are built in μ framework, K_{mod} and K_{blk}. The simulation results for the vehicle handling performance on three-dimensional road surface is illustrated. Chapter 7 also discusses, analysis and interprets the results found in the simulations. Chapter 8 summarizes all the finddings in the study and discusses the originality of the project.

The purpose of this research project is to provide people with 1) a clear understanding of the importance of terrestrial navigation algorithm on a three-dimensional road surface ,2) a clear insight into the performance of optimal H_∞ controller in vehicle lateral maneuvering subjected to unstructured disturbance in a hostile environment, and 3) a demonstration of a prototype design of an autonomous navigation system which is for civilian used..

1.2 The Nature, Scope and Goal of the Research Project

In this study, an autonomous navigation system (ANS) for an electric vehicle is designed. The ANS consists of a control system and a multi-sensor system, in which control system is extensively studied in this project. The control system is responsible for the lateral control of the running vehicle, while the longitudinal speed is kept constant. With the ANS, the vehicle can run in an environment where static information has been stored. The ANS is target for commercial vehicle, which is running a majority of time on the roads in a city where the roads is always undulating. The ANS is also target for the highway centralized control system. When the ANS is incorporated with the highway system, the ultimate goals of the efficient usage of highways and the establishment of a safe and comfortable driving condition would be achieved.

1.3 Objectives

In order to meet the aforementioned purposes of the research, the following objectives are drawn. The objective of this research project is to develop an optimal robust controller for an electric vehicle. This control system is highly robust, has a fast response to the exogenous disturbances in the unstructured environment and has a large operating range in the highly nonlinear system. Another objective of this research is to develop a 3-D vehicle model, which is appropriated for the simulation of robust control system on general real 3-D road surface. In the multi-sensor system, all the signals, which are coming from the vehicle sensors (gyro, tilt-sensor, accelerometer), Digital Magnetic Compass (DMC) and the Global Positing System (GPS), are integrated. Combining the vehicle sensors, DMC and GPS provide a reliable and accurate vehicle sensoring system.

2. LITERATURE REVIEW

2.1 Control System

In recent years, extensive work has been done on the automated steering control for road vehicle [10-16]. The research aimed to steer a ground vehicle along a reference line located in the middle of the lane. The reference lines, which can be a magnetic marker, color marker or guidance cable, mark the desired path of the steering controller. The heading angle with respect to the tangent of the desired path and the lateral offset are normally used as the feedback signals to the controller. The choice of the reference lines is based on the fact that less work is done on the pre-construction of the operating environment and that low cost sensors can be used.

Some of the researchers then choose not to use the reference line. Rather, they try to track the lane of the road by using a low-cost CCD camera [17][18]. The machine vision itself has led to another large research topic, but the use of the CCD camera in control problem has brought a number of applications, such as industrial automatic assembly, indoor Automatic Guide Vehicle (AGV) and trajectory planning for robotic arms. The CCD camera can be considered as a sophisticated sensor, since it can extract a wide range of information in unstructured environment. Therefore, the CCD camera is very suitable for the control system that has a great demand on the capability to adapt to a new environment. On the other hand, the CCD camera can also obtain preview information. Such kind of information gives anticipatory capability to the control system. Parson and Zhang [19] suggested that an intelligent reference system for automated steering should possess anticipatory capability rather than compensatory behavior. The information from the preview image is available on

the feed-forward path of the controller. Although the output of the controller seems to be more stable and has less amount of overshoot, which gives a comfortable driving condition for the driver, the computational effort on a piece of information extracted from an image becomes larger. In other words, a large computational effort is needed before the data become meaningful (low-level representation) to the control system. Without preview of the road curvature, Fenton et al. [20] used root locus methods to select a steering controller and obtained a satisfactory performance in maintaining passenger comfort and safety.

The prevalent sliding mode and H_∞ [22-26] are likely to be the two most popular controller applied in automatic steering control of the road vehicle, as they have been theoretically proven and are robust to system modeling error and system disturbance [27]. In such a system with high order of dynamic non-linearity, such as vehicle steering, there remain many uncertain or unmeasurable states, such as road adhesion factor, slip angle, pneumatic tires deformation and aerodynamics factor. The automatic steering control is a very challenging problem to control engineers. Devotees of the sliding mode and H_∞ will test their proposed steering controller for the road vehicle in order to find new possibilities for the control system. With these nonlinear control methods, the autonomous vehicle can run as fast as 25m/s [25], and the controllers show an excellent robustness to model uncertainty. Although these nonlinear control methods are less dependent on system model precision, the laborious system model development cannot be avoided. The formulation of the system model is laborious, since repeated work on system modeling and analysis must be done before the formulation of the system model can be put into use in another system with different complexity and structure. Also, the fine tuning of the controller

is necessary after a period of operation because of the system's degradation. In this situation, knowledge transfer of the system controller's implicit operating principle becomes more important.

2.2 Multi-sensor System

Running in an unknown environment in which there are at least some basic information (i.e., static map), the primary requirements for the development of a fully automatically controlled road vehicle are its intelligent sensor system and an adaptive controller with a high degree of robustness to the uncertainties in the car/environment system.

An intelligent sensor system consists of vehicle local sensors, vehicle global sensors, a decision-maker and a integration/fusion module. The vehicle local sensors are used to measure the internal states of the vehicles with respect to the dynamic coordinate frame (fixed by the orientation of the vehicle). The vehicle global sensors are used to measure the states of the vehicle with respect to the absolute static coordinate frame (fixed by the oriental of the earth). With the use of the local sensors, the speed, displacement and heading angle can be measured. Some researchers used more sensors to observe or measure additional states, such as the use of CCD camera to observe the departure distance to the side of the road [44], the use of encoders to perform a real time estimation of adhesion characteristic [45] and the use of radar to measured the heading angle information of the vehicle. [46]. The use of these sensors enhanced the knowledge of the control system in terms of the response to changes or disturbances in such measured states. Some navigators that integrated all measuring devices have appeared in the market, such as Portable Advanced Navigation Support

(PANS) [47] and Modular Azimuth Positioning System (MAPS) [48]. These systems aim to locate the relative position and velocity of the vehicle and would be subjected to the operating time-dependent errors that need to be compensated by absolute position sensors, such as global positioning system (GPS) and digital magnetic compass (DMC).

In mid-1993, GPS reached its full operation status. Since then, the global coverage and the high accuracy can be achievable through GPS. GPS pinpoints the absolute longitude and latitude coordinate of a position on earth, receiving radio information from a network of satellites that orbit around the Earth. GPS can be considered a position fixed navigation system [82], since it determines position without references to any former position. Some of the GPS-based vehicle navigation systems can be found in [49] and [50]. Unfortunately, since July 1, 1991, the signal degradation by Selective Availability (SA) [51] was imposed on Block II satellites. At present, GPS for civilian use is said to have 100 m of radial error at 2 sigma, the equivalent of 40 m of CEP radius according to the Federal Radionavigation Plan (FRD). The purpose of the differential global position system (DGPS) is to ameliorate the effects of SA. DGPS can achieve positioning accuracy of 2-8 m RMS [52]. Besides, the GPS information may be unavailable or unreliable due to jamming susceptibility and shading effects by buildings or tree-covered area. However, no other system has yet been devised which serves the same functions and capability as GPS. During obscuration of satellite signals, the radio navigation system needs additional inputs to reflect the vehicle position.

Map Matching can be thought of as an enhanced or additional navigation scheme to Dead-Reckoning System. Map Matching aims to prevent the error from propagation by making correction for corners, such as at intersections or at some specific designed spots where their coordinates are recorded in a map database system. Sony Electronics MVX-F160 mobile navigation system is a system to utilize the GPS in combination with digital maps on CD-ROM, as developed by Etak Inc. [55]. There are also many improved MM techniques developed for and applied to commercial system [56-59]. J. B. Bullock has done a detailed research on the use of digital road maps in vehicle navigation [60]. From his research, we can see that, of a total of 147 vehicle navigation systems in the world, 89 use in-vehicle maps, with 35 employing map matching and 31 offering real-time route guidance. The MM scheme seems to be very popular among all other schemes in navigation system. On the other hand, the development of MM is obstructed by the unavailability of map databases, either technically or economically.

2.3 Sensors Integration/Fusion

The success of building a stand-alone navigation system depends very much on the choice of proper vehicle sensors. Gyro, wheel speed encoder, speedometer, accelerometer, magnetic field sensors, etc. are normally used in the measuring system of a navigation system [61-63]. The problem remaining includes how to integrate these sensors to become a reliable and accurate sensoring system. Sensor integration and fusion have then became popular areas for research. Sensor fusion can provide variables that are not directly measurable [61].

Bayesian's approach is a well-known fusion strategy. It is very useful in combining multiple sensor values. The state of the environment is decided based upon sensor measurements, prior knowledge about the types of states, as well as sensor uncertainty. However, Bayesian method shows difficulty in maintaining consistency when propositions are related. Also, it requires complete information since an independent measurement about the environment must be done. Dempster-Shafer approaches extend the Bayesian approaches in such a way that only an interval based upon the uncertainly needed to be computed. The Dempster-Shafer approach made use of Shafer-Dempster Evidential Reasoning whilst the Bayesian approach made use of maximum likelihood. The sensor fusion techniques discussed so far are known as static fusion methods and they show difficulty when used in dynamic multisensor model.

In addition, the optimal H_∞ control ithemself provide a mean of sensors integration [25]. The characteristic of each sensor can be model as in weighting functions either in frequency or time domain. That may be a reason that H_∞ control are extensively used in vehicle steering control. Also, a loosely coupled fusion of measured variables can be achieved by redundant use of sensors, which measure the same physical variable but they perform well on different operation range. A typical example [66] is the use of GPS and accelerometer as vehicle positioning sensors, GPS performs well in low dynamic range whilst accelerometer performs well in a dynamic range that is higher than that in GPS.

2.4 Mathematical Model of Vehicle

There are many vehicles models available in the research area of Advanced Vehicle Control System [91]. Some of them have frequently been referenced in the area of study. One of the most popular complex vehicle model has been developed [93] in conjunction with Johns Hopkins University Applied Physics Laboratory [94]. Another popular complex vehicle model was developed by Lugner [92]. Both vehicle model can described the vehicle dynamics on superelevated/ bank road surface, but not the vehicle dynamics on uphill/downhill(inclined) road surface.

Another complex vehicle model can be found in [88]. The model can describe the vehicle motion on 2-D road surface. In this study, the vehicle complex model will be presented based on the complex vehicle model developed in [88] and [92].

Smith [91] studied the effect of model complexity on the performance of vehicle steering controller. The simulation showed that tire nonlinearity is the dominant modeling factor. The study reported that tire nonlinearity contributed approximately 90% of travel distance errors, and 66% of the overshoot errors.

2.5 Conclusion of Literature Survey

To develop the control system in an autonomous vehicle, researchers aimed to develop a system with the following properties:

1. Large operating range
2. Robust to modeling error
3. Adaptive to the unstructured environment
4. Able to solve the global optimizing solution
5. Fast response (especially for highly dynamic system)
6. Guaranteed stability

In the current trends, researchers, on one side, focused their studies on the development of accurate tire model [45] since majority of nonlinear dynamics are believed to be owing to the forces reacted in the contact patch of each tire. However, researchers, on the other side, focused their studies on effective robust control design. They hoped that the control methodology can be robust enough to deal with the model uncertainty, resulting from the imperfect tire model explicitly developed, and/or higher mode unmodelled vehicle dynamics.

The effect of the dynamics of the vehicle on normal force acting on each tire has been studied in [17][88]. However, the effect on normal forces of static load and the variation in the vehicle dynamics on undulating road surface has long been left off. In papers [89], the superelevation angle are taken into account. The results of the simulation report the importance of the road geometry parameters in the steering tracking controller. In paper [90], the simulation on undulating road were done. The road surface is varying in a rather small scale that the four contact patches doesn't

form a plane. However, the conclusions are drawn to state the importance of the road geometry parameters in vehicle control maneuvers.

In the multisensor system of autonomous vehicle, map-matching is a very popular candidate, since MM is most suitable for use in the environment where there are at least some static information. Static information includes the location of buildings, cross-sections, T-joint sections, traffic lights, etc. If static information is stored, the vehicle can adapt to the dynamic objects within that environment. This matches very well to the practical situation. Moreover, there would be no need for modification of the environment.

In this study, the static information are collected and the reference path is virtually available for the control system through the reference path and 3-D road model. It is more or less the same as the methodology used in Map-matching. The difference is that the reference path is virtual and not a physical path for the vehicle tracking controller.

3. VEHICLE DYNAMIC MODEL

This section investigates the mechanics of the road vehicle and the mathematical approximation of the tire model. The models of the vehicle dynamics are developed, showing the effect of the undulating road surface on the steady-state and transient vehicle performance. The section draws on the assumption that the normal force on each tire is in the same direction. Thus, the profile of the road surface is changing in a global sense but is not changing on the region which is the projection of the vehicle body on the road surface. The tire model used in this paper is from [95], which concerns the lateral forces on each tire.

In the development of the vehicle model, the following assumptions are made:

1. The vehicle is running at a constant speed at all times, and the variation of speed due to cornering and the profile of the road is negligible.
2. The body of the vehicle can be treated as three separate point masses at their respective center of gravity in the front sprung, rear sprung and unsprung masses.
3. The dynamic forces resulting from pitching and rolling can be combined together to obtain the total dynamic forces on the vehicle, due to the rotation of the body along both the pitch and roll axes.
4. The road is even, and the road slant angles vary with time at a much slower rate, such that assumption (1) holds at all times.
5. The banking angle along the vehicle lateral axis and the inclination angle along the vehicle longitudinal axis are small enough such that the small angle assumption can be applied.

6. The vehicle suspension stretched-spring equation $\varepsilon_1+\varepsilon_3=\varepsilon_2+\varepsilon_4$ always holds.
7. The vehicle remains grounded such that the vehicle's four tires remain in contact with the ground at all times.
8. The aerodynamics forces and moments, and the tire-rolling resistance are negligible.

Figure 3.1 shows the forces acting on each tire and the basic notation of the parameters describing the base of the vehicle. Although F_{xi} and F_{yi} are shown alone, they are actually the forces induced by L_i, where i = 1,2,3,4 because there is no traction force on each tires.

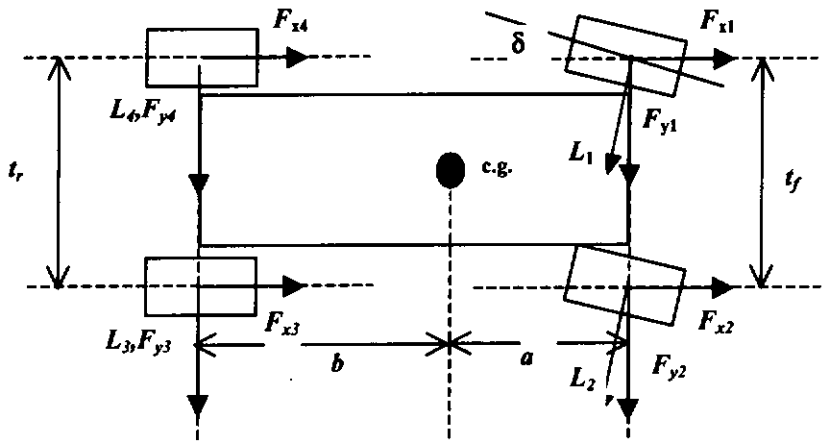

Figure 3.1 Vehicle Free Body Diagram

The coordinate systems are then defined in Figure 3.2 and the two coordinate systems, *XYZ* and *xyz*, are related by the following equations:

$$\begin{cases} \dot{X} = \dot{x}\cos\theta_z - \dot{y}\sin\theta_z \\ \dot{Y} = -\dot{x}\sin\theta_z - \dot{y}\cos\theta_z \end{cases} \qquad (3.1)$$

When a vehicle is running on a slanted road surface, the steepest angle of the road is obtained and defined as road banking angle. After making a free turning of a vehicle on the road surface, the deviation of θ_z can be measured. With the road banking angle

and $\Delta\theta_z$ known, the inclination angle with respect to the vehicle body, which is the angle between the longitudinal axis of the vehicle body and the projection of vehicle body on the horizontal plane, is calculated with simple geometric equations.

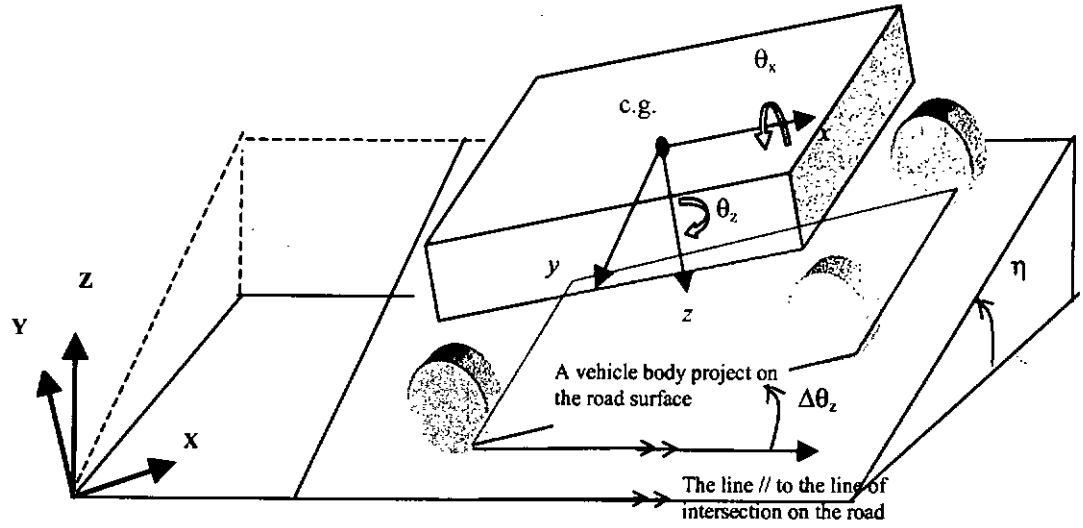

Figure 3.2 Vehicle Coordinate System

In developing vehicle mathematical model, the vehicle system is first decoupled into two sub-systems: System A & System B shown in the figure 3.3. The diagram between System A and System B shows the interconnection between these two systems. System A includes the unsprung mass of the vehicle system and System B includes two sprung masses in the vehicle body.

Firstly, the rolling dynamics of a vehicle is considered with η=0.

Considering the free body diagram in system A

and the moment balance equation,

$$mgl\sin\theta_x - M_R = I\ddot{\theta}_x + m\ddot{y}l\cos\theta_x \qquad (3.2)$$

where $M_R = K_{roll}\theta_x + B_{roll}\dot{\theta}_x$, K_{roll} and B_{roll} are the equivalent angular stiffness and angular damping coefficient along the rolling axis of the vehicle respectively.

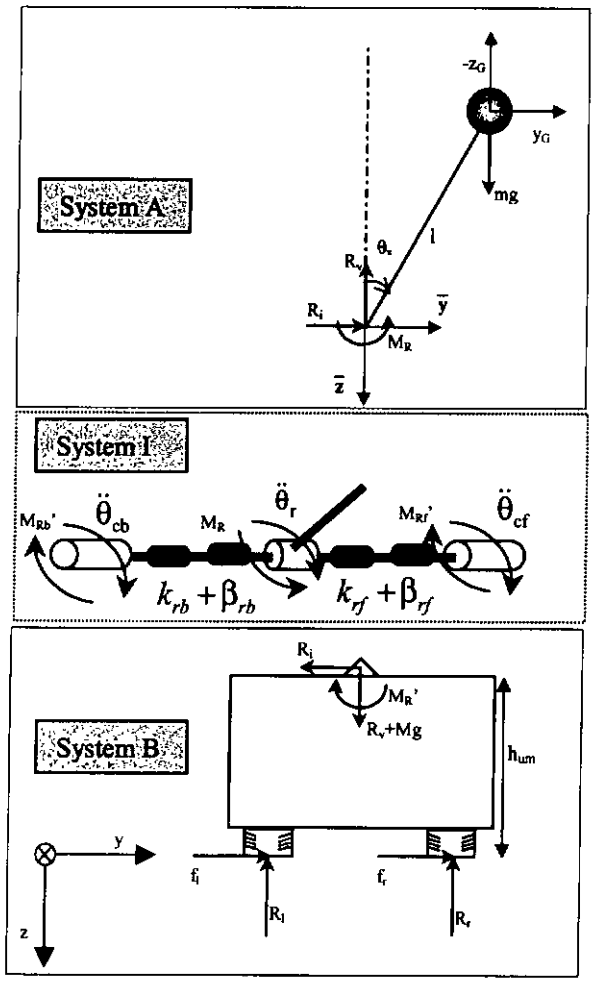

Figure 3.3 Vehicle Free Body Diagrams for System A & B

Considering the force balanced equations:

$$R_i = m\frac{d^2}{dt^2}(\bar{y} + y_G)$$
$$= m\frac{d^2}{dt^2}(\bar{y} + l\sin\theta_x) \qquad (3.3)$$

$$R_v - mg = -m\frac{d^2}{dt^2}(z_G)$$
$$= -m\frac{d^2}{dt^2}(l\cos\theta_x) \qquad (3.4)$$

Note that $\bar{z}$ has positive quantity in downward direction and θ_x has positive quantity clockwise when viewing from the back of the vehicle.

Now, considering the free body diagram in system B

and the moment balance equation, assuming $t = t_f = t_r$

$$R_l \frac{t}{2} + M_R' = F_s h_{um} + R_r \frac{t}{2} \qquad (3.5)$$

where h_{um} is the height of the unsprung mass from the rolling axis and $F_s = f_l + f_r$.

From this point forward, the subscribe x in θ_x , I_x are dropped for simplification.

Considering the force balance equations,

$$F_s = f_l + f_r = M\ddot{y} + R_i \qquad (3.6)$$

$$R_l + R_r = Mg + R_v \qquad (3.7)$$

From equation (3.3),

$$\begin{aligned} R_i &= m(\ddot{y} + l\cos\theta\ddot{\theta} - l\sin\theta\dot{\theta}^2) \\ &= m(\ddot{y} + l\ddot{\theta} - l\theta\dot{\theta}^2) \quad , assume \cos\theta = 1 \,\&\, \sin\theta = \theta \; when \; \theta \; is \; small \\ &= m(\ddot{y} + l\ddot{\theta}) \quad , assume \; \theta\dot{\theta}^2 \approx 0 \; when \; \theta \; is \; small \end{aligned} \qquad (3.8)$$

From equation (3.4),

$$\begin{aligned} mg - R_v &= ml(-\cos\theta\dot{\theta}^2 - \sin\theta\ddot{\theta}) \\ &= ml(-\dot{\theta}^2 - \theta\ddot{\theta}) \quad , assume \cos\theta = 1 \,\&\, \sin\theta = \theta \; when \; \theta \; is \; small \\ &\approx 0 \quad , assume \; \dot{\theta}^2, \theta\ddot{\theta} \approx 0 \; when \; \theta \; and \; \dot{\theta} \; are \; both \; small \end{aligned} \qquad (3.9)$$

$\therefore R_v = mg$

Putting equation (3.8) into equation (3.6),

$$F_s - m(\ddot{y} + l\ddot{\theta}) = M\ddot{y}$$

$$F_s = (M + m)\ddot{y} + l\ddot{\theta} \qquad (3.10)$$

To obtain the resultant moment acting on System B, the relative rotational motion between the unsprung and the sprung masses must be considered:

$$M_R' - M_R = I\ddot{\theta}$$
$$\therefore M_R' = M_R + I\ddot{\theta}$$
using equation (3.2),
$$\therefore M_R' = -m\ddot{y}l\cos\theta + mgl\sin\theta \qquad (3.11)$$

i.e., the reaction moment acting on the unsprung mass is $-m\ddot{y}l\cos\theta + mgl\sin\theta$

Since the stiffness and the damping force at the rear and front part of the vehicle are not the same, the distribution of the reaction moment at the rear (M_{Rb}') and the front (M_{Rf}') is written as follows:

$$M_{Rf}' = \frac{k_{rf}\theta + \beta_{rf}\dot{\theta}}{K_{roll}\theta + B_{roll}\dot{\theta}} M_R' \qquad (3.12)$$
$$M_{Rb}' = \frac{k_{rb}\theta + \beta_{rb}\dot{\theta}}{K_{roll}\theta + B_{roll}\dot{\theta}} M_R'$$

Using equations (3.5), (3.7), (3.11), R_l and R_r can be solved:

$$\begin{cases} R_l + R_r = (M+m)g \\ R_l - R_r = \frac{2}{t}(F_s h_{um} + m\ddot{y}l\cos\theta - mgl\sin\theta) \end{cases}$$

$$\Rightarrow \begin{cases} R_l = \frac{1}{2}[(M+m)g + \frac{2}{t}(F_s h_{um} + m\ddot{y}l\cos\theta - mgl\sin\theta)] \\ R_r = \frac{1}{2}[(M+m)g - \frac{2}{t}(F_s h_{um} + m\ddot{y}l\cos\theta - mgl\sin\theta)] \end{cases}$$

$$\Rightarrow \begin{cases} R_1 + R_4 = \frac{1}{2}(M+m)g + \frac{1}{t}[(M+m)\ddot{y}h_{um} + ml\ddot{\theta}h_{um} + m\ddot{y}l\cos\theta - mgl\sin\theta] \\ R_2 + R_3 = \frac{1}{2}(M+m)g - \frac{1}{t}[(M+m)\ddot{y}h_{um} + ml\ddot{\theta}h_{um} + m\ddot{y}l\cos\theta - mgl\sin\theta] \end{cases} \qquad (3.13)$$

By considering system B in Figure 3.3, the force and moment on the 3-dimensional free body diagram is obtained in System B' shown in Figure 3.4.

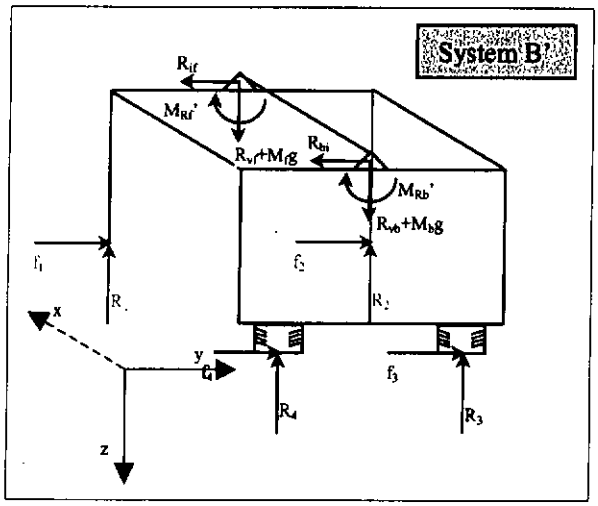

Figure 3.4 Vehicle Free Body Diagram, System B'

However, the individual reaction force on each tire is difficult to solve. Thus assumptions 3.1, 3.2, 3.3. are made,

Assumption 3.1: The vertical reactions forces are distributed on the front and rear unsprung masses in a ratio of b:a

Assumption 3.2 The horizontal reactions forces are distributed on the front and rear unsprung masses in a ratio of b:a

Assumption 3.3 The reaction moment are distributed on front and rear unprung masses in a ration of k_{rf} : k_{rb} *(hereafter, k_f and k_b for simplification).*

Considering the forces on the x-y plane and using the moment balance equation $bR_{ib} = aR_{if}$,where a, b are defined in figure 3.1.

The force balance equation,

$$R_{ib} + R_{if} = R_i$$

$$\Rightarrow \begin{cases} R_{if} = \frac{b}{a+b} R_i \\ R_{ib} = \frac{a}{a+b} R_i \end{cases}$$, by assumption 3.1

Also, considering the forces and moment on the x-z plane,

$$\Rightarrow \begin{cases} R_{vf} = \frac{b}{a+b} R_v \\ R_{vb} = \frac{a}{a+b} R_v \end{cases}, \text{ by assumption 3.2}$$

$$\text{and} \begin{cases} K\theta + B\dot{\theta} = k_f\theta + \beta_f\dot{\theta} + k_b\theta + \beta_b\dot{\theta} \\ K\theta + B\dot{\theta} = (k_f + k_b)\theta + (\beta_f + \beta_b)\dot{\theta} \\ K\theta = (k_f + k_b)\theta \end{cases}$$

$$\text{then } M_R' = M_{Rf}' + M_{Rb}'$$

$$\frac{M_R'}{K} = \frac{M_{Rf}'}{k_f} = \frac{M_{Rb}'}{k_b}$$

$$\Rightarrow \begin{cases} M_{Rf}' = \frac{k_f}{k_f + k_b} M_R' \\ M_{Rb}' = \frac{k_b}{k_f + k_b} M_R' \end{cases}, \text{ by assumption 3.3}$$

$$\therefore R_2 + R_1 = R_{vf} + M_f g = \frac{b}{a+b} mg + M_f g$$

$$R_1 - R_2 = \frac{2}{t}(F_{sf} h_f - M_{Rf}')$$

where h_f is the height of the front unsprung mass from the rolling axis and F_{sf} is the side force acting at the front of the vehicle.

$$\Rightarrow \begin{cases} R_1 = \frac{1}{2}(\frac{b}{a+b} mg + M_f g) + \frac{1}{t}(F_{sf} h_f - M_{Rf}') \\ R_2 = \frac{1}{2}(\frac{b}{a+b} mg + M_f g) - \frac{1}{t}(F_{sf} h_f - M_{Rf}') \end{cases} \quad (3.14)$$

Similarity,

$$\Rightarrow \begin{cases} R_3 = \frac{1}{2}(\frac{a}{a+b} mg + M_b g) - \frac{1}{t}(F_{sb} h_b - M_{Rb}') \\ R_4 = \frac{1}{2}(\frac{a}{a+b} mg + M_b g) + \frac{1}{t}(F_{sb} h_b - M_{Rb}') \end{cases} \quad (3.15)$$

where h_b is the height of the front unsprung mass from the rolling axis and F_{sb} is the side force acting at the rear of the vehicle.

Obviously, corresponding to equations (3.14) and (3.15), R_1+R_4 and R_2+R_3 are not equivalent to that in equation (3.13), due to the difference between h_{um}, $h_f$and h_b. If h_{um}=h_f=h_r, then equations R_1+R_4 and R_2+R_3 are equivalent to that in equation (3.13).

Now, R_1, R_2, R_3 and R_4 can each be interpreted.

$$\begin{cases} R_1 = \frac{1}{2}(\frac{b}{a+b}m + M_f)g + \frac{1}{t}(F_{sf}h_f - M_{Rf}') \\ R_2 = \frac{1}{2}(\frac{b}{a+b}m + M_f)g - \frac{1}{t}(F_{sf}h_f - M_{Rf}') \\ R_3 = \frac{1}{2}(\frac{a}{a+b}m + M_b)g - \frac{1}{t}(F_{sb}h_b - M_{Rb}') \\ R_4 = \frac{1}{2}(\frac{a}{a+b}m + M_b)g + \frac{1}{t}(F_{sb}h_b - M_{Rb}') \end{cases} \qquad (3.16)$$

where $F_{sf} = (M_f + \frac{b}{a+b}m)\ddot{y} + \frac{b}{a+b}ml\ddot{\theta}_r$

$F_{sb} = (M_b + \frac{a}{a+b}m)\ddot{y} + \frac{a}{a+b}ml\ddot{\theta}_r$

$\therefore R_{i,i=1,2,3,4}$ is the reaction force on the ith tire resulting from the static weight, the dynamic force induced by the moment resulting from the contact force on the ith tire, and the dynamic force induced by the rolling moment of the sprung mass on the vehicle base.

$$\begin{cases} R_1 = \frac{1}{2}(\frac{b}{a+b}m + M_f)g + \frac{1}{t}[(M_f + \frac{b}{a+b}m)\ddot{y}h_f + \frac{b}{a+b}ml\ddot{\theta}_x h_f + \frac{k_f}{k_f+k_b}(m\ddot{y}l\cos\theta_x - mgl\sin\theta_x)] \\ R_2 = \frac{1}{2}(\frac{b}{a+b}m + M_f)g - \frac{1}{t}[(M_f + \frac{b}{a+b}m)\ddot{y}h_f + \frac{b}{a+b}ml\ddot{\theta}_x h_f + \frac{k_f}{k_f+k_b}(m\ddot{y}l\cos\theta_x - mgl\sin\theta_x)] \\ R_3 = \frac{1}{2}(\frac{a}{a+b}m + M_b)g - \frac{1}{t}[(M_b + \frac{a}{a+b}m)\ddot{y}h_b + \frac{a}{a+b}ml\ddot{\theta}_x h_b + \frac{k_b}{k_f+k_b}(m\ddot{y}l\cos\theta_x - mgl\sin\theta_x)] \\ R_4 = \frac{1}{2}(\frac{a}{a+b}m + M_b)g + \frac{1}{t}[(M_b + \frac{a}{a+b}m)\ddot{y}h_b + \frac{a}{a+b}ml\ddot{\theta}_x h_b + \frac{k_b}{k_f+k_b}(m\ddot{y}l\cos\theta_x - mgl\sin\theta_x)] \end{cases} \qquad (3.17)$$

Equation (3.17) has the same form as given in equations (27)-(30) of [88].

Considering the small bank angle of the road, η, the dynamic force has an additional term $(M+m)g\sin\eta$ in F_s. Thus, $F_s = (M+m)\ddot{y} + ml\ddot{\theta}_x - (M+m)g\sin\eta$ and the additional parameter, η, is absorbed in M_R', resulting in $M_R' = -m\ddot{y}l\cos\theta_r + mgl\sin(\theta_r + \eta)$. However, the static reaction (normal) forces acting on each tire are refined with geometric consideration and will be considered later. Moreover, $\theta_p(t>0)$ is no longer equal to zero. The calculation of the pitching dynamics of the vehicle is found in the *Appendix A*.

After obtaining the dynamic part on each reaction force $R_{i,\ i=1,2,3,4}$, the static part on each reaction force is now investigated.

The lateral weight transfer ratio at the tires due to the road slant angle is defined by equation (3.18).

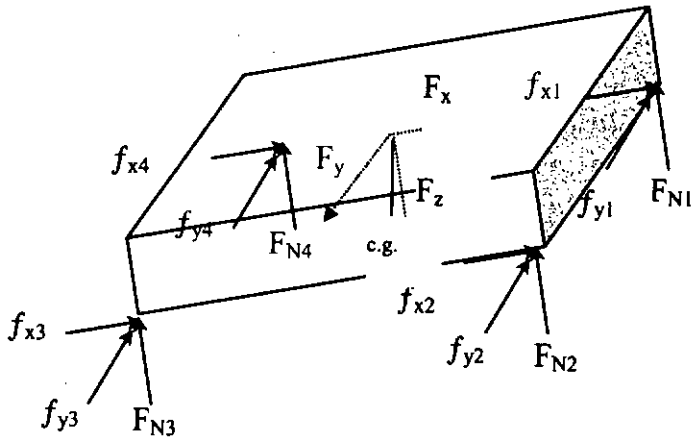

Figure 3.5 Static Reaction Forces on Each Tire

$$\begin{cases} F_{N1}+F_{N2}=(hF_x+bF_z)/(a+b) \\ F_{N2}+F_{N3}=(hF_y+\frac{1}{2}t_fF_z)/t_f \\ F_{N3}+F_{N4}=(aF_z-hF_x)/(a+b) \\ F_{N4}+F_{N1}=(\frac{1}{2}t_fF_z-hF_y)/t_f \\ \varepsilon_1+\varepsilon_3=\varepsilon_2+\varepsilon_4 \Rightarrow \frac{F_{N1}}{k_1}+\frac{F_{N3}}{k3}=\frac{F_{N2}}{k2}+\frac{F_{N4}}{k4} \end{cases} \qquad (3.18)$$

$$\text{where } \begin{aligned} F_x &= M_{tot}g\sin\theta_x\sin\theta_z \\ F_y &= M_{tot}g\sin\theta_x\cos\theta_z \\ F_z &= M_{tot}g\cos\theta_x \end{aligned}, \quad \theta_x=\eta, \quad M_{tot}=M+m$$

Therefore, the normal forces acting on the four tires are

$$F_{DNi}=F_{Ni}+F_{DPi}+F_{DRi},\ \mathrm{i}=1,2,3,4 \qquad (3.19)$$

where F_{DPi} = dynamic force resulting from pitching

F_{DRi} = dynamic force resulting from rolling

F_{Ni} = static force resulting from road slant angle

Together with the pitching dynamics, the total reaction force on each tire ,$R_{tot\ i,\ i=1,2,3,4}$, can be obtained as follows,

$$\begin{cases} R_{tot1} = F_{N1} + \frac{1}{t}\{(M_f + \frac{b}{a+b}m)(\ddot{y} - g\sin\eta)h_f + \frac{b}{a+b}ml\ddot{\theta}_x h_f + \frac{k_f}{k_f+k_b}[m\ddot{y}l\cos\theta_x - mgl\sin(\theta_x+\eta)]\} \\ \qquad -\frac{1}{a+b}\frac{1}{2}[(M+m)(\ddot{x} + g\sin\zeta)h_{cg} - ml\ddot{\theta}_y h_{cg} + m\ddot{x}l\cos\theta_y + mgl\sin(\theta_y+\zeta)] \\ R_{tot2} = F_{N2} - \frac{1}{t}\{(M_f + \frac{b}{a+b}m)(\ddot{y} - g\sin\eta)h_f + \frac{b}{a+b}ml\ddot{\theta}_x h_f + \frac{k_f}{k_f+k_b}[m\ddot{y}l\cos\theta_x - mgl\sin(\theta_x+\eta)]\} \\ \qquad -\frac{1}{a+b}\frac{1}{2}[(M+m)(\ddot{x} + g\sin\zeta)h_{cg} - ml\ddot{\theta}_y h_{cg} + m\ddot{x}l\cos\theta_y + mgl\sin(\theta_y+\zeta)] \\ R_{tot3} = F_{N3} - \frac{1}{t}\{(M_b + \frac{a}{a+b}m)(\ddot{y} - g\sin\eta)h_b + \frac{a}{a+b}ml\ddot{\theta}_x h_b + \frac{k_r}{k_f+k_b}[m\ddot{y}l\cos\theta_x - mgl\sin(\theta_x+\eta)]\} \\ \qquad +\frac{1}{a+b}\frac{1}{2}[(M+m)(\ddot{x} + g\sin\zeta)h_{cg} - ml\ddot{\theta}_y h_{cg} + m\ddot{x}l\cos\theta_y + mgl\sin(\theta_y+\zeta)] \\ R_{tot4} = F_{N4} + \frac{1}{t}\{(M_b + \frac{a}{a+b}m)(\ddot{y} - g\sin\eta)h_b + \frac{a}{a+b}ml\ddot{\theta}_x h_b + \frac{kr}{k_f+k_b}[m\ddot{y}l\cos\theta_x - mgl\sin(\theta_x+\eta)]\} \\ \qquad +\frac{1}{a+b}\frac{1}{2}[(M+m)(\ddot{x} + g\sin\zeta)h_{cg} - ml\ddot{\theta}_y h_{cg} + m\ddot{x}l\cos\theta_y + mgl\sin(\theta_y+\zeta)] \end{cases} \quad (3.20)$$

where h_{cg}, η, ζ are height of the c.g. of the vehicle base, road bank angle and road inclination angle respectively.

To obtain the dynamic equations of the vehicle, the total forces acting on the vehicle in the x and y directions are first written.

$$F_x = \sum_{i=1}^{4} F_{xi} = M_{tot}a_x + M_{tot}g\sin\zeta - ml\ddot{\theta}_y = M(\ddot{x} - \dot{y}\dot{\theta}_z) + Mg\sin\zeta - ml\ddot{\theta}_y \quad (3.21)$$

$$F_y = \sum_{i=1}^{4} F_{yi} = M_{tot}a_y - M_{tot}g\sin\eta + ml\ddot{\theta}_x = M(\ddot{y} + \dot{x}\dot{\theta}_z) - Mg\sin\eta + ml\ddot{\theta}_x \quad (3.22)$$

and the total torque acting about the z-axis is written as below,

$$\Gamma_z = a(F_{y1} + F_{y2}) - b(F_{y3} + F_{y4}) + \frac{t_f}{2}(F_{x1} - F_{x2}) + \frac{t_r}{2}(F_{x3} - F_{x4}) \quad (3.23)$$
$$= I_z\ddot{\theta}_z$$

3.1 Vehicle Tire Model

After calculating the normal force acting on each tire, the lateral force acting at the point of contact of each tire can be obtained by using Segel's model [95]. The model is shown below:

$$L_i = \frac{C_{\alpha_i} \tan\alpha_i}{1-\lambda_s} f(S_i),$$

where

$$S_i = \frac{\mu R_i (1-\varepsilon_v U\sqrt{\lambda_s^2 + \tan^2\alpha_i})}{2\sqrt{C_x^2\lambda_s^2 + C_{\alpha_i}^2 \tan^2\alpha_i}}(1-\lambda_s),$$

and

$$f(S_i) = \begin{cases} S_i(2-S_i) & \text{if } S_i < 1 \\ 1 & \text{if } S_i \geq 1 \end{cases} \quad \text{for } i = 1,2,3,4.$$

The expressions for the slip angles are of the form:

$$\alpha_1 = \delta_f - \arctan\frac{\dot{y} + a\dot{\theta}_z}{\dot{x} + \frac{t}{2}\dot{\theta}_z},$$

$$\alpha_2 = \delta_f - arctan\frac{\dot{y} + a\dot{\theta}_z}{\dot{x} - \frac{t}{2}\dot{\theta}_z},$$

$$\alpha_3 = arctan\frac{b\dot{\theta}_z - \dot{y}}{\dot{x} - \frac{t}{2}\dot{\theta}_z},$$

$$\alpha_4 = arctan\frac{b\dot{\theta}_z - \dot{y}}{\dot{x} + \frac{t}{2}\dot{\theta}_z}.$$

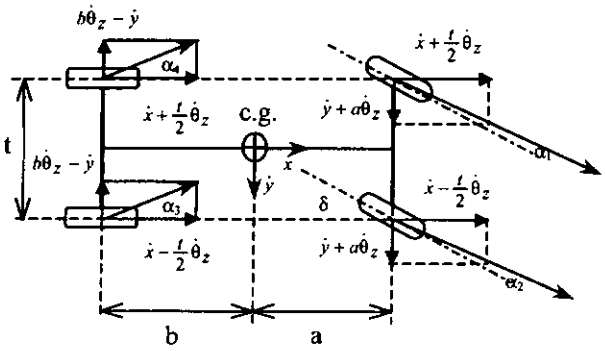

Figure 3.1.1 The Definition of Slip Angles

The above expressions are written under the assumption that the vehicle is undergoing understeering during the majority of the turning maneuvers. This is desirable from a directional stability point of view, since the increased understeer at higher lateral accelerations would provide the required stability during tight turns. In order to visualize the effect of the slip angle and normal force on the lateral force for the *i*th

tire, L_i is plotted against slip angle α_i and normal force R_i in Figure 3.1.2

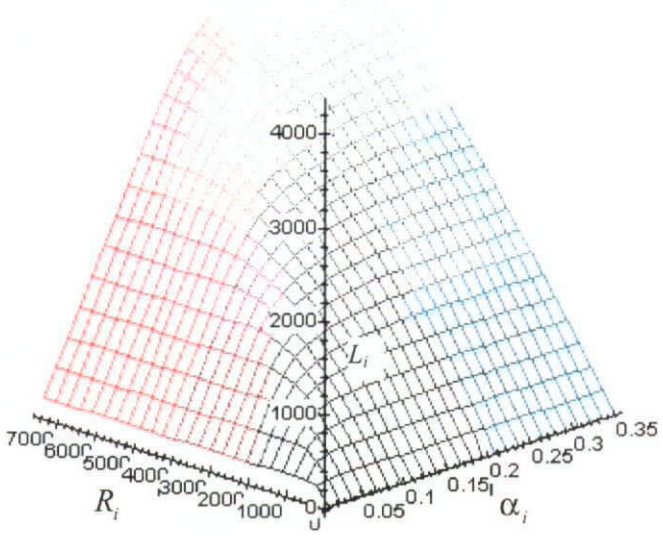

Figure 3.1.2 The Effect of R_i and α_i on L_i

From the formula for *f(S)* in Segel's model, $f(S) = 1$ for $S>1$. To investigated the effect of R_i and α_i on *f(S)*, the plot of *S* against R_i *and* α_i are shown in Figure 3.1.3.

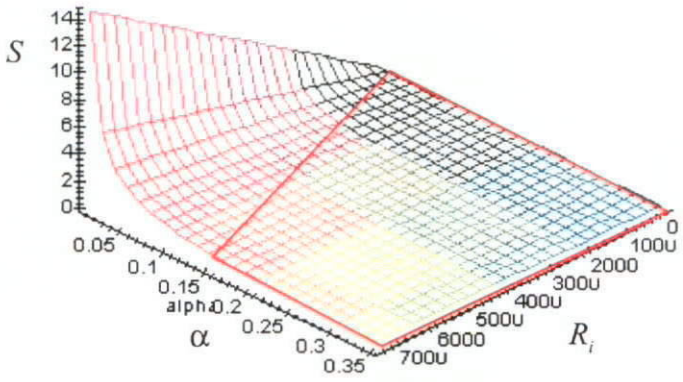

Figure 3.1.3 The Effect of R_i and α_i on S

In Figure 3.1.3, we see that $S>1$ as long as α_i and R_i extend beyond the region encircled by the red line. The solution for α in the equation $S=1$ for varying R_i is illustrated in Figure 3.1.4.

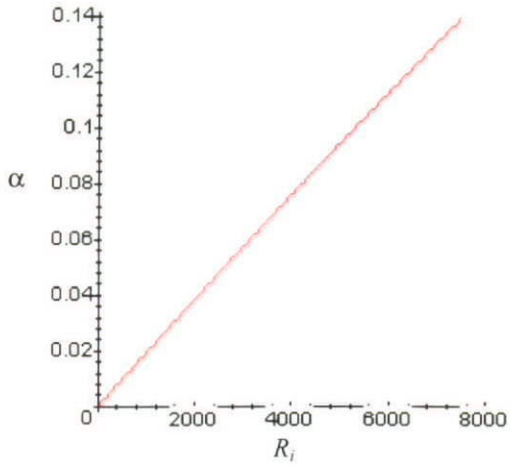

Figure 3.1.4 Solution for α in S=1

The equation to relate R_i and α_{max} is

$R_i=53681x\alpha_{max}$

where α_{max} is the maximum value of α that makes $S \geq 1$ and thus $f(S)=1$. Thereby, $L_i= C_{\alpha i}tan\alpha_i$ is a sufficient equation to obtain the lateral force from Segel's tire model, with other model parameters, collected in [95], fixed as follows:

$\mu := .78$
$U := 18.3$
$\varepsilon_v := .015$
$\lambda_s := 0$
$C_x := 50000$
$C_{\alpha i} := 20000$

Actually, $f(S)$ can be considered as the correction factor for the lateral forces. It is interesting to examine the value of $f(S)$ with both α_i and R_i lying within the region as shown in Figure 3.1.5.

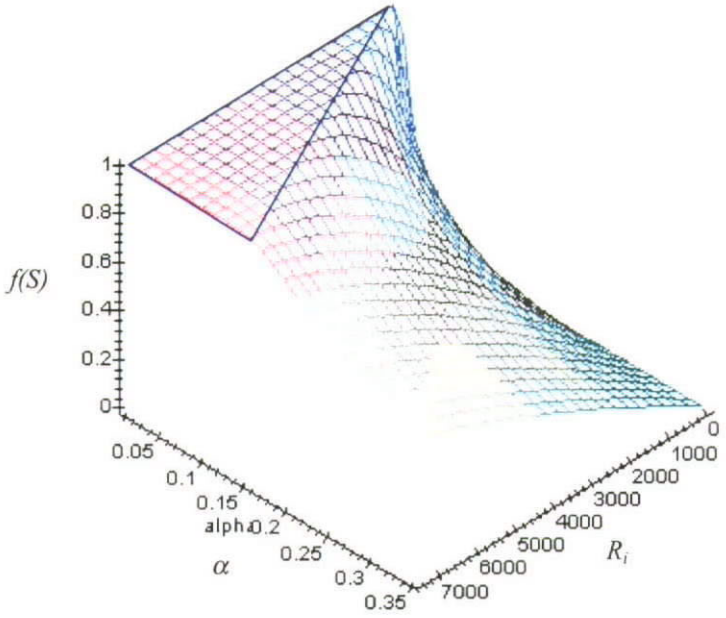

Figure 3.1.5 Effect of R_i and α_i on f(S)

From Figure 3.1.5, we see that the approximate tire model, $L_i = C_{\alpha i} tan\alpha_i$ would no longer hold if the slip angle is too large and/or the reaction force is too small. Segel's model includes the nonlinear properties in the vehicle model. With the assumption that the dynamic force will not bring the normal reaction force of a tire down below 2000 N from the nominal value of about 3666.5 N and the maximum possible slip angle of 0.3 rad, the maximum error on lateral force calculated with the simplified tire model is 78.2%. If the lateral force is further linearized by $L_i = C_\alpha \alpha_i$, then the maximum error of the lateral force calculated would become 83.6%, because the error in the approximation of tan α_i by α_i is approximately 3.01%.

3.2 Complex Vehicle Model

Recall equations (3.2), (3.21), (3.22), (3.23) and (A1.1),

Note that $\theta_r = \theta_x$, $\theta_p = \theta_y$.

$$mgl\sin\theta_r - K_{roll}\theta_r - B_{roll}\dot{\theta}_r = I_x\ddot{\theta}_r + m(\ddot{y} + \dot{x}\dot{\theta}_z)l\cos\theta_r$$

$$F_x = M_{tot}(\ddot{x} - \dot{y}\dot{\theta}_z) + M_{tot}g\sin\zeta - ml\ddot{\theta}_p$$

$$F_y = M_{tot}(\ddot{y} + \dot{x}\dot{\theta}_z) - M_{tot}g\sin\eta + ml\ddot{\theta}_r$$

$$\Gamma_z = I_z\ddot{\theta}_z$$

$$mgl\sin\theta_p - K_{pitch}\theta_p - B_{pitch}\dot{\theta}_p = I_y\ddot{\theta}_p - m(\ddot{x} - \dot{y}\dot{\theta}_z)l\cos\theta_p$$

Let $\mathbf{X} = [\ddot{x} \quad \ddot{y} \quad \ddot{\theta}_z \quad \ddot{\theta}_r \quad \ddot{\theta}_p]^T$

$$\begin{bmatrix} \ddot{x} \\ \ddot{y} \\ \ddot{\theta}_z \\ \ddot{\theta}_r \\ \ddot{\theta}_p \end{bmatrix} = \begin{bmatrix} M_{tot} & 0 & 0 & 0 & -ml \\ 0 & M_{tot} & 0 & ml & 0 \\ 0 & 0 & I_z & 0 & 0 \\ 0 & ml\cos\theta_r & 0 & I_x & 0 \\ ml\cos\theta_p & 0 & 0 & 0 & -I_y \end{bmatrix}^{-1} \begin{bmatrix} M_{tot}\dot{y}\dot{\theta}_z - M_{tot}g\sin\zeta + F_x \\ -M_{tot}\dot{x}\dot{\theta}_z + M_{tot}g\sin\eta + F_y \\ \Gamma_z \\ -K_{roll}\theta_r - B_{roll}\dot{\theta}_r + mgl\sin(\theta_r + \eta) - m\dot{x}\dot{\theta}_z l\cos\theta_r \\ K_{pitch}\theta_p + B_{pitch}\dot{\theta}_p - mgl\sin(\theta_p + \zeta) + m\dot{y}\dot{\theta}_z l\cos\theta_p \end{bmatrix}$$

Let $\Lambda_p = -M_{tot}I_y + (mh)^2\cos\theta_p$

$\Lambda_r = -M_{tot}I_x + (mh)^2\cos\theta_r$

$$\begin{bmatrix} \ddot{x} \\ \ddot{y} \\ \ddot{\theta}_z \\ \ddot{\theta}_r \\ \ddot{\theta}_p \end{bmatrix} = \begin{bmatrix} \frac{-I_y(M_{tot}\dot{y}\dot{\theta}_z - M_{tot}g\sin\zeta) + mh(mh\dot{y}\dot{\theta}_z - mgh\sin(\theta_p+\zeta) + B_{pitch}\dot{\theta}_p + K_{pitch}\theta_p)}{\Lambda_p} \\ \frac{-I_x(-M_{tot}\dot{x}\dot{\theta}_z + M_{tot}g\sin\eta + mh(-m\dot{x}\dot{\theta}_z h + mgh\sin(\theta_r+\eta) - B_{roll}\dot{\theta}_r - K_{roll}\theta_r)}{\Lambda_r} \\ 0 \\ \frac{mh\cos(\theta_r)(-M_{tot}\dot{x}\dot{\theta}_z + M_{tot}g\sin\eta) - M_{tot}(-m\dot{x}\dot{\theta}_z h + mgh\sin(\theta_r+\eta) - B_{roll}\dot{\theta}_r - K_{roll}\theta_r)}{\Lambda_r} \\ \frac{-mh\cos(\theta_y)(M_{tot}\dot{y}\dot{\theta}_z - M_{tot}g\sin\zeta) + M_{tot}(m\dot{y}\dot{\theta}_z h - mgh\sin(\theta_p+\zeta) + B_{pitch}\dot{\theta}_p + K_{pitch}\theta_p)}{\Lambda_p} \end{bmatrix} + \begin{bmatrix} \frac{-I_y F_x}{\Lambda_p} \\ \frac{-I_x F_y}{\Lambda_r} \\ \frac{\Gamma_z}{I_z} \\ \frac{mh\cos\theta_r F_y}{\Lambda_r} \\ \frac{-mh\cos\theta_p F_x}{\Lambda_p} \end{bmatrix} \qquad (3.24)$$

where , as mentioned in the very beginning of the chapter, F_x and F_y are the induced force of L_i and can be obtained by the following equations:

$$\begin{aligned} F_x &= F_{x1} + F_{x2} + F_{x3} + F_{x4} = -(L_1 + L_2)\sin\delta \\ F_y &= F_{y1} + F_{y2} + F_{y3} + F_{y4} = (L_1 + L_2)\cos\delta + L_3 + L_4 \\ \Gamma_z &= a(L_1 + L_2)\cos\delta - b(L_3 + L_4) + \tfrac{t_f}{2}(L_2 - L_1)\sin\delta \end{aligned} \qquad (3.25)$$

Up to this point, the simulated vehicle model has been developed. The procedure to obtaine the state of the vehicle is shown below:

Step 1 - Calculate the normal reaction force on each tire.

Step 2 - Calculate the lateral force via Segel's tire model.

Step 3 - With the lateral force on each tire known, calculate the total force acting in the x and y directions and the torque about the z axis.

Step 4 - Obtain the interested state of the vehicle using equation (3.24) by numerical integration.

3.3 Complex Vehicle Model in State Space

This section converted the model developed in the last section into a state space formulation. Recalling equation (3.24) and applying the small angle assumption on $\theta_r, \theta_p, \zeta, \eta$, the equation becomes:

$$\begin{bmatrix} \ddot{x} \\ \ddot{y} \\ \ddot{\theta}_z \\ \ddot{\theta}_r \\ \ddot{\theta}_p \end{bmatrix} = \underbrace{\begin{bmatrix} \dot{y}\dot{\theta}_z - g\zeta + \frac{-(mh)^2 g\theta_p + mhB_{pitch}\dot{\theta}_p + mhK_{pitch}\theta_p)}{\Lambda_p'} \\ -\dot{x}\dot{\theta}_z + g\eta + \frac{(mh)^2 g\theta_r - mhB_{roll}\dot{\theta}_r - mhK_{roll}\theta_r)}{\Lambda_r'} \\ 0 \\ \frac{-M_{tot}(mhg\theta_r - B_{roll}\dot{\theta}_r - K_{roll}\theta_r)}{\Lambda_r'} \\ \frac{M_{tot}(-mhg\theta_p + B_{pitch}\dot{\theta}_p + K_{pitch}\theta_p)}{\Lambda_p'} \end{bmatrix}}_{\text{matrix } A} + \underbrace{\begin{bmatrix} \frac{-l_y F_x}{\Lambda_p'} \\ \frac{-l_x F_y}{\Lambda_r'} \\ \frac{\Gamma_z}{I_z} \\ \frac{mh\cos\theta_r F_y}{\Lambda_r'} \\ \frac{-mh\cos\theta_p F_x}{\Lambda_p'} \end{bmatrix}}_{\text{matrix } B} \qquad (3.26)$$

$$\Lambda_p' = -M_{tot} I_y + (mh)^2$$

$$\Lambda_r' = -M_{tot} I_x + (mh)^2$$

Putting the equation (3.25) into the matrix B in equation (3.26),

$$\begin{bmatrix} \frac{-I_y}{\Lambda_p'} & 0 & 0 \\ 0 & \frac{-I_x}{\Lambda_r'} & 0 \\ 0 & 0 & \frac{1}{I_z} \\ 0 & \frac{mh}{\Lambda_r'} & 0 \\ \frac{-mh}{\Lambda_p'} & 0 & 0 \end{bmatrix} \begin{bmatrix} F_x \\ F_y \\ \Gamma_z \end{bmatrix} \rightarrow \begin{bmatrix} \frac{-I_y}{\Lambda_p'} & 0 & 0 \\ 0 & \frac{-I_x}{\Lambda_r'} & 0 \\ 0 & 0 & \frac{1}{I_z} \\ 0 & \frac{mh}{\Lambda_r'} & 0 \\ \frac{-mh}{\Lambda_p'} & 0 & 0 \end{bmatrix} \left[\begin{bmatrix} -(L_1+L_2) \\ 0 \\ \frac{tf}{2}(L_2-L_1) \end{bmatrix} \delta + \begin{bmatrix} 0 \\ L_1+L_2+L_3+L_4 \\ a(L_1+L_2)-b(L_3+L_4) \end{bmatrix} \right]$$

$$\rightarrow \begin{bmatrix} \frac{I_y}{\Lambda_p'}(L_1+L_2) \\ 0 \\ \frac{1}{I_z}\frac{tf}{2}(L_2-L_1) \\ 0 \\ \frac{mh}{\Lambda_p'}(L_1+L_2) \end{bmatrix} \delta + \begin{bmatrix} 0 \\ \frac{-I_x}{\Lambda_r'}(L_1+L_2+L_3+L_4) \\ \frac{1}{I_z}\{a(L_1+L_2)-b(L_3+L_4)\} \\ \frac{mh}{\Lambda_r'}(L_1+L_2+L_3+L_4) \\ 0 \end{bmatrix}$$

Now, the maximum error involved in the new matrix B will be investigated. The error involved in replacing $sin\delta$ by δ is 6.5% when δ_{max} is supposed to be 0.61 rad. Moreover, the error involved in replacing $cos\delta$ by 1 is about 22%. Therefore, L_1 and L_2 each suffers from maximum error of 22%. As a whole, together with the error obtained in the linearized Segel's tire model, L_1 and L_2 each suffers from the maximum error of 123.95%, while L_3 and L_4 each suffer from maximum error of 83.56%.

Writing equation (3.26) into state space form,

$$\begin{bmatrix} \dot{x} \\ \ddot{x} \\ \dot{y} \\ \ddot{y} \\ \dot{\theta}_z \\ \ddot{\theta}_z \\ \dot{\theta}_r \\ \ddot{\theta}_r \\ \dot{\theta}_p \\ \ddot{\theta}_p \end{bmatrix} = \begin{bmatrix} 0 & 1 & 0 & 0 & 0 & 0 & 0 & 0 & 0 & 0 \\ 0 & 0 & 0 & \dot{\theta}_z & 0 & 0 & 0 & 0 & \frac{mh(K_{pitch}-mhg)}{\Lambda_p'} & \frac{mhB_{pitch}}{\Lambda_p'} \\ 0 & 0 & 0 & 1 & 0 & 0 & 0 & 0 & 0 & 0 \\ 0 & -\dot{\theta}_z & 0 & 0 & 0 & 0 & \frac{mh(mhg-K_{roll})}{\Lambda_r'} & \frac{-mhB_{roll}}{\Lambda_r'} & 0 & 0 \\ 0 & 0 & 0 & 0 & 0 & 1 & 0 & 0 & 0 & 0 \\ 0 & 0 & 0 & 0 & 0 & 0 & 0 & 0 & 0 & 0 \\ 0 & 0 & 0 & 0 & 0 & 0 & 0 & 1 & 0 & 0 \\ 0 & 0 & 0 & 0 & 0 & 0 & \frac{-M_{tot}(mhg-K_{roll})}{\Lambda_r'} & \frac{M_{tot}B_{roll}}{\Lambda_r'} & 0 & 0 \\ 0 & 0 & 0 & 0 & 0 & 0 & 0 & 0 & 0 & 1 \\ 0 & 0 & 0 & 0 & 0 & 0 & 0 & 0 & \frac{M_{tot}(-mhg+K_{pitch})}{\Lambda_p'} & \frac{M_{tot}B_{pitch}}{\Lambda_p'} \end{bmatrix} \begin{bmatrix} x \\ \dot{x} \\ y \\ \dot{y} \\ \theta_z \\ \dot{\theta}_z \\ \theta_r \\ \dot{\theta}_r \\ \theta_p \\ \dot{\theta}_p \end{bmatrix} +$$

System Matrix A

$$\underbrace{\begin{bmatrix} 0 \\ \frac{I_y}{\Lambda_p'}(L_1+L_2) \\ 0 \\ 0 \\ 0 \\ \frac{1}{I_z}\frac{tf}{2}(L_2-L_1) \\ 0 \\ 0 \\ 0 \\ \frac{mh}{\Lambda_p'}(L_1+L_2) \end{bmatrix}}_{\text{Matrix B}} \delta + \underbrace{\begin{bmatrix} 0 \\ -g\zeta \\ 0 \\ \frac{-I_x}{\Lambda_r'}(L_1+L_2+L_3+L_4)+g\eta \\ 0 \\ \frac{1}{I_z}\{a(L_1+L_2)-b(L_3+L_4)\} \\ 0 \\ \frac{mh}{\Lambda_r'}(L_1+L_2+L_3+L_4) \\ 0 \\ 0 \end{bmatrix}}_{\text{Matrix L}}, \qquad (3.27)$$

3.4 Vehicle Design Model

In this section, a vehicle design model is obtained from the complex vehicle model developed in section 3.3. The design model includes the lateral, roll and yaw motions of the mass center of the vehicle. It is expressed in state space form as below,

$$\dot{X} = \begin{bmatrix} \ddot{y} \\ \dot{\varepsilon}_r \\ \dot{y}_r \\ \ddot{\theta}_z \\ \dot{\theta}_r \\ \ddot{\theta}_r \end{bmatrix} = \begin{bmatrix} 0 & 0 & 0 & -U & A3 & A4 \\ 0 & 0 & 0 & 1 & 0 & 0 \\ 1 & U & 0 & 0 & 0 & 0 \\ 0 & 0 & 0 & 0 & 0 & 0 \\ 0 & 0 & 0 & 0 & 0 & 1 \\ 0 & 0 & 0 & 0 & A9 & A0 \end{bmatrix} \begin{bmatrix} \dot{y} \\ \varepsilon_r \\ y_r \\ \dot{\theta}_z \\ \theta_r \\ \dot{\theta}_r \end{bmatrix} + \begin{bmatrix} g & 0 \\ 0 & -1 \\ 0 & 0 \\ 0 & 0 \\ 0 & 0 \\ 0 & 0 \end{bmatrix} \begin{bmatrix} \eta \\ \dot{\theta}_d \end{bmatrix} + \begin{bmatrix} D1 \\ 0 \\ 0 \\ D2 \\ 0 \\ D3 \end{bmatrix}. \qquad (3.28)$$

$$D_1 = -\frac{I_x}{\Lambda_r'}(L_1+L_2+L_3+L_4)$$

where $D_2 = \frac{1}{I_z}(a(L_1+L_2)-b(L_3+L_4))$

$$D_3 = \frac{mh}{\Lambda_r'}(L_1+L_2+L_3+L_4)$$

$$\Rightarrow \begin{cases} D_1 = -\dfrac{I_x}{\Lambda_r}(2C_f(\delta - \dfrac{\dot{y}+a\dot{\theta}_z}{U}) + 2C_r(\dfrac{b\dot{\theta}_z - \dot{y}}{U})) \\ D_2 = \dfrac{1}{I_z}(2aC_f(\delta - \dfrac{\dot{y}+a\dot{\theta}_z}{U}) - 2bC_r(\dfrac{b\dot{\theta}_z - \dot{y}}{U})) \\ D_3 = \dfrac{mh}{\Lambda_r}(2C_f(\delta - \dfrac{\dot{y}+a\dot{\theta}_z}{U}) + 2C_r(\dfrac{b\dot{\theta}_z - \dot{y}}{U})) \end{cases}$$

$$\Rightarrow \begin{cases} D_1 = -\dfrac{I_x}{\Lambda_r}(2C_f\delta - 2C_f\dfrac{\dot{y}+a\dot{\theta}_z}{U} + 2C_r\dfrac{b\dot{\theta}_z - \dot{y}}{U}) \\ D_2 = \dfrac{1}{I_z}(2aC_f\delta - 2aC_f\dfrac{\dot{y}+a\dot{\theta}_z}{U} - 2bC_r(\dfrac{b\dot{\theta}_z - \dot{y}}{U})) \\ D_3 = \dfrac{mh}{\Lambda_r}(2C_f\delta - 2C_f\dfrac{\dot{y}+a\dot{\theta}_z}{U} + 2C_r\dfrac{b\dot{\theta}_z - \dot{y}}{U}) \end{cases}$$

$$\Rightarrow \begin{cases} D_1 = -\dfrac{I_x}{\Lambda_r}(2C_f\delta - 2C_f\dfrac{\dot{y}}{U} - 2C_r\dfrac{\dot{y}}{U} - 2C_f\dfrac{a\dot{\theta}_z}{U} + 2C_r\dfrac{b\dot{\theta}_z}{U}) \\ D_2 = \dfrac{1}{I_z}(2aC_f\delta - 2aC_f\dfrac{\dot{y}}{U} + 2bC_r\dfrac{\dot{y}}{U} - 2aC_f\dfrac{a\dot{\theta}_z}{U} - 2bC_r\dfrac{b\dot{\theta}_z}{U}) \\ D_3 = \dfrac{mh}{\Lambda_r}(2C_f\delta - 2C_f\dfrac{\dot{y}}{U} - 2C_r\dfrac{\dot{y}}{U} - 2C_f\dfrac{a\dot{\theta}_z}{U} + 2C_r\dfrac{b\dot{\theta}_z}{U}) \end{cases}$$

$$\Rightarrow \begin{cases} D_1 = -\dfrac{I_x}{\Lambda_r}(2C_f\delta - \dot{y}(2C_f\dfrac{1}{U} + 2C_r\dfrac{1}{U}) - \dot{\theta}_z(2aC_f\dfrac{1}{U} - 2bC_r\dfrac{1}{U})) \\ D_2 = \dfrac{1}{I_z}(2aC_f\delta - \dot{y}(2aC_f\dfrac{1}{U} - 2bC_r\dfrac{1}{U}) - \dot{\theta}_z(2a^2C_f\dfrac{1}{U} - 2b^2C_r\dfrac{1}{U})) \\ D_3 = \dfrac{mh}{\Lambda_r}(2C_f\delta - \dot{y}(2C_f\dfrac{1}{U} + 2C_r\dfrac{1}{U}) - \dot{\theta}_z(2aC_f\dfrac{1}{U} - 2bC_r\dfrac{1}{U})) \end{cases}$$

$$\Rightarrow \begin{cases} D_1 = -2C_f\dfrac{I_x}{\Lambda_r}\delta + \dfrac{I_x}{\Lambda_r}(2C_f\dfrac{1}{U} + 2C_r\dfrac{1}{U})\dot{y} + \dfrac{I_x}{\Lambda_r}(2aC_f\dfrac{1}{U} - 2bC_r\dfrac{1}{U})\dot{\theta}_z \\ D_2 = 2aC_f\dfrac{1}{I_z}\delta - \dfrac{1}{I_z}(2aC_f\dfrac{1}{U} - 2bC_r\dfrac{1}{U})\dot{y} - \dfrac{1}{I_z}(2a^2C_f\dfrac{1}{U} - 2b^2C_r\dfrac{1}{U})\dot{\theta}_z \\ D_3 = 2C_f\dfrac{mh}{\Lambda_r}\delta - \dfrac{mh}{\Lambda_r}(2C_f\dfrac{1}{U} + 2C_r\dfrac{1}{U})\dot{y} - \dfrac{mh}{\Lambda_r}(2aC_f\dfrac{1}{U} - 2bC_r\dfrac{1}{U})\dot{\theta}_z \end{cases}$$

$$\dot{X} = \begin{bmatrix} \ddot{y} \\ \dot{\varepsilon}_r \\ \dot{y}_r \\ \ddot{\theta}_z \\ \dot{\theta}_r \\ \ddot{\theta}_r \end{bmatrix} = \begin{bmatrix} \frac{2I_x(C_f+C_r)}{U\Lambda_r} & 0 & 0 & -U + \frac{2I_x(aC_f-bC_r)}{U\Lambda_r} & \frac{m^2h^2g-mhK_r}{\Lambda_r} & \frac{-mhB_r}{\Lambda_r} \\ 0 & 0 & 0 & 1 & 0 & 0 \\ 1 & U & 0 & 0 & 0 & 0 \\ \frac{-2(aC_f-bC_r)}{UI_z} & 0 & 0 & \frac{-2(a^2C_f+b^2C_r)}{UI_z} & 0 & 0 \\ 0 & 0 & 0 & 0 & 0 & 1 \\ \frac{-2mh(C_r+C_f)}{U\Lambda_r} & 0 & 0 & \frac{-2mh(aC_f-bC_r)}{U\Lambda_r} & \frac{-Mmhg+MK_r}{\Lambda_r} & \frac{MB_r}{\Lambda_r} \end{bmatrix} \begin{bmatrix} \dot{y} \\ \varepsilon_r \\ y_r \\ \dot{\theta}_z \\ \theta_r \\ \dot{\theta}_r \end{bmatrix}$$

$$+\begin{bmatrix} g & 0 \\ 0 & -1 \\ 0 & 0 \\ 0 & 0 \\ 0 & 0 \\ 0 & 0 \end{bmatrix}\begin{bmatrix} \eta \\ \dot{\theta}_d \end{bmatrix}+\begin{bmatrix} \frac{-2l_xC_f}{\Lambda_r} \\ 0 \\ 0 \\ \frac{2aC_f}{I_z} \\ 0 \\ \frac{2mhC_f}{\Lambda_r} \end{bmatrix}\delta \qquad (3.29)$$

3.5 Steering Actuator Dynamics

The electromechanical steering system consists of dc servomotors, electrical control clutch and gear trains. The dc servomotor is driven by a servodriver. The servodriver controls the motion of the dc servomotor with point-to-point positioning. Armature control of dc servomotors is used, since the time constant of the armature-controlled dc motor is generally small, as compared to the time constant of a field-controlled dc motor. The layout of the armature control of a dc servomotor is given in the following figure:

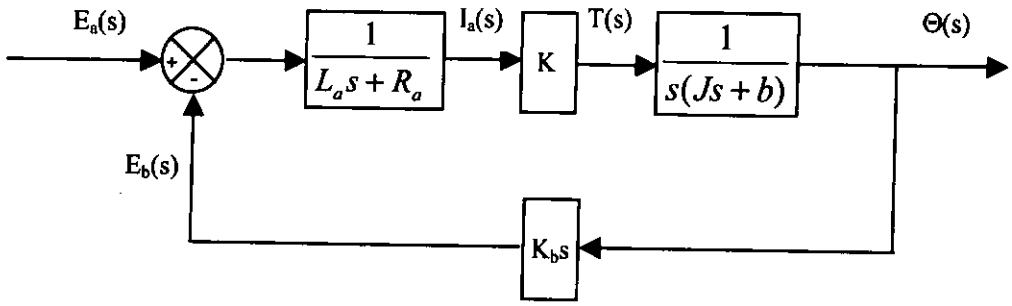

Figure 3.5.1 Block Diagram of Armature Control of Steering Mechanism

In the system,

R_a = *armature resistance, 12.1 Ω*

L_a = *armature inductance, negligibly small*

i_a = *armature current, 2.8 A max*

i_f = *field current*

e_a = *applied armature voltage*

e_b = *back emf*

θ = *angular displacement of the motor shaft*

T = *torque developed by the motor, 0.235 Nm max*

J_{eq} = *equivalent moment of inertia of the motor and load referred to the motor shaft*

B_{eq} = *equivalent viscous fiction coefficient of the motor and load referred to the motor shaft*

The transfer function for the dc servomotor is easily obtained as:

$$\frac{\Theta(s)}{E_a(s)} = \frac{K}{s[L_a J_{eq} s^2 + (L_a B_{eq} + R_a J_{eq})s + R_a B_{eq} + KK_b]}$$

where K = torque constant, 0.182 NmA^{-1}

K_b = back emf constant, 0.182 $V/rads^{-1}$

J_{eq} and B_{eq} are calculated as follows:

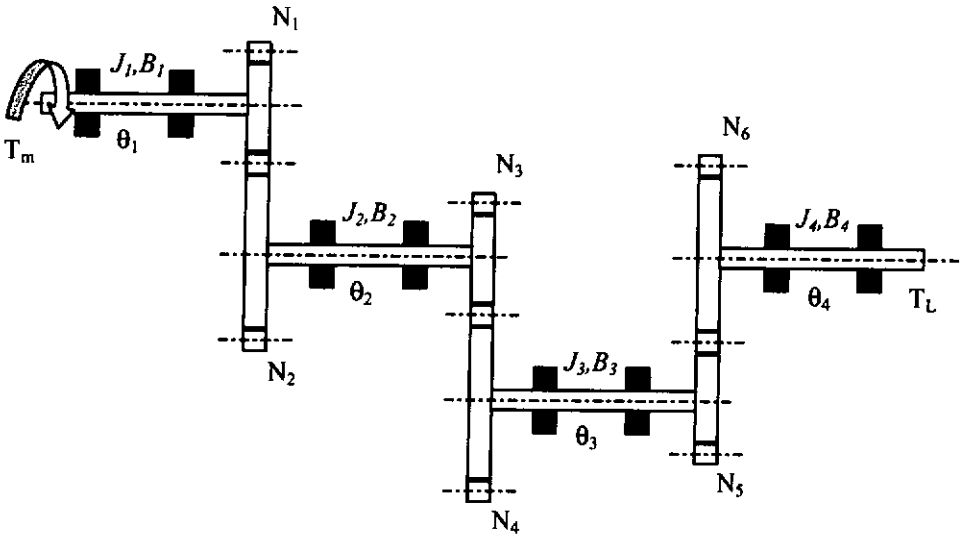

Figure 3.5.2 Gear Box in Steering Maneuver

With N_1:N_2=1:50, N_3:N_4=1:2, N_5:N_6=1:12.86

J_1=*Motor inertia,* 0.214x10^{-4} Kgm^2

B_1=*Motor viscous friction,* 0.38875x10^{-2} Nm/rad/sec

J_2=*Gear box inertia, with nominal value of* 0.5x10^{-5} Kgm^2

B_2=*Gear box viscous friction, with nominal value of* 2x10^{-3} Nm/rad/sec

J_3=*Steering shaft inertia, with nominal value of* 1x10^{-5} Kgm^2

B_3=*Steering shaft viscous fiction, with nominal value of* 2x10^{-3} Nm/rad/sec

J_4=*Steering mechanism inertia, with nominal value of* 0.918x10^{-2} Kgm^2

B_4=*Steering mechanism viscous-fiction, with nominal value of* 2x10^{-3} Nm/rad/sec

The equivalent moment of inertia J_{eq} referred to the motor shaft and equivalent viscous friction coefficient B_{eq} referred to the motor shaft are written as:

$$J_{eq} = J_1 + \left(\frac{N_1}{N_2}\right)^2 J_2 + \left(\frac{N_1}{N_2}\right)^2\left(\frac{N_3}{N_4}\right)^2 J_3 + \left(\frac{N_1}{N_2}\right)^2\left(\frac{N_3}{N_4}\right)^2\left(\frac{N_5}{N_6}\right)^2 J_4 = 2.1409\,x\,10^{-5}$$

$$B_{eq} = B_1 + \left(\frac{N_1}{N_2}\right)^2 B_2 + \left(\frac{N_1}{N_2}\right)^2\left(\frac{N_3}{N_4}\right)^2 B_3 + \left(\frac{N_1}{N_2}\right)^2\left(\frac{N_3}{N_4}\right)^2\left(\frac{N_5}{N_6}\right)^2 B_4 = 3.8885\,x\,10^{-3}$$

Since the inductance L_a in the armature circuit is usually small and may be neglected, the transfer function of the servo system reduces to

$$\frac{\Theta(s)}{E_a(s)} = \frac{K_m}{s(T_m s + 1)}$$

where $T_m = R_a J_{eq}/(R_a B_{eq} + KK_b)$, $= 2.467 \times 10^{-3}$

$K_m = K/(R_a B_{eq} + KK_b)$, $= 1.734$

3.5.1 Servo Control System

To control the servo system, a command angular position $\Theta_d(s)$ is input to the servo control system. A simple servo control system is shown below:

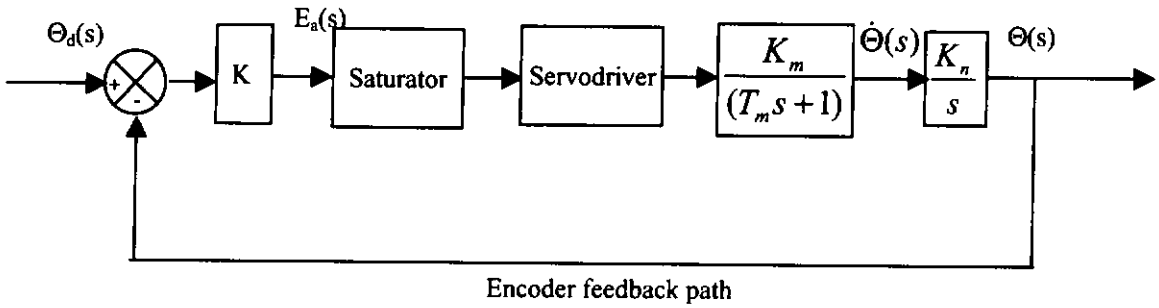

Figure 3.5.1.1 Block Diagram of Servo Control System

where the transfer function of the servodriver is written in a very simplified version of the mathematical model, say $\frac{K_s}{T_E s + 1}$. Moreover, $K_n = (N_1/N_2)(N_3/N_4)(N_5/N_6)$

$=7.776\text{x}10^{-4}$, K_s = voltage gain in the servodriver = 7.5, K = controller gain and T_E = electrical time constant = $0.47\text{x}10^{-3}$.

The transfer function is

$$\frac{\theta_o}{\theta_d} = \frac{KK_sK_mK_n}{s(T_Es+1)(T_ms+1)+KK_sK_mK_n}$$

Now, define $K_1=KK_sK_mK_n$. Then, the transfer function can be written as:

$$\frac{\theta_o}{\theta_d} = \frac{K_1}{T_{s1}s^3+T_{s2}s^2+s+K_1}$$

where $T_{s1} = T_ET_m = 1.1597x10^{-6}$ and $T_{s2}=T_E+T_m = 0.00294$

Let $G(s)$ be the open loop transfer function of the system,

$$G(s) = \frac{K_1}{s(T_{s1}s^2+T_{s2}s+1)}$$

The root locus plotted with G(s) is shown in Figure 3.5.1.2.

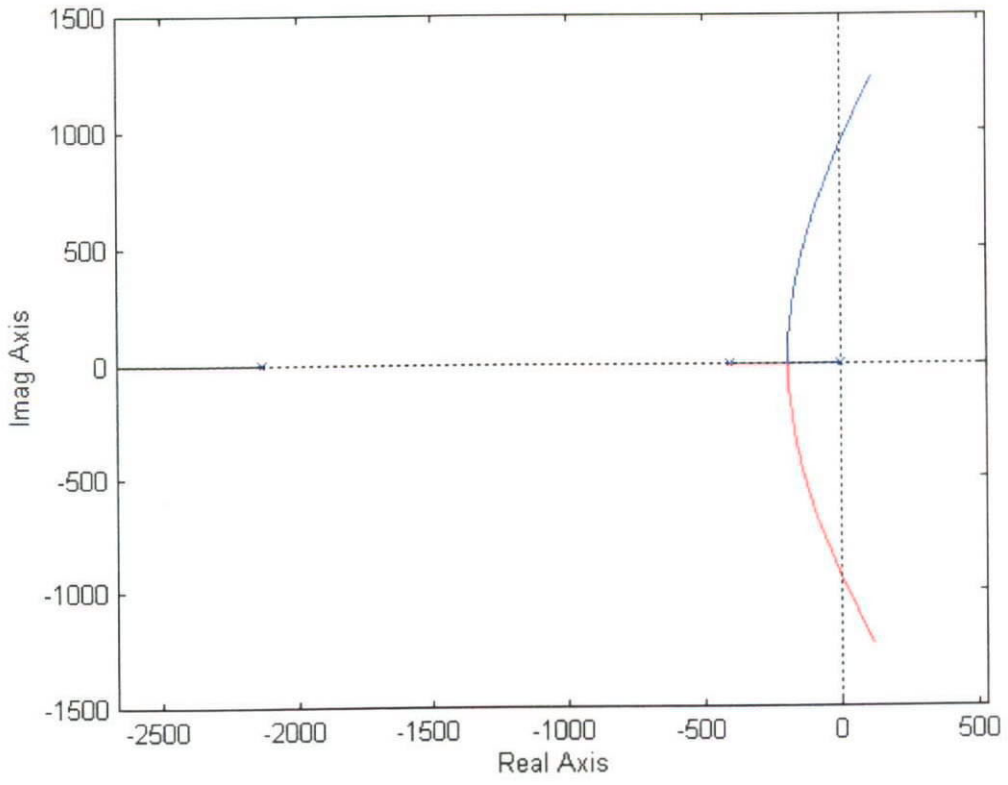

Figure 3.5.1.2 Root Locus of G(s)

With the help of Matlab Control Toolbox, the system gain at the breakaway point is found in the root locus plot of the system. The system gain is 9.0907×10^3 at the breakaway point (K_c). Thus, the system will not sustain oscillation with system gain below K_c. Although the system will have a good performance when the gain is chosen such that the dominant closed-loop poles are complex conjugate pair, the system gain is too large that the control variable is saturated in the practical system. Therefore, an applicable system gain is selected such that the system performance is optimized. In fact, if the system gain is selected under the condition that the control variable does not saturate, the transient response of the system would be too slow to be applicable. Thus, the system gain is maximized in the transient response but is small towards the end of the transient state. Then, the system gain is chosen such that a control variable is saturated in the transient state and becomes small towards the end of the transient response of the system.

The system closed-loop poles are located at

-2.1281×10^3, -0.4028×10^3, -0.0020×10^3

The system gain selected is 2×10^2, and the system response for step input and sine input is shown below:

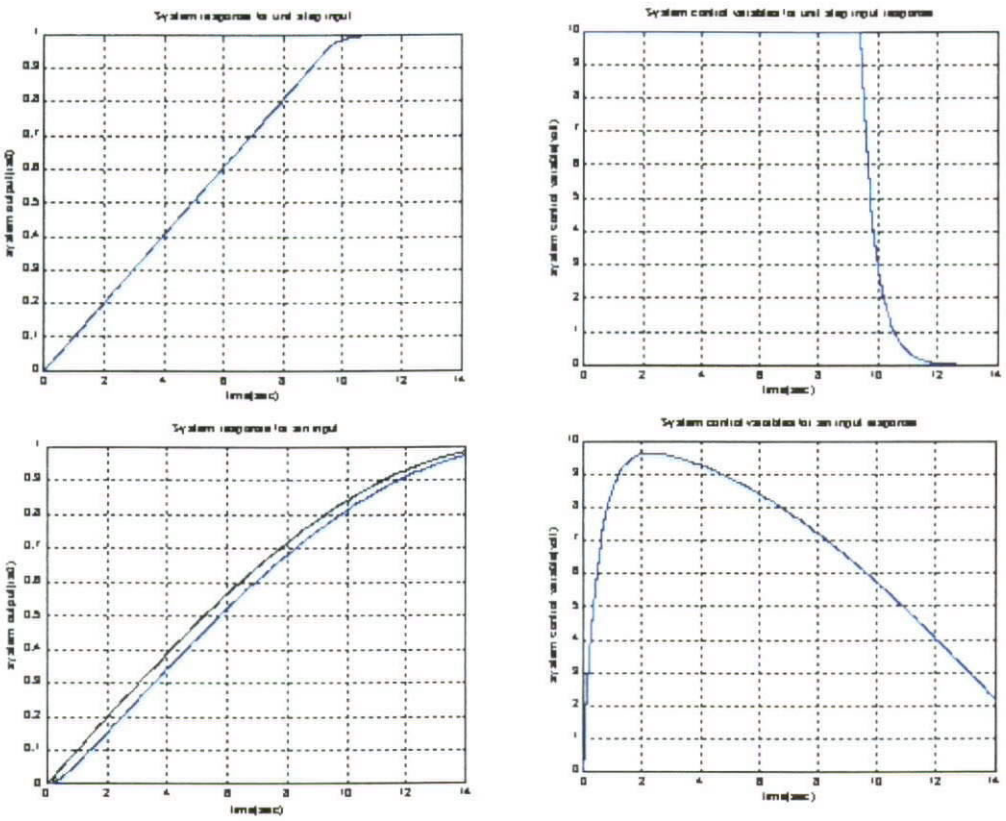

Figure 3.5.1.3 System Response of Steering Mechanism

From figure 3.5.1.3, it shows that the system response of the steering mechanism follow both the unit step and sin system input well enough for practical implementation. For the sin system input the deviation of the system response from the desired input does not exceed 0.08rad.

4. NAVIGATION SCHEME IN 3-DIMENSIONAL SPACE

This study investigates the effect of the road profile on the vehicle handling performance. The vehicle is not assumed to be running on the flat road surface. Rather, the assumption is taken away to cope with the more realistic situation of a vehicle running on the three-dimensional road surface. Although most highway infrastructures are as straight and flat as possible, highways are unavoidably inclined when running across a mountain or when the superelevation angle (bank angle) is constructed on each turn of the highway. An effective navigation scheme should be able to fully describe the behavior of the vehicle with respect to a reference coordinate frame and be easily linked up with a control system.

Consider the following road profile:

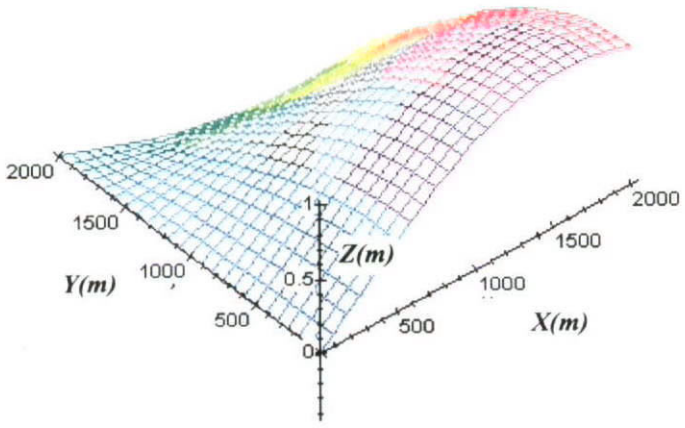

Figure 4.1 Profile of the Road (Surface R)

In Figure 4.1, the change of Z is very slow with respect to X and Y, and thus the assumption (4) made in chapter 3 holds throughout the study. The maximum slope on the surface R is about 0.001, and thus the maximum inclination of the road surface R

is 0.001 rad. In the design of the control and navigation system for this study, the maximum inclination angle is 0.2 rad (11.5 degrees).

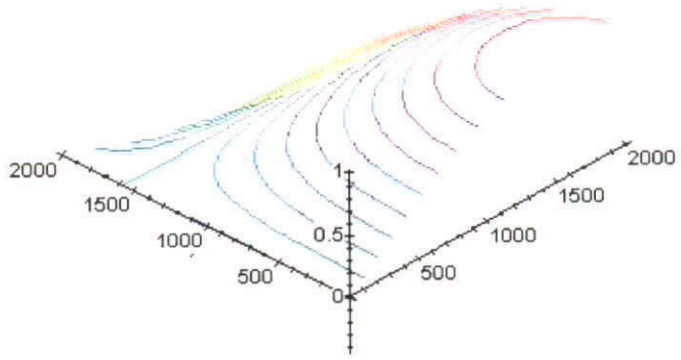

Figure 4.2 Contour Map of Surface R

Figure 4.1 is redrawn with the above contour plot. The red line on Figure 4.2 is the path of the vehicle across the surface *R*. The contour line each indicates the specific height with reference to the water level height. The steepest slope of any point is located at the tangent of that point on the blue line. In other words, the blue line is perpendicular to each contour line at the point of intersection. In order to introduce the method to describe the behavior of the vehicle on the three-dimensional road surface, the top view of Figure 4.2 is shown below:

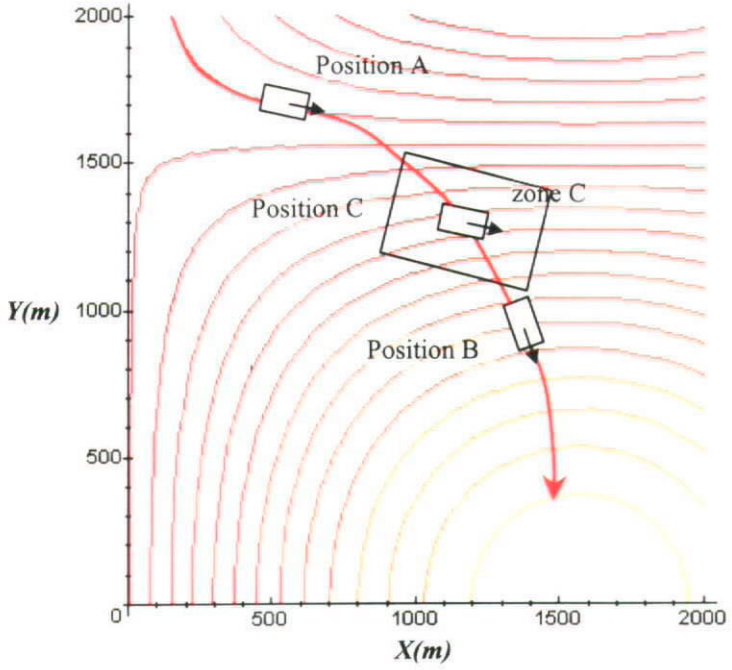

Figure 4.3 2-D Contour Map of Surface R

Note: The car shown in Figure 4.3 is not in scale with the road surface

Figure 4.3 shows two particular positions of the vehicle on the surface *R*--position A and position B. At position A, with reference to the vehicle, the road exhibits banking angle η and no inclined angle ($\zeta=0$), and the passenger would feel that the vehicle is inclined solely on his side, i.e. at constant roll angle. At position B, with reference to the vehicle, the road exhibits inclined angle ζ,and no banking angle ($\eta=0$), and the passenger would feel that the vehicle is inclined solely on his line of sight, i.e. at constant pitch angle.

Every slanted road surface has a direction that is steepest when going up the road. Every slanted road surface also has a direction that will enable a person to make the least effort in moving about on the road. We will call this the restful direction. When a person is moving in this restful direction, the steepest direction is to his left (we

don't consider the case where the steepest direction is to the right of the person). In this study, the steepest angle of a road surface is called road-banking angle. Every time a person moves on the road surface, he is moving in the direction in which the steepest direction is on his left. If this is not the case, then the person has made an initial angle away from the restful direction. However, when a person goes on the road surface, the only information he can have is from his feeling about the side force and the forward/backward force. The person may know where the steepest direction is, but he may not know how much he has moved away from the restful direction. Therefore, from the point of view of a person standing on a slanted road surface, he should be able to tell the side angle (banking angle) and the forward/backward angle (inclination angle), but he may not be able to tell the steepest angle immediately. For a vehicle on a slanted road surface, the side angle of the vehicle is vehicle banking angle and the forward/backward angle is vehicle inclination angle, or simply banking angle and inclination angle. The vehicle banking angle and vehicle inclination angle should not be confused with the roll angle and the pitch angle, respectively. The roll angle is due to the side force acting on the vehicle, and the pitch angle is due to the forward/backward force acting on the vehicle.

In what follows, the focus is kept on zone *C* of Figure 4.3, where the vehicle is at position *C*. The method to locate the position and the behavior of the vehicle is discussed later.

4.1 Reference Frame

Development of the inertial navigation theory requires the precise definitions of a number of coordinate frame. Two of these are related to the geometry of the earth

relative to an inertial frame of reference, while the other one defines a set of vehicle axes. All frames are orthogonal, right-handed coordinate frames. Three additional frames are introduced to define the sets of platform, gyro, and accelerometer axes. The accelerometer frame and the gyro frame in which the measurements are coordinated are represented by their sensitive axes and would not be discussed in this study.

Inertial frame is defined as those which are not accelerated relative to the earth. ***Geographic frame*** is a local navigational frame which has its origin at the vehicle's location and its axes aligning with the north, east, and down directions. Down, *D,* is

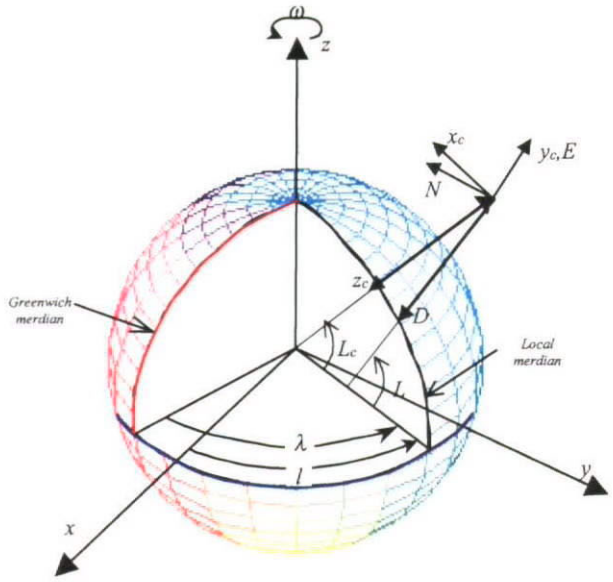

Figure 4.1.1 Coordinate Frame Geometry, (N, E, D)-Geographic; (x,y,z)-Inertial; (x_c, y_c, z_c)-Geocentric

defined to be normal to the reference ellipsoid, an analytically defined surface which is an approximation to the mean sea level gravity equipotential surface. The north axis, *N,* is in the direction of the projection of the earth's inertial angular velocity

vector into the local horizontal plane. The east direction, E, completes the right-handed orthogonal set. Two coordinate frames are shown in Figure 4.1.1

Body frame constitutes the vehicle axes of roll, pitch, and yaw, which has its origin at the vehicle center of mass. As illustrated by Figure 4.1.2, the roll axis points forward, the pitch axis points out of the right-hand side, and the yaw axis points downward, all with respect to the vehicle.

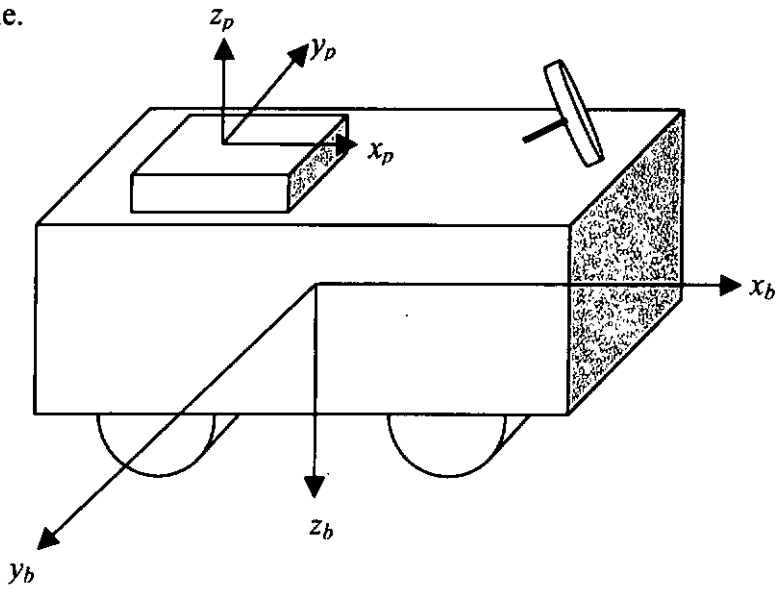

Figure 4.1.2 Body Frame and Platform Frame

Platform frame is defined as a right-hand orthogonal set of platform axes, which can be thought of as three fiducial lines which are physically inscribed on the platform. The frame origin is at the system location (see Figure 4.1.2).

Tangent frame is defined to be an earth-fixed frame, which is aligned with a geographic frame at a fixed location on earth. This location is typically taken to be concurrent with the desired tracking path. The convenient point of reference is shown in Figure 4.1.3, where y_t is pointing to the center of curvature, z_t is pointing vertically downward, and x_t completes the right-handed orthogonal set.

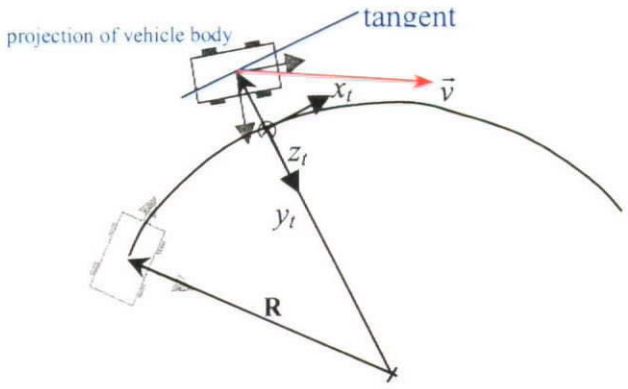

Figure 4.1.3 Tangent Frame

Landscape frame is also a local navigational frame which has its origin at the vehicle's location, coinciding with the origin of the geographic frame and its axes aligning with the north, east, and normal directions on the road surface. Normal, n, is defined to be normal to the road surface at where the vehicle body is projected. The north axis, x_r, is in the direction of the projection of the earth's inertial angular velocity vector onto the local vehicle's projection plane. The east direction, y_r, completes the right-handed orthogonal set.

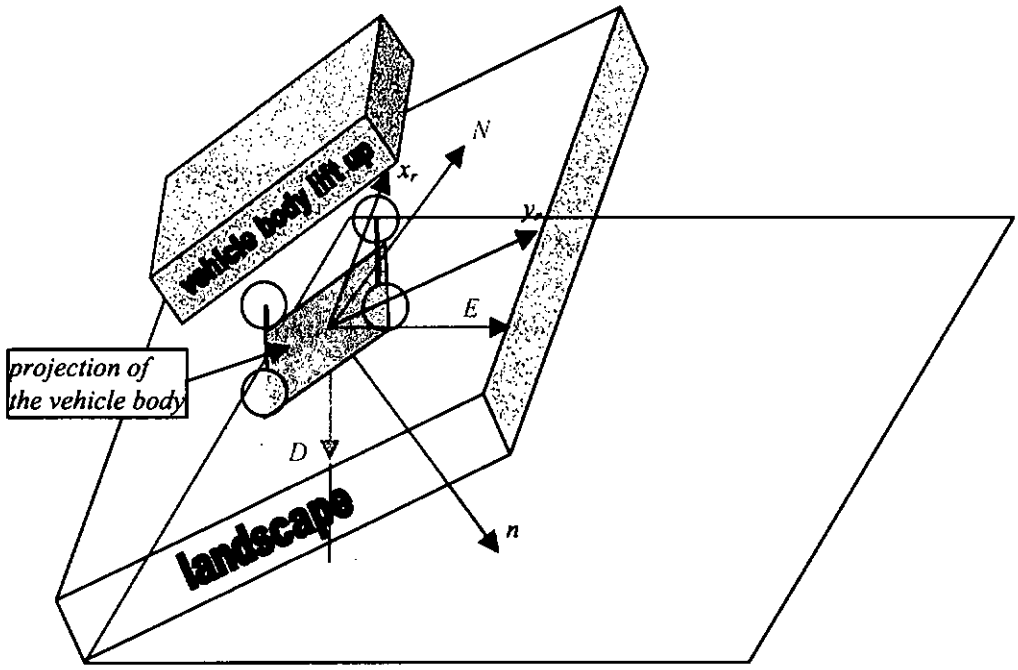

Figure 4.1.4 Landscape Frame and the Vehicle Body Projection

4.2 Coordinate Transformations

Many comprehensive texts expounding on the theory of matrix algebra, with the application to coordinate transformations, have found widespread use in navigation system design. This project only concentrates on the transformation between the tangent frame, the body frame, and the landscape frame.

Referring to Figure 4.1.4, the landscape is shown in definite dimension, shaped by a rectangular block. All the boundary lines of the block are straight and orthogonal to each other. The 'mask' of a object is first defined to include all the boundary lines of the object to be shaped. The 'principal edges' of a object are defined to be the primary boundary lines to describe the shape (e.g., the principal edges of a rectangle block are its width, length and height). In general, there is no specific mask for a landscape, since it can be infinitely extended and rotated about the normal. Therefore,

the mask of a landscape needs to be investigated. The projection of the vehicle's base on the landscape (*vehicle projection*) is a good choice, if assumption 7 in chapter 3 holds. If the vehicle projection formed by four contact points (the center of the area in the contact patch of each tire) between the tires and the road surface is considered, the mask of the landscape contains only two principal edges, with the dimensions of the other edges equal to zero.

To define the inclination angle of the landscape, two angles can be used—the angle between x_r and N and the angle between y_r and E. However, before these two angles can be measured, the direction *North* should be found on the vehicle. As mentioned before, the landscape can be infinitely extended and rotated. For convenient use as reference coordinate frame by navigation system on the vehicle, the landscape is rotated in such a way, as illustrated in Figure 4.2.1:

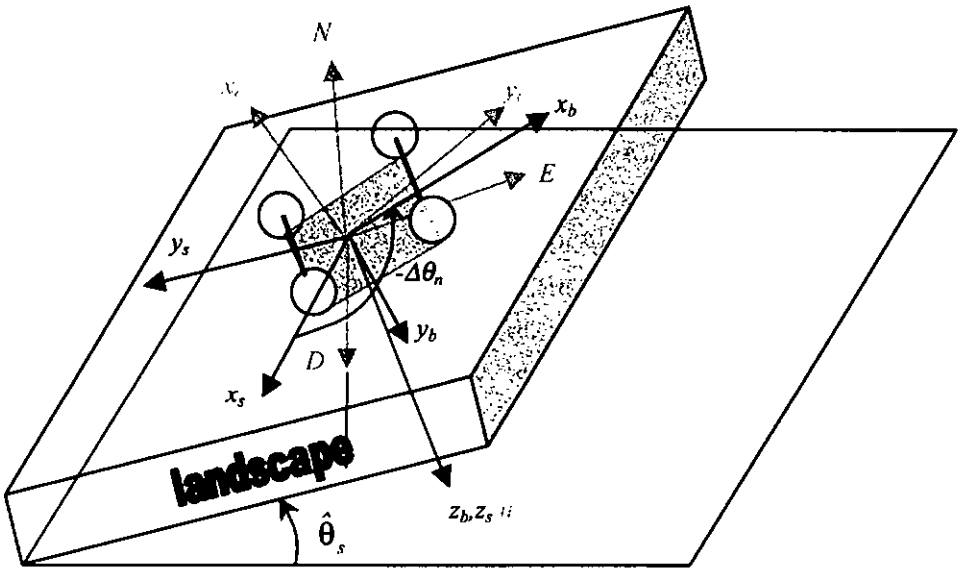

Figure 4.2.1 Landscape Deepest Slope Frame and the Body Frame

If the rectangular block is used to represent the landscape, the rectangular block in Figure 4.1.4 is rotated about normal, and the orientation of the resulting rectangular block is illustrated in Figure 4.2.1. In Figure 4.2.1, a new reference coordinate frame

is introduced—***landscape steepest slope frame***, in which y_s is pointing to the steepest direction on the landscape, z_s is the normal of the vehicle projection, and x_s completes the right-handed orthogonal set.

In view of vehicle projection, two inclination angles of the road surface can be instrumented, road banking angle η and road inclined angle ζ. The road banking angle is defined, from the view of vehicle projection, as the angle between y_b and its projection on the horizontal plane (at selected height from sea level). The road inclined angle is defined as the angle between x_b and its projection on the horizontal plane. The horizontal plane is selected at specific height above sea level. On this level, the reference path is paved. It is important to note that the reference path is paved on the horizontal level and not on the road surface where the vehicle is running. With the angles ζ and η measured, the steepest angle $\hat{\theta}_s$ and $\Delta\theta_n$ can be obtained from the following equations:

$$\eta = -\sin^{-1}\left\{\beta \frac{\sin\hat{\theta}_s}{\sqrt{1+\frac{1}{\tan^2(\theta_0+\Delta\theta_n)}}}\right\} \qquad \beta = \begin{cases} +1 & \text{if } \sin(\theta_0+\Delta\theta_n) > 0 \\ -1 & \text{if } \sin(\theta_0+\Delta\theta_n) < 0 \end{cases} \tag{4.1}$$

$$\zeta = \sin^{-1}\left\{\beta \frac{\sin\hat{\theta}_s}{\sqrt{1+\tan^2(\theta_0+\Delta\theta_n)}}\right\} \qquad \beta = \begin{cases} +1 & \text{if } \cos(\theta_0+\Delta\theta_n) > 0 \\ -1 & \text{if } \cos(\theta_0+\Delta\theta_n) < 0 \end{cases} \tag{4.2}$$

where $\theta_0 = \pi/2$

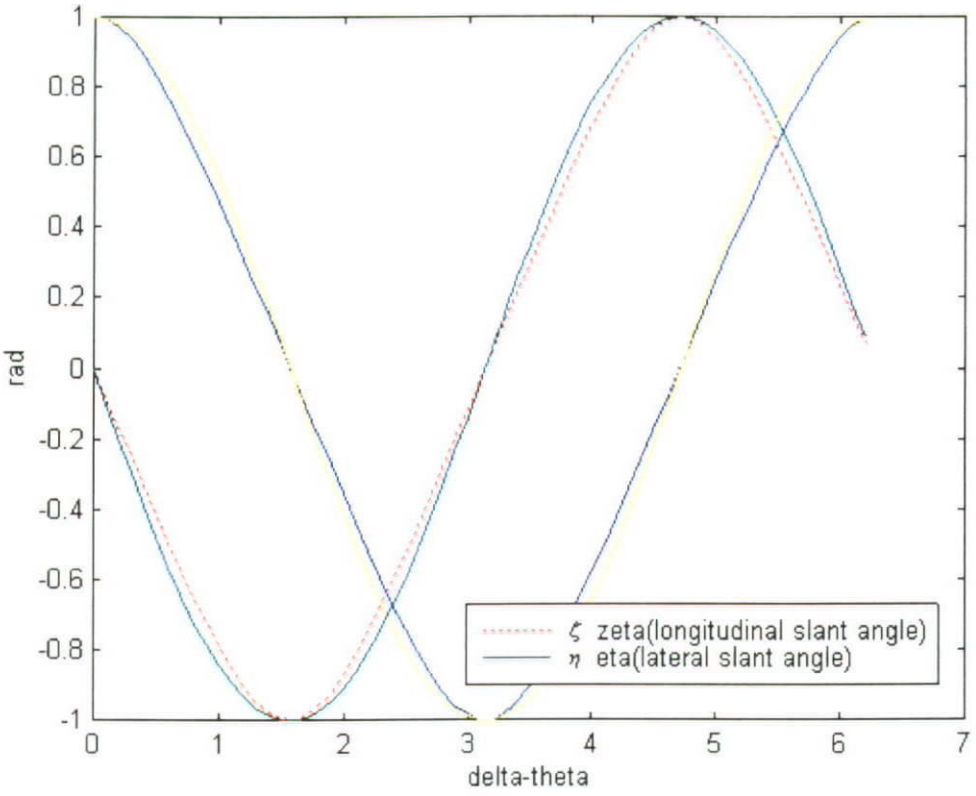

Figure 4.2.2 Physical Representation of Equations (4.1) and (4.2)

Both η and ζ can be instrumented by bi-axial inclinometer or inertial gyro. In order to obtain the angles of $\Delta\theta_n$ and $\hat{\theta}_s$ from equations (4.1) and (4.2), two equations must be solved simultaneously with both η and ζ known. However, equations (4.1) and (4.2) are both highly nonlinear in nature and thus are difficult to solve. Nevertheless, the two plots of the equation for η and the equation for ζ in Figure 4.2.2 are observed to be very similar to those plots of cos and –sin functions, respectively. In Figure 4.2.2, $\hat{\theta}_s$ has the

value of 1 rad, which is not the ordinary case to be considered. Figure 4.2.3 is another plot for equations (4.1) and (4.2), with $\hat{\theta}_s$ having the value of 0.2618 rad (15 degrees), which is the maximum inclination angle of the road surface to be considered in this study.

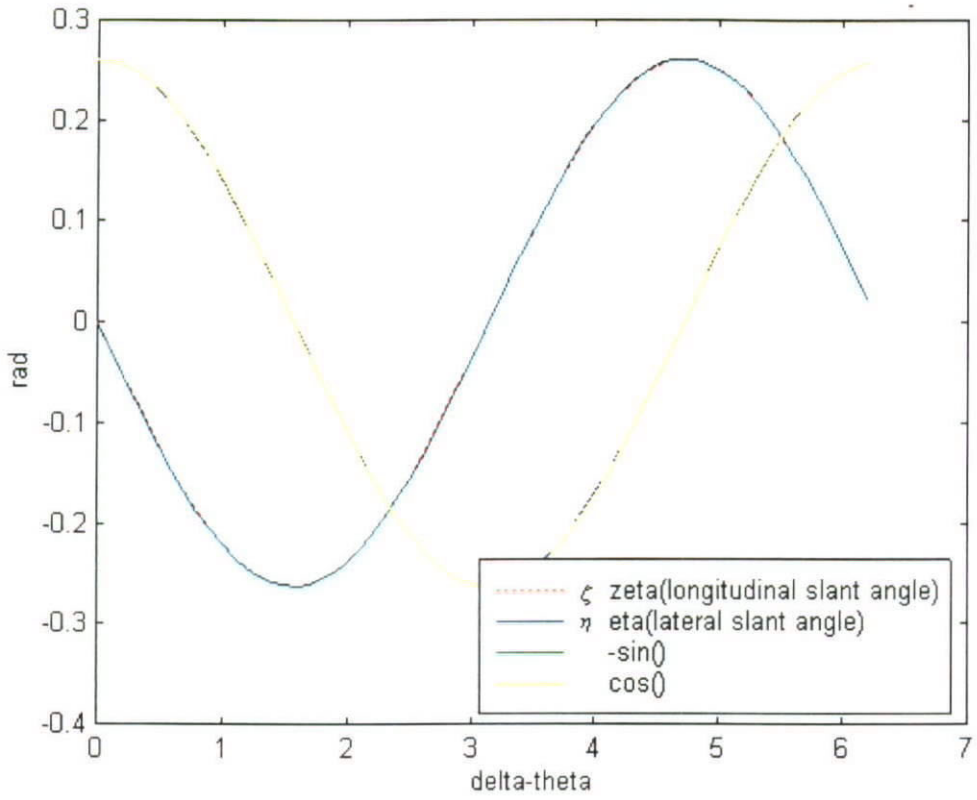

Figure 4.2.3 Sin() and Cos() vs Plot of Equations 4.1 and 4.2 with $\hat{\theta}_s$ *=0.2618*

It is interesting to find that both pairs of lines -- ζ and –sin(); η and cos() are almost coincident with each other. Thereby, the following two equations can be analogous to equations (4.1) and (4.2) with a very high degree of confidence.

$$\begin{cases} \zeta = -\hat{\theta}_s \, sin(\theta_0 + \Delta\theta_n) & (4.3) \\ \eta = \hat{\theta}_s \, cos(\theta_0 + \Delta\theta_n) & (4.4) \end{cases}$$

$$\Rightarrow \begin{cases} \left(\frac{\zeta}{\hat{\theta}_s}\right)^2 + \left(\frac{\eta}{\hat{\theta}_s}\right)^2 = 1 \Rightarrow \hat{\theta}_s = \sqrt{\zeta^2 + \eta^2} \\ (\theta_0 + \Delta\theta_n) = \beta \cos^{-1}\left(\frac{\eta}{\hat{\theta}_s}\right), \quad \beta = \begin{cases} +1 \\ -1 \end{cases} \text{, satisfying equations (4.3) and (4.4)} \end{cases} \quad (4.5)$$

Now, without requiring much computational efforts, either $\hat{\theta}_s$ or $\Delta\theta_n$ can be obtained directly from equation (4.5) with an error of less than 0.01%. Note that θ_o in the above equations are the angles between the axes x_b and x_s at the vehicle's initial position on the landscape. $\theta_o = 0$ means that the vehicle is initially at the position where the axis x_b is coincident with the axis x_s. The initial angular position with

respect to the landscape's steepest slope frame is incorporated with equations (4.1-4.5), due to the following two reasons:

1. The vehicle projection initially can be at any angular orientation on the landscape.
2. The navigation of vehicle over several landscape is possible. When the vehicle is moving form one landscape to the other, $\hat{\theta}_s$ and θ_o are both refined in such a way that their values are suitable to define the new landscape. In other words, it becomes possible for the performance analysis of vehicle running on a road profile which is varying with time slowly (assumption 4 in Chapter 3).

Using the algorithm discussed above to describe the behavior of the vehicle on a landscape, we can track the vehicle on the reference path even though there is no information on the direction *North* and/or *East*. The reference path model will be discussed in the following sections.

4.3 Model of the Reference Path

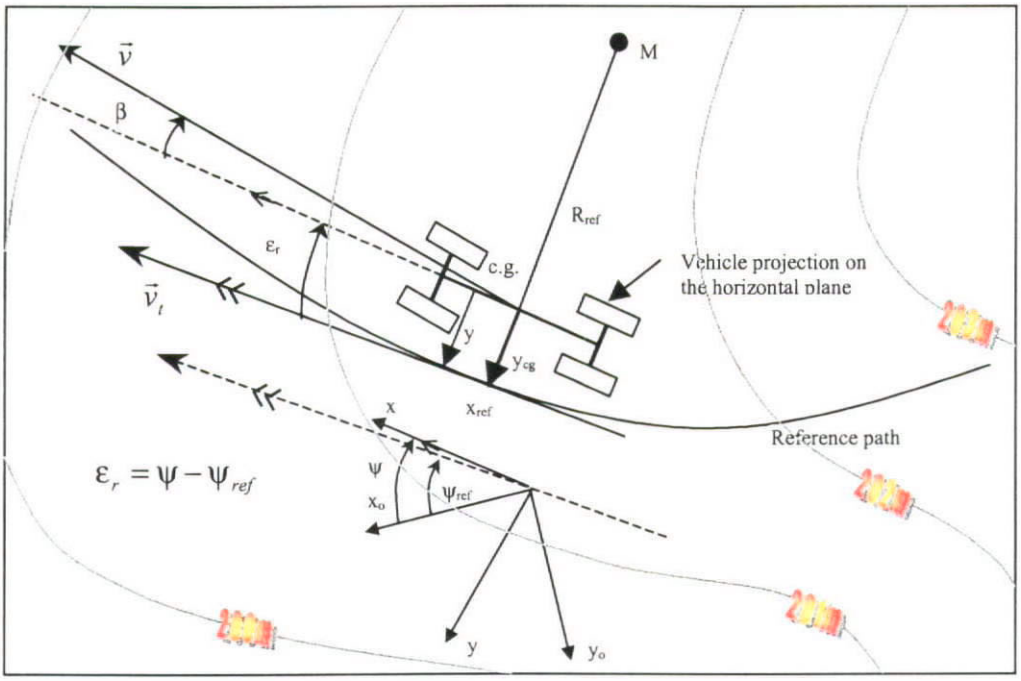

Figure 4.3.1 Model of Reference Path

Figure 4.3.1 shows the model of reference path. The vehicle projection, in what follows, is on the horizontal plane at specific height, say 203 m, on which the path of reference is defined. With this configuration, the tracking control system of the vehicle can be imagined so as to control the position of the hanged mass attached to the center of mass of the running vehicle, regardless of the height of the vehicle about the path of reference. Thus, we can directly integrate the digital map into the navigation and control system.

To analyze the tracking performance of the vehicle, the vehicle design model developed in chapter 3 has included the vehicle heading, ε_r, and lateral position, y_r, with respect to the reference path. For simplicity in the model derivation, a continuous guideline is assumed. The assumption is not strict, since the guideline is formulated by a continuous mathematical curve, which involves all the mark-points

on a digital map with known position. The measurements of the lateral displacement and angular displacement are obtained with GPS, DMC, gyros and accelerometers. The lateral displacement, y_{cg}, is defined as distance between the center of gravity (c.g.) of the vehicle and the intersection point, x_{ref}, of the radial line from the center *M* passing through the c.g. of the vehicle and the reference path. The angular displacement, $\varepsilon_r = \Psi - \Psi_{ref}$, is defined as the angle between the tangent to the reference path at x_{ref} and the centerline of the vehicle. In the model, the road curvature $\rho_{ref} := \frac{1}{R_{ref}}$ is the reference input, defined positive for right cornering.

The model is to be linearized using the small angle assumption. Therefore, the dynamics of y_{cg} can be written as

$$\dot{y}_{cg} = |\vec{v}| sin(\beta + \varepsilon_r) \approx |\vec{v}|(\beta + \varepsilon_r),$$

where β is the car sideslip angle, ε_r is the angle between the tangent to the reference path at x_{ref} and the centerline of the car.

Suppose the sensor *S* is mounted at a distance l_s in front of the c.g., then the lateral velocity with respect to the reference path reported by the sensor is

$$\dot{y}_r = \dot{y} + v(\beta + \varepsilon_r) + l_s\dot{\theta}_z$$

$$\dot{y}_r = \dot{y} + v\varepsilon_r + l_s\dot{\theta}_z, \beta \text{ is small}$$

The angular displacement ε_r is obtained by integration from

$$\begin{aligned}\dot{\varepsilon}_r &= \dot{\psi} - \dot{\psi}_{ref} \\ &= \dot{\theta}_z - v\rho_{ref}\end{aligned}$$

Combining the dynamics of the lateral and angular displacement with the vehicle model, the extended state space model containing the following additional row and/or column elements have been shown in section 3.4

$$\begin{bmatrix} \dot{\varepsilon}_r \\ \dot{y}_r \end{bmatrix} = \begin{bmatrix} 0 & 1 & 0 \\ 1 & l_s & v \end{bmatrix} \begin{bmatrix} \dot{y} \\ \dot{\theta}_z \\ \varepsilon_r \end{bmatrix} + \begin{bmatrix} -v \\ 0 \end{bmatrix} \rho_{ref}$$

In this study, the velocity (v) of the vehicle are kept constant as U, then the equation becomes,

$$\begin{bmatrix} \dot{\varepsilon}_r \\ \dot{y}_r \end{bmatrix} = \begin{bmatrix} 0 & 1 & 0 \\ 1 & l_s & v \end{bmatrix} \begin{bmatrix} \dot{y} \\ \dot{\theta}_z \\ \varepsilon_r \end{bmatrix} + \begin{bmatrix} -U \\ 0 \end{bmatrix} \rho_{ref}$$

5. ROBUST CONTROL DESIGN USING STRUCTURED SINGULAR VALUE

5.1 Structured Singular Value (μ) Framework

μ is an extremely useful analytical tool for uncertain, multivariable system. Because of μ, the classical frequency response Bode plot can be extended to multivariable system [96].

Lemma 5.1[97] **(Singular values and Eigenvalues).**

The singular values of a complex matrix $A \in C^{m \times n}$, denoted by $\sigma_i(A)$, are the k largest non-negative square roots of the eigenvalues of A^*A where $k=\min\{n,m\}$. Thus

$$\sigma_i(A) = \sqrt{\lambda_i(A^*A)} \qquad i = 1,2,\ldots,k.$$

It is usually assumed that the singular values are in the order such that $\sigma_i \geq \sigma_{i+1}$.

With this Lemma, the maximum and minimum singular values can be related to the 2-norm of the transfer function matrix *G(s)*:

Thus

$$\overline{\sigma}(A) = \sigma_1(A) = \sup_{u \in C^n, u \neq 0} \frac{\|Au\|_2}{\|u\|_2} = \|A\|_2$$

$$\underline{\sigma}(A) = \sigma_k(A) = \inf_{u \in C^n, u \neq 0} \frac{\|Au\|_2}{\|u\|_2} = \left\|A^{-1}\right\|_2^{-1}, \text{ if } A^{-1} \text{ exists.}$$

Refer to *Appendix B*, the 2-norm of the transfer function matrix can be interpreted as maximum "gain" of the transfer matrix *G(s)* for every possible inputs and for every frequency ω (see Appendices).

Lemma 5.2 [97] **(Singular Value Decomposition).**

Let $G \in C^{m \times n}$ be a complex matrix. Then there exist two unitary matrixes $Y \in C^{m \times m}$, $U \in C^{n \times n}$ and a diagonal matrix $\Sigma \in R^{m \times n}$ such that

$$G = Y\Sigma U^*$$

$$= \begin{bmatrix} y_1 & y_2 & \cdots & y_m \end{bmatrix} \begin{bmatrix} \Sigma_k & 0 \\ 0 & 0 \end{bmatrix} \begin{bmatrix} u_1^* \\ u_2^* \\ \vdots \\ u_n^* \end{bmatrix}$$

$$= \sum_{i=1}^{k} y_i \sigma_i u_i^*$$

where $\Sigma_k : diag(\sigma_1, \sigma_2, \cdots, \sigma_k)$

$y_1 \rightarrow y_m$ *: The m columns of Y.*

$u_1^* \rightarrow u_n^*$ *: The n rows of* U^*.

With singular value decomposition, an input-output matrix equation

$$y(j\omega) = G(j\omega)\, u(j\omega)$$

can be decomposed as

$$y(j\omega) = \sum_{i=1}^{k} y_i \sigma_i u_i^* u(j\omega)$$

$$= \sum_{i=1}^{k} y_i \sigma_i u_i^* u_j \alpha \qquad \text{, assume } u(j\omega) = \alpha u_j$$

$$= \sigma_j \alpha y_j \quad \text{, } U \text{ is unitary}$$

Therefore, if the input vector $u(j\omega)$ is in the direction of u_j, then the gain of the system is precisely σ_j, and the output vector $y(j\omega)$ is then precisely in the direction of y_j. The singular value σ_i is consequently known as the principal/directional gains of the system matrix G. With SVD, multivariable generalization of the SISO Bode plot can be easily obtained with a plot of singular values $\sigma_i(G(j\omega))$ for i=1,...,k as functions of frequency ω.

In other words, the "gain" of a transfer function matrix of a multivariable system actually depends on the direction of the input vector. The maximum and minimum singular values bound the gain of $G(j\omega)$ over all possible direction of the input vector.

Considering matrices $M \in C^{n\times n}$, in the definition of $\mu(M)$ [98], there is an underlying structure Δ on which all of the following theory depends. This structure is defined according to the uncertainty and performance objectives of each case. In the next section, the formulations of M and the underlying structure Δ are derived from the perturbed plant model $G'(s)$, where $G'(s)$ can be in form of $G'(s) = G(s) + \Delta(s)$, $G'(s) = G(s)\ \{I + \Delta(s)\}$ or $G'(s) = \left\{\dfrac{N(s)+\Delta_N(s)}{D(s)+\Delta_M(s)}\right\}$ where $G = \dfrac{N(s)}{D(s)}$

A general perturbation set Δ should contain both real and complex blocks. There are three types of blocks in Δ: repeated real scalar, repeated complex scalar and complex full blocks. Three nonnegative integers, S, F and V, denote the number of repeated complex scalar blocks, the number of complex full blocks and the number of repeated real scalar blocks, respectively. The block dimensions of complex scalar blocks, complex full blocks and real scalar blocks are denoted by the positive integers $r_1,\ldots,r_S$, $m_1,\ldots m_F$ and $t_1,\ldots,t_V$, respectively. Given all these integers, Δ is defined as:

Definition 5.1 [97]

$$\Delta = \{\mathrm{diag}[\delta_1^r I_{r_1},\cdots,\delta_V^r I_{t_V},\delta_{V+1}^c I_{r_1},\cdots,\delta_{V+S}^c I_{r_S},\Delta_{V+S+1},\cdots,\Delta_{V+S+F}],$$
$$\delta_k^r \in R,\ \delta_{V+i}^c \in C,\ \Delta_{V+S+j} \in C^{m_j\times m_j},\ k\in[1,V],\ i\in[1,S],\ j\in[1,F]\}$$

For consistency among all the dimensions, $\sum_{k=1}^{V} t_k + \sum_{i=1}^{S} r_i + \sum_{j=1}^{F} m_j$ must equal to n.

Often, a norm-bounded subset of Δ is defined as:

$$B_{\Delta s}=\{\Delta \in \Delta_s : \overline{\sigma}(\Delta) \leq 1\}$$

Definition 5.2 [97]

For $M \in C^{nxn}$, $\mu_{\Delta}(M)$ is defined

$$\mu_{\Delta}(M) := 1 / \min\{\overline{\sigma}(\Delta) : \Delta \in \Delta, \det(I-M\Delta) = 0\}$$

unless no $\Delta \in \Delta$ makes $I-M\Delta$ singular, in which case $\mu_{\Delta}(M) := 0$. Obviously, $\mu_{\Delta}(M)$ is dependent on the set Δ.

Consider the loop shown in the following figure:

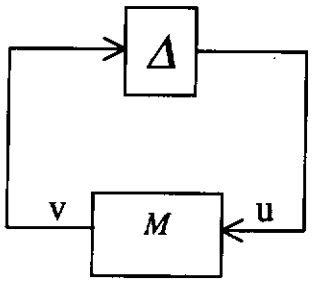

The loop can be represented by the equations:

$$\begin{cases} v = Mu \\ u = \Delta v \end{cases}$$
$$\Rightarrow v = M\Delta v$$
$$\Rightarrow (I-M\Delta)v = 0$$
$$\Rightarrow v = 0 \text{ or } (I-M\Delta) = 0$$

If $I-M\Delta$ is singular, there are infinitely many solutions to the equations, and the norms $||u||$ and $||v||$ of the solutions can be arbitrarily large and thus result in an "unstable" interconnection. The physical interpretation of the $\mu_{\Delta}(M)$ represents the smallest

"size" perturbation that results in an unstable system. Therefore, $1/\mu_{\Delta}(M)$ represents the "size" of the perturbation set Δ.

An alternative expression for $\mu_{\Delta}(M)$ follows from the lemma 5.3:

Lemma 5.3 [97]

$$\mu_{\Delta}(M) = \max \{\rho(\Delta M) : \Delta \in B_{\Delta}\}$$

In view of this lemma, continuity of the function $\mu : C^{n\times n} \to R$ is apparent. In general, the function $\mu : C^{n\times n} \to R$ is not a norm (see Appendices for the definition of norm), because it does not satisfy the triangle inequality. However, for any $\alpha \in C$, $\mu(\alpha M) = |\alpha|\mu(M)$. Thus, μ is related to the size of the matrix by the definition of norm.

Δ can be one of two extreme sets:

- If $\Delta = (\delta I : \delta \in C)$ (S=1, F=0, V=0, r_1=n), then $\mu_{\Delta}(M) = \rho(M)$, and minimum of $\mu_{\Delta}(M)$ can be written as $\rho(M)$.
- If $\Delta = C^{n\times n}$ (S=0, F=1, V=0, m_1=n), then $\mu_{\Delta}(M) = \bar{\sigma}(M)$, and maximum of $\mu_{\Delta}(M)$ can be written as $\bar{\sigma}(M)$.

(See *Appendices C* for proof.)

The conclusion is that:

$$\rho(M) \le \mu_{\Delta}(\mathrm{M}) \le \bar{\sigma}(M)$$

Although the inequality provides information about the value of μ, the bounded value of $\rho(M)$ and $\bar{\sigma}(M)$ do not depend on Δ. Thus, the gap between ρ and $\bar{\sigma}(M)$ may be quite large. The inequality may be refined by considering transformations on M that

do not affect $\mu_{\Delta}(M)$ but affect ρ and $\bar{\sigma}$ only. The transformation is described in details in [99]. The bounds can be tightened to

$$\max_{Q \in Q} \rho(QM) \leq \mu_{\Delta}(M) \leq \inf_{D \in D} \bar{\sigma}(DMD^{-1})$$

where the definition of **Q** and **D** can be found in the *Appendix D*, and the theorem used to refine the inequality and its proof can be found in [99].

The theory for a mixed real/complex upper bound is more complicated to describe than the upper bound theory for purely complex μ. The upper bound for a mixed real/complex μ is derived in [100] and written as follows:

If there is a $\beta > 0$, $D \in \mathbf{D}$ and $G \in \mathbf{G}$ such that

$$\bar{\sigma}[(I+G^2)^{\frac{1}{2}}(\tfrac{1}{\beta}DMD^{-1} - jG)(I+G^2)^{\frac{1}{2}}] \leq 1$$

then $\mu_{\Delta}(M) \leq \beta$

The lower bound can be obtained from a power iteration which finds matrices $\Delta \in \mathbf{\Delta}$ that results in a singular $I\text{-}M\Delta$. The generalization of the power iteration is described in [101].

The interpretation of the bounds on μ is as follows:

- The upper bounds provide a guarantee on the worst-case performance degradation that can occur under perturbation.
- The lower bounds exhibit a perturbation that causes significant performance degradation.

5.1.1 Linear Fractional Transformations and μ *[102]*

The use of μ in control theory depends to a great extent on its intimate relationship with a class of general linear feedback loops called Linear Fractional Transformations.

Consider a complex matrix M partitioned as:

$$M = \left[\begin{array}{c|c} M_{11} & M_{12} \\ \hline M_{21} & M_{22} \end{array}\right]$$

Suppose there is a defined block structure Δ which is compatible in size with M_{21} (for any $\Delta_u \in \Delta_u$, $M_{22}\Delta_u$ is square). For $\Delta_u \in \Delta_u$, consider the following loop equations:

$$\left.\begin{aligned} e &= M_{21}w + M_{22}d \\ z &= M_{11}w + M_{12}d \\ w &= \Delta_u z \end{aligned}\right\} \qquad (5.1)$$

which correspond to the following block diagram: in the following figure

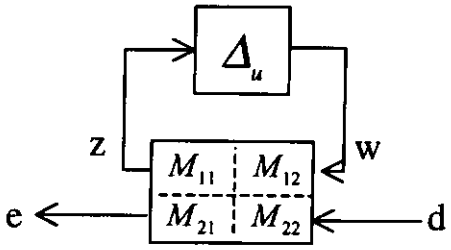

Equations 5.1 is well-posed if for any vector d, there exist unique vectors w, z and e satisfying the loop equations. In other words, Eq (5.1) is well-posed if and only if the inverse of $I\text{-}M\Delta_u$ exists. Otherwise, the equation $e = F_u(M,\Delta_u)d$ will be undefined, where $F_u(M,\Delta_u) = M_{22} + M_{21}\Delta_u (I - M_{11}\Delta_u)^{-1} M_{12}$.

Proof:

$$e = M_{21}w + M_{22}d \qquad (5.2)$$

$$z = M_{11}w + M_{12}d \qquad (5.3)$$

$$w = \Delta_\mu z \qquad (5.4)$$

putting (5.4) in (5.3),

$$z = M_{11}\Delta_u z + M_{12} d$$
$$z = (I - M_{11}\Delta_u)^{-1} M_{12} d$$
$$\therefore w = \Delta_u (I - M_{11}\Delta_u)^{-1} M_{12} d$$
$$e = \{M_{22} + M_{21}\Delta_u (I - M_{11}\Delta_u)^{-1} M_{12}\} d$$

if $\det (I - M_{11}\Delta_u) \neq 0$

$\Rightarrow (I - M_{11}\Delta_u)^{-1}$ does exit

$\Rightarrow$ Mapping function from d to e is defined

$F_u(M,\Delta_u)$ is a Linear Fractional Transformation on M by Δ_u. The subscript u in F_u pertaining to the "upper" loop of M is closed by Δ_u. An analogous formula describes $F_l(M,\Delta_l)$, which is the resulting matrix obtained by closing the "lower" loop of M with a matrix $\Delta_l \in \mathbf{\Delta_l}$.

In this formulation, the matrix M_{22} is assumed to be nominal, since $M_{22}=F_u(M,\Delta_0)$ where $\Delta_0 \in \{\Delta \in \mathbf{\Delta} ; ||\Delta|| = 0\}$

$\Rightarrow e=M_{22}d$

Moreover, $\Delta_u \in B_{\Delta u}$ is viewed as a norm-bounded perturbation in perturbation set $\mathbf{\Delta_u}$. The matrices M_{12}, M_{21} and M_{11} and the formula $F_u(M,\Delta_u)$ present how the unknown perturbation affects the nominal map M_{22}.

All types of uncertainty considered in the literature are linear fractional. The perturbed transfer function can be formulated by $F_u(M, \Delta_u)$.

Main Loop Theorem [103]:

$$\mu_\Delta(M) < 1 \text{ iff } \begin{cases} \mu_{\Delta_u}(M_{11}) < 1, and \\ \max\limits_{\Delta_u \in B_{\Delta_u}} \mu_{\Delta_l}(F_u(M,\Delta_u)) < 1 \end{cases}$$

With the main loop theorem, the robust performance tests of a system can be easily performed using μ. This will be discussed in the coming sections of this chapter.

5.2 Generalized Structured Plant Uncertainty in μ Framework

Uncertainty in the control system can be classified into two categories: 1) uncertain signals such as disturbances and/or sensor noise and 2) uncertainty in the way plant maps input signals into output signals such as plant uncertainty. These uncertainties may be caused by unmodelled plant dynamics or the system designer's limited knowledge in the plant behavior.

There is one special disturbance in the control system at which designers have injected an artificial disturbance (input command), since the designers viewed the tracking control problem as a disturbance rejection problem in the classical regulating control problem. While designing a robust steering controller for a vehicle, lane keeping is viewed as a disturbance rejection problem in [93].

The following sections describe in details how to formulate a plant family G by specifying a nominal plant model together with a family of perturbations D away from the nominal into a μ framework, enabling an easier analysis and design process for a control system. In other words, by imposing structure on a perturbation model, uncertainty can be captured more precisely.

5.2.1 Model Uncertainty

This section presents the plant uncertainty models that are used for controller design and synthesis in this project. In what follows, *G(s)* denotes the nominal plant model;

$G_r(s)$ denotes the transfer function matrix of the perturbed plant model; and $\Delta_A(s)$ denotes the transfer function matrix of a perturbation. The number of unstable poles of G and G_r are denoted by m_G and m_{Gr}.

5.2.2 Additive Modeling Perturbations

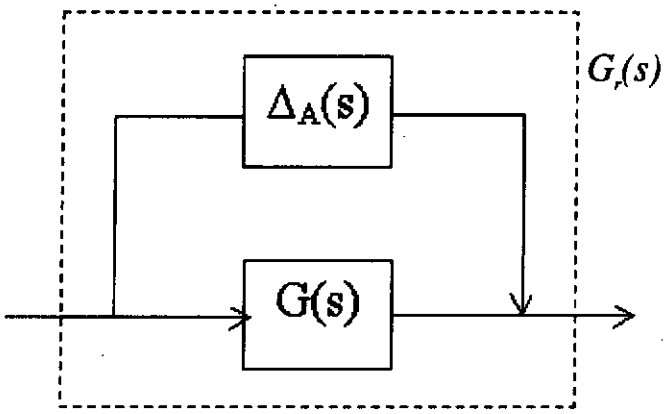

Figure 5.2.2.1 Additive Modeling Perturbations

In the above figure, additive perturbations are defined as

$$G_r(s) := G(s) + \Delta_A(s)$$

where the "size" of Δ_A must not be unbounded and a set of admissible Δ_A is given by:

$$D_A := \{\Delta_A : \bar{\sigma}(\Delta_A(j\omega)) < I_A(\omega) \ ; \ \Delta_A \text{ stable}\}$$

Before structured perturbations can be written, generalized unstructured perturbations and a "new" transfer function matrix must be introduced.

$$\Theta(s) = \begin{bmatrix} \Theta_{11}(s) & \Theta_{12}(s) \\ \Theta_{21}(s) & \Theta_{22}(s) \end{bmatrix}$$

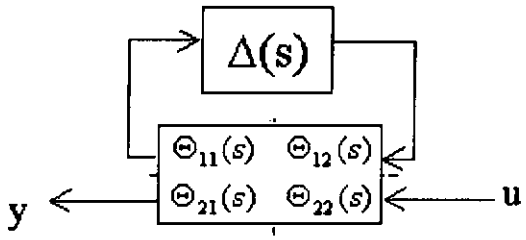

Obviously, the transfer function matrix G_r of the perturbed model is given as an upper linear functional transformation of $\Delta(s)$ with respect to $\Theta(s)$:

$$G_r = \Theta_{22} + \Theta_{21}\Delta\,(I_{c\Delta} - \Theta_{11}\Delta)^{-1}\,\Theta_{12}$$

where c_Δ represents the number of columns of Δ,

by comparing with:

$$G_r(s) = G(s) + \Delta(s)$$

$$\Rightarrow \begin{cases} \Theta_{22} = G \\ \Theta_{21} = I_p \ , \textit{where } p \textit{ is the no. of row of } G \\ \Theta_{12} = I_q \ , \textit{ where } q \textit{ is the no. of column of } G \\ \Theta_{11} = 0 \ , \ \textit{where } 0 \textit{ is the zero matrix with compatitable size} \end{cases}$$

$$\therefore G_r = G + I_p\Delta(I_{C\Delta} - 0\Delta)^{-1}I_q \qquad (5.5)$$

$$\therefore \Theta = \left[\begin{array}{c|c} 0 & I_q \\ \hline I_p & G \end{array}\right]$$

The fact that mu-theory [98][104] provides analysis and synthesis tools to deal with structured uncertainty sets motivates the formulation of a general perturbation model such that

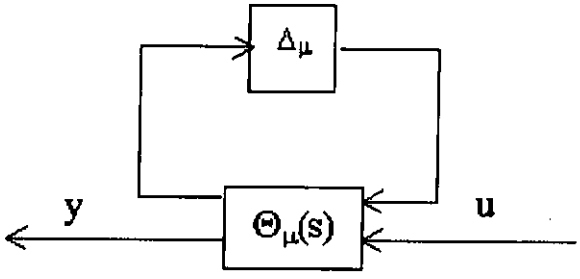

where $\Theta_\mu(s)$ is a transfer function matrix and Δ_μ is an underlying block diagonal structure of the perturbation matrix corresponding to $\Theta_\mu(s)$, which mirrors the structure of the underlying perturbation model.

If $\Delta_\mu \in \{\Delta : \bar{\sigma}(\Delta(j\omega)) < 1\}$

defines a stable minimum-phase transfer functions $w_\mu(s)$ where the magnitude of a frequency response $w_\mu(j\omega) = I_A(\omega)$

i.e. $|w_\mu(j\omega)| = I_A(\omega)$

then Θ_μ can be defined as follows:

$$\Theta_\mu(s) = \begin{bmatrix} 0 & I_q \\ w_3 I_p & G \end{bmatrix}$$

$$\Delta_\mu = \frac{1}{w_3}\Delta_A$$

This fact can be easily shown by upper linear fractional transformation. Recall equation 5.5:

$$G_s = \Theta_{22} + I_p\Delta_A (Ic_\Delta - O\Delta_A)^{-1} I_q$$

$$= G + w_3 I_p \Delta_\mu (Ic_A - O\Delta_\mu w_3)^{-1} I_q$$

5.2.2.1 Example For Additive Modeling Perturbations

Let $G(s)$ be a 2x2 plant model with additive unstructured uncertainty $\Delta_A(s)$ where

$$G(s) = \begin{bmatrix} G_{11}(s) & G_{12}(s) \\ G_{21}(s) & G_{22}(s) \end{bmatrix}, \text{ and}$$

$$\Delta_A(s) = \begin{bmatrix} \Delta_{11}(s) & \Delta_{12}(s) \\ \Delta_{21}(s) & \Delta_{22}(s) \end{bmatrix}$$

$$= \begin{bmatrix} w_{11}(s)\delta_{11} & w_{12}(s)\delta_{12} \\ w_{21}(s)\delta_{21} & w_{22}(s)\delta_{22} \end{bmatrix}$$

$$= \begin{bmatrix} w_{11}(s) & w_{12}(s) & 0 & 0 \\ 0 & 0 & w_{21}(s) & w_{22}(s) \end{bmatrix} \begin{bmatrix} \delta_{11} & 0 & 0 & 0 \\ 0 & \delta_{12} & 0 & 0 \\ 0 & 0 & \delta_{21} & 0 \\ 0 & 0 & 0 & \delta_{22} \end{bmatrix} \begin{bmatrix} 1 & 0 \\ 0 & 1 \\ 1 & 0 \\ 0 & 1 \end{bmatrix}$$

By comparing the two formulations:

$$G_r(s) = G(s) + \Delta_A(s)$$

$$G_r(s) = \Theta_{22}(s) + \Theta_{21}(s)\Delta_A(s)\,(Ic_{\Delta A} - \Theta_{11}(s)\Delta_A(s))^{-1}\,\Theta_{12}(s)$$

$$\Theta_{11}(s) = [0]$$

where $\Theta_{21}(s) = \begin{bmatrix} w_{11}(s) & w_{12}(s) & 0 & 0 \\ 0 & 0 & w_{21}(s) & w_{22}(s) \end{bmatrix}$

$$\Theta_{12}(s) = \begin{bmatrix} 1 & 0 \\ 0 & 1 \\ 1 & 0 \\ 0 & 1 \end{bmatrix}$$

$\because$ Two formulations are equivalent:

$$\therefore \Theta_{\mu}(s) = \left[\begin{array}{cccc:c} & & 0 & & \begin{matrix} 1 & 0 \\ 0 & 1 \\ 1 & 0 \\ 0 & 1 \end{matrix} \\ \hdashline w_{11}(s) & w_{12}(s) & 0 & 0 & G(s) \\ 0 & 0 & w_{21}(s) & w_{22}(s) & \end{array}\right], \text{and}$$

$$\Delta = \begin{bmatrix} \delta_{11} & 0 & 0 & 0 \\ 0 & \delta_{12} & 0 & 0 \\ 0 & 0 & \delta_{21} & 0 \\ 0 & 0 & 0 & \delta_{22} \end{bmatrix}$$

where Δ is the admissible perturbation sets used in the μ framework.

The generalized structured perturbation model is presented in the following figure:

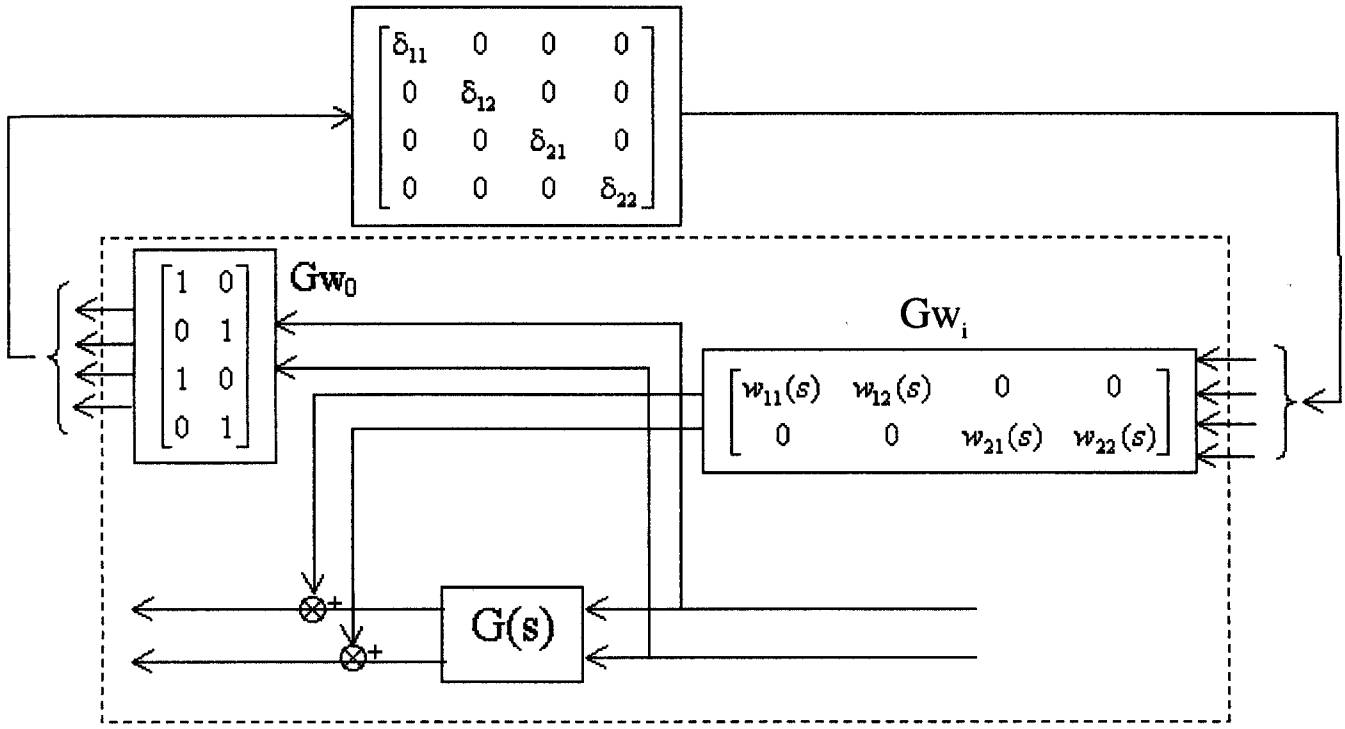

Figure 5.2.2.1.1 General Plant for Additive Modeling Perturbations with Weighting Functions

In this example, the structured perturbation has been forced into a repeated real scalar block diagonal structure. By alternating the matrix form in Gw_i and Gw_0, the block diagonal structure can be formulated in full blocks. However, the value of μ associated with real full blocks is difficult to calculate, since the convenient upper and lower bounds for structures with these types of blocks are not well-developed yet. This is an ongoing area of research [105][106][107][108].

5.2.3 Multiplicative Modeling Perturbations

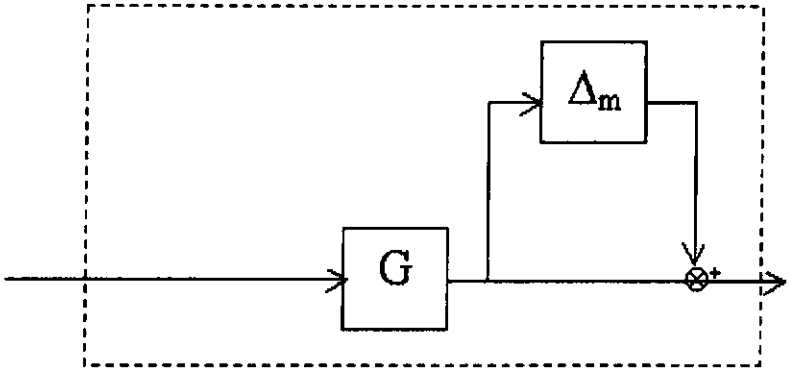

Figure 5.2.3.1 Multiplicative Modeling Perturbations

In the above figure, multiplicative perturbations are defined as:

$$G_r(s) = G(s)\,(I + \Delta_m(s))$$

Again, the "size" of Δ_m is bounded in the same way as that for additive perturbations, and the set of admissible Δ_m is given by:

$$D_m := \{\Delta_m : \bar{\sigma}[\Delta_m(j\omega)] < l_m(\omega);\ \Delta_m \text{ stable and } m_{Gr} = m_G\}$$

The restrictive condition in D_A is looser than D_m, since the additive stable perturbation matrix does not affect the number of unstable poles of the nominal system.

A generalized unstructured multiplicative perturbation is written below:

$$\Theta(s) = \begin{bmatrix} 0 & G \\ I_p & G \end{bmatrix}$$

The form of the perturbation results from the upper linear function transformation of $\Delta_m(s)$ with respect to $\Theta(s)$:

$$G_r = \Theta_{22} + \Theta_{21}\Delta\,(Ic_\Delta - \Theta_{11}\Delta)^{-1}\,\Theta_{12}$$

where c_Δ represents the number of columns of Δ.

By comparing $G_r = G(s) + G(s)\Delta_m(s)$ with the linear functional condition, Θ_{11} is kept as a zero matrix, which renders the inverse of $(Ic_\Delta - \Theta_{11}\Delta_m)$ always exists.

$$\Rightarrow \Theta_{22} = G$$
$$\Theta_{21} = I_p$$
$$\Theta_{12} = G$$
$$\Theta_{11} = 0$$

$$\therefore G_r = G + I_p\Delta_m\,(Ic_\Delta - \theta\Delta_m)^{-1}\,G \qquad (5.6)$$

Now, a general structured perturbation model is formulated.

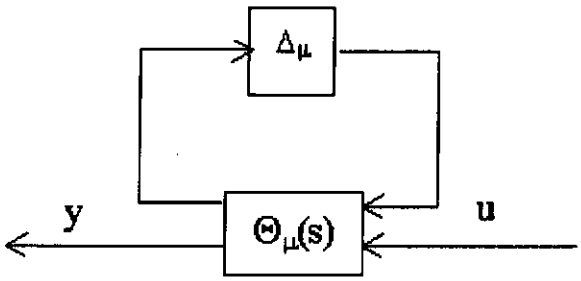

$\Theta_\mu(s)$ is the transfer function matrix, and Δ_μ is an underlying block diagonal structure of the perturbation matrix corresponding to $\Theta_\mu(s)$, which mirrors the structure of the underlying perturbation model.

If $\quad \Delta_\mu \in \{\Delta : \bar{\sigma}(\Delta(j\omega)) < 1\}$

a stable minimum-phase transfer function $w_u(s)$ can be defined where the magnitude of a frequency response $w(j\omega) = I_m(\omega)$

i.e. $|w_u(j\omega)| = I_m(\omega)$

The $\Theta_\mu(s)$ can be defined as follows:

$$\Theta_\mu(s) = \begin{bmatrix} 0 & G \\ w_3 I_p & G \end{bmatrix}$$

The above equation can be illustrated by upper linear fractional transformation. Recall equation 5.6:

$$G_r = G + I_p \Delta_m (Ic_\Delta - 0\Delta_\mu)^{-1} G$$

$$= G + I_p w_3 \Delta_\mu (Ic_\Delta - 0\Delta_\mu w_3)^{-1} G$$

5.2.3.1 Example for Multiplicative Modeling Perturbations

Let $G(s)$ be a 2x2 plant model with multiplicative unstructured uncertainty $\Delta_m(s)$ where

$$G(s) = \begin{bmatrix} G_{11}(s) & G_{12}(s) \\ G_{21}(s) & G_{22}(s) \end{bmatrix}, \text{ and}$$

$$\Delta_m(s) = \begin{bmatrix} \Delta_{11}(s) & \Delta_{12}(s) \\ \Delta_{21}(s) & \Delta_{22}(s) \end{bmatrix}$$

$$= \begin{bmatrix} w_{11}(s) & w_{12}(s) & 0 & 0 \\ 0 & 0 & w_{21}(s) & w_{22}(s) \end{bmatrix} \begin{bmatrix} \delta_{11} & 0 & 0 & 0 \\ 0 & \delta_{12} & 0 & 0 \\ 0 & 0 & \delta_{21} & 0 \\ 0 & 0 & 0 & \delta_{22} \end{bmatrix} \begin{bmatrix} 1 & 0 \\ 0 & 1 \\ 1 & 0 \\ 0 & 1 \end{bmatrix}$$

By comparing two formulations

$$G_r(s) = G(s) + \Delta_m(s)$$

$$G_r(s) = \Theta_{22}(s) + \Theta_{21}(s)\Delta_m(s) (Ic_{\Delta A} - \Theta_{11}(s)\Delta_m(s))^{-1} \Theta_{12}(s)$$

$$\Theta_{11}(s) = [0]$$

where $\Theta_{21}(s) = \begin{bmatrix} w_{11}(s) & w_{12}(s) & 0 & 0 \\ 0 & 0 & w_{21}(s) & w_{22}(s) \end{bmatrix}$

$$\Theta_{12}(s) = \begin{bmatrix} 1 & 0 \\ 0 & 1 \\ 1 & 0 \\ 0 & 1 \end{bmatrix}$$

The two formulations are now equivalent

$$\therefore \Theta_\mu(s) = \left[\begin{array}{cccc|c} & & & & \begin{bmatrix}1 & 0\\ 0 & 1\\ 1 & 0\\ 0 & 1\end{bmatrix} G(s) \\ \multicolumn{4}{c|}{0} & \\ \hline w_{11}(s) & w_{12}(s) & 0 & 0 & \\ 0 & 0 & w_{21}(s) & w_{22}(s) & G(s) \end{array}\right], \text{and}$$

$$\Delta_\mu = \begin{bmatrix} \delta_{11} & 0 & 0 & 0 \\ 0 & \delta_{12} & 0 & 0 \\ 0 & 0 & \delta_{21} & 0 \\ 0 & 0 & 0 & \delta_{22} \end{bmatrix}$$

where Δ_μ is the admissible perturbation sets used in the μ framework.

The generalized structured multiplicative perturbation model is illustrated in the following figure:

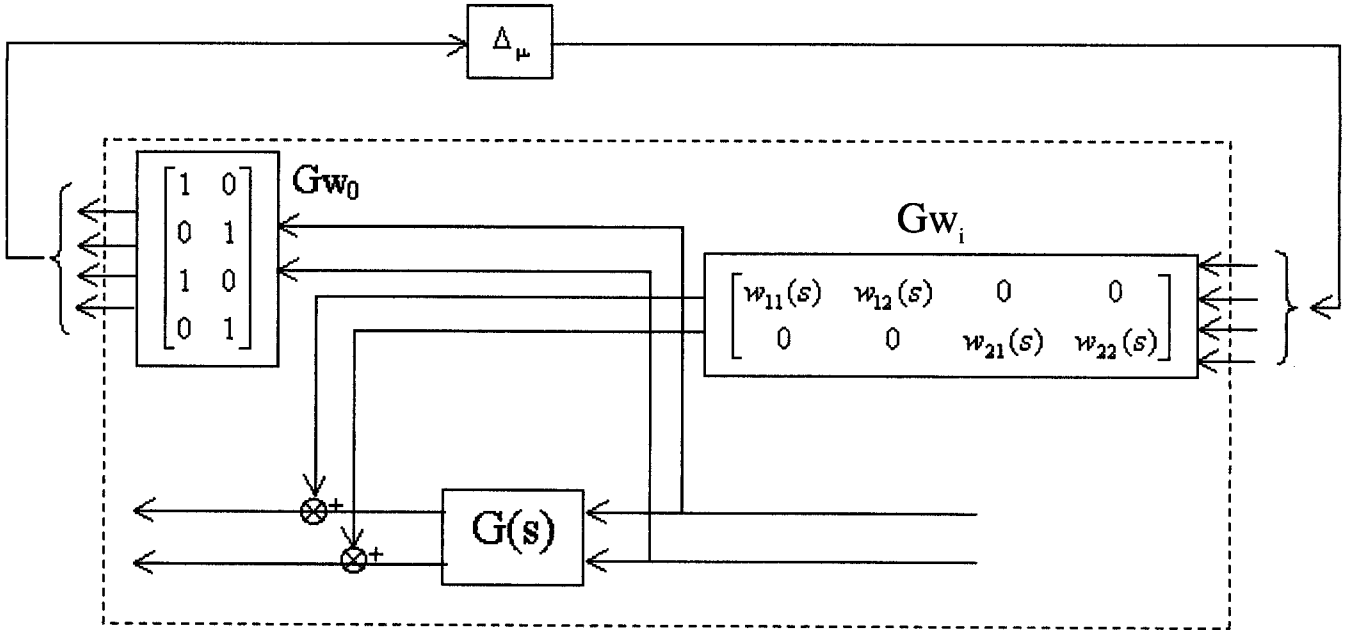

Figure 5.2.3.1.1 General Plant for Multiplicative Modeling Perturbations with Weighting Functions

In this iteration, multiplicative model perturbation is used to capture the high-order dynamics of the system that have been neglected in the design process. While additive mode perturbation is used to capture the unmodelled dynamics of the system that have been neglected in the design process, the additive mode perturbation indeed affects the control system performance in the operating frequency range.

5.2.4 Uncertain Parameters

Theoretical model building usually results in a state model. The model uncertainty in the form of parameter uncertainty is reflected in the real parameters of the state model, and there is physical meaning in these parameters. In controller design, the parameter uncertainties are limited to lie within given intervals. However, a fairly complicated set of admissible parameters are always obtained when converting a state model with uncertain parameters to a transfer function matrix, since each parameter of the resulting transfer function matrix always depends on several parameters of the underlying state model. In this section, a straight-forward conversion process from a MIMO transfer function matrix to a state model is first introduced. Uncertain parameters in the elements of transfer system matrix is then "pulled out" from the matrix and rearranged in a block diagonal structure to be ready for analysis and controller synthesis in the μ framework.

Before a matrix transformation can be discussed, a final matrix formulation, say P, must first be introduced. The P matrix will incorporate all the information about the system and controller synthesis and will enable the synthesis of the controller to be straight-forward. All the formulas will be based on the following state space realization of P:

$$P := \left[\begin{array}{c|cc} A & B_1 & B_2 \\ \hline C_1 & D_{11} & D_{12} \\ C_2 & D_{21} & D_{22} \end{array}\right]$$

This notation is a short-hand representation for the system of equations:

$$\dot{x}(t) = Ax(t) + B_1 w(t) + B_2 u(t)$$
$$z(t) = C_1 x(t) + D_{11} w(t) + D_{12} u(t)$$
$$y(t) = C_2 x(t) + D_{21} w(t) + D_{22} u(t)$$

where $w(t)$ is a disturbance input of the system and $z(t)$ is a disturbance output of the system.

Consider the following special case: $w=\Delta z$, $\Delta \in \{\Delta : \bar{\sigma}(\Delta(j\omega)) < I(j\omega), \Delta \text{ is stable}\}$. The above notations can be reformulated into the μ framework.

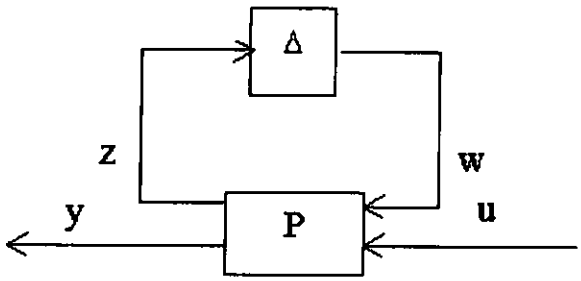

Thus, this special case considers the dynamics of internal system discrepancy. Consider a plant model $G(s)$, which is described by the 2x2 transfer system matrix

$$G(s) = \begin{bmatrix} G_{11}(s) & G_{12}(s) \\ G_{21}(s) & G_{22}(s) \end{bmatrix}$$

Let $$G_{ij}(s) = \frac{Y_{ij}(s)}{U_{ij}(s)} = \frac{b_0 s^n + b_1 s^{n-1} + \cdots b_{n-1} s + b_n}{s^n + a_1 s^{n-1} + \cdots a_{n-1} s + a_n} \qquad (5.6)$$

With direct programming methods (see Appendix E), a controllable canonical form of state model is obtained.

$$\underbrace{\begin{bmatrix} \dot{x}_1 \\ \dot{x}_2 \\ \vdots \\ \dot{x}_{n-1} \\ \dot{x}_n \end{bmatrix}}_{\dot{X}_n} = \underbrace{\begin{bmatrix} 0 & 1 & 0 & \cdots & 0 \\ 0 & 0 & 1 & \cdots & 0 \\ \vdots & \vdots & \vdots & \ddots & \vdots \\ 0 & 0 & 0 & \cdots & 1 \\ -a_n & -a_{n-1} & -a_{n-2} & \cdots & -a_1 \end{bmatrix}}_{A_n} \underbrace{\begin{bmatrix} x_1 \\ x_2 \\ \vdots \\ x_{n-1} \\ x_n \end{bmatrix}}_{X_n} + \underbrace{\begin{bmatrix} 0 \\ 0 \\ \vdots \\ 0 \\ 1 \end{bmatrix}}_{B_n} u$$

and the system dynamic equations are as follows:

$$Y(s) = G(s)U(s)$$

$$y = \underbrace{\begin{bmatrix} b_n - a_n b_0 & | & b_{n-1} - a_{n-1} b_0 & | & \cdots & | & b_1 - a_1 b_0 \end{bmatrix}}_{C_n} \begin{bmatrix} x_1 \\ x_2 \\ \vdots \\ x_{n-1} \\ x_n \end{bmatrix} + b_0 u$$

Now, a MIMO state model is ready to be developed with the following procedures. First, a transfer system matrix is decomposed to individual system dynamics:

$$\begin{bmatrix} y_1 \\ y_2 \end{bmatrix} = \begin{bmatrix} G_{11}(s) & G_{12}(s) \\ G_{21}(s) & G_{22}(s) \end{bmatrix} \begin{bmatrix} u_1 \\ u_2 \end{bmatrix}$$

$$\Rightarrow \begin{cases} y_1 = G_{11}(s)u_1 + G_{12}(s)u_2 \\ y_2 = G_{21}(s)u_1 + G_{22}(s)u_2 \end{cases}$$

A set of new variables is introduced:

$$\begin{cases} y_1 = y_{11} + y_{12} \\ y_2 = y_{21} + y_{22} \end{cases}$$

where $\begin{cases} y_{11} = G_{11}(s)u_1 \\ y_{12} = G_{12}(s)u_2 \\ y_{21} = G_{21}(s)u_1 \\ y_{22} = G_{22}(s)u_2 \end{cases}$, system dynamic equation

By direct programming methods, each individual system dynamic equation is converted into individual system state models:

$$\because y_1 = y_{11} + y_{12}$$
$$= C_{11}x_{11} + C_{12}x_{12}$$

$$\therefore y_1 = \begin{bmatrix} C_{11} & 0 \\ 0 & C_{12} \end{bmatrix}\begin{bmatrix} x_{11} \\ x_{12} \end{bmatrix}, \text{ and}$$

$$\begin{bmatrix} \dot{x}_{11} \\ \dot{x}_{12} \end{bmatrix} = \begin{bmatrix} A_{11} & 0 \\ 0 & A_{12} \end{bmatrix}\begin{bmatrix} x_{11} \\ x_{12} \end{bmatrix} + \begin{bmatrix} B_{11} & 0 \\ 0 & B_{12} \end{bmatrix}\begin{bmatrix} u_1 \\ u_2 \end{bmatrix}$$

Similarly,

$$y_2 = y_{21} + y_{22}$$
$$= C_{21}x_{21} + C_{22}x_{22}$$
$$= \begin{bmatrix} C_{21} & 0 \\ 0 & C_{22} \end{bmatrix}\begin{bmatrix} x_{21} \\ x_{22} \end{bmatrix}, \text{ and}$$

$$\begin{bmatrix} \dot{x}_{21} \\ \dot{x}_{22} \end{bmatrix} = \begin{bmatrix} A_{21} & 0 \\ 0 & A_{22} \end{bmatrix}\begin{bmatrix} x_{21} \\ x_{22} \end{bmatrix} + \begin{bmatrix} B_{21} & 0 \\ 0 & B_{22} \end{bmatrix}\begin{bmatrix} u_1 \\ u_2 \end{bmatrix}$$

These two decomposed system state models are combined:

$$\begin{bmatrix} \dot{x}_{11} \\ \dot{x}_{12} \\ \dot{x}_{21} \\ \dot{x}_{22} \end{bmatrix} = \begin{bmatrix} A_{11} & 0 & 0 & 0 \\ 0 & A_{12} & 0 & 0 \\ 0 & 0 & A_{21} & 0 \\ 0 & 0 & 0 & A_{22} \end{bmatrix} \begin{bmatrix} x_{11} \\ x_{12} \\ x_{21} \\ x_{22} \end{bmatrix} + \begin{bmatrix} B_{11} & 0 \\ 0 & B_{21} \\ B_{21} & 0 \\ 0 & B_{22} \end{bmatrix} \begin{bmatrix} u_1 \\ u_2 \end{bmatrix}$$

$$\begin{bmatrix} y_1 \\ y_2 \end{bmatrix} = \begin{bmatrix} C_{11} & 0 & C_{21} & 0 \\ 0 & C_{12} & 0 & C_{22} \end{bmatrix} \begin{bmatrix} x_{11} \\ x_{12} \\ x_{21} \\ x_{22} \end{bmatrix}$$

$\therefore G(s)$ can now be converted into a formulation of system P:

$$P := \left[\begin{array}{c|cc} A & 0 & B_2 \\ \hline 0 & 0 & 0 \\ C_2 & 0 & 0 \end{array}\right]$$

$$A := \text{diag}\{A_{11}, A_{12}, A_{21}, A_{22}\}$$

$$\text{where} \quad B_2 := \begin{Bmatrix} \text{diag}\{B_{11}, B_{12}\} \\ \text{diag}\{B_{21}, B_{22}\} \end{Bmatrix}$$

$$C_2 := \{\text{diag}\{C_{11}, C_{12}\} \mid \text{diag}\{C_{21}, C_{22}\}\}$$

In what follows, the uncertain parameters in the transfer function matrix and their effect on the matrix is reflected on system P are considered. Recall the upper linear fractional transformation on M by Δ_s:

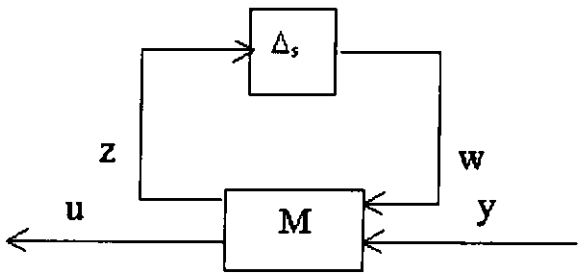

The perturbed system model G_r is described by

$$G_r(s) = G(s) + \underbrace{\{\Theta_{21}(s)\Delta_s(s)\,(I - \Theta_{11}(s)\Delta_s(s))^{-1}\,\Theta_{12}(s)\}}_{\Delta_G(s)}$$

5.2.4.1 *Example for μ-Formulation of 2x2 Plant with Perturbation in System Parameters (Constant in Denominator)*

Consider a 2nd order transfer function:

$$G_r(s) = \frac{b_0 s^2 + b_1 s + b_2}{s^2 + a_1 s + a_2\{1 - \rho\delta\}},\ |\delta| \le 1\ ,\ \textit{system 1}$$

This is a perturbed system with ρ% uncertainty in frequency-squared coefficient. Obviously,

$$G(s) = \frac{b_0 s^2 + b_1 s + b_2}{s^2 + a_1 s + a_2}$$

$$\therefore \Delta_G(s) = G_r(s) - G(s)$$

$$= b_0 s^2 + b_1 s + b_2 \left\{ \frac{1}{s^2 + a_1 s + a_2\{1 - \rho\delta\}} - \frac{1}{s^2 + a_1 s + a_2} \right\}$$

$$= b_0 s^2 + b_1 s + b_2 \left\{ \frac{\rho\delta a_2}{\left(s^2 + a_1 s + a_2\right)^2 \left\{1 - \frac{\rho\delta a_2}{s^2 + a_1 s + a_2}\right\}} \right\}$$

Comparing this with $\Delta_G(s) = \Theta_{21}(s)\Delta_s(s)\,\{I - \Theta_{11}(s)\Delta_s(s)\}^{-1}\,\Theta_{12}(s)$, it is convenient to make the following selection:

$$\Theta_{21}(s) = \frac{b_0 s^2 + b_1 s + b_2}{s^2 + a_1 s + a_2}$$

$$\Theta_{11}(s) = \Theta_{12}(s) = \frac{a_2 \rho}{s^2 + a_1 s + a_2}$$

$$\Delta_s(s) = \delta$$

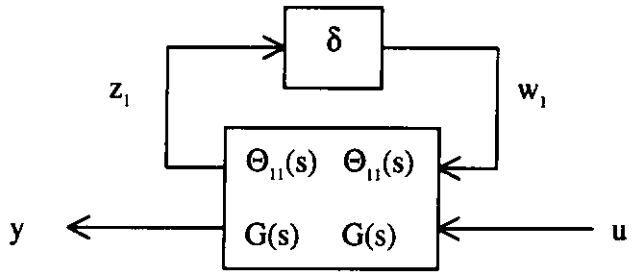

5.2.4.2 Example for μ-Formulation of 2x2 Plant with Perturbation in System Parameters (First Order Coefficient in Denominator)

Consider a 2nd order system with transfer function of

$$G_r(s) = \frac{b_0 s^2 + b_1 s + b_2}{s^2 + a_1\{1 - \rho_1\delta_1\}s + a_2}\ , \textit{system 2}$$

This is a perturbed system with ρ% uncertainty in two times the product of damping and frequency coefficients.

$$\therefore \Delta_G(s) = b_0 s^2 + b_1 s + b_2\left\{\frac{1}{s^2 + a_1 s + a_2 - a_1\rho_1\delta_1 s} - \frac{1}{s^2 + a_1 s + a_2}\right\}$$

$$= b_0 s^2 + b_1 s + b_2\left\{\frac{a_1\rho_1\delta_1 s}{\left(s^2 + a_1 s + a_2\right)^2\left\{1 - \frac{a_1\rho_1\delta_1 s}{s^2 + a_1 s + a_2}\right\}}\right\}$$

The following selection is developed:

$$\Theta_{21}(s) = \frac{b_0 s^2 + b_1 s + b_2}{s^2 + a_1 s + a_2}$$

$$\Theta_{11}(s) = \Theta_{12}(s) = \frac{a_1\rho_1 s}{s^2 + a_1 s + a_2}$$

$$\Delta_s(s) = \delta_1$$

5.2.4.3 Example for μ-Formulation of 2x2 Plant with Perturbation in System Parameters (Both First Order Coefficient and Constant in Denominator)

Now, two uncertain parameters are considered at the same time:

$$\therefore \Delta_G(s) = b_0 s^2 + b_1 s + b_2 \left\{ \frac{a_1\rho_1\delta_1 s + a_2\rho_2\delta_2}{(s^2 + a_1 s + a_2)^2 \left\{ 1 - \frac{a_1\rho_1\delta_1 s + a_2\rho_2\delta_2}{s^2 + a_1 s + a_2} \right\}} \right\}$$

The perturbed model is shown below:

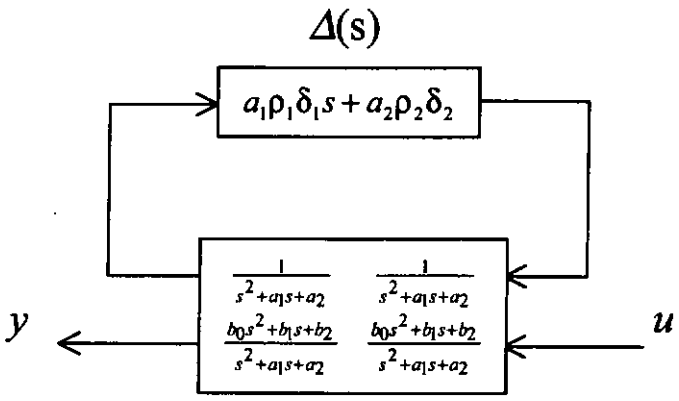

By converting Δ(s) into block diagonal structure, the perturbed model becomes:

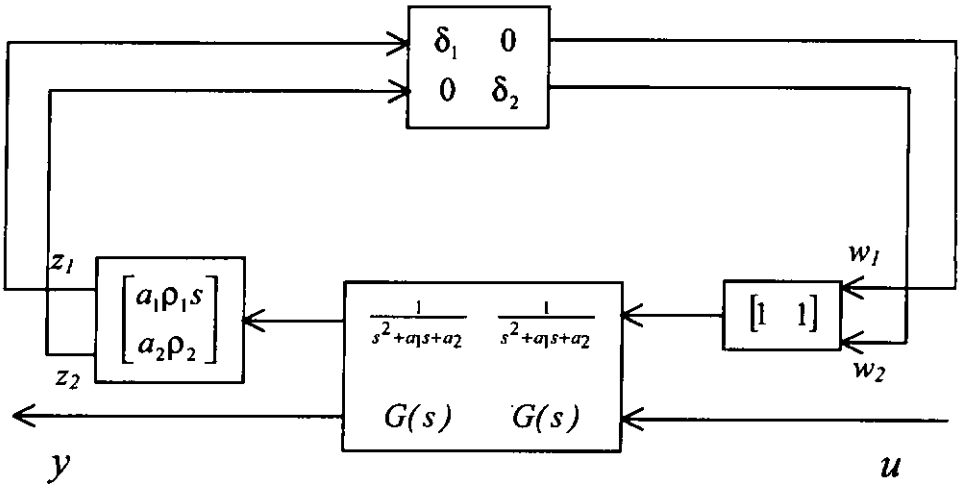

$$\begin{cases} z = \Theta_{11} w + \Theta_{12} u \\ y = \Theta_{21} w + \Theta_{22} u \end{cases}$$

$$\Rightarrow \begin{cases} z = \Theta_{11}\{w_1 + w_2\} + \Theta_{12} u \\ y = \Theta_{21}\{w_1 + w_2\} + \Theta_{22} u \end{cases}$$

$$\Rightarrow \begin{cases} z_1 = a_1\rho_1 s\Theta_{11}\{w_1 + w_2\} + a_1\rho_1 s\Theta_{12} u \\ z_2 = a_2\rho_2\Theta_{11}\{w_1 + w_2\} + a_2\rho_2\Theta_{12} u \\ y = \Theta_{21}\{w_1 + w_2\} + \Theta_{22} u \end{cases}$$

$$\Rightarrow \begin{cases} \begin{bmatrix} z_1 \\ z_2 \end{bmatrix} = \begin{bmatrix} a_1\rho_1 s\Theta_{11} & a_1\rho_1 s\Theta_{11} \\ a_2\rho_2\Theta_{11} & a_2\rho_2\Theta_{11} \end{bmatrix} \begin{bmatrix} w_1 \\ w_2 \end{bmatrix} + \begin{bmatrix} a_1\rho_1 s\Theta_{12} \\ a_2\rho_2\Theta_{12} \end{bmatrix} u \\ y = \begin{bmatrix} \Theta_{21} & \Theta_{21} \end{bmatrix} \begin{bmatrix} w_1 \\ w_2 \end{bmatrix} + \Theta_{22} u \end{cases}$$

Recall system 1 in 5.2.4.1

$$\begin{aligned} z_1 &= \Theta_{11}{}^{1}(s) w_1 + \Theta_{12}{}^{1}(s) u \\ y &= \Theta_{21}{}^{1}(s) w_1 + \Theta_{22}{}^{1}(s) u \end{aligned}$$, where superscript 1 shows that Θ_{ij} comes from system 1.

and system 2 in 5.2.4.2

$$\begin{aligned} z_2 &= \Theta_{11}{}^{2}(s) w_2 + \Theta_{12}{}^{2}(s) u \\ y &= \Theta_{21}{}^{2}(s) w_2 + \Theta_{22}{}^{2}(s) u \end{aligned}$$

The combined perturbed system model is rewritten as:

$$\Rightarrow \begin{cases} \begin{bmatrix} z_1 \\ z_2 \end{bmatrix} = \begin{bmatrix} \Theta_{11}{}^{1} & \Theta_{11}{}^{1} \\ \Theta_{11}{}^{2} & \Theta_{11}{}^{2} \end{bmatrix} \begin{bmatrix} w_1 \\ w_2 \end{bmatrix} + \begin{bmatrix} \Theta_{12}{}^{1} \\ \Theta_{12}{}^{2} \end{bmatrix} u \\ y = \begin{bmatrix} \Theta_{21}{}^{1/2} & \Theta_{21}{}^{1/2} \end{bmatrix} \begin{bmatrix} w_1 \\ w_2 \end{bmatrix} + \Theta_{22}{}^{1/2} u \end{cases}$$, where the superscript 1/2 shows that Θ_{ij}

comes from either system 1 or 2.

5.2.4.4 Example for μ-Formulation of 2x2 Plant with Perturbation in System Parameters (Constant in Numerator)

For the uncertain parameters to occur in the numerator polynomials of a transfer function, the following perturbation model is delivered:

Consider a 2nd order system with transfer function of:

$$G_r(s) = \frac{b_0 s^2 + b_1 s + b_2\{1 + \rho_3 \delta_3\}}{s^2 + a_1 s + a_2} \quad \text{„system 3}$$

It is rather straight-forward to obtain:

$$\therefore \Delta_G(s) = \frac{b_2 \rho_3 \delta_3}{s^2 + a_1 s + a_2}$$

and the following selection is made:

$$\Theta_{21}(s) = I$$
$$\Theta_{11}(s) = 0$$
$$\Theta_{12}(s) = \frac{b_2 \rho_3}{s^2 + a_1 s + a_2}$$
$$\Delta(s) = \delta_3$$

5.2.4.5 General μ-Formulation for Plant Perturbation in Parameters

However, a problem exists regarding how to write a perturbation model for the *n*th order system with transfer function of:

$$G_r(s) = \frac{b_0 s^m + \ldots + b_{m-1}\{1 + \rho_{n(m-1)}\delta_{n(m-1)}\}s + b_m\{1 + \rho_{nm}\delta_{nm}\}}{s^n + \cdots + a_{n-1}\{1 - \rho_{d(n-1)}\delta_{d(n-1)}\}s + a_n\{1 - \rho_{dn}\delta_{dn}\}}, \text{m} \le \text{n}$$

Using lemma 5.4 below, the perturbation model for the *n*th order system with uncertain parameters both in the numerator and denominator polynomials can be formulated.

Lemma 5.4

For the perturbed system with transfer function of $G_r(s) = \sum_{i=0}^{n} \frac{b_i s^{n-i}}{a_i s^{n-i}}$, $a_0 = 1$, *a perturbation model is defined, for each uncertain parameter in* $G_r(s)$, *with the following transfer function matrix:*

$$z_i = \Theta_{z_i w_i}{}^{i}(s) w_i + \Theta_{z_i u_i}{}^{i}(s) u$$
$$y = \Theta_{y_i w_i}{}^{i}(s) w_i + \Theta_{y_i u_i}{}^{i}(s) u \quad , w_i = \delta_i z_i$$

where the superscript i represents the ith uncertain parameter in $G_r(s)$ and $\Theta m_i n_i$ represents the transfer function between m_i *and* n_i.

The perturbation model of $G_r(s)$ is

$$\begin{bmatrix} z_1 \\ \vdots \\ \vdots \\ z_p \end{bmatrix} = \begin{bmatrix} \Theta_{z_1 w_1}{}^{1} & \cdots & \cdots & \Theta_{z_1 w_1}{}^{1} \\ \vdots & \ddots & & \vdots \\ \vdots & & \ddots & \vdots \\ \Theta_{z_p w_p}{}^{p} & \cdots & \cdots & \Theta_{z_p w_p}{}^{p} \end{bmatrix} \begin{bmatrix} w_1 \\ \vdots \\ \vdots \\ w_p \end{bmatrix} + \begin{bmatrix} \Theta_{z_1 u_1}{}^{1} \\ \vdots \\ \vdots \\ \Theta_{z_p u_p}{}^{p} \end{bmatrix} u$$

$$y = \begin{bmatrix} \Theta_{y_1 w_1}{}^{1} & \cdots & \cdots & \Theta_{y_p w_p}{}^{p} \end{bmatrix} \begin{bmatrix} w_1 \\ \vdots \\ \vdots \\ w_p \end{bmatrix} + Gu$$

if the following conditions are fulfilled:

1. $\Theta_{y_1 u_1} = \Theta_{y_2 u_2} = \cdots\cdots = \Theta_{y_p u_p} = G(s)$

2. $\Theta_{y_1 w_1} = \Theta_{y_2 w_2} = \cdots\cdots = \Theta_{y_p w_p} = C(s)$, where $C(s)$ is an abitary transfer function

The proof of lemma 5.4 is in *Appendix F*.

According to lemma 5.4, the perturbation model of system 3 can now be rewritten as:

$$\Delta_G(s) = \frac{b_2\rho_3\delta_3}{s^2 + a_1 s + a_2}$$

$$= \frac{b_0 s^2 + b_1 s + b_2}{s^2 + a_1 s + a_2}\left\{\frac{b_2\rho_3\delta_3}{b_0 s^2 + b_1 s + b_2}(I - 0\Delta)^{-1} I\right\}$$

Now, $\begin{cases} \Theta_{21}(s) = \dfrac{b_0 s^2 + b_1 s + b_2}{s^2 + a_1 s + a_2} = G(s) \\ \Theta_{11}(s) = 0 \\ \Theta_{12}(s) = \dfrac{b_2\rho_3}{b_0 s^2 + b_1 s + b_2} \end{cases}$

$\because \Theta_{21}^{3}(s) = \Theta_{21}^{2}(s) = \Theta_{21}^{1}(s) = G(s)$

$\therefore$ The combined perturbation model for system 1, system 2 and system 3 are formulated below:

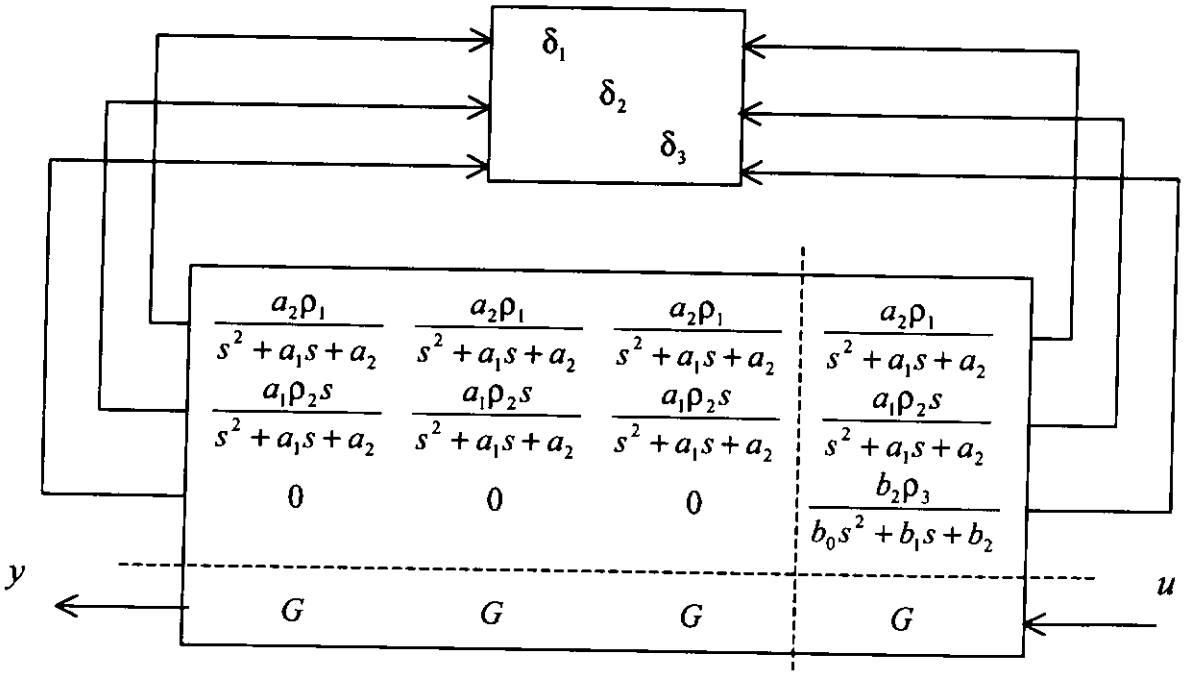

Figure5.2.4.5.1 The μ-Formation of Perturbation Plant with Uncertainty System Parameters (Combined Effect in System 1, 2 & 3)

5.2.5 Disturbance

Two types of disturbances will be discussed in this section: input and output disturbances. The effect of output disturbance, such as undulating road surface, which primarily affects the pitching and rolling of a vehicle, is modeled as the output of a shaping filter driver with unit intensity white noise, $\upsilon(t)$. A white noise is assumed, since the surface of the road is flat most of the time and the inclined angle of the undulating road surface is assumed to be random. The effect of input disturbance, such as the self-alignment torque on the contact point between the tires and the road, which primarily affects the steering angle (δ) that the driver commands the vehicle, is modeled as the output of shaping filter driven by unit intensity white noise, $d(t)$. The assumption is made since δ=0 is the normal operating condition, or $\delta(t)$=0.

Consider the following state equations:

$$\begin{aligned} \dot{x}(t) &= Ax(t) + Bu(t) + Ld(t) \\ y(t) &= Cx(t) + \nu(t) \end{aligned} \qquad (5.7)$$

Without great effort, the state equations can be directly translated into the P system:

$$P := \left[\begin{array}{c|c|c} A & [L \mid 0] & B \\ \hline 0 & 0 \quad 0 & 0 \\ \hline C & [0 \mid I] & 0 \end{array}\right] \left[\begin{array}{c} \left[\begin{array}{c} d \\ v \end{array}\right] \\ \hline u \end{array}\right]$$

Take the Laplace transformation of the state equations (5.7):

$$\begin{cases} x = (sI - A)^{-1} Bu + (sI - A)^{-1} Ld \\ y = Cx + \nu \end{cases}$$

$$\Rightarrow \begin{cases} x = (sI - A)^{-1} \{Bu + Ld\} \\ y = Cx + \nu \end{cases} \qquad (5.8)$$

The generalized system *P(s)* is constructed:

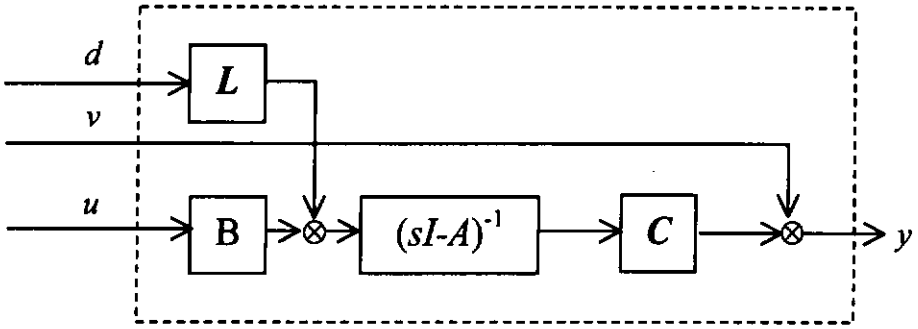

The case concerning the uncertain parameter in L is considered in the following section.

Recall state equation (5.7):

$$\dot{x}(t) = Ax(t) + Bu(t) + Ld(t)$$
$$y(t) = Cx(t) + v(t)$$

By introducing a new variable $u_d = [u,d]^T$

$$\Rightarrow \begin{cases} \dot{x}(t) = Ax(t) + B_d u_d \quad , \; B_d = [B \mid L] \\ y(t) = Cx(t) + v(t) \end{cases}$$
$$\Rightarrow y = C(sI - A)^{-1} B_d u_d + v$$

Omitting v, $y = G(s)u$

Transforming *G(s)* into a transfer function matrix, the system can be formulated as a perturbation model using the same procedure discussed in the last section.

5.2.6 Sensor Noise

Other than considering sensor noise as white noise, sensor models are built to capture the characterization of the sensors. The following widely used models for uncertain signals are in the norm sense:

$$W_2(c) := \left\{ w_u(t) \mid \|w_u(t)\|_2 := \left(\int_{-\infty}^{\infty} w_u(t)^T w_u(t) dt \right)^{1/2} \le c \right\}$$

where the admissible signal set consists of all signals with energy less than or equal to a given constant c;

$$W_\infty(c) := \left\{ w_u(t) \mid \|w_u(t)\|_\infty := \sup_t \max_i |w_{u_i}(t)| \le c \right\}$$

where the admissible signal set consists of all signals with maximum magnitude less than or equal to a given constant c.

In order to capture the characterization of the sensor, the aforementioned models can be refined by introducing suitable weights on filters, and the model becomes

$$\tilde{w}_u(t) := \int_{-\infty}^{t} W(t-\tau) w_u(\tau) d\tau$$

where $w_u(\tau)$ ranges over the admissible signal sets as defined before.

Now, the characterization of a gyro can be captured in the model. The measurement by a gyro is corrupted with sensor noise, which becomes more severe with increasing frequency. Let g be the measurement made by a gyro. The sensor noise weight is defined as:

$$W_g = 0.0003 \frac{1 + \frac{s}{0.01}}{1 + \frac{s}{0.5}}$$

The weighting functions imply a low frequency measurement error in g of 0.0003 rads/sec and high frequency error of 0.015 rads/sec. The model of the measured value of G, denoted G_{meas} is given by

$$G_{meas} = G + W_g \eta_g$$

where η_g is an arbitrary signal, with $||\eta_g||_2 \le 1$. This type of weighted, additive L_2 sensor noise is assumed for a gyro.

5.2.7 Input Command

As mentioned in the very beginning of this chapter, the input command to a control system can be viewed as a special disturbance, which is rather artificial. If the control system is designed in such a way that it aims to reject the disturbance, then a tracking controller can be designed as a regulating controller where the input command acts as an artificial disturbance. The input command is corresponding to a predesigned model of the reference path. The model is first designed and then discussed in the last chapter.

In a vehicle steering control, the driver (or controller) takes a turn through a series of gear chain and electronic clutch to steer the front wheels of the vehicle. These require accurate tracking of a steering command. Typical steering angle commands are modelled as:

$$\theta_{cmd} = W_{\theta cmd}\eta_{\theta cmd}$$

where $\eta_{\theta cmd}$ is assumed to be an arbitary signal $||\eta_{\theta cmd}||_2 \leq 1$. The weighting function on the steering command is chosen as:

$$W_{\phi_{cmd}} = 0.6\frac{1+\frac{s}{2}}{1+\frac{s}{0.5}}$$

The particular choice roughly implies that the steering angle commands are dominated by low frequency signals, with maximum magnitude of approximately 0.6 radians.

5.3 H_∞ Controller Design

H_∞ syntheses are carried out in the modern control paradigm. In this paradigm, both performance and robustness specifications can be incorporated in a common

framework, say μ framework, along with the controller synthesis. The incorporation with μ framework will be discussed in the next section.

H_∞ controller synthesis is incorporated in a framework, such that all the information about a system is casted into the generalized block diagram shown in Figure 5.3.1:

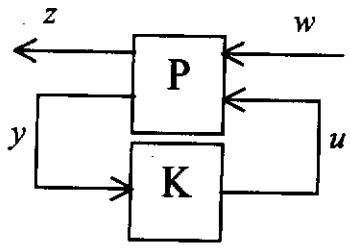

Figure 5.3.1 Generalized Block Diagram of the Modern Paradigm

The augmented plant, P, which is assumed to be linear and time-invariant, contains all the information a designer would like to incorporate into the synthesis of the controller, K. System dynamics, models of the uncertainty in the system dynamics, frequency weights to influence the controller synthesis, actuator dynamics, sensor dynamics and the effects of digital implementation of the control system are all included in augmented model P. In the block diagram, y is the sensor measurements that are used by the feedback controller, and u is the inputs generated by the controller. All the exogenous input to the system is represented by the vector w, which typically consists of disturbances, sensor noise, reference commands and fictitious signals that drive frequency weights and models of the uncertainty in the dynamics of the system. All the variables needed to be controlled are represented by z. These include the performance variables of interest, tracking errors between reference signals and plant output and the actuator signals which cannot be arbitrarily large and fast.

In the controller synthesis, the design of the feedback controller $K(s)$ aims to fulfill the following goals:

- Nominal closed loop stability
- Rejection of disturbances and/or measurement noise for the nominal closed loop system (i.e., nominal performance)
- Robust closed loop stability
- Robust performance

To fulfill the second goal, the size of the performance variable, z, should be kept small to drive exogenous signal, w, away from zero. Obviously, this depends on the "size" of the closed-loop transfer function from w to z, which is a sensitivity function defined later. Therefore, in this framework, controllers in the "size" of the closed-loop transfer function $T_{zw}(s)$ are used, where the "size" of $T_{zw}(s)$ is the H_∞ norm.

Robust closed loop stability means that the closed loop system is stable under all possible perturbations to the plant $G(s)$ and is absorbed in the augmented plant P. Robust performance is used to indicate that the closed loop system is stable and that the performance requirements are met under all possible perturbations to the plant $G(s)$.

To access nominal closed loop stability, the theorem of Generalized Nyquist Stability Criteria I is used.

Theorem 5.3.1 (Generalized Nyquist Stability Criteria I)

If the open loop transfer function matrix $G(s)$ x $K(s)$ has p poles in the right-half s-plane, then the closed loop system is stable if and only if the characteristic loci of $G(s)$ x $K(s)$ encircle the point $(-1,0j)$ p times anti-clockwise, assuming no right-half s-plane zero-pole cancellations have occurred.

To access nominal performance, consider the general multivariable feedback scheme shown in Figure 5.3.2:

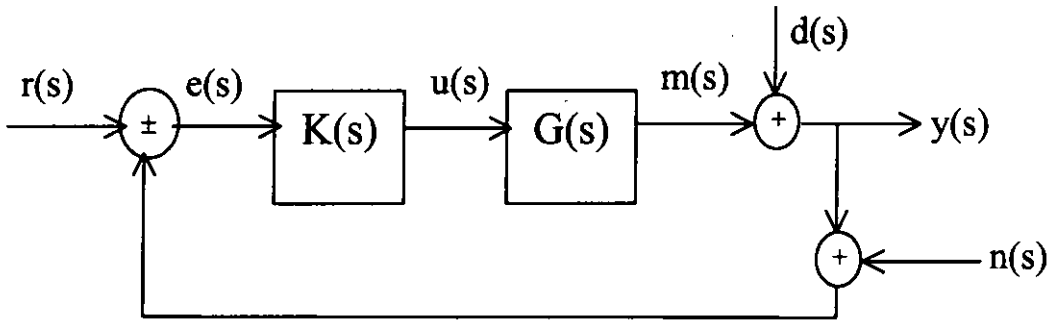

Figure 5.3.2 General Feedback Control Configuration

The figure easily shows that:

$$y(s)=\underbrace{(I+G(s)K(s))^{-1}\,G(s)K(s)}_{T_0(s)}(r(s)-n(s))+\underbrace{(1+G(s)K(s))^{-1}}_{S_0(s)}d(s)$$

$$e(s)=\underbrace{(1+G(s)K(s))^{-1}}_{S_0(s)}(r(s)-d(s)-n(s))$$

$$e_o(s)=r(s)-y(s)=\underbrace{(1+G(s)K(s))^{-1}}_{S_0(s)}(r(s)-d(s))+\underbrace{\{[1+G(s)K(s)]^{-1}\,G(s)K(s)\}}_{T_0(s)}n(s)$$

$$u(s)=\underbrace{K(s)(1+G(s)K(s))^{-1}}_{M_0(s)}(r(s)-n(s)-d(s))$$

where $T_0(s)$, $S_0(s)$ and $M_0(s)$ are the complementary sensitivity, sensitivity and control sensitivity functions, respectively. The subscript $(\bullet)_0$ emphasizes that the sensitivity functions are all evaluated at the plant output.

With these sensitivity functions defined, the nominal performance, robust stability and robust performance can be accessed and related to the "size" of those functions. Let a "generic" external disturbance be defined as $\delta(s) := r(s) - d(s)$. The sensitivity $S_0(s)$ should be small for good disturbance error reduction; the complementary sensitivity $T_0(s)$ should be small for good sensor noise error reduction; and the control sensitivity $M_0(s)$ should be small for disturbance $\delta(s)$ and noise $n(s)$ to affect the control input $u(s)$ to the least extent.

By incorporating the weighting functions onto the sensitivity functions, the frequency area of interest may be selected. The weighted sensitivity specification is actually a typical performance specification for robust control.

$$\sup_{\omega} \bar{\sigma}(W_{p2}(j\omega)S_o(j\omega)W_{p1}(j\omega)) = \left\|W_{p2}(j\omega)S_o(j\omega)W_{p1}(j\omega)\right\|_{H_\infty} \leq 1$$

where $W_{p1}(s)$ denotes the input weight used to transform the normalized $\delta^1(s)$ to the physical input $\delta(s) = W_{p1}(s)\delta^1(s)$ and W_{p2} denotes the output weight used to track off the relative importance of the individual errors in $e(s)$ and to weigh the frequency range of primary interest.

Therefore, the performance specification is interpreted as follows:

$$\left\|W_{p2}(j\omega)S_o(j\omega)W_{p1}(j\omega)\right\|_{H_\infty} \le 1$$

$$\Leftrightarrow \sup_{\delta' \in L_2 \neq 0} \frac{\|e'\|_{2,2}}{\|\delta'\|_{2,2}} \le 1$$

$$\Rightarrow \sup_{\delta' \in D_t \neq 0} \|e'\|_{2,2} \le 1$$

$$\Leftrightarrow \sup_{\delta' \in D_t \neq 0} \sqrt{\int_{-\infty}^{\infty} e'(t)^T e'(t) dt} \le 1 \text{ , where } D_t = \{\delta(t) \mid \|\delta\|_{2,2} = \sqrt{\int_{-\infty}^{\infty} \delta(t)^T \delta(t) dt} \le 1$$

The nominal performance objective is then defined as follows:

Definition 5.3.1:

The nominal performance problem is, given weighting functions $W_{p1}(s)$ and $W_{p2}(s)$, to design a stabilizing controller $K(s)$ such that the cost function

$$J_{np} = \left\|W_{p2}(j\omega)S_o(j\omega)W_{p1}(j\omega)\right\|_{H_\infty}$$

is minimized.

To access robust stability, the following two theories are used.

Theorem 5.3.2 (Small Gain Theorem)

Assumed that the interconnection $P(s)$ is stable and that the perturbation $\Delta(s)$ is of such a form that the perturbed closed loop system is stable if and only if the map of $det((I - P(s)\,\Delta(s))$ as s traverses the D contour does not encircle the origin. Then, the closed loop system is stable for all perturbations $\Delta(s)$ with $\bar{\sigma}(\Delta(j\omega)) \le 1$ if and only if one of the following four equivalent conditions are satisfied:

$$\begin{aligned} & det(I - P(j\omega)\Delta(j\omega)) \neq 0 \ , \ \forall\omega, \forall\Delta(j\omega) \ni \bar{\sigma}(\Delta(j\omega)) \le 1 \\ \Leftrightarrow\ & \rho(P(j\omega)\Delta(j\omega)) < 1 \quad , \ \forall\omega, \forall\Delta(j\omega) \ni \bar{\sigma}(\Delta(j\omega)) \le 1 \\ \Leftrightarrow\ & \bar{\sigma}(P(j\omega)) < 1 \quad , \ \forall\omega \\ \Leftrightarrow\ & \|P(s)\|_{H_\infty} < 1 \end{aligned}$$

The Small Gain Theorem can be found in [109]. It states that, for an open-loop stable system, a sufficient condition for closed loop stability is to keep the loop "gain" measured by $\rho(P(j\omega))$ less than unity. The theorem for Robust Stability is due to [110], which states that if $||P(s)||_{H\infty} < 1$, then there is no perturbation $\Delta(s)(\bar{\sigma}(\Delta(jw)) \leq 1)$ which makes $det(I - P(s)\Delta(s))$ encircle the origin as s traverses the Nyquist D contour. The assumption of the absence of encirclements is necessary and sufficient to maintain stability. This is the case when all perturbations $\Delta(s)$ are stable or when the perturbed mode, nominal model $G_T(s)$ and $G(s)$ have the same number of unstable poles. Finally, the robust performance objective is derived from nominal performance objective with nominal sensitivity $S_0(s)$ replaced by perturbed sensitivity $T_0(s)$:

$$J_{np} = \left\| W_{p2}(j\omega)\tilde{S}_o(j\omega)W_{p1}(j\omega) \right\|_{H_\infty}$$

where $\tilde{S}_o(s)$ is defined as follows:

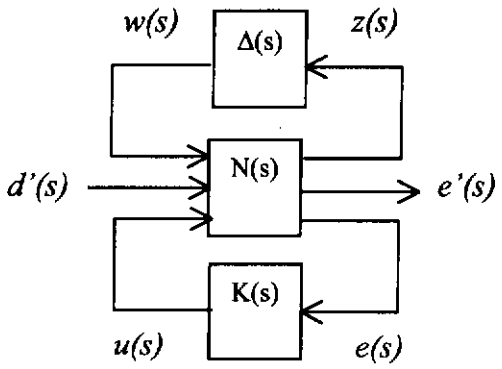

By LFT, the transfer function from $d'(s)$ to $e'(s)$ is:

$$e'(s)/d'(s) = F_u(P(s),\Delta(s))$$

$$= [P_{22}(s) + P_{21}(s)\Delta(s)(I - P_{11}(s)\Delta(s))^{-1}P_{12}(s)]$$

$$= W_{p2}(s)\tilde{S}_o(s)W_{p1}(s)$$

Theorem 5.3.3 (Robust Performance)

Assume that the interconnection $P(s) = F_l(N(s),K(s))$ is stable and that the perturbation $\tilde{\Delta}(s)$ is of such a form that the perturbed closed loop system in Figure 5.3.3 is stable if and only if the map of $det(I - P(s)\tilde{\Delta}(s))$ as s traverses the D contour does not encircle the origin. Then, the system $F_u(P(s),\Delta(s))$ will satisfy the robust performance criterion $||F_u(P(s),\Delta(s)||_{H\infty} < 1$ if and only if $P(s)$ is stable for all perturbations $\tilde{\Delta}(s)$ with $\bar{\sigma}(\tilde{\Delta}(s)) \leq 1$:

$$\begin{aligned} & \det(I - P(j\omega)\tilde{\Delta}(j\omega)) \neq 0 \ , \ \forall\omega, \forall\tilde{\Delta}(j\omega) \in \bar{\sigma}(\tilde{\Delta}(j\omega)) \leq 1 \\ \Leftrightarrow\ & \rho(P(j\omega)\tilde{\Delta}(j\omega)) < 1 \quad , \ \forall\omega, \forall\tilde{\Delta}(j\omega) \in \bar{\sigma}(\tilde{\Delta}(j\omega)) \leq 1 \\ \Leftrightarrow\ & \left\| P(s) \right\|_{H_\infty} < 1 \end{aligned}$$

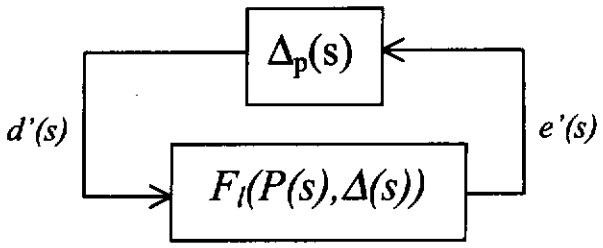

Figure 5.3.3 Block Diagram Structure for Robust Performance Check

H_∞ controller is obtained with the following theory.

Theorem 5.3.4

Let $P(s)$ be given by its state-space matrices A, B, C and D and introduce the notation

$$P := \left[\begin{array}{c|cc} A & B_1 & B_2 \\ \hline C_1 & D_{11} & D_{12} \\ C_2 & D_{21} & D_{22} \end{array}\right]$$

The following assumptions are made:

1. (A_1,B_1) and (A,B_2) are stabilizable
2. (C_1,A) and (C_2,A) are detectable
3. $D_{12}^T D_{12} = I$ and $D_{21} D_{21}^T = I$
4. $D_{11} = D_{22} = 0$

Let $\quad \bar{D}_{12} = I - D_{12} D_{12}^T,\ \bar{D}_{21} = I - D_{21}^T D_{21}$

And solve the two Ricatti equations:

$$X_\infty = Ric\begin{bmatrix} A - B_2 D_{12}^T C_1 & \gamma^{-2} B_1 B_1^T - B_2 B_2^T \\ -C_1^T \bar{D}_{12}^T \bar{D}_{12} C_1 & -(A - B_2 D_{12}^T C_1)^T \end{bmatrix}$$

$$Y_\infty = Ric\begin{bmatrix} (A - B_1 D_{21}^T C_2)^T & \gamma^{-2} C_1^T C_1 - C_2^T C_2 \\ -B_1 \bar{D}_{12} \bar{D}_{12}^T B_1^T & -(A - B_1 D_{21}^T C_2)^T \end{bmatrix}$$

From the state feedback matrix K_0, the output injection matrix K_τ and the matrices Z_∞, B_Q and B_Y:

$$K_c = (D_{12}^T C_1 + B_2^T X_\infty)$$
$$K_f = (B_1 D_{21}^T + Y_\infty C_2^T)$$
$$Z_\infty = (I - \gamma^{-2} Y_\infty X_\infty)^{-1}$$
$$B_Q = Z_\infty (B_2 + \gamma^{-2} Y_\infty C_1^T D_{12})$$
$$B_Y = \gamma^{-2} D_{21} B_1^T X_\infty$$

If $X_\infty \geq 0$ and $Y_\infty \geq 0$ exist and if the spectral radius $\rho(X_\infty Y_\infty) < \gamma^2$, then the H_∞ DGKF

Parameterization is given by:

$$P := \left[\begin{array}{c|cc} A_\infty & Z_\infty K_f & B_Q \\ \hline -K_c & 0 & I \\ -(C_2 + B_Y) & I & 0 \end{array}\right]$$

$$= \begin{bmatrix} J_{11}(s) & J_{12}(s) \\ J_{21}(s) & J_{22}(s) \end{bmatrix}$$

where A_∞ is given by

$$A_\infty = A - B_2 K_c + \gamma^{-2} B_1 B_1^T X_\infty - Z_\infty K_f (C_2 + B_\gamma)$$

Stabilizing controllers $K(s)$ may now be constructed by connecting $J(s)$ to any stable transfer function matrix $Q(s)$ with $||Q(s)||_{H\infty} < \gamma$

$$K(s) = F_L(J(s), Q(s))$$

$$= J_{11}(s) + J_{12}(s)Q(s)(I - J_{22}(s)Q(s))^{-1} J_{21}(s)$$

The ∞-norm of the closed loop system $F_e(N(s), F_e(J(s),Q(s)))$ satisfy

$$||F_e(N(s), F_e(J(s), Q(s)))||_{H\infty} < \gamma$$

The controller obtained for $Q(s) = 0$ is known as the central H_∞ controller.

5.4 H_∞ Controller design using μ Framework

The H_∞ control theory can be characterized as being extremely useful and practical, because it is a robust control theory which can positively treat uncertainty. The concepts found in the last section of the H_∞ control theory include robust stability based on the small gain theorem with H^∞ norm as its scale and sensitivity reductions in relation to nominal models. The robust stability condition is that a closed loop is stable even if uncertainty exists, while the nominal performance condition is that the H^∞ norm from generated signals to the control quantity for nominal models without

variations is limited below a certain value. As a result, the synthesis of the H^{∞} control theory is based on these conditions trade off:

$$T_o(j\omega)+S_o(j\omega)=1$$
$$\Rightarrow \left\| |W_2T|+|W_1T| \right\|_{\infty} < 1$$

However, there are some limitations in connection with the H_{∞} control theory. Probably the most important is that only full complex perturbation structures $\Delta(s) \in C^{nxm}$ can be handled in an H_{∞} robustness test. Recall the assumption [the perturbation block used in the last section]:

$$|| \hat{\Delta}(j\omega) ||_2 = \bar{\sigma} (\hat{\Delta}(j\omega)) \leq I(jw), \ \forall w \geq 0$$

This becomes too conservative, since the H^{∞} control theory over estimates errors by not structuring uncertainty but rather by treating it as the maximum singular value.

By connecting H^{∞} control theory with μ framework, the uncertainty Δ is formulated into μ framework, and a μ controller is synthesized that achieves robust stability, nominal performance and robust performance at the same time. The general framework for robustness analysis and synthesis of linear systems are illustrated in the following figure:

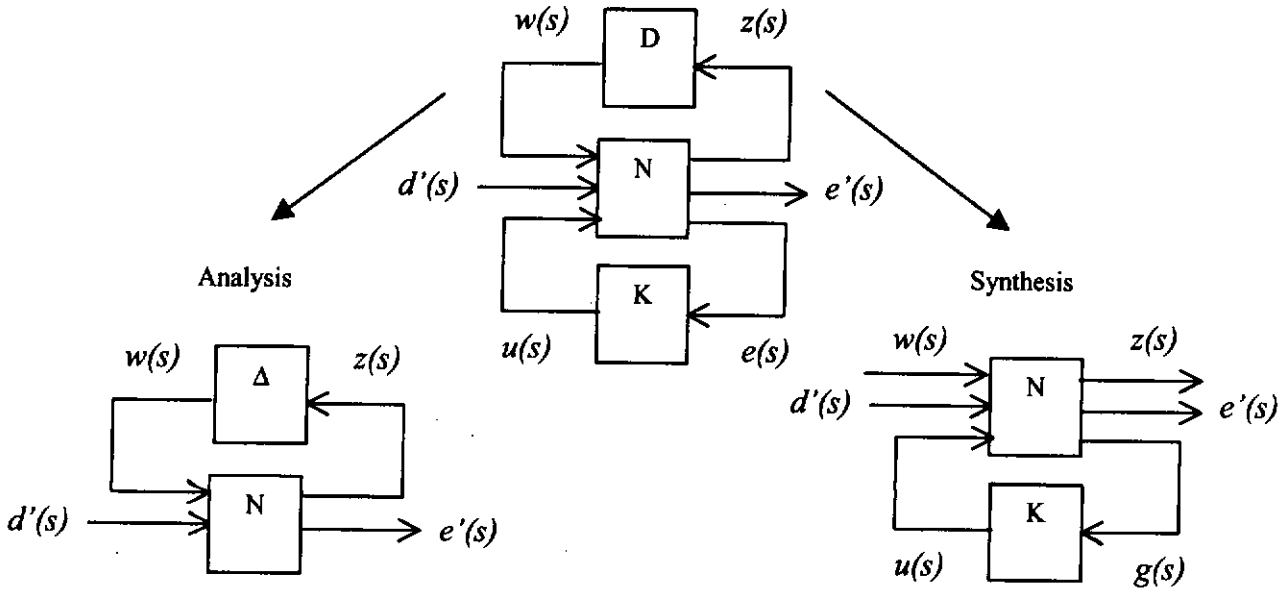

In the above figure, the generalized framework is obtained from

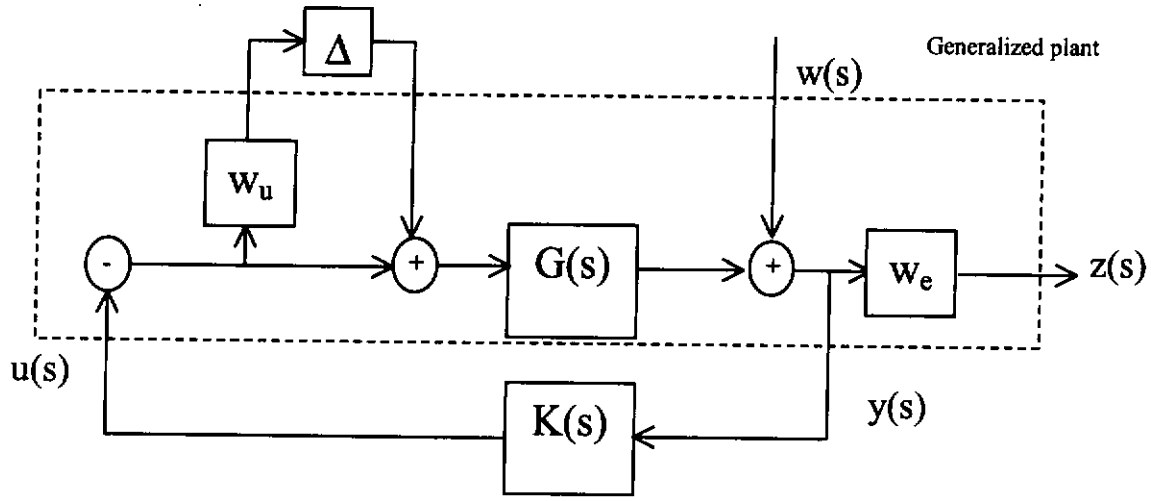

Figure 5.4.1 General Framework for Robustness Analysis and Synthesis of Linear Systems

The uncertainty model is in the form of multiplicative uncertainty in the input signal to the plant and Δ belongs to B_Δ.

The robust stability under structured perturbation $\Delta(s) \in B_\Delta$ is determined by the following theorem:

Theorem 5.4.1

Let H_∞ performance specification be given on the transfer function from d' to e' – typically a weighted sensitivity specification – of the form:

$$||F_u(P(s),\Delta(s))||_\infty = \sup_\omega \bar{\sigma}\,(F_u(P(j\omega),\Delta(j\omega))) < 1$$

Then $F_u(P(s),\Delta(s))$ is stable and $||F_u(P(s),\Delta(s)||_\infty < 1,\ \forall\, \Delta(s) \in \boldsymbol{B}_\Delta$ if and only if

$$\left\|\mu_{\tilde{\Delta}}(P(s))\right\|_\infty \le 1$$

where the perturbation set is augmented with a full complex performance block:

$$\tilde{\Delta} = \{diag(\Delta,\Delta_p) \mid \Delta \in \boldsymbol{\Delta},\ \Delta_p \in \boldsymbol{C}^{k\,xk}\}$$

Using μ, the test for both robust stability and robust performance is possible in a non-conservative manner. Indeed, if the uncertainty is modeled exactly by $\Delta(s)$, then the μ condition for robust performance is necessary and sufficient. However, since μ cannot be calculated directly, the upper bound problem is considered instead. For complex perturbation that sets an iterative scheme, *D-K* iteration is used [D-K].

5.5 μ-Formulation of Perturbation Vehicle Design Model

In this section, the vehicle design model in Chapter 3.4 is recalled. And the perturbation vehicle design model will be developed using the methodology developed in the last few sections. The state space formulation of the vehicle design model is shown below.

$$\dot{X} = \begin{bmatrix} \ddot{y} \\ \dot{\varepsilon}_r \\ \dot{y}_r \\ \ddot{\theta}_z \\ \dot{\theta}_r \\ \ddot{\theta}_r \end{bmatrix} = \begin{bmatrix} A_1 & 0 & 0 & A_2 & A_3 & A_4 \\ 0 & 0 & 0 & 1 & 0 & 0 \\ 1 & U & 0 & 0 & 0 & 0 \\ A_5 & 0 & 0 & A_6 & 0 & 0 \\ 0 & 0 & 0 & 0 & 0 & 1 \\ A_7 & 0 & 0 & A_8 & A_9 & A_0 \end{bmatrix} \begin{bmatrix} \dot{y} \\ \varepsilon_r \\ y_r \\ \dot{\theta}_z \\ \theta_r \\ \dot{\theta}_r \end{bmatrix} + \begin{bmatrix} g & 0 \\ 0 & -1 \\ 0 & 0 \\ 0 & 0 \\ 0 & 0 \\ 0 & 0 \end{bmatrix} \begin{bmatrix} \eta \\ \dot{\theta}_d \end{bmatrix} + \begin{bmatrix} B_1 \\ 0 \\ 0 \\ B_2 \\ 0 \\ B_3 \end{bmatrix} \delta , \quad (5.5.1)$$

where the expressions of A_0-A_9, B_1-B_3 are listed in Section 3.4.

The transfer functions for δ to θz and δ to y are formulated as below,

$$\ddot{y} = A_1\dot{y} + A_2\dot{\theta}_z + A_3\theta_r + A_4\dot{\theta}_r + g\eta + B_1\delta$$
$$\ddot{\theta}_z = A_5\dot{y} + A_6\dot{\theta}_z + B_2\delta$$
$$\ddot{\theta}_r = A_7\dot{y} + A_8\dot{\theta}_z + A_9\theta_r + A_0\dot{\theta}_r + B_3\delta$$

$$(s^2 - A_1 s)y = A_2 s\theta_z + (A_3 + A_4 s)\theta_r + g\eta + B_1\delta$$
$$\Rightarrow \quad (s^2 - A_6 s)\theta_z = A_5 sy + B_2\delta$$
$$(s^2 - A_0 s - A_9)\theta_r = A_7 sy + A_8 s\theta_z + B_3\delta$$

$$\Rightarrow \quad \theta z = -(\delta s^3 B_2 + (A_5 g\eta - A_1 \delta B_2 + A_5 \delta B_1 - B_2 \delta A_0) s^2 + (-A_5 g\eta A_0 - \delta A_4 A_7 B_2 + A_5 B_3 \delta A_4 - A_9 \delta B_2 + A_1 \delta B_2 A_0 - A_5 \delta B_1 A_0) s - A_5 A_9 g\eta - A_5 A_9 \delta B_1 - \delta A_3 A_7 B_2 + A_5 B_3 \delta A_3 + A_1 A_9 \delta B_2) / s\{(-s^4 + (A_6 + A_0 + A_1) s^3 + (A_4 A_7 + A_9 - A_6 A_0 - A_1 A_6 - A_1 A_0 + A_5 A_2) s^2 + (A_3 A_7 - A_6 A_4 A_7 - A_2 A_5 A_0 - A_1 A_9 - A_9 A_6 + A_5 A_4 A_8 + A_1 A_6 A_0) s - A_5 A_9 A_2 - A_6 A_3 A_7 + A_1 A_9 A_6 + A_5 A_3 A_8)\}$$ and

$$y = ((-g\eta-\delta B_1)s^3+(-B_2\delta A_2+A_6 B_1\delta+\delta B_1 A_0+g\eta A_0-A_4 B_3\delta+A_6 g\eta)s^2+(B_2\delta A_2 A_0+A_6 A_4 B_3\delta-A_6\delta B_1 A_0-A_6 g\eta A_0+g\eta A_9-B_2\delta A_4 A_8-A_3 B_3\delta+B_1\delta A_9)s-A_9 A_6 g\eta+A_9\delta A_2 B_2+B_3 A_6\delta A_3-\delta A_3 A_8 B_2-A_9 A_6\delta B_1)/s\{(-s^4+(A_6+A_0+A_1)s^3+(A_4 A_7+A_9-A_6 A_0-A_1 A_6-A_1 A_0+A_5 A_2)s^2+(A_3 A_7-A_6 A_4 A_7-A_2 A_5 A_0-A_1 A_9-A_9 A_6+A_5 A_4 A_8+A_1 A_6 A_0)s-A_5 A_9 A_2-A_6 A_3 A_7+A_1 A_9 A_6+A_5 A_3 A_8)\}$$

$$\theta_r = -(B_3\delta s^2+(A_7 B_1\delta+A_8 B_2\delta+A_7 g\eta-B_3\delta A_6-B_3\delta A_1)s-A_5 B_3\delta A_2-A_6 g\eta A_7-A_6\delta B_1 A_7+\delta A_2 A_7 B_2-A_1\delta A_8 B_2+A_5 g\eta A_8+A_5\delta B_1 A_8+A_1 B_3 A_6\delta)/(-s^4+(A_6+A_0+A_1)s^3+(A_4 A_7+A_9-A_6 A_0-A_1 A_6-A_1 A_0+A_5 A_2)s^2+(A_3 A_7-A_6 A_4 A_7-A_2 A_5 A_0-A_1 A_9-A_9 A_6+A_5 A_4 A_8+A_1 A_6 A_0)s-A_5 A_9 A_2-A_6 A_3 A_7+A_1 A_9 A_6+A_5 A_3 A_8)$$

$$\Rightarrow\quad \theta_z = -(s^3B_2+(-A_1B_2+A_5B_1-B_2A_0)s^2+(-A_4A_7B_2+A_5B_3A_4-A_9B_2+A_1B_2A_0-A_5B_1A_0)s-A_5A_9B_1-A_3A_7B_2+A_5B_3A_3+A_1A_9B_2)/s/(-s^4+(A_6+A_0+A_1)s^3+(A_4A_7+A_9-A_6A_0-A_1A_6-A_1A_0+A_5A_2)s^2+(A_3A_7-A_6A_4A_7-A_2A_5A_0-A_1A_9-A_9A_6+A_5A_4A_8+A_1A_6A_0)s-A_5A_9A_2-A_6A_3A_7+A_1A_9A_6+A_5A_3A_8)\delta-(-A_5A_9g-A_5gA_0s+gA_5s^2)/s/(-s^4+(A_6+A_0+A_1)s^3+(A_4A_7+A_9-A_6A_0-A_1A_6-A_1A_0+A_5A_2)s^2+(A_3A_7-A_6A_4A_7-A_2A_5A_0-A_1A_9-A_9A_6+A_5A_4A_8+A_1A_6A_0)s-A_5A_9A_2-A_6A_3A_7+A_1A_9A_6+A_5A_3A_8)\eta$$ and

$$y = (-B_1s^3+(-B_2A_2+B_1A_0-A_4B_3+A_6B_1)s^2+(A_6A_4B_3-A_6B_1A_0+B_2A_2A_0-B_2A_4A_8-A_3B_3+B_1A_9)s+A_9A_2B_2+B_3A_6A_3-A_3A_8B_2-A_9A_6B_1)/(-s^4+(A_6+A_0+A_1)s^3+(A_4A_7+A_9-A_6A_0-A_1A_6-A_1A_0+A_5A_2)s^2+(A_3A_7-A_6A_4A_7-A_2A_5A_0-A_1A_9-A_9A_6+A_5A_4A_8+A_1A_6A_0)s-A_5A_9A_2-A_6A_3A_7+A_1A_9A_6+A_5A_3A_8)/s\delta+(-s^3g+(A_6g+gA_0)s^2+(gA_9-A_6gA_0)s-A_9A_6g)/(-s^4+(A_6+A_0+A_1)s^3+(A_4A_7+A_9-A_6A_0-A_1A_6-A_1A_0+A_5A_2)s^2+(A_3A_7-A_6A_4A_7-A_2A_5A_0-A_1A_9-A_9A_6+A_5A_4A_8+A_1A_6A_0)s-A_5A_9A_2-A_6A_3A_7+A_1A_9A_6+A_5A_3A_8)/s\eta$$

$$\theta_r = -((A_7B_1+A_8B_2-B_3A_6-B_3A_1)s-A_5B_3A_2-A_6B_1A_7+A_2A_7B_2-A_1A_8B_2+B_3s^2+A_5B_1A_8+A_1B_3A_6)/(-s^4+(A_6+A_0+A_1)s^3+(A_4A_7+A_9-A_6A_0-A_1A_6-A_1A_0+A_5A_2)s^2+(A_3A_7-A_6A_4A_7-A_2A_5A_0-A_1A_9-A_9A_6+A_5A_4A_8+A_1A_6A_0)s-A_5A_9A_2-A_6A_3A_7+A_1A_9A_6+A_5A_3A_8)\delta-(-A_6gA_7+A_7sg+A_5gA_8)/(-s^4+(A_6+A_0+A_1)s^3+(A_4A_7+A_9-A_6A_0-A_1A_6-A_1A_0+A_5A_2)s^2+(A_3A_7-A_6A_4A_7-A_2A_5A_0-A_1A_9-A_9A_6+A_5A_4A_8+A_1A_6A_0)s-A_5A_9A_2-A_6A_3A_7+A_1A_9A_6+A_5A_3A_8)\eta$$

$$\theta_z = -(Z_1 s^3 + Z_2 s^2 + Z_3 s + P_1)\delta / \{ s(-s^4 + Z_4 s^3 + Z_5 s^2 + Z_6 s + Z_7) \}$$

$$+ Q_1 \eta / \{ s(-s^4 + Z_4 s^3 + Z_5 s^2 + Z_6 s + Z_7) \}$$

$$y = (Y_1 s^3 + Y_2 s^2 + Y_3 s + Y_4)\delta / \{ s(-s^4 + Z_4 s^3 + Z_5 s^2 + Z_6 s + Z_7) \}$$

$$+ Q_2 \eta / \{ s(-s^4 + Z_4 s^3 + Z_5 s^2 + Z_6 s + Z_7) \}$$

$$\theta_r = -((R_1 s + R_2)\delta / (-s^4 + Z_4 s^3 + Z_5 s^2 + Z_6 s + Z_7)$$

$$+ Q_3 \eta / (-s^4 + Z_4 s^3 + Z_5 s^2 + Z_6 s + Z_7)$$

where Z_i and Y_i are the corresponding coefficients and Q_i is the corresponding expression.

Therefore the transfer functions from control input δ to variables θ_z , y, θ_r and disturbance η to variables θ_z , y, θ_r are listed below.

$$G_{z\delta} = \frac{\theta_z}{\delta} = \frac{-(Z_1 s^3 + Z_2 s^2 + Z_3 s + P_1)}{s(-s^4 + Z_4 s^3 + Z_5 s^2 + Z_6 s + Z_7)}$$

$$G_{y\delta} = \frac{y}{\delta} = \frac{Y_1 s^3 + Y_2 s^2 + Y_3 s + P_2}{s(-s^4 + Z_4 s^3 + Z_5 s^2 + Z_6 s + Z_7)}$$

$$G_{r\delta} = \frac{y}{\delta} = \frac{R_1 s^2 + R_2 s + R_3}{-s^4 + Z_4 s^3 + Z_5 s^2 + Z_6 s + Z_7}$$

$$G_{z\eta} = \frac{\theta_z}{\eta} = \frac{Q_{11} s^2 + Q_{12} s + Q_{13}}{s(-s^4 + Z_4 s^3 + Z_5 s^2 + Z_6 s + Z_7)}$$

$$G_{y\eta} = \frac{y}{\eta} = \frac{Q_{21} s^3 + Q_{22} s^2 + Q_{23} s + Q_{24}}{s(-s^4 + Z_4 s^3 + Z_5 s^2 + Z_6 s + Z_7)}$$

$$G_{r\eta} = \frac{\theta_r}{\eta} = \frac{Q_{31} s + Q_{32}}{-s^4 + Z_4 s^3 + Z_5 s^2 + Z_6 s + Z_7}$$

Note that A_1, A_2, A_5, A_6, A_7 and A_8 in Equation 5.5.1 are all obtained by linearization of the tire model in complex vehicle model developed in Section 3.3.

A_1 and A_2, A_5 and A_6, A_7 and A_8 are obtained from D_1, D_2, D_3 respectively, where

$$D_1 = -\frac{I_x}{\Lambda_r}(L_1 + L_2 + L_3 + L_4)$$

$$D_2 = \frac{1}{I_z}(a(L_1 + L_2) - b(L_3 + L_4))$$

$$D_3 = \frac{mh}{\Lambda_r}(L_1 + L_2 + L_3 + L_4)$$

$$D_1 = -2C_f \frac{I_x}{\Lambda_r}\delta + \frac{I_x}{\Lambda_r}(2C_f \frac{1}{U} + 2C_r \frac{1}{U})\dot{y} + \frac{I_x}{\Lambda_r}(2aC_f \frac{1}{U} - 2bC_r \frac{1}{U})\dot{\theta}_z$$

and $$D_2 = 2aC_f \frac{1}{I_z}\delta - \frac{1}{I_z}(2aC_f \frac{1}{U} - 2bC_r \frac{1}{U})\dot{y} - \frac{1}{I_z}(2a^2C_f \frac{1}{U} - 2b^2C_r \frac{1}{U})\dot{\theta}_z$$

$$D_3 = 2C_f \frac{mh}{\Lambda_r}\delta - \frac{mh}{\Lambda_r}(2C_f \frac{1}{U} + 2C_r \frac{1}{U})\dot{y} - \frac{mh}{\Lambda_r}(2aC_f \frac{1}{U} - 2bC_r \frac{1}{U})\dot{\theta}_z$$

From Section 3.3, the maximum error obtained in L_1 and L_2 is 123.95% and the maximum error obtained in L_3 and L_4 is 83.56%. For simplification, we assume that 60% of maximum error in D_1 is equally distributed in A_1, A_2, and B_1 and the same assumption is also applied to D_2 and D_3. The percentage of 60 in maximum error of D_i is chosen since only the moderately hostile conditions are considered in simulation throughout the study.

Both D_1 and D_3 involve the summation of four lateral forces, L_i , therefore, 60% of maximum error in D_1 and D_3 becomes 223.11%. However, D_2 involves the subtraction between front lateral forces, $L_{1,2}$ and rear lateral forces, $L_{3,4}$, therefore, the maximum error occurred would be expected to be relatively small when compare to D_1 and D_2. 60% of maximum error in D_2 is 96.936. This value is obtained with the assumption that the errors in the front lateral forces and the rear lateral forces are 50% interdependent.

Now the errors in A_1, A_2, A_7, A_8, B_1, B_3 are all 73.8% and the errors in A_5, A_6 and B_2 is 32.31%. The errors occurs in Z_1-Z_7 , Y_1-Y_3 , R_1-R_2 , P_1-P_2 , Q_{ij} are listed in the table 5.5.1

Table 5.5.1 Possible Errors Encountered in Zs, Ys, Rs, Ps, Qs

Parameters	Expressions	Numerical Value	Possible
Z_1	B_2	19.2480	32.31
Z_2	$-A_1B_2+A_5B_1-B_2A_0$	138.7098	0
Z_3	$-A_4A_7B_2+A_5B_3A_4-A_9B_2+A_1B_2A_0-A_5B_1A_0$	*2212*	*Nil*
Z_4	$A_6+A_0+A_1$	-9.7494	106.11
Z_5	$A_4A_7+A_9-A_6A_0-A_1A_6-A_1A_0+A_5A_2$	-133.4799	0
Z_6	$A_3A_7-A_6A_4A_7-A_2A_5A_0-A_1A_9-A_9A_6+A_5A_4A_8+A_1A_6A_0$	*-594.7297*	*Nil*
Z_7	$-A_5A_9A_2-A_6A_3A_7+A_1A_9A_6+A_5A_3A_8$	*-790.3460*	*Nil*
Y_1	$-B_1$	-27.1526	73.8
Y_2	$-B_2A_2+B_1A_0-A_4B_3+A_6B_1$	169.3659	0
Y_3	$A_6A_4B_3-A_6B_1A_0+B_2A_2A_0-B_2A_4A_8-A_3B_3+B_1A_9$	*-1546.4*	*Nil*
P_1	$-A_5A_9B_1-A_3A_7B_2+A_5B_3A_3+A_1A_9B_2$	*5803*	*Nil*
P_2	$A_9A_2B_2+B_3A_6A_3-A_3A_8B_2-A_9A_6B_1$	*29044*	*Nil*
R_1	$-B_3$	4.6340	73.8
R_2	$-(A_7B_1+A_8B_2-B_3A_6-B_3A_1)$	11.9326	0
R_3	$A_5B_3A_2+A_6B_1A_7-A_2A_7B_2+A_1A_8B_2-A_5B_1A_8-A_1B_3A_6$	179.4303	0
Q_{11}	$-A_5g$	-0.1201	32.31
Q_{12}	A_5A_0g	*-0.5069*	*Nil*
Q_{13}	A_5A_9g	*-12.3087*	*Nil*
Q_{21}	$-g$	*-9.81*	*Nil*
Q_{22}	A_6g+A_0g	-66.5309	32.31
Q_{23}	$A_9g-A_6A_0g$	*-1111.6*	*Nil*
Q_{24}	$-A_6A_9g$	*-2574.5*	*Nil*
Q_{31}	$-A_7g$	-4.9683	73.8
Q_{32}	$A_6A_7g-A_5A_8g$	-12.7197	0

By using Lemma 5.4, the perturbation model of those subsystems G_{ij} are written as followings.

$$Gr_{z\delta} = \frac{Z_1\{1+\rho_{z1}\delta_{z1}\}s^3 + Z_2s^2 + Z_3s + P_1}{s^5 - Z_4\{1-\rho_{z4}\delta_{z1}\}s^4 - Z_5s^3 - Z_6s^2 - Z_7s}$$

$$Gr_{y\delta} = \frac{-Y_1\{1+\rho_{y1}\delta_{y1}\}s^3 - Y_2s^2 - Y_3s - P_2}{s^5 - Z_4\{1-\rho_{z4}\delta_{z4}\}s^4 - Z_5s^3 - Z_6s^2 - Z_7s}$$

$$Gr_{r\delta} = \frac{-R_1\{1+\rho_{r1}\delta_{r1}\}s^2 - R_2s - R_3}{s^4 - Z_4\{1-\rho_{z4}\delta_{z4}\}s^3 - Z_5s^2 - Z_6s - Z_7}$$

$$Gr_{zq} = \frac{-Q_{11}\{1+\rho_{q11}\delta_{q11}\}s^2 - Q_{12}s - Q_{13}}{s^5 - Z_4\{1-\rho_{z4}\delta_{z4}\}s^4 - Z_5 s^3 - Z_6 s^2 - Z_7 s)}$$

$$Gr_{yq} = \frac{-Q_{21}s^3 - Q_{22}\{1+\rho_{q22}\delta_{q22}\}s^2 - Q_{23}s - Q_{24}}{s^5 - Z_4\{1-\rho_{z4}\delta_{z4}\}s^4 - Z_5 s^3 - Z_6 s^2 - Z_7 s)}$$

$$Gr_{rq} = \frac{-Q_{31}\{1+\rho_{q31}\delta_{q31}\}s - Q_{32}}{s^4 - Z_4\{1-\rho_{z4}\delta_{z4}\}s^3 - Z_5 s^2 - Z_6 s - Z_7}$$

For perturbation model $Gr_{z\delta}$, $Gr_{z\delta} = \dfrac{Z_1\{1+\rho_{z1}\delta_{z1}\}s^3 + Z_2 s^2 + Z_3 s + P_1}{s^5 - Z_4\{1-\rho_{z4}\delta_{z1}\}s^4 - Z_5 s^3 - Z_6 s^2 - Z_7 s}$

$$\begin{aligned} z_i &= \Theta_{z_i w_i} i(s) w_i + \Theta_{z_i u_i} i(s) u \\ y &= \Theta_{y w_i} i(s) w_i + \Theta_{y u_i} i(s) u \end{aligned}$$, where

$$\Theta_{11} = \begin{bmatrix} \dfrac{Z_4\rho_{z4}s^4}{s^5 - Z_4 s^4 - Z_5 s^3 - Z_6 s^2 - Z_7 s} & \dfrac{Z_4\rho_{z4}s^4}{s^5 - Z_4 s^4 - Z_5 s^3 - Z_6 s^2 - Z_7 s} \\ 0 & 0 \end{bmatrix}$$

$$\Theta_{12} = \begin{bmatrix} \dfrac{Z_4\rho_{z4}s^4}{s^5 - Z_4 s^4 - Z_5 s^3 - Z_6 s^2 - Z_7 s} \\ \dfrac{Z_1\rho_{z1}s^3}{Z_1 s^3 + Z_2 s^2 + Z_3 s + P_1} \end{bmatrix}$$

$$\Theta_{21} = \begin{bmatrix} \dfrac{Z_1 s^3 + Z_2 s^2 + Z_3 s + P_1}{s^5 - Z_4 s^4 - Z_5 s^3 - Z_6 s^2 - Z_7 s} & \dfrac{Z_1 s^3 + Z_2 s^2 + Z_3 s + P_1}{s^5 - Z_4 s^4 - Z_5 s^3 - Z_6 s^2 - Z_7 s} \end{bmatrix}$$

$$\Theta_{22} = \frac{Z_1 s^3 + Z_2 s^2 + Z_3 s + P_1}{s^5 - Z_4 s^4 - Z_5 s^3 - Z_6 s^2 - Z_7 s}$$

The perturbation model of $Gr_{z\delta}$ are shown below:

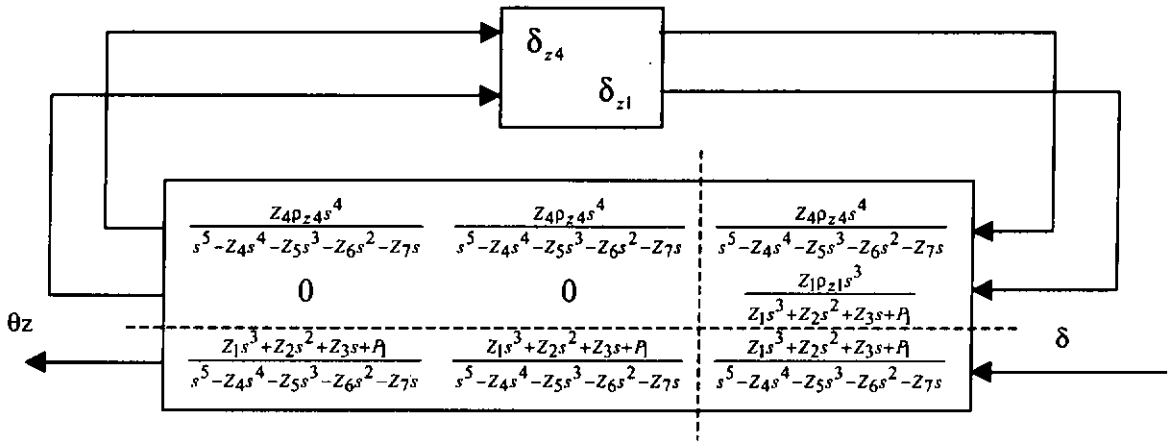

6. COMPLEX VEHICLE MODEL AND DESIGN VEHICLE MODEL

6.1 Open Loop Simulation

In this section, the differences between complex vehicle model and design vehicle model are investigated. Firstly, the open loop simulations are performed to confirm that the responses of the complex and the design models remain close to each other under typical operating conditions. Three types of input signals are used in the simulations: sinusoidal, trapezoidal and lane change reference. For the steering commands shown in Figure 6.1, the simulated responses by complex and design model are as shown in Figure 6.2.

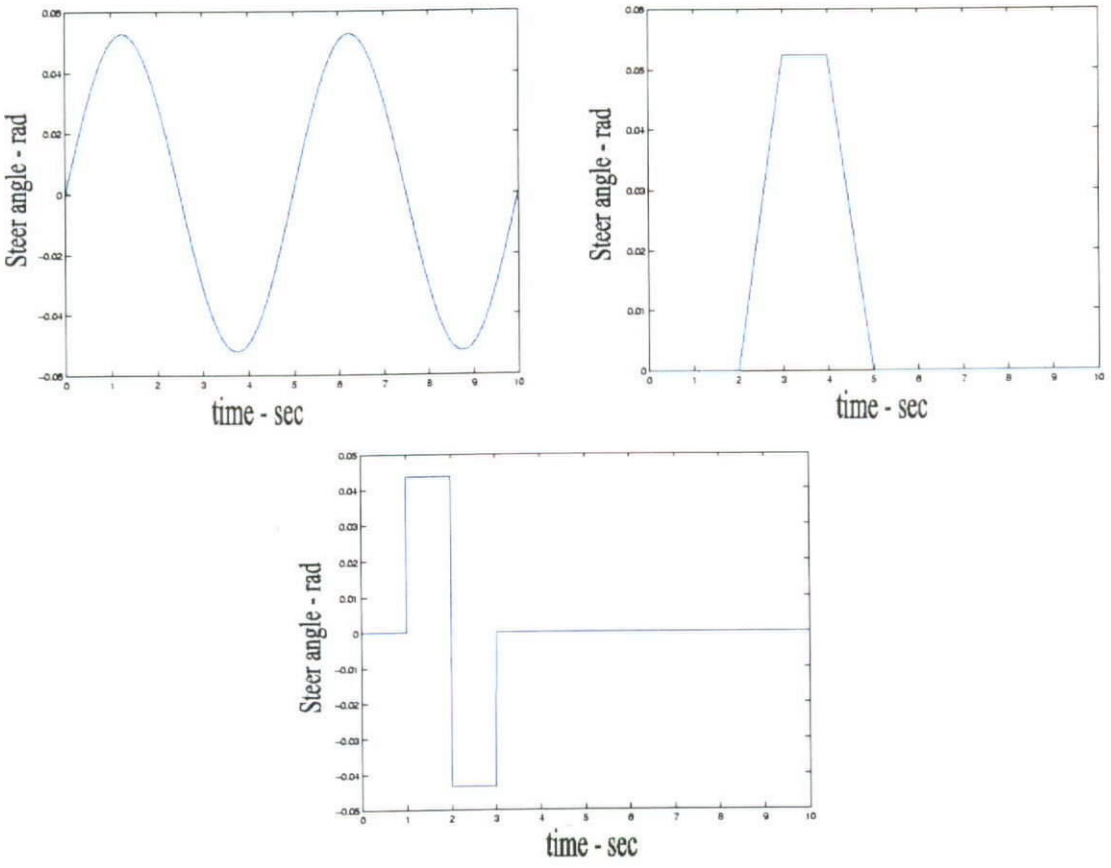

Figure 6.1 Steering Commands in Open Loop Simulations

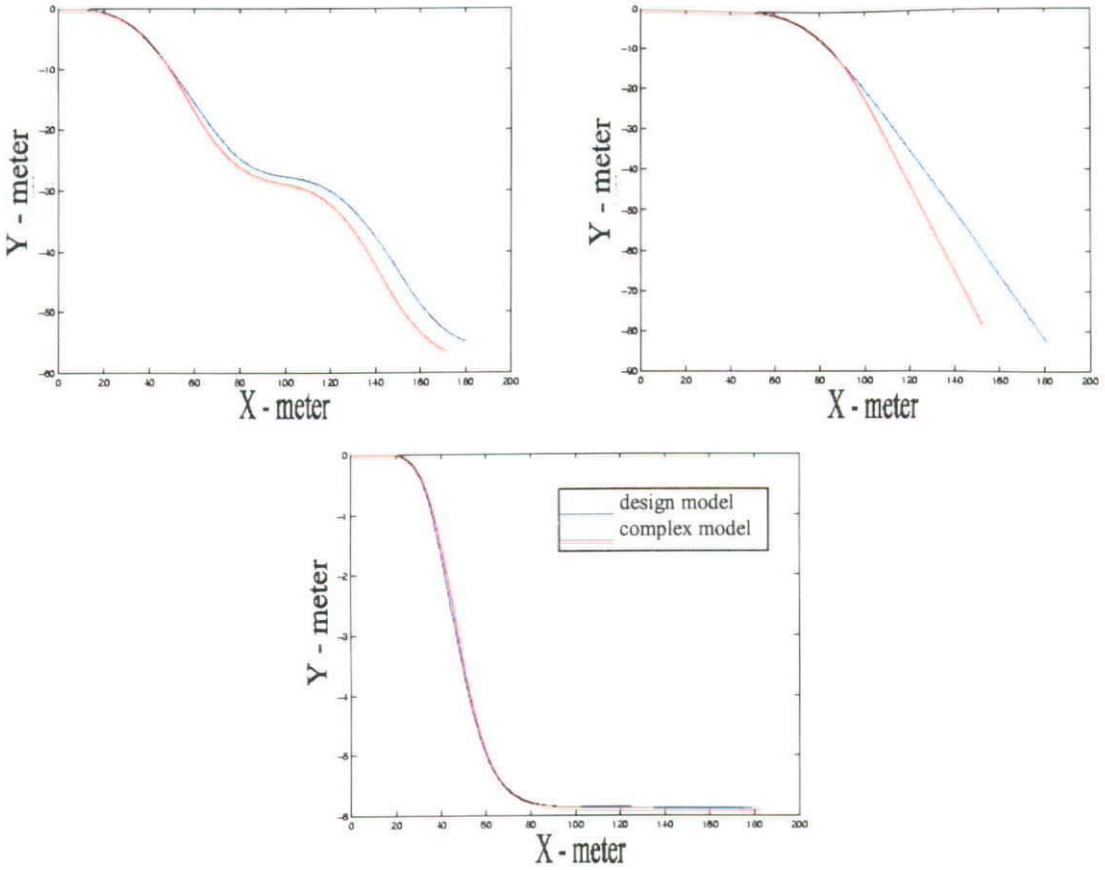

Figure 6.2 Responses of Vehicle in Open Loop Simulations

Responses of the complex model and those of the design model remain close to each other, therefore the design model is a good approximation of the complex model for those typical inputs. However, the final justification of the control system will be based on the closed-loop simulation with the complex model.

Two additional types of input signals are used in the simulations: high frequency sinusoidal, ramp. For the steering commands shown in Figure 6.3, the simulated responses by the complex and design models are as shown in Figure 6.4.

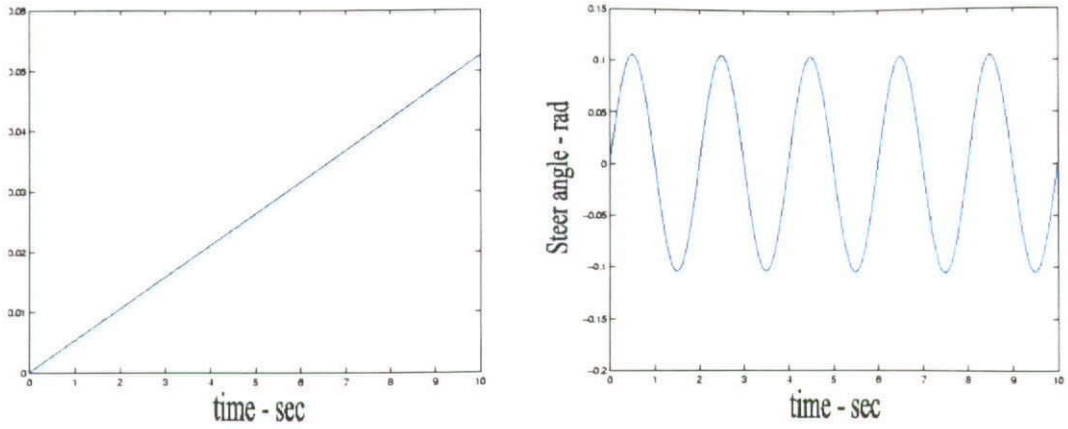

Figure 6.3 Steering Commands in Open Loop Simulation, Ramp and Sin(0.5Hz)

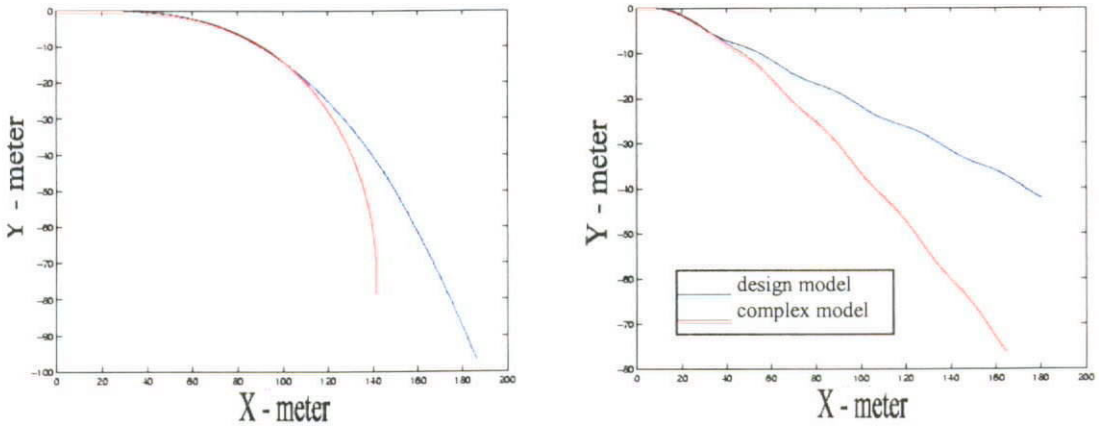

Figure 6.4 Responses of Vehicle in Open Loop Simulation, Ramp and Sin(0.5Hz)

Responses of the complex model and those of the design model do not remain close to each other in this case. Therefore, the design model is no longer a good approximation of the complex model for those inputs with relatively higher frequency. Therefore, some nonlinearities in the complex model should be included in the design model, which is called the perturbation design model. With the perturbation design model, robust control system can be developed. The responses of vehicle running on a slanted road surface in open loop simulation are shown in Appendix G.

6.2 Detail Comparison of Complex and Design Vehicle Model

In this section, the discrepancies between the complex and design vehicle model are investigated by way of lateral forces acting on each tire of the vehicle. In Section 3.1, we understood that the main source of the vehicle's nonlinear property is due to the nonlinearities in the vehicle tire model. Tire reduction factor $F(S)$ draws the function of lateral forces, which is dependent on side slip angles, away from having a linear property. If $F(S)$ <1, the linear functions $L_I = C_i\alpha_i$ are no longer a good approximation to the lateral force. The more the value of $F(S)$ moves away from unity, the more the vehicle tire model has the nonlinear property which, in turn, causes the nonlinear property of the vehicle model.

Figures 6.5 – 6.7 show the distribution of the lateral force in the open loop simulation with sinusoidal input. Figures 6.8 – 6.10 show the distribution of the lateral force in the open loop simulation with high frequency sinusoidal input.

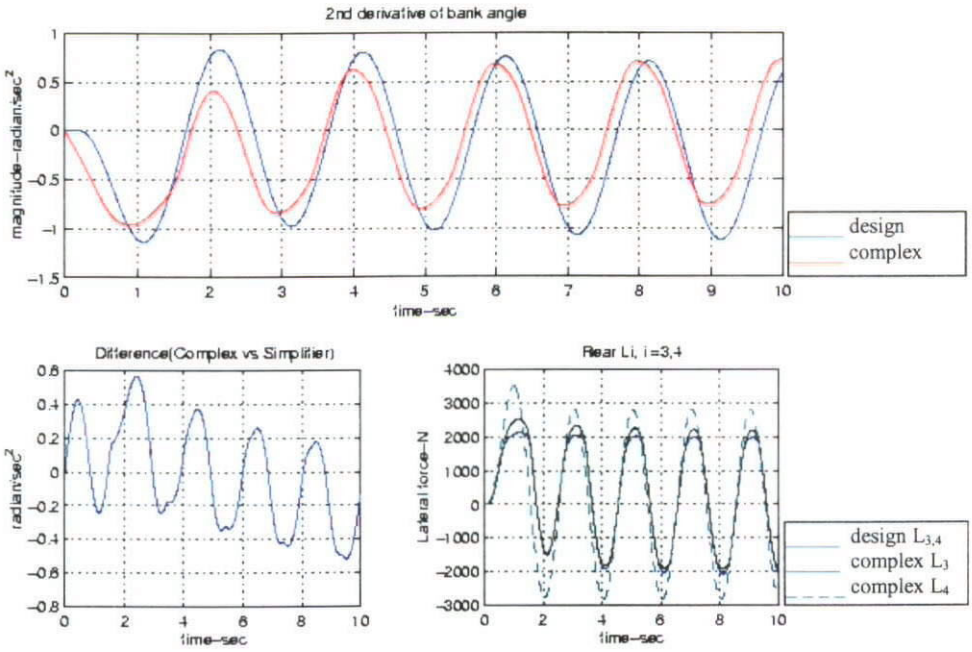

Figure 6.5 Responses of Rear Lateral Forces in Open Loop Simulation with Sinusoidal Input of Steering Angle (0.6rad - 0.5Hz)

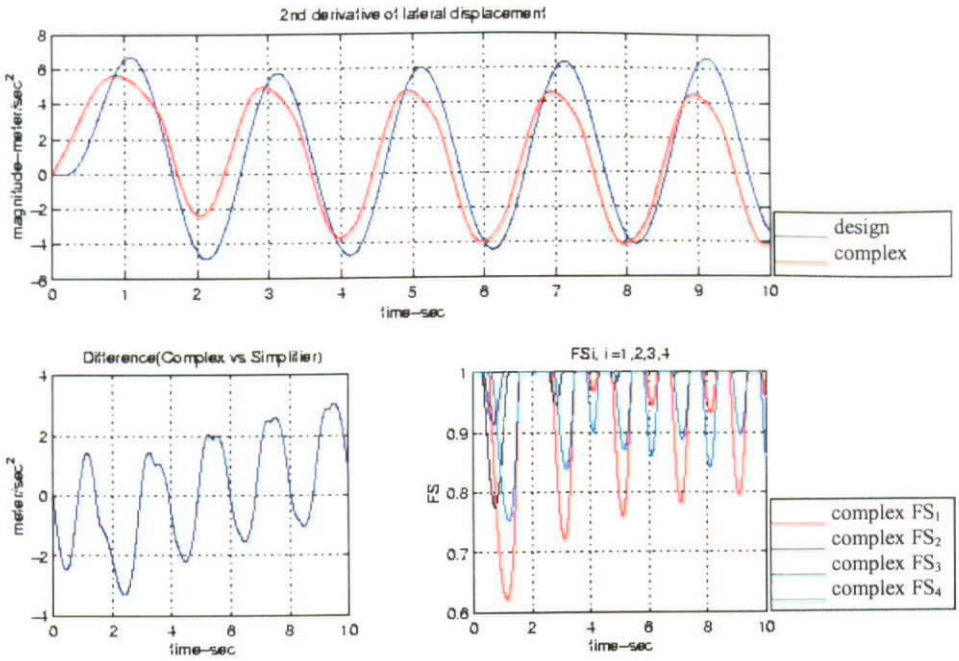

Figure 6.6 Responses of Reduction Factor, F(S), in Open Loop Simulation with Sinusoidal Input of Steering Angle(0.6rad - 0.5Hz)

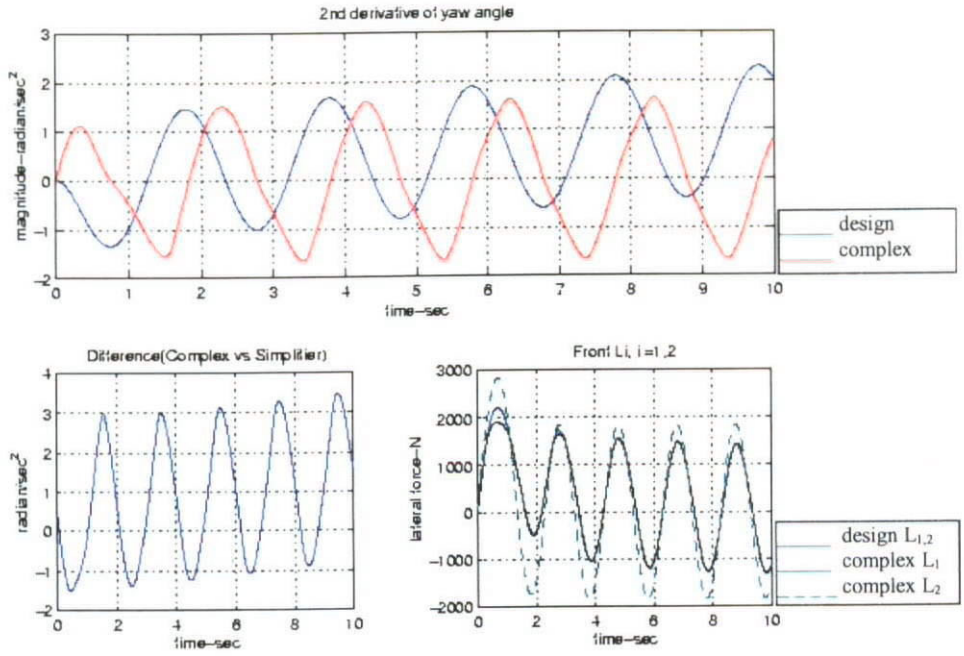

Figure 6.7 Responses of Front Lateral Forces in Open Loop Simulation with Sinusoidal Input of Steering Angle (0.6rad - 0.5Hz)

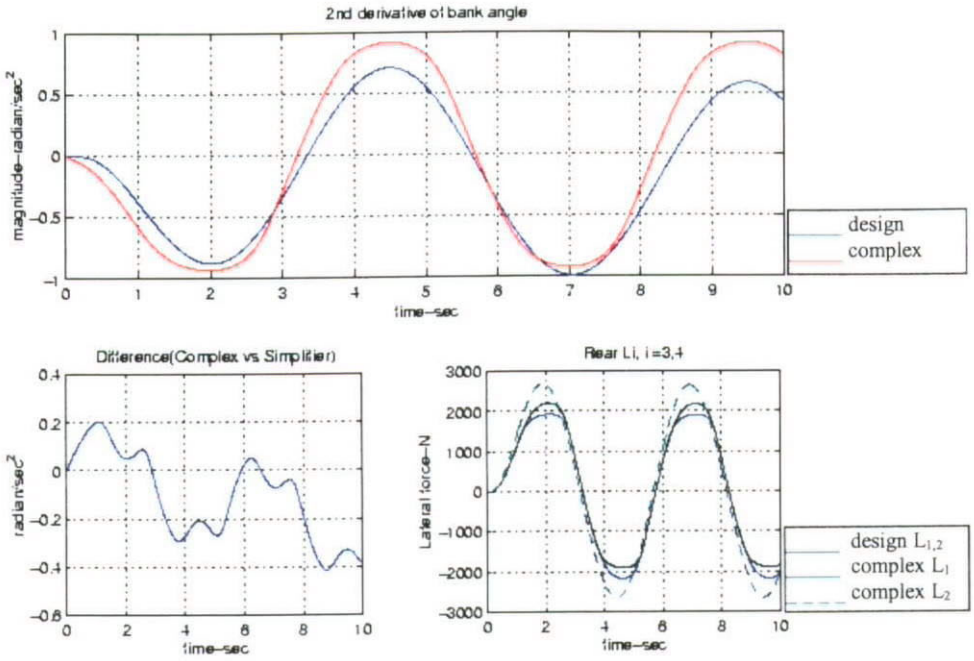

Figure 6.8 Responses of Rear Lateral Forces in Open Loop Simulation with Sinusoidal Input of Steering Angle (0.3rad - 0.2Hz)

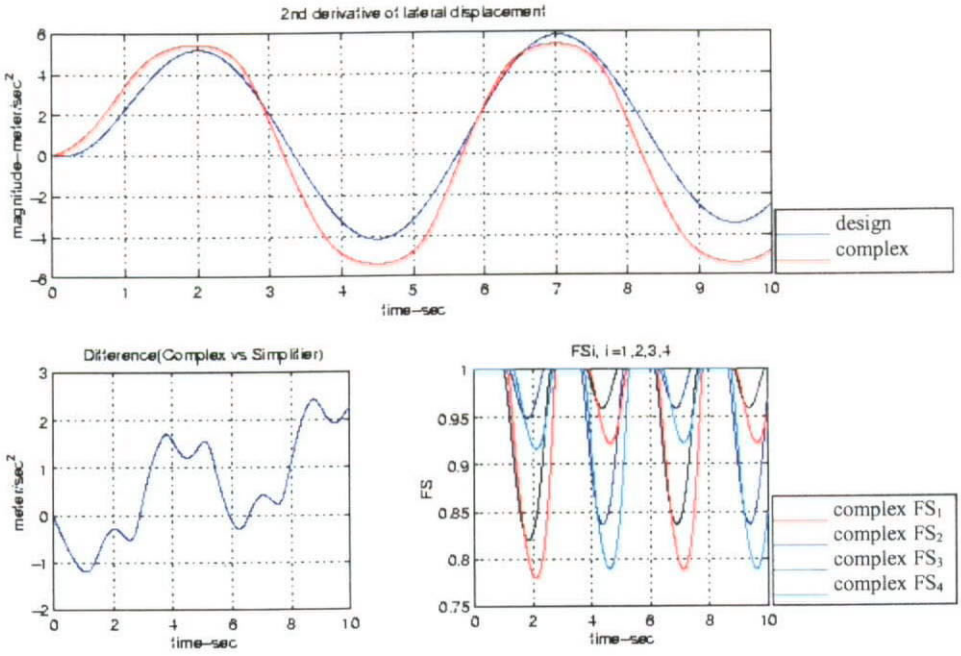

Figure 6.9 Responses of Reduction Factor, F(S), in Open Loop Simulation with Sinusoidal Input of Steering Angle (0.3rad - 0.2Hz)

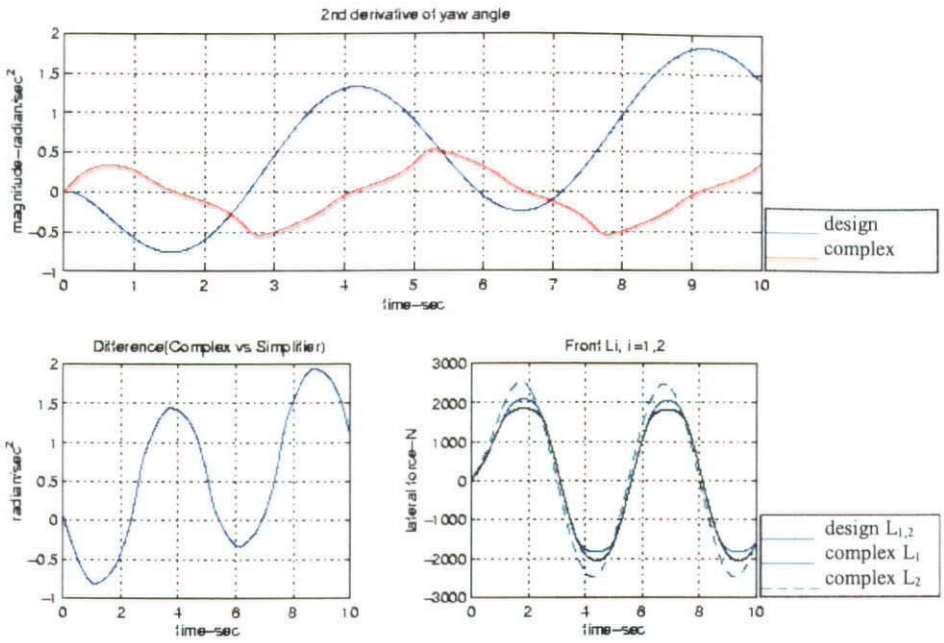

Figure 6.10 Responses of Front Lateral Forces in Open Loop Simulation with Sinusoidal Input of Steering Angle (0.3rad - 0.2Hz)

By comparing Figure 6.7 and Figure 6.9, the peaks of $F(S)$ are about 0.625 and 0.78, respectively. In addition, the area between $F(S) = 1$ and the curve of $F(S)$ in Figure 6.7 is much larger than that in Figure 6.9. Actually, the dynamics of the vehicle in which $F(S)$ is under unity are highly nonlinear, which is the reason why the design vehicle does not come close to the complex vehicle model. Those responses of reduction factors, rear and front lateral forces in open loop simulations with other types of inputs are shown in Appendix H.

6.3 Effect of Lateral Forces on Vehicle Dynamics

In Section 5.5, a perturbation design model is developed. By changing the value in perturbation block matrix, the bode plots of the following transfer functions: steering command to lateral velocity, steering command to yaw rate, vehicle bank angle to lateral velocity, and vehicle bank angle to yaw rate can be obtained. Figure 6.11

devotes to the bode plots of those transfer functions with 50% perturbation in their denominators and up to 80% perturbation in their numerators. A full set of bode plots which show four transfer functions: steering command to lateral velocity, steering command to yaw rate, vehicle bank angle to lateral velocity, and vehicle bank angle to yaw rate, with perturbation in denominators up to 50% and perturbation in numerators up to 80%, are shown in Appendix I.

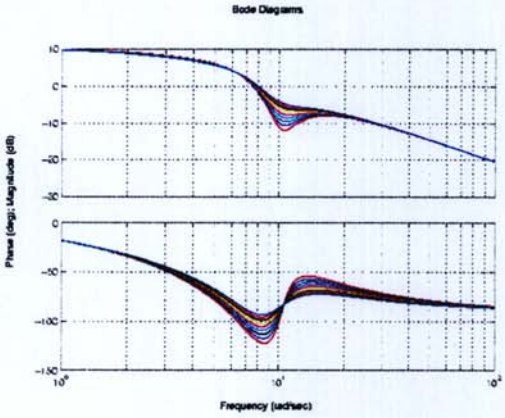

Vehicle Bank Angle to Lateral Velocity

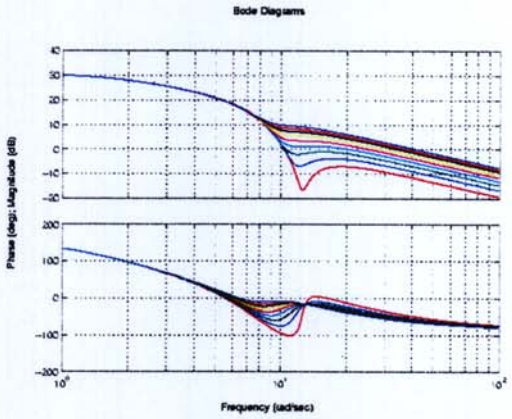

Steering Command to Lateral Velocity

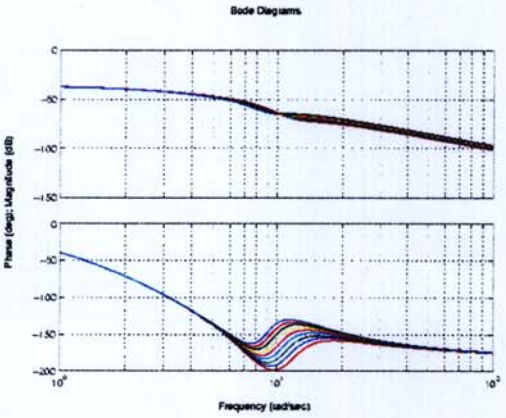

Vehicle Bank Angle to Yaw Rate

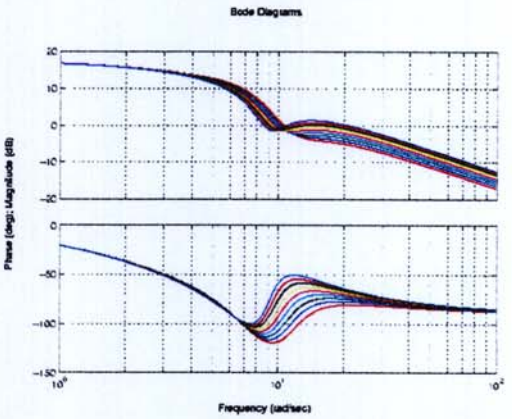

Steering Command to Yaw Rate

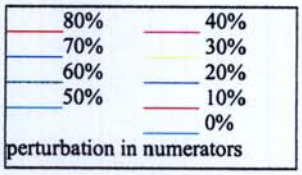

Figure 6.11 Bode Diagrams of the Vehicle System with the Input of Steering Command and Vehicle Bank Angle and Output of Lateral Velocity and Yaw Rate, under Perturbation in System Parameters

Form Figure 6.11, the vehicle system is shown as minimum phase system, which means that there are neither poles nor zeros in the right half s plane. Moreover, the vehicle bank angle has much effect on the vehicle dynamics around ω=1. This shows that the effect of the steering command and the vehicle bank angle on the vehicle system cannot be decoupled. However, acceptable tracking of both steering command and the vehicle bank angle are obtained in this simulation.

7. CONTROL IMPLEMENTATION AND ANALYSIS

7.1 Vehicle Model and Control Objectives

The vehicle model is based on the model developed in Section 3.4. The controller design will consider the lateral-directional dynamics only, which is taken to be uncoupled from the longitudinal dynamics. Linearized models for a collection of running conditions on a flat road can be found in [88]. With some modifications, the vehicle design models are developed for a 3-D road surface:

$$\dot{x} = \begin{bmatrix} \ddot{y} \\ \dot{\varepsilon}_r \\ \dot{y}_r \\ \ddot{\theta}_z \\ \dot{\theta}_r \\ \ddot{\theta}_r \end{bmatrix} = \begin{bmatrix} A_1 & 0 & 0 & A_2 & A_3 & A_4 \\ 0 & 0 & 0 & 1 & 0 & 0 \\ 1 & U & 0 & 0 & 0 & 0 \\ A_5 & 0 & 0 & A_6 & 0 & 0 \\ 0 & 0 & 0 & 0 & 0 & 1 \\ A_7 & 0 & 0 & A_8 & A_9 & A_0 \end{bmatrix} \begin{bmatrix} \dot{y} \\ \varepsilon_r \\ y_r \\ \dot{\theta}_z \\ \theta_r \\ \dot{\theta}_r \end{bmatrix} + \begin{bmatrix} g & 0 \\ 0 & -1 \\ 0 & 0 \\ 0 & 0 \\ 0 & 0 \\ 0 & 0 \end{bmatrix} \begin{bmatrix} \eta \\ \dot{\theta}_d \end{bmatrix} + \begin{bmatrix} B_1 \\ 0 \\ 0 \\ B_2 \\ 0 \\ B_3 \end{bmatrix} \delta$$

where the expressions of $A_{0\text{-}9}$, $B_{1\text{-}3}$ were found in Section 3.4.

The state vector $x^T = [\, \dot{y}\ \varepsilon_r\ y_r\ \dot{\theta}_z\ \theta_r\ \dot{\theta}_r \,]$ consists of the vehicle basic rigid body variables. The state vector represents, respectively, the lateral velocity, lateral off-path heading angle, lateral off-path distance, yaw rate, roll angle and roll rate. The lateral off-path heading angle (ε_r) is defined as $\varepsilon_r = \theta_z - \theta_d$, and $\dot{\theta}_d$ is obtained from the reference path model in Section 4.3. The desired rate of turning, $\dot{\theta}_d$, is defined as $\dot{\theta}_d = U\rho_{ref}$. Since U is kept constant in the design, ρ_{ref} is solely dependent on the variable $\dot{\theta}_d$. Thus, the tracking control can be achieved by tracking $\dot{\theta}_d$, in other words, rejected the disturbance $\dot{\theta}_d$ from affecting the system outputs, y_r, ε_r.

The control input is the steering angle δ. The command input is the desired rate of turning $\dot{\theta}_d$. The variables to be measured are $\dot{y}, \varepsilon_r, y_r, \dot{\theta}_z, \dot{\theta}_r, \eta$ and δ_i. δ_i is the measured steering angle feedback.

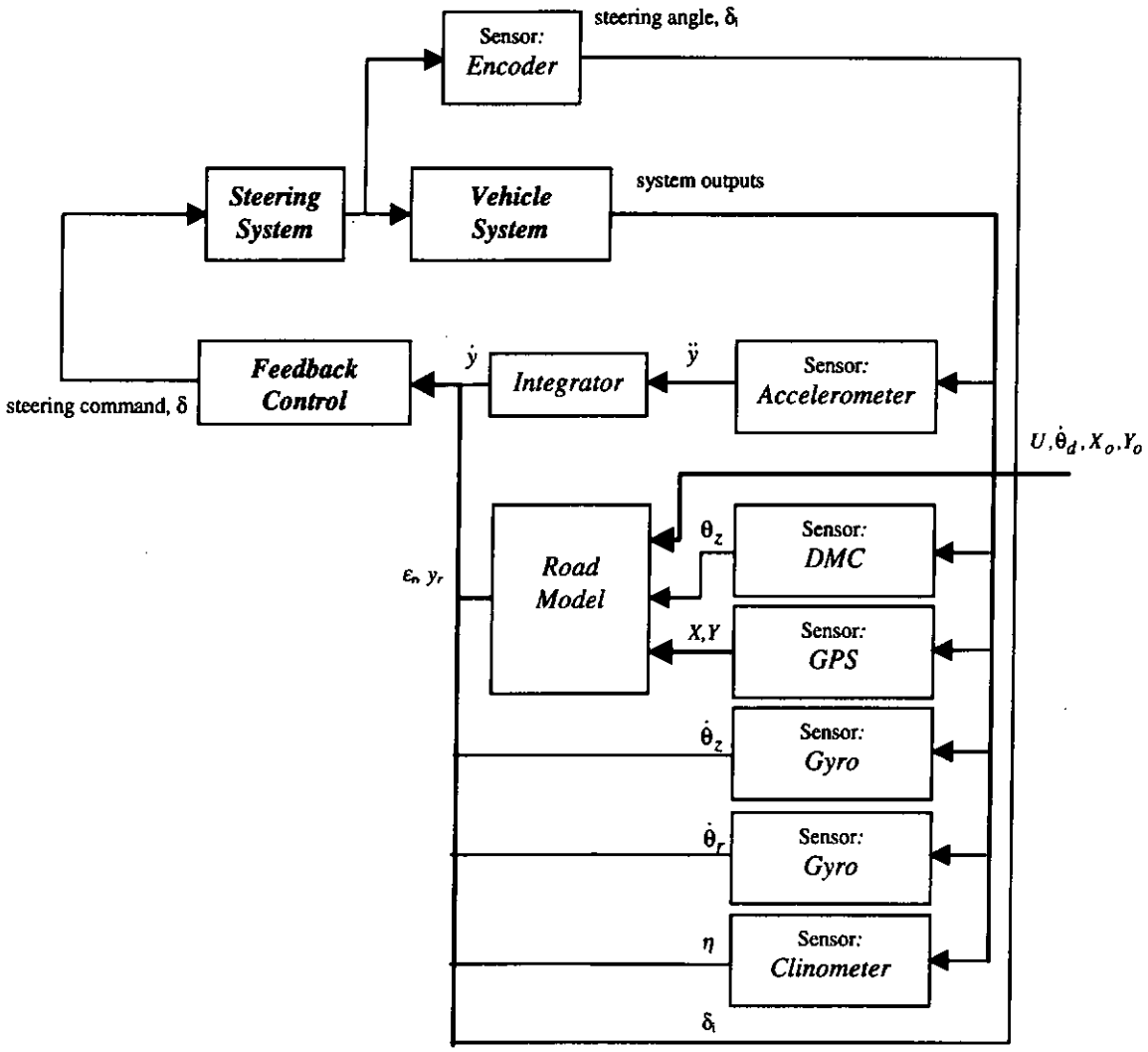

Figure 7.1 Control & Measurement Systems of Vehicle System

There are two lateral-directional maneuvers to be considered:

Path Tracking: Control the running direction of the vehicle such that the vehicle is tracking the path with maximum lateral offset of 20cm and heading angle error of 0.15rad.

Passenger Comfort: Control the steering angle of the vehicle such that the maximum roll angle should not exceed 0.15rad.

7.2 Closed-Loop Feedback Structure

A diagram for the closed-loop system, which includes the feedback structure of the plant and controller, as well as elements associated with the uncertainty models and performance objectives, is shown in Figure 7.2.

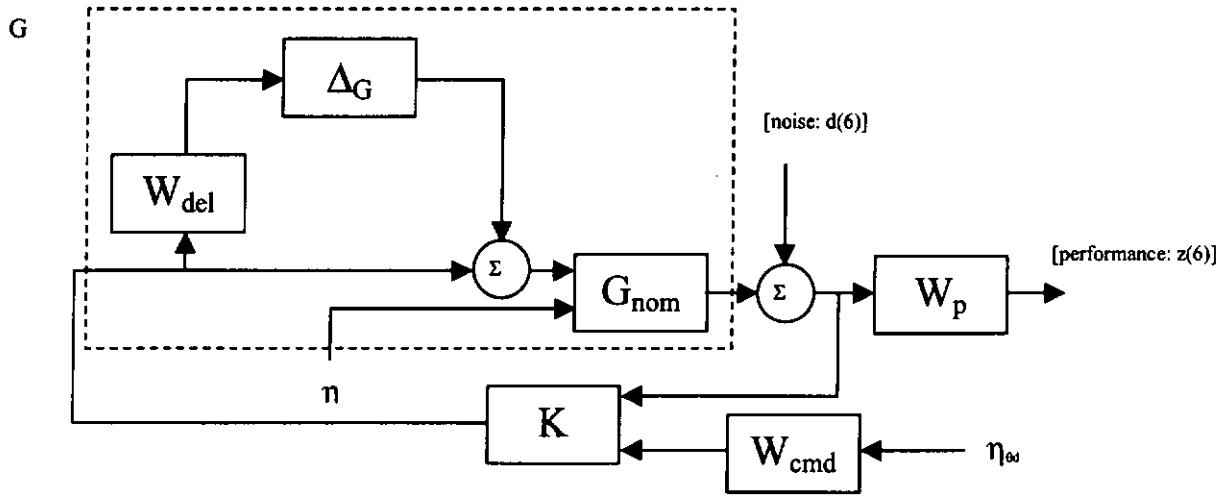

Figure 7.2 Vehicle Control System with Weighted Performance Matrix

The dashed box represents the modelled "true" vehicle, with transfer function G. Inside the box is the nominal model of the vehicle dynamics G_{nom} and two elements, W_{del} and Δ_G. These elements reflect the amount of uncertainty in the model. The transfer function W_{del} is assumed known, and the transfer function Δ_G is assumed to be stable and unknown, except for the norm condition, $\|\Delta_G\|_\infty<1$. The performance

objective is to keep the transfer function from noise (e.g., d(6)), to performance (e.g., z(6)) small in the H_∞ norm sense for all of the possible uncertainty transfer function Δ_G. The weighting function W_p is used to reflect the relative importance of various frequency ranges for the desired performance. The weighting function W_{cmd} reflects the typical desired yaw angle rate, where $\eta_{\theta d}$ is assumed to be an arbitrary signal with $||\eta_{\theta d}||_2 \leq 1$.

The control objective is to design a stabilized controller K such that for all stable perturbations $\Delta_G(s)$, with $||\Delta_G||_\infty<1$, the perturbed closed-loop system remains stable and the perturbed weighted sensitivity transfer function,

$S(\Delta_G) := W_p(I + P(I + \Delta_G W_{del})K)^{-1}$, satisfies the inequality $\|S(\Delta_G)\|_\infty < 1$. These mathematical objectives exactly fit the structured singular value framework.

7.3 Nominal Models, Uncertainty Models and Performance Objectives

The vehicle model considered has:

- One manipulated variable: steering angle command (δ);
- One tracking command input: desired rate of turning ($\dot{\theta}_d$); and
- Six measured outputs: lateral off-path heading angle(ε_r), lateral off-path distance (y_r), yaw rate ($\dot{\theta}_z$), roll rate ($\dot{\theta}_r$), road banking angle (η), and steering feedback angle (δ_i).

A possible set of uncertainties about the vehicle model includes:

1. Uncertainty in the steering actuator. The electrical signals that command path tracking are fed to the actual steering system via the electronics and mechanical gear chain of the actuators. This is not done perfectly in the actual system, unlike the nominal model.
2. Uncertainly in the forces and moments generated on the contact points between the tire surfaces and the road surfaces at different front wheel positions. This may be due to uncertainties in the parameters of the tire model, which vary with the running conditions.
3. Uncertainty in the force and moments generated on the vehicle suspension system produced by the relative movement of the vehicle body on the vehicle base. This is due to the uncertainty in the various inertial parameters of the vehicle and the neglected dynamics, such as the coupled roll and pitch dynamics and vehicle support frame flexibility.

In this design, the above uncertainties in the vehicle are modeled by lumping all of the effects together into one single uncertainty at the input of the nominal model of the vehicle rigid body. This nominal model of the vehicle has 6 states—one input and six outputs, including five state variable feedback and one feedforward input.

The partitioned matrix represents the [A B; C D] state-space data, where [A B; C D] represents the matrix in the form of $\begin{bmatrix} \mathbf{A} & \mathbf{B} \\ \mathbf{C} & \mathbf{D} \end{bmatrix}$. In Figure 7.2, the 1 x 1 transfer matrix $W_{del}(s)$ is called the uncertainty weight. These two transfer matrices reflect an entire set of plants $\wp$, which must be controlled by the robust controller K.

$$\wp := \{ G_{nom}(I + \Delta_G W_{del}) : \Delta_G \text{ is stable}, \|\Delta_G\|_\infty \le 1 \}$$

All the uncertainties in modeling the vehicle are captured in the normalized, unknown transfer function Δ_G. The unknown transfer function $\Delta_G(s)$ is used to reflect the possible differences between the nominal model $G_{nom}(s)$ and the actual behavior of the real vehicle G. The uncertainty weight's dependence on frequency indicates that the level of uncertainty in the vehicle's behavior depends on frequency.

In this design, the uncertainty weight W_{del} is of the form $W_{del}(s) := w_{del}(s)I_1$ for the scalar function $w_{del}(s)$. Since the uncertainty weight is diagonal, with equal diagonal entries, the modeled uncertainty is shown to be in some sense surrounding the nominal model G_{nom}. The scalar weight associated with the multiplicative input uncertainty is chosen as $w_{del} = \frac{120(s+250)}{s+10000}$.

Hence, the set of plants represented by this uncertainty weight is:

$$\wp := \{ G_{nom}(I_1 + \Delta_G(s) \frac{120(s+250)}{s+10000}) : \Delta_G \text{ is stable}, \|\Delta_G\|_\infty \le 1 \}$$

The weighting function is used to normalize the size of the unknown perturbation Δ_G. At any frequency ω, the value of $|w_{del}(j\omega)|$ can be interpreted as the percentage of uncertainty in the model at that frequency.

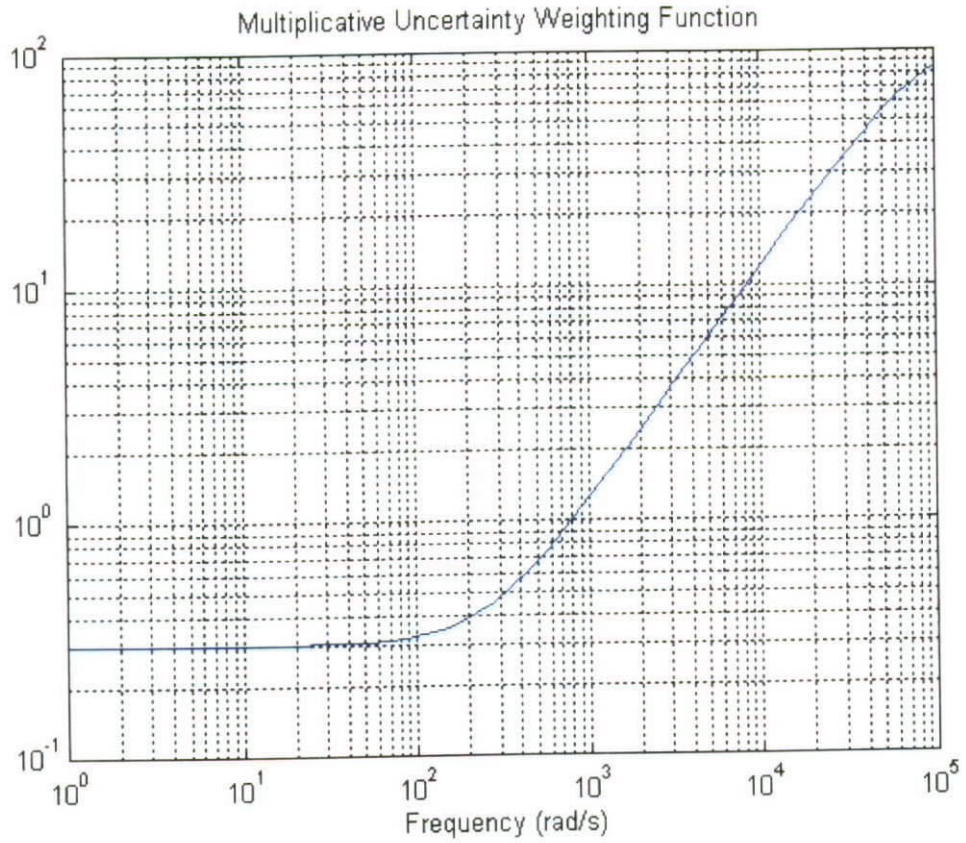

Figure 7.3 Multiplication Uncertainty Weighting Function

The uncertainty weight chosen for this example indicates that at low frequency, there is potentially a 30% modeling error, and that at a frequency of 794 rad/sec, the uncertainty in the model is up to 100% and could get larger at higher and higher frequencies.

7.4 Specifications of Closed-Loop Performance

The performance of the closed-loop system is evaluated using the output sensitivity transfer function, $(1+GK)^{-1}$. Good performance is characterized in terms of a weighted H_∞ norm on this transfer function. Given a 6 x 6 stable, rational transfer matrix W_p, the system achieves nominal performance if $||W_p(I+GK)^{-1}||_\infty < 1$. As in the uncertainty modeling, the weighting function W_p is used to define performance as

whether a particular norm is less than 1. The 6 x 6 weighting matrices in the interconnection involve the scalar functions and identity matrices of dimension 6; that is, $Wp = [w_{p1},\ldots,w_{pn}]*I_n$, thus $Wp = diag[w_{p1}, w_{p2}, \ldots, w_{p6}]$, where $w_{p2} = w_{p\varepsilon_r} = \frac{0.2(s+3)}{s+0.03}$ and $w_{p3} = w_{pyr} = \frac{2(s+2.5)}{s+0.1}$.

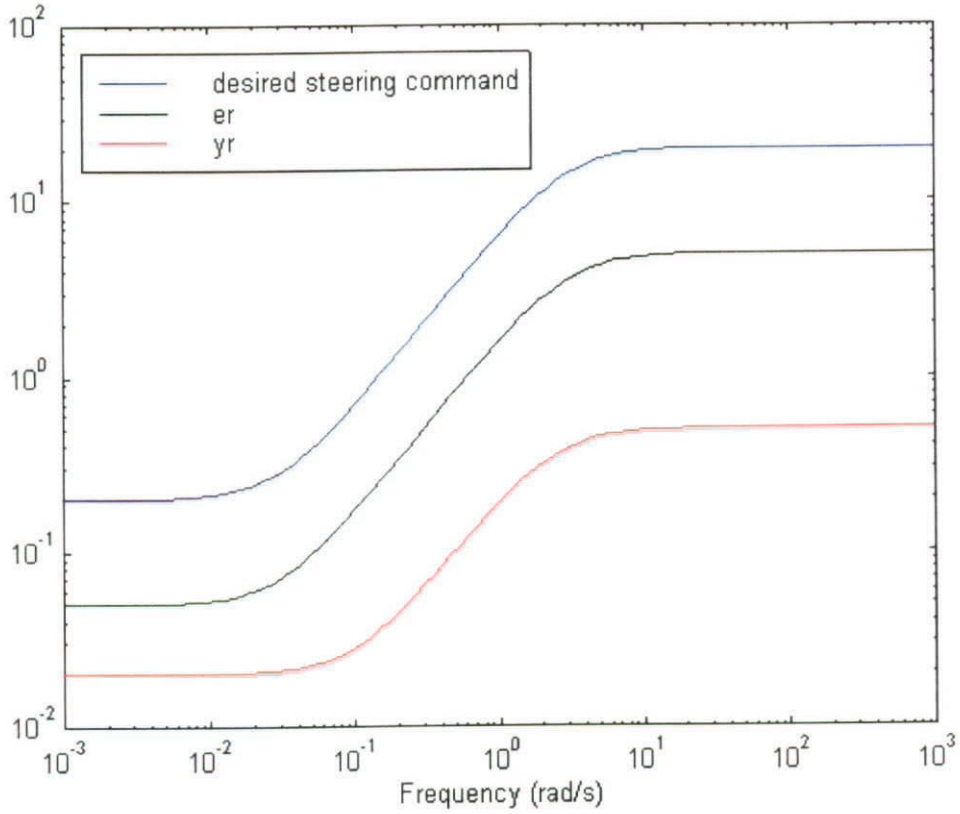

Figure 7.4 Inverse of Performance Weighting Function (Partially)

In the design, a weight of the form diag[w_{p1} w_{p2} ...w_{p6} w_{pn}] is chosen. For performance, $||W_p(I+GK)^{-1}||_\infty < 1$, to be achieved, since W_p is a scalar, the maximum singular value plot of the sensitivity transfer function, $(I+GK)^{-1}$, must lie below the plot of the reciprocal of $|W_p|$ at every frequency—that is, if $||W_p(I+GK)^{-1}||_\infty < 1$, then at all frequencies, $\bar{\sigma}[(I+GK)^{-1}(j\omega)] < |1/w_p(j\omega)|$.

This sensitivity weight indicates that at low frequencies, the closed-loop should reject disturbances at the output ε_r y_r by a factor of 20-to-1 and 50-to-1 respectively; that

is, steady-state tracking errors in both measured variables ε_r y_r, due to reference step-inputs in either channel, should be on the order of 0.05 and 0.02 or smaller, respectively. This performance requirement becomes less and less stringent at higher frequencies. The closed-loop system should perform better than open-loop for frequencies up to 1.73rad/sec. For higher frequencies, the closed-loop performance should degrade gradually, always below the reciprocal of the weight, W_p.

To be able to have independent tracking of lateral displacement and heading angle is the engineering reason for a performance specification like this. This allows the vehicle to be pointed in lateral displacement independently from the heading direction. It is expected that this is difficult to achieve, given that it is easier for the vehicle to simultaneously approach the tracking path and head to the direction of the desired path.

7.4.1 Building the Open-Loop Interconnection

An open-loop interconnection is constructed for the vehicle model in order to provide correct information about the interconnection in the MATLAB workspace. With the open-loop interconnection, the H_∞ controller can be designed in the coming Sections. Below is the 10-input, 13-output system matrix, called Velmod_ic

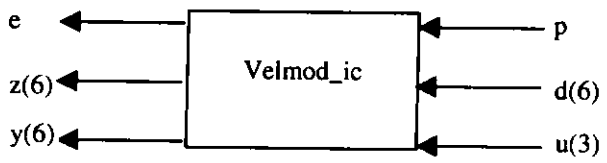

Figure 7.5 Input/Output Variables of Velmod_ic

which has the internal structure shown in Figure 7.6.

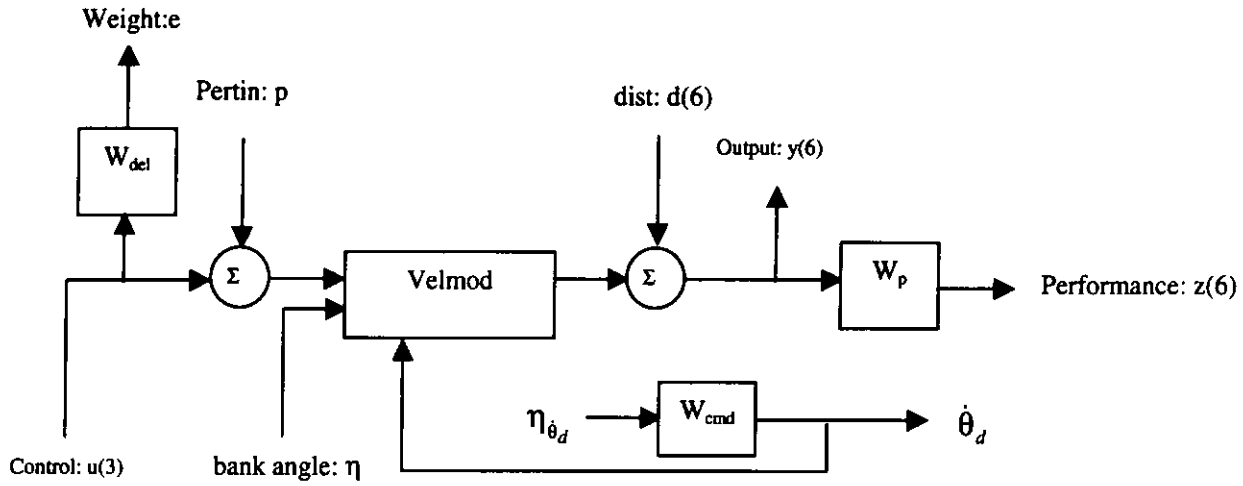

Figure 7.6 Velmod_ic Open-loop Interconnection Structure

7.5 H_∞ Design on the Open-Loop Interconnection

In this section, the first step of the D-K iteration is performed. The D-K iteration is an H_∞ suboptimal control design for Velmod_ic, the open-loop interconnection designed in the last section. In the design, the open-loop interconnection has six measurements and three inputs. Figure 7.7 shows the closed-loop Linear Fractional Transformation of Velmod_ic.

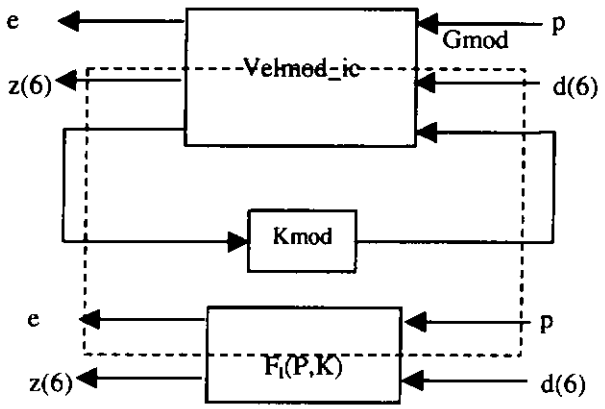

Figure 7.7 Closed-loop Linear Fractional Transformation of Velmod_ic

The algorithm will search for the optimal achievable closed loop norm to an absolute tolerance of 0.06, between lower and upper limits of 0.8 and 6.0, respectively. The resulting controller is labeled as K_{mod}, and the resulting closed loop system is labeled as G_{mod}.

Before performing synthesis and analysis on the vehicle control system, the H_∞ control system is first designed for the unperturbed vehicle model, Velnom_ic. The unperturbed vehicle system is shown in Figure 7.7.

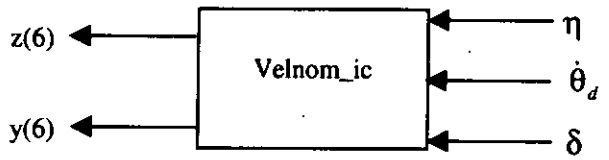

Figure 7.8 Input/Output Variables of Nominal Vehicle System, Velnom_ic

Recalled the system dynamics equations:

$$\dot{X} = AX + B_1 w + B_2 u$$
$$Z = CX + D_{11} w + D_{12} u \text{ , where } w = \begin{bmatrix} \eta \\ \dot{\theta}_d \end{bmatrix} \text{ and } u = \delta.$$
$$Y = \begin{bmatrix} I \\ 0 \end{bmatrix} X + \begin{bmatrix} 0 \\ I \end{bmatrix} u$$

The vehicle system is scaled with the scaling matrices S_1, S_2 and S_3. In this way, the size of each input variable can contribute equally to the system, and the size of each output variable reflects its relative importance in performance analysis.

$$\dot{X}\{S_1\} = AX\{S_1\} + B_1S_2w + B_2S_3u$$
$$Z = CS_1X + D_{11}S_2w + D_{12}S_3u \qquad \text{, where } w = \begin{bmatrix} \eta \\ \dot{\theta}_d \end{bmatrix} \text{ and } u = \delta$$
$$Y = \begin{bmatrix} I \\ 0 \end{bmatrix} X + \begin{bmatrix} 0 \\ I \end{bmatrix} u$$

$S_1 = \text{diag}[w_{p1}, w_{p2}, \ldots, w_{p6}]$, where w_{p2} and w_{p3} is shown in the previous section.

$S_2 = \text{diag}[0.15, 0.35]$

$S_3 = 0.4189$

The closed-loop interconnection with H_∞ controller is shown below:

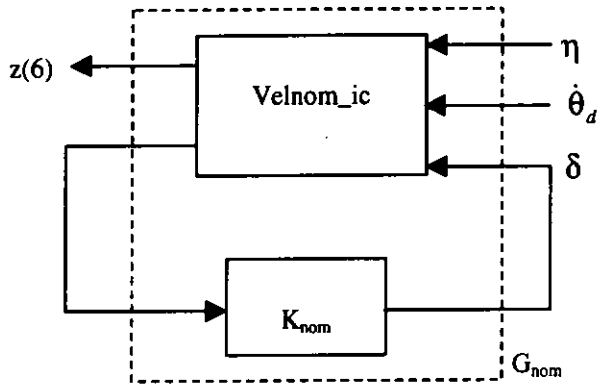

Figure 7.9 Closed-Loop Interconnection of Vehicle System, G_{nom}

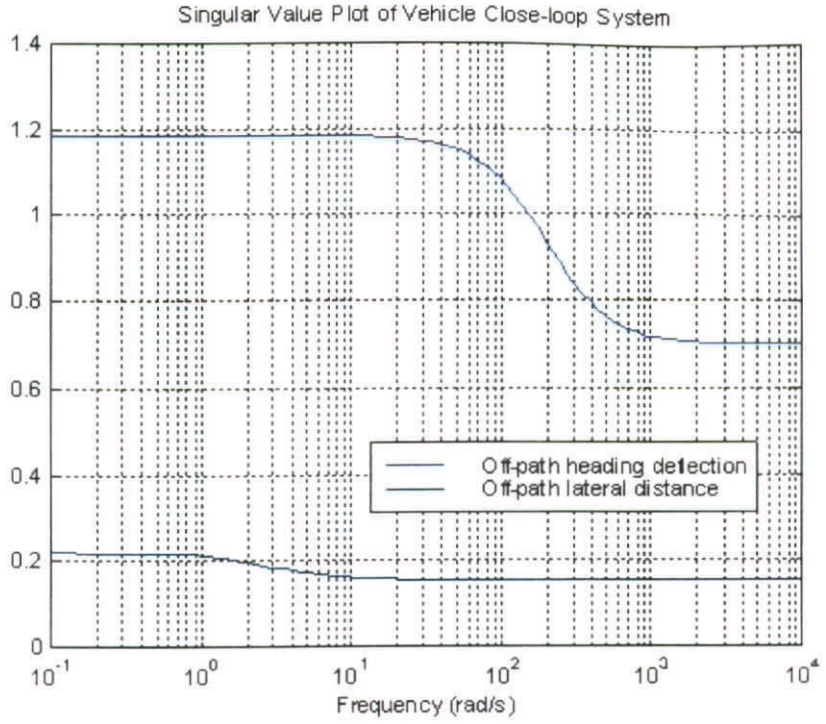

Figure 7.10 Singular Value Plot of G_{nom}

Now, the nominal performance is evaluated. The frequency response of G_{nom} and its norm is plotted below:

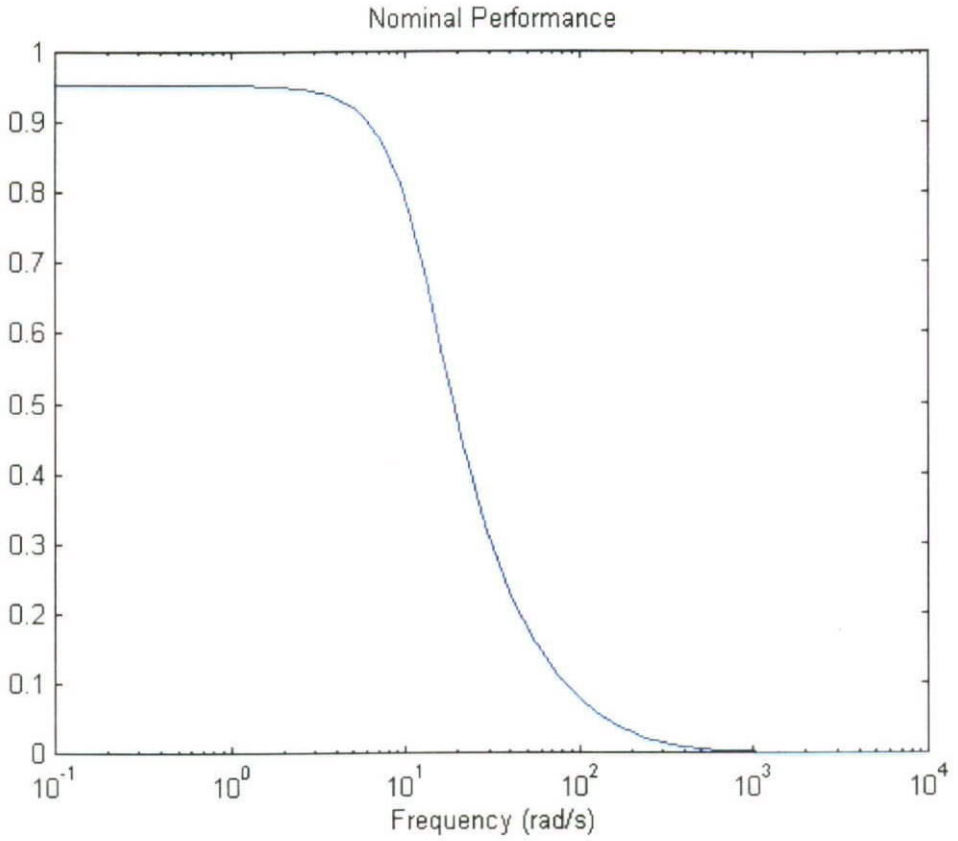

Figure 7.11 Nominal Performance of G_{nom}

From Figure 7.11, the controlled system achieves nominal performance. This conclusion follows from the singular value plot of the nominal weighed output sensitivity function, which has a peak value of 0.967.

7.5.1 Time Simulation Model on Complex Vehicle System

In the simulation, it is assumed that all the values of θ_d, U, m, I_z, C_f, C_r, K_η and B_η are available, and all the output variables are available to be measured and used by the H_∞ controller. The measurement rates are assumed to be sufficiently large to be used as the analog input to the controller. The vehicle speeds have been fixed to 18.3m/s

throughout the study. The curve parameters are shown in Table 7.1. Zero initial conditions have been set in the simulations. To evaluate the effect of the road banking angle on the control system, simulations with road bank angle as a sin function with magnitude of 0, 0.05, 0.1 and 0.15rad are presented for comparison. The period of these sin functions is obtained from Section 4.2, according to the parameters of the desired trajectories shown below:

Table 7.1 Parameters of the Desired Trajectories

Road Bank Angle : Sin Function with Magnitude(rad)	$X_{start}(m)$	$d\theta_d(rad/sec)/\rho(m^{-1})$	*duration(sec)*
0	*0*	*0.1 / 0.00546*	*10*
0.05	*0*	*0.1 / 0.00546*	*10*
0.1	*0*	*0.1 / 0.00546*	*10*
0.15	*0*	*0.1 / 0.00546*	*10*
0	*0*	*0.2 / 0.01929*	*10*
0.05	*0*	*0.2 / 0.01929*	*10*
0.1	*0*	*0.2 / 0.01929*	*10*
0.15	*0*	*0.2 / 0.01929*	*10*

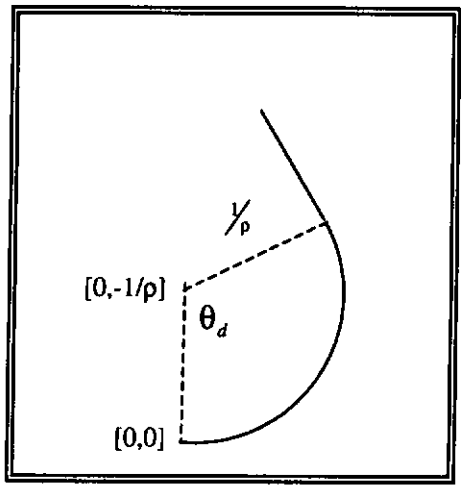

Figure 7.12 The Desired Trajectory with Center at [0, -1/ρ]

The simulated complex model has 14 states, containing the additional state variables and output variables. Some particularly important variables are lateral displacement Y and yaw angle θ_z. In addition, the lateral off-path heading deflection and the lateral off-path distance are obtained from the reference path model developed in Section 4.3. Figure 7.13 shows the closed-loop simulation model with the controller and reference path models.

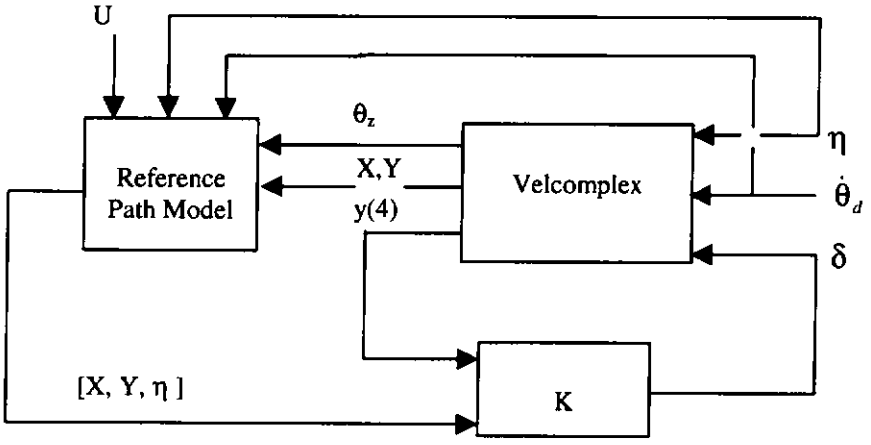

Figure 7.13 Closed-Loop Simulation of Complex Vehicle Model

Figures 7.15 and 7.16 show the simulation results of the vehicle trajectory as well as the desired trajectory, without any vehicle modeling uncertainty and measurement noises and with the desired turning rate of 0.1rad/sec and 0.2rad/sec, respectively.

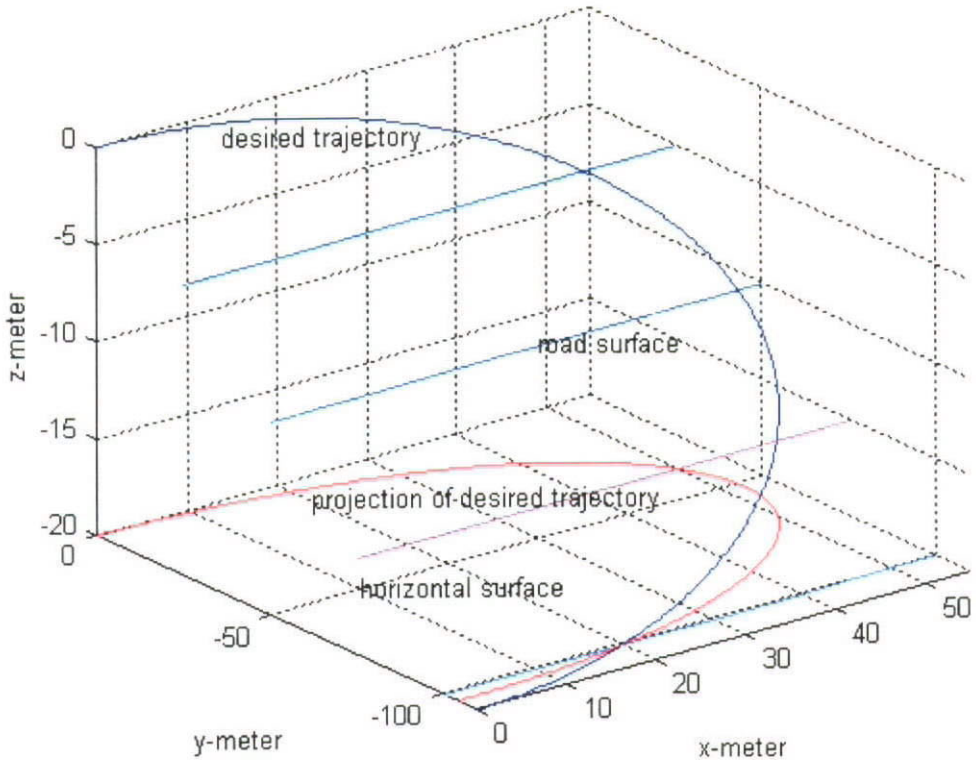

Figure 7.14 Projection of Vehicle Trajectory at Desired Yaw Rate is 0.1 rad/sec

Figure 7.14 shows the 3-D road profile, as well as the desired trajectory, on the horizontal level and its projection on the road surface. The steering is limited to the physical constraints of maximum steering angle 0.5 rad. The nonlinear effect of that saturated control signal on the control system would not be considered in this study. Figures 7.17 and 7.18 show the areas marked in Figures 7.15 and 7.16, respectively. They are presented in order to get a close look at the marked areas. Figures 7.19 to 7.22 show the lateral off-path heading deflection and lateral off-path deflection for each simulation.

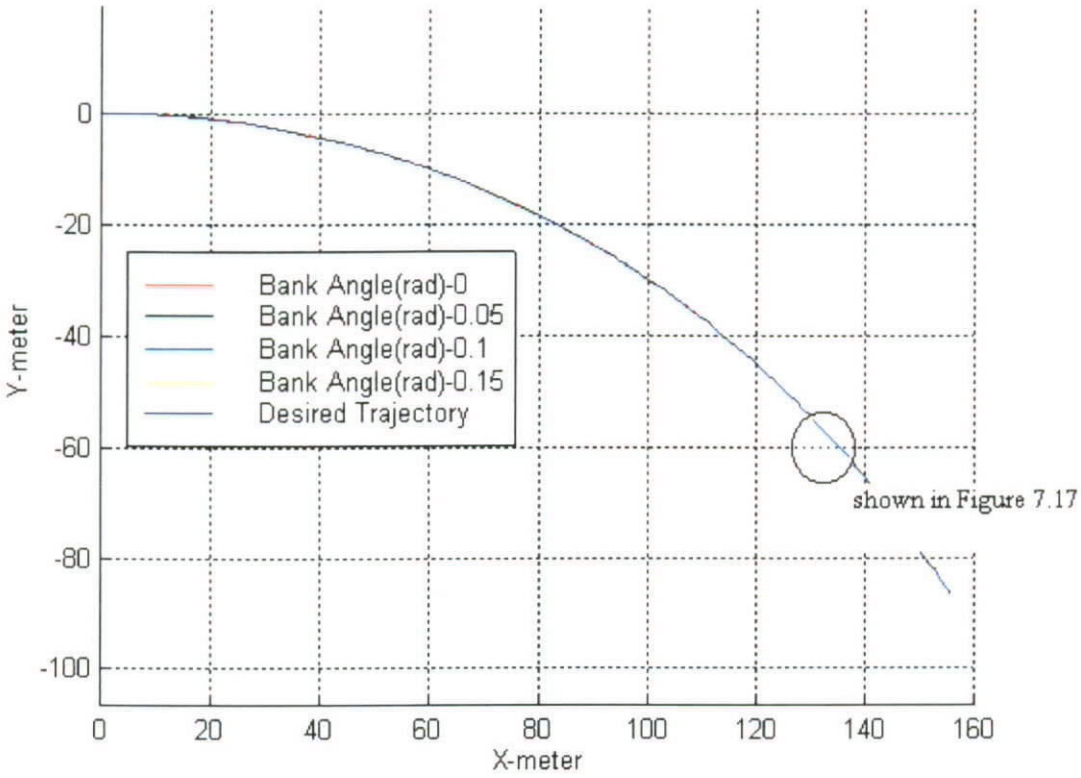

Figure 7.15 Vehicle Trajectory at Desired Yaw Rate is 0.1 rad/sec

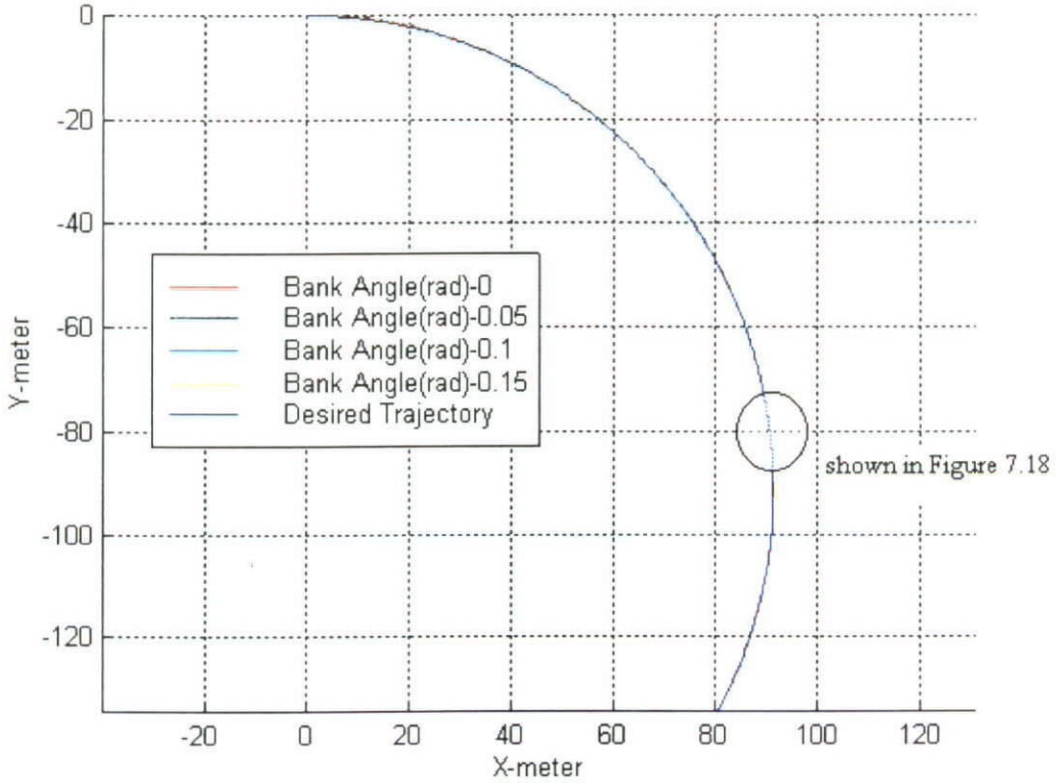

Figure 7.16 Vehicle Trajectory at Desired Yaw Rate of 0.2 rad/sec

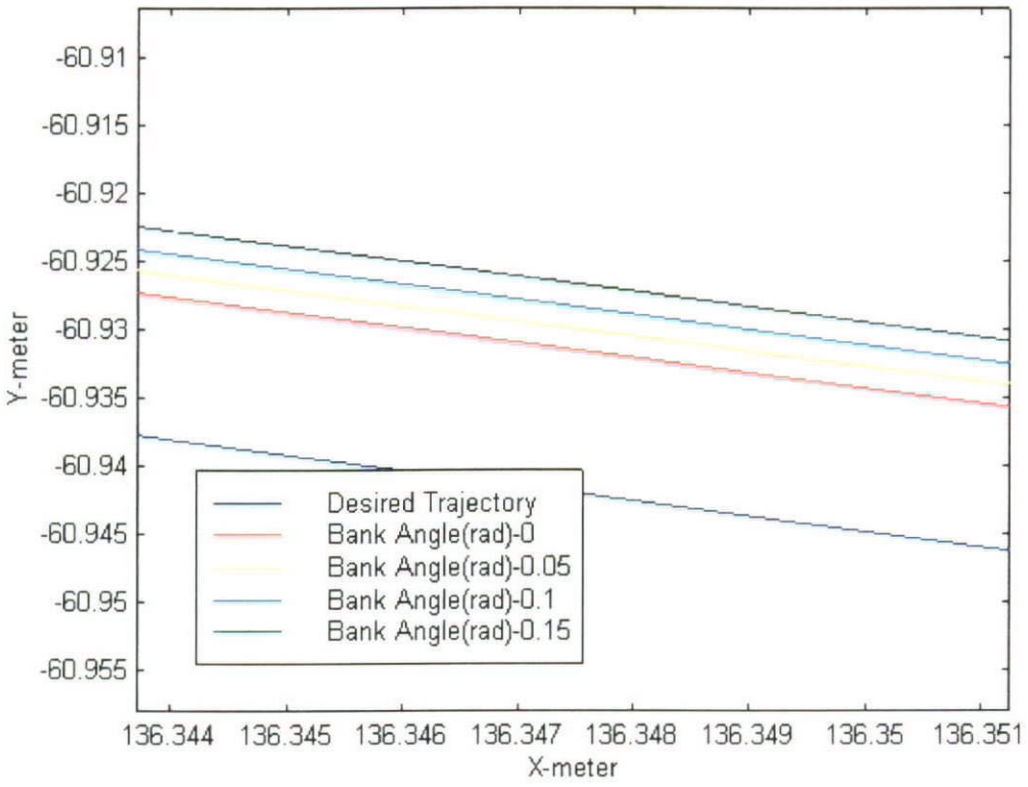

Figure 7.17 Close Look at Vehicle Trajectory at Desired Yaw Rate of 0.1 rad/sec

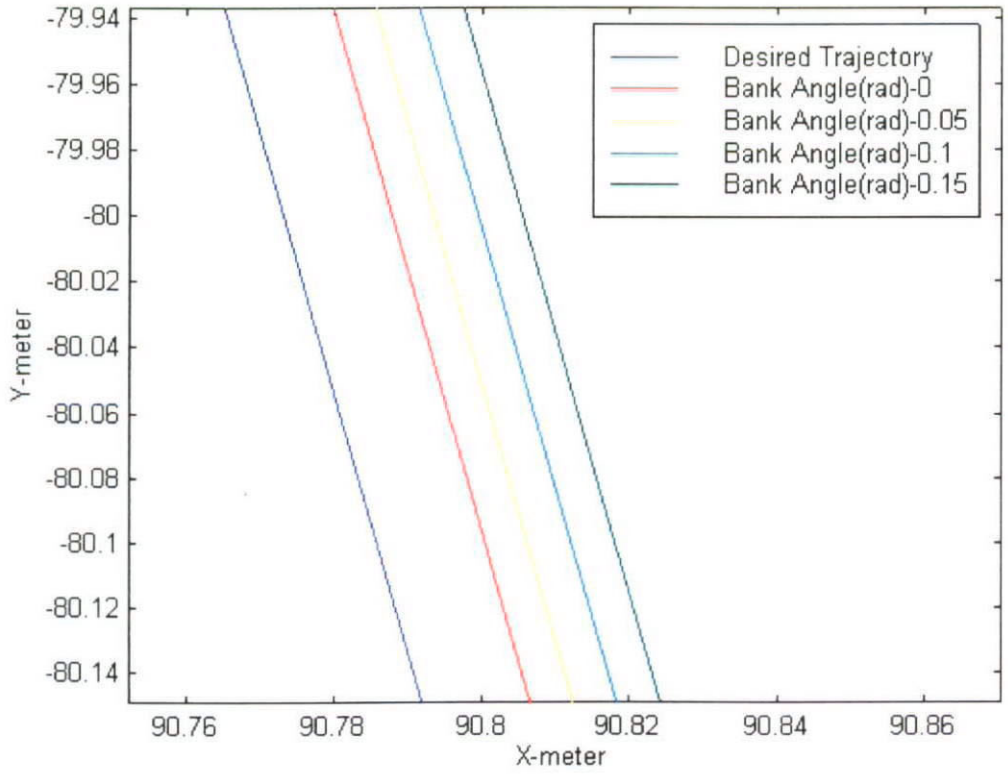

Figure 7.18 Close Look at Vehicle Trajectory at Desired Yaw Rate of 0.2 rad/sec

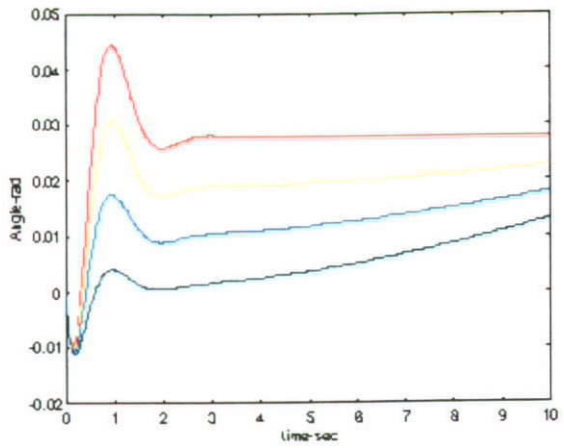

Figure 7.19 ε_r for bank angles: 0, 0.05, 0.1, 0.15 at desired yaw rate of 0.1 rad/sec

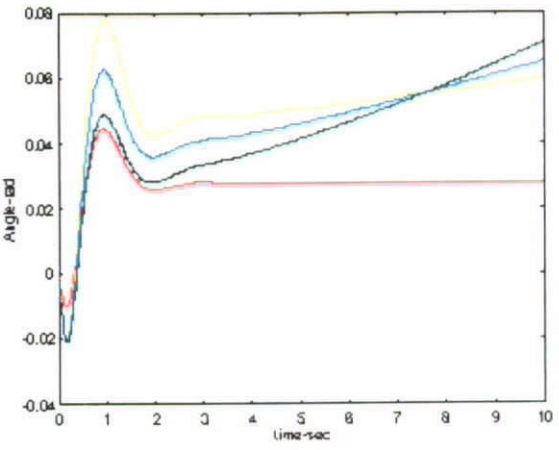

Figure 7.20 ε_r for bank angles: 0, 0.05, 0.1, 0.15 at desired yaw rate of 0.2 rad/sec

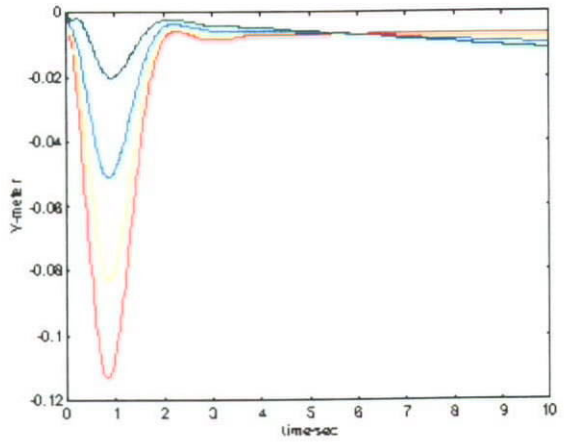

Figure 7.21 y_r for bank angles: 0, 0.05, 0.1, 0.15 at desired yaw rate of 0.1 rad/sec

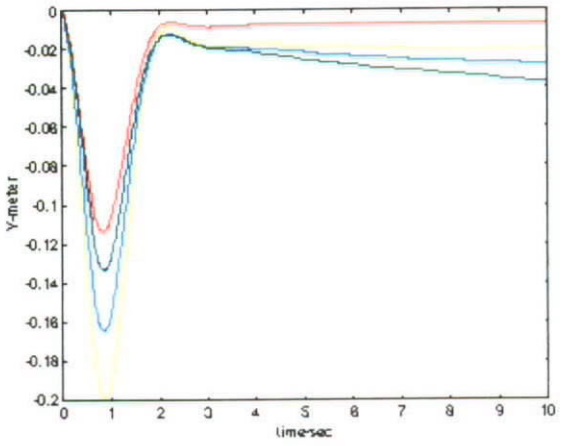

Figure 7.22 y_r for bank angles: 0, 0.05, 0.1, 0.15 at desired yaw rate of 0.2 rad/sec

In Figure 7.21, the y_r of the other three lines do not fall below the red line; however, the y_r of those in Figure 7.22 do. This is because the lateral motion of the vehicle is dependent on the vehicle's static weight and the vehicle's lateral dynamics. When the turning rate of the vehicle is not significant, as in Figure 7.21, the effect of the static weight on the turning motion of a vehicle becomes dominant; however, the effect of the turning rate on the turning motion of a vehicle becomes dominant if the turning rate is sufficiently large, as in Figure 7.22.

7.5.2 Simulation on Complex Vehicle Model (Including Sensor Noise and Steering Mechanism)

Recall the Vehicle model, Velnom_ic, in Section 7.5 where the steering mechanism is considered and the sensor noise is incorporated into the measured variables. In the simulation, the Gaussian noise is assumed. The combined effect of this noise in the measured output, as well as the steering mechanism on the vehicle control system, is investigated. The curve parameters are shown in Table 7.1. Zero state initial conditions have been set in the simulations. To evaluate the effectiveness of H_∞ designed by rejecting the measurement noise (i.e., the sensitivity transfer function of the vehicle control system), the Gaussian noise on y_r and θ_d with magnitude of 0.02 and 0.005, respectively, are presented. The parameters used in this simulation are shown in Table 7.2.

Table 7.2 Parameters of the Simulation on Complex Vehicle Model (Including Sensor Noise and Steering Mechanism)

Road Bank Angle Sin Function with Magnitude(rad)	$X_{start}(m)$	$d\theta_d(rad/sec)/\rho(m^{-1})$	*Noise Magnitude* y_r / θ_d	*Duration(sec)*
0.05	*0*	*0.1 / 0.00546*	*0.02 / 0.005*	*10*

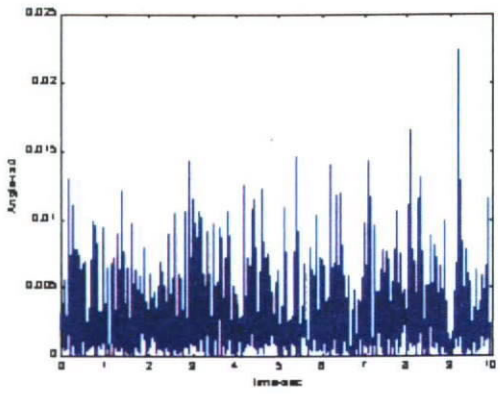

Figure 7.23 Gaussian noise on ε_r

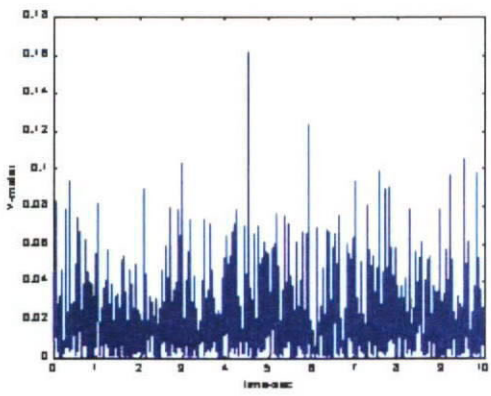

Figure 7.24 Gaussian noise on y_r

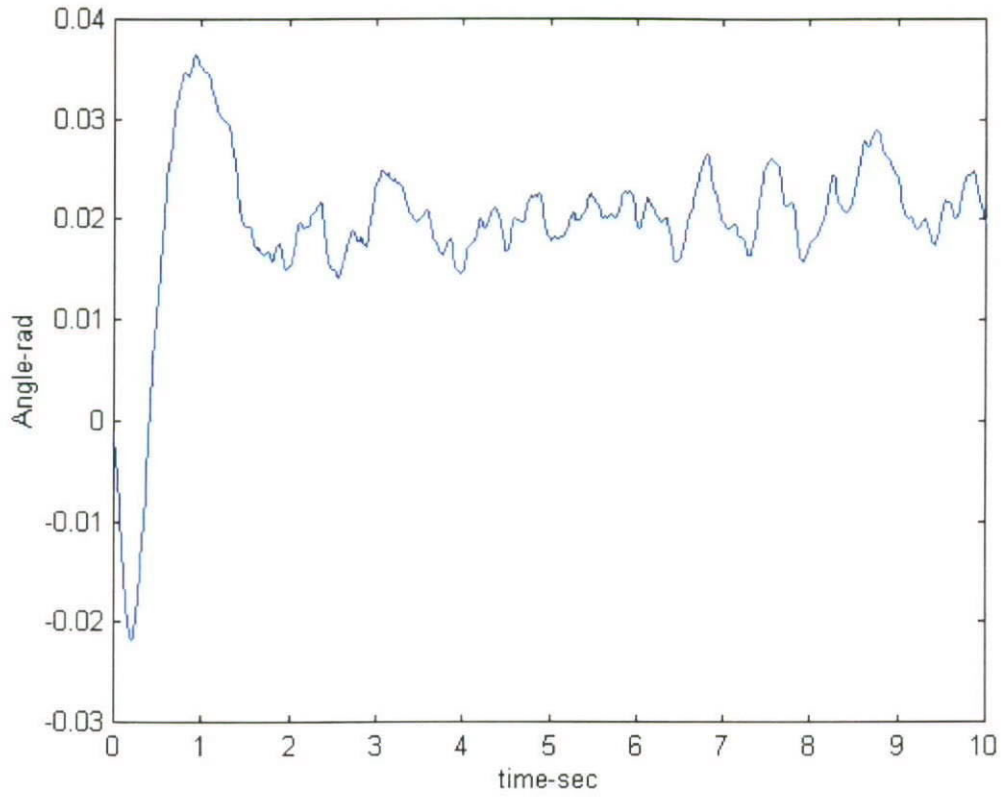

Figure 7.25 System Output ε_r

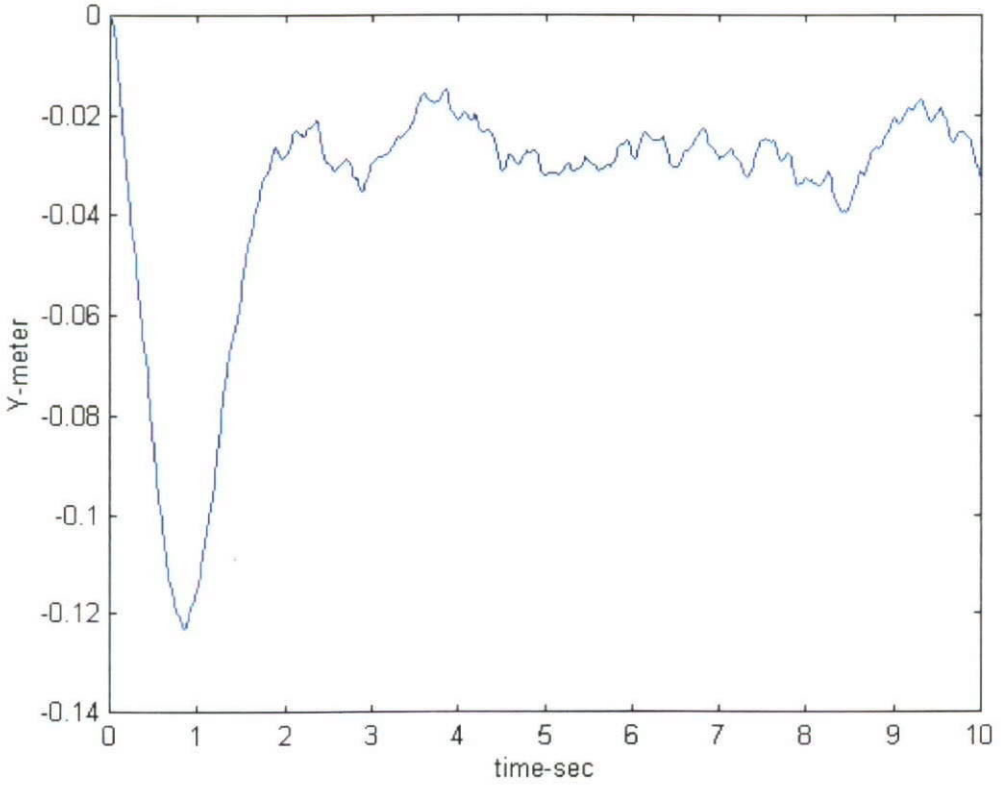

Figure 7.26 System Output y_r

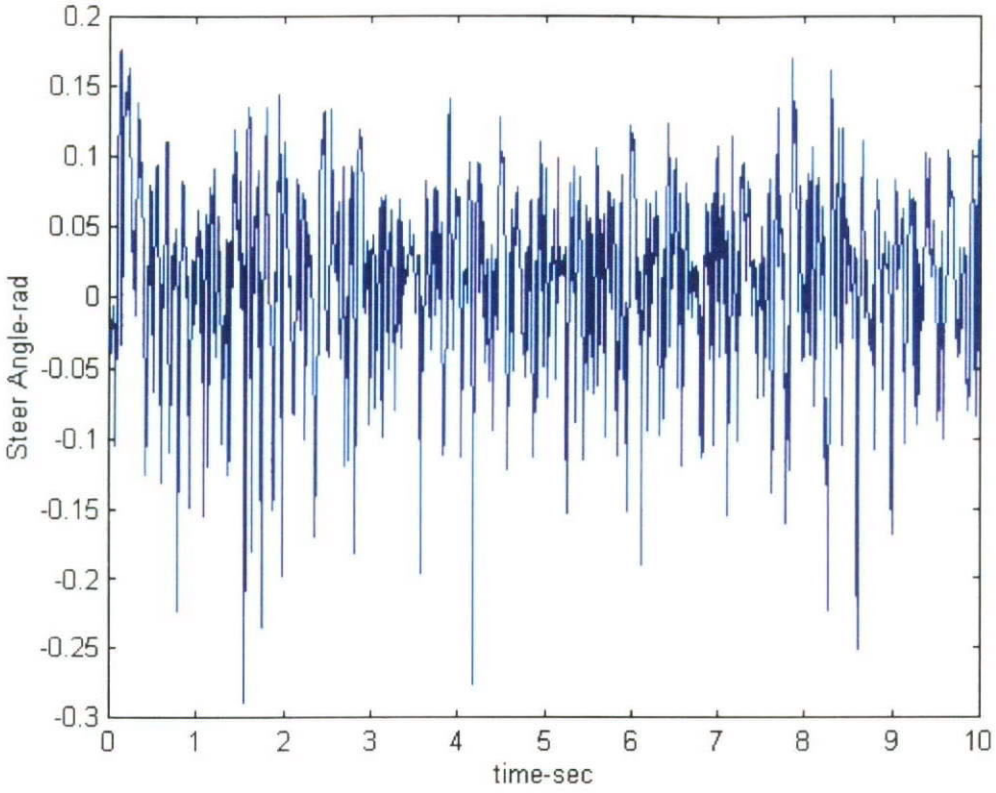

Figure 7.27 Controller Output

From Figures 7.25 and 7.26, they show that the effectiveness of H_∞ in rejecting the measurement noise is high especially in transient response of the system. Even in the steady-state response, the measurement noise and the non-linear effect in the steering mechanism do not bring the system to unstable conditions.

7.5.3 Simulation on Complex Vehicle Model (Including Sensor Noise, Steering Mechanism and Modeling Uncertainty)

In order to capture the model uncertainty, two perturbed models are considered in this Section. The multiplicative uncertainty model is first used in the simulation. Perturbed model, Velmod_ic, has already been shown in Section 7.5. The uncertainty model is then captured into a block matrix, and the H_∞ is synthesized using μ. Theorem 5.4 developed in section 5.2.4.5 is handy in the conversion of the physical model uncertainty into a block matrix. The simulation parameters are listed in Table 7.3. Two uncertainty models will be compared in such a way that variances around the nominal values are used in the vehicle system parameters. Figures 7.28 – 7.30 are devoted to the vehicle simulation where the H_∞, named K_{mod}, are developed using μ on the multiplicative perturbation design model. Figures 7.31 – 7.33 are devoted to the vehicle simulation where the H_∞ named K_{blk}, are developed using μ on the μ-formulated perturbation design model.

Table 7.3 Parameters of the Simulation

Road Bank Angle - Sin Function with Magnitude(rad)	*X_{start}(m)*	*$d\theta_d$(rad/sec)/ρ(m^{-1})*	*Magnitude Offset(%) m_s / I_z / C_{rf}*	*Duration(sec)*
0.1	*0*	*0.1 / 0.00564*	*10 / 5 / 10*	*10*
0.1	*0*	*0.1 / 0.00564*	*-10 / -5 / -10*	*10*
0.1	*0*	*0.1 / 0.00564*	*10 / 0 / -10*	*10*
0.1	*0*	*0.1 / 0.00564*	*-10 / 0 / 10*	*10*

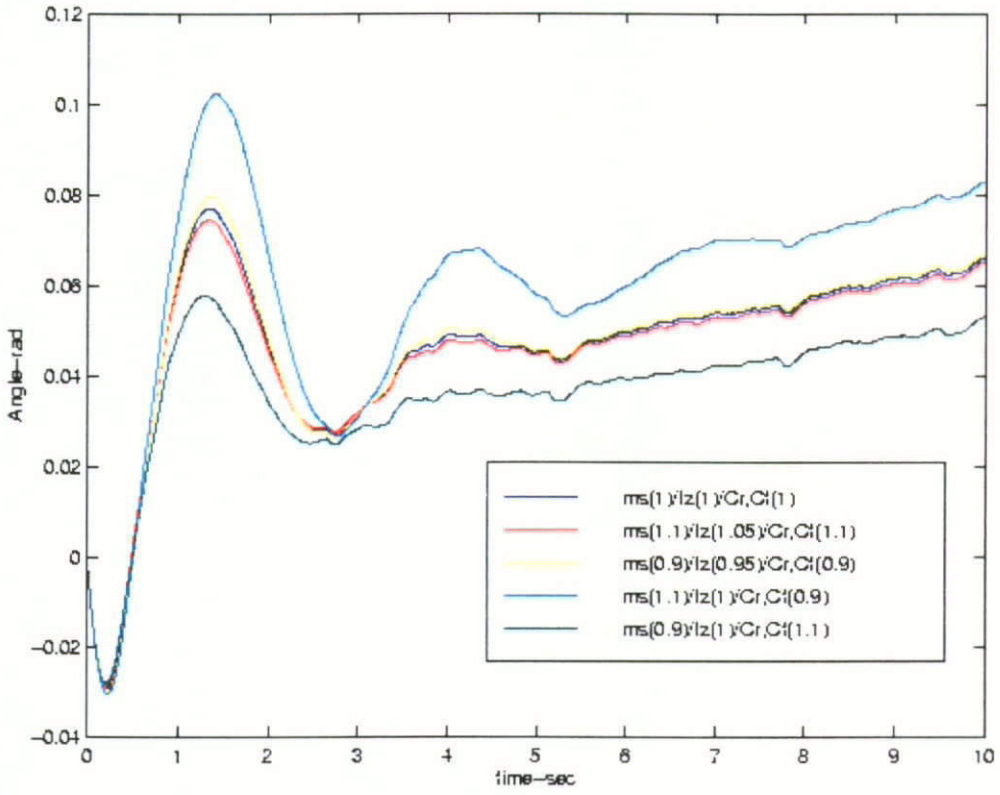

Figure 7.28 System Output ε_r in Simulation Vehicle Model with Multiplication Uncertainty

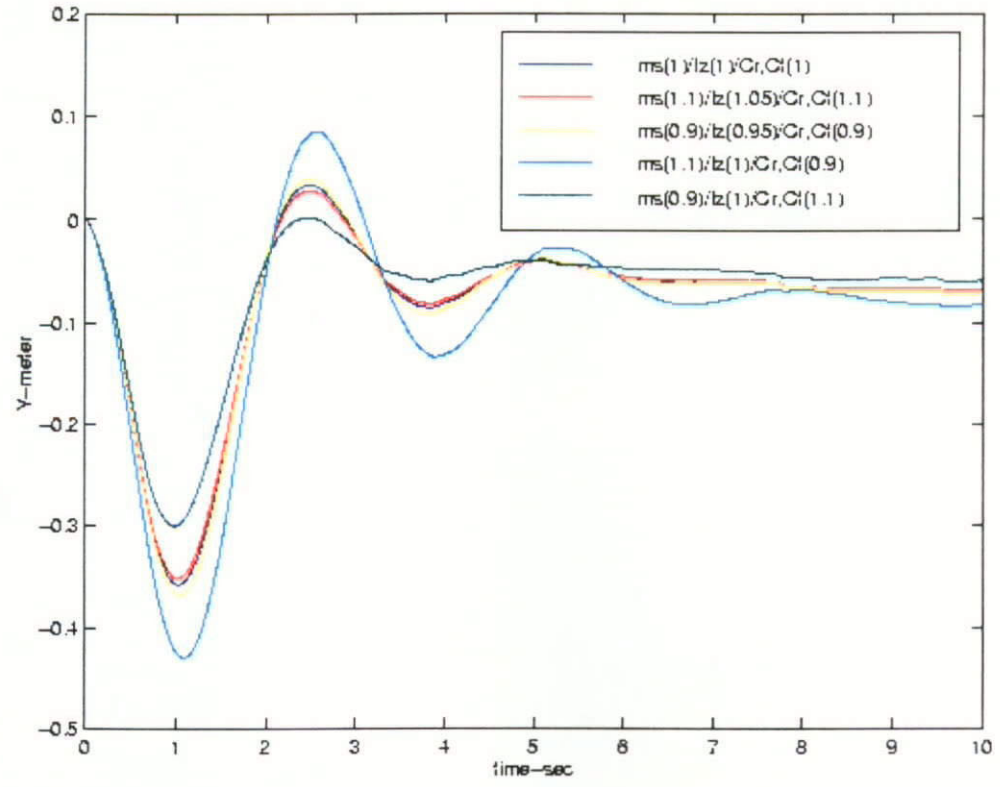

Figure 7.29 System Output y_r in Simulation Vehicle Model with Multiplication Uncertainty

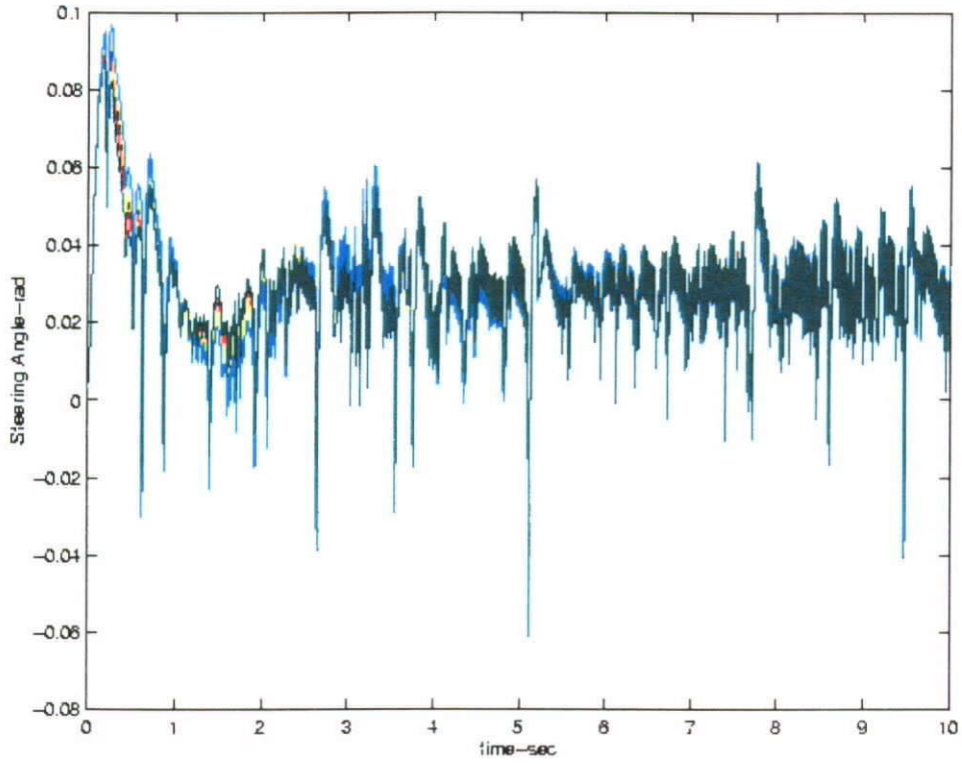

Figure 7.30 Controller Output in Simulation Vehicle Model with Multiplication Uncertainty

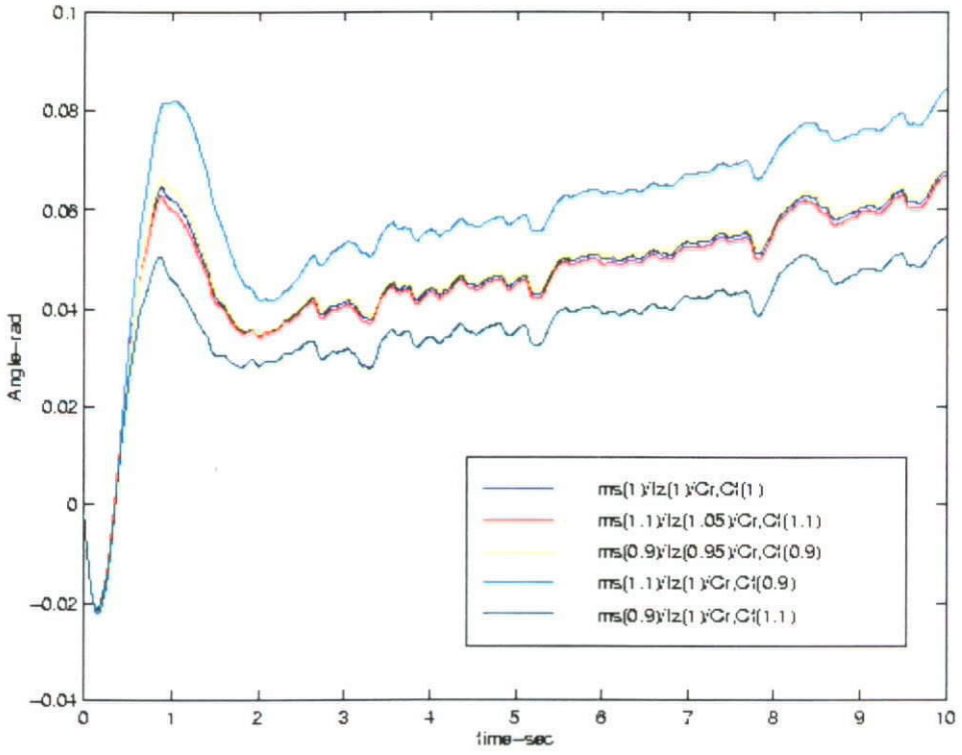

Figure 7.31 System Output ε_r in Simulation Vehicle Model with Structured Block Uncertainty

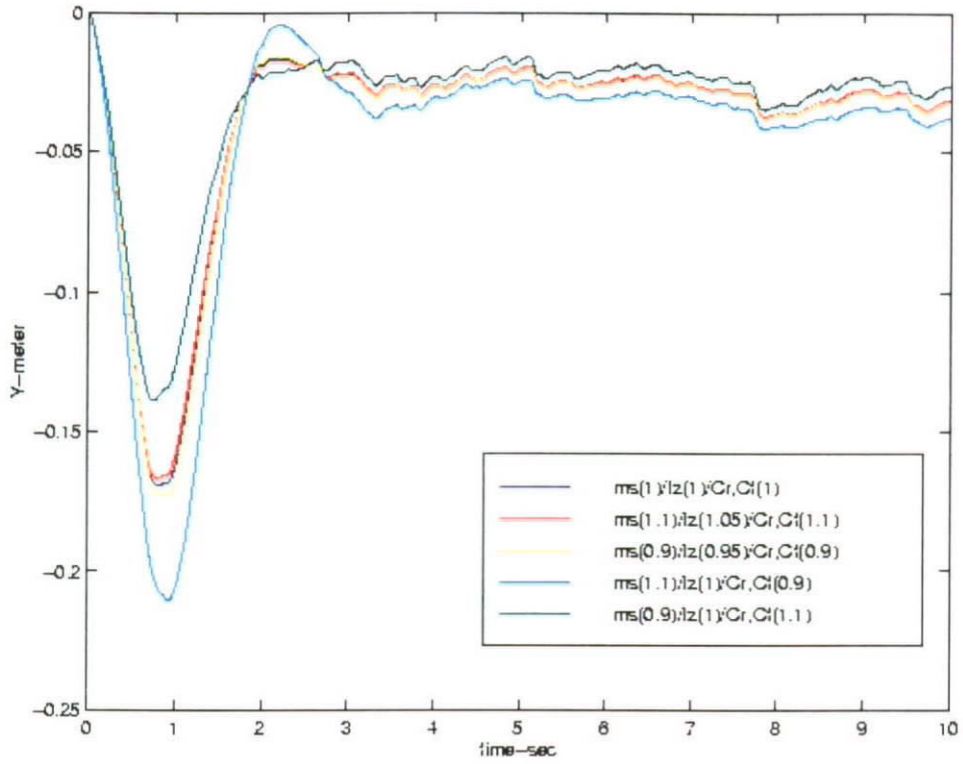

Figure 7.32 System Output y_r in Simulation Vehicle Model with Structured Block Uncertainty

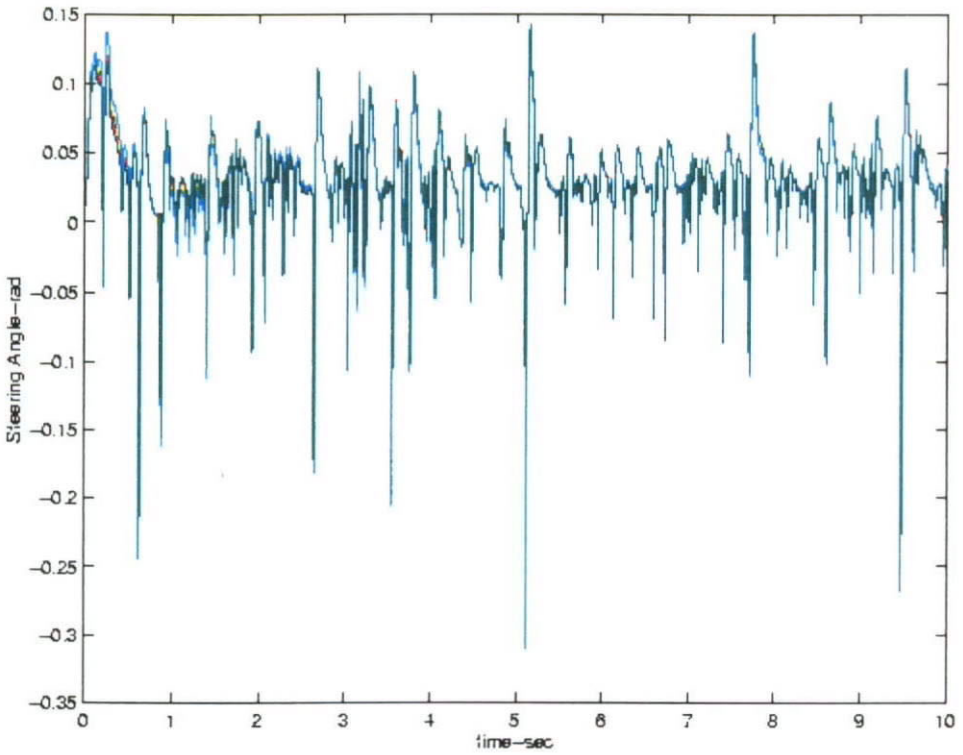

Figure 7.33 Controller Output in Simulation Vehicle Model with Structured Block Uncertainty

7.5.4 Simulation on Complex Vehicle Model on 3-D Road Profile

In this section, the vehicle is simulated on two 3-D road profiles in a city. Two profiles of the road are developed here and illustrated in Figures 7.34 – 7.35. The vehicle is running across the city, where the road are undulating. The total simulation time is 90 sec. The initial conditions are all zero, except $y_r(0)$, where $y_r(0) = -0.1$m.

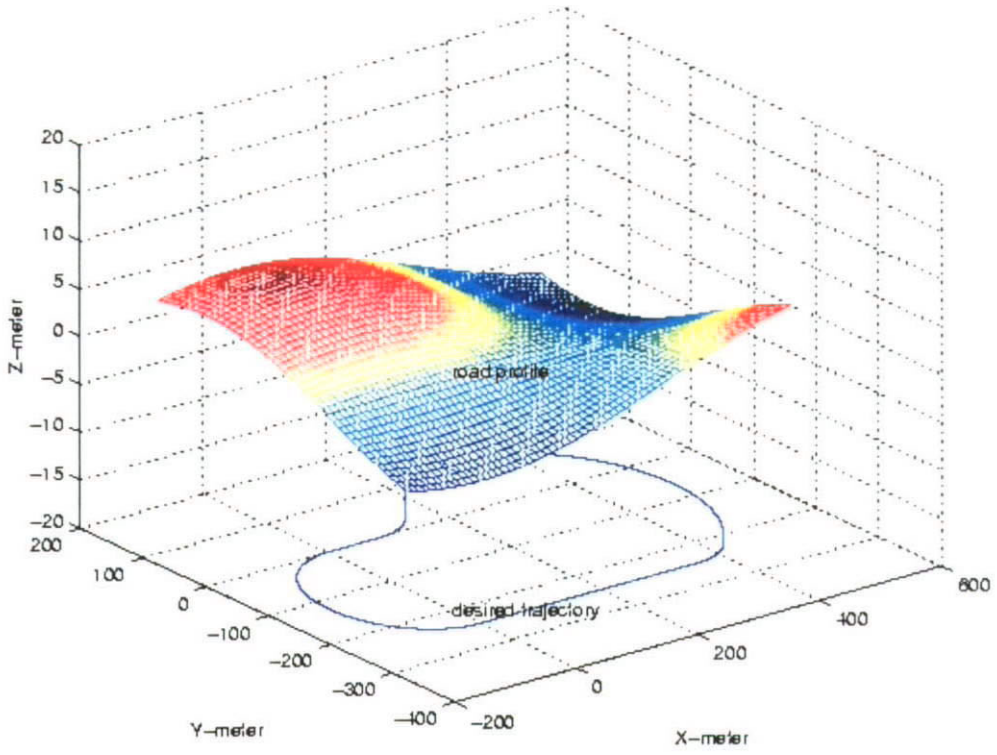

Figure 7.34 3-D Illustration of Road Profile 1

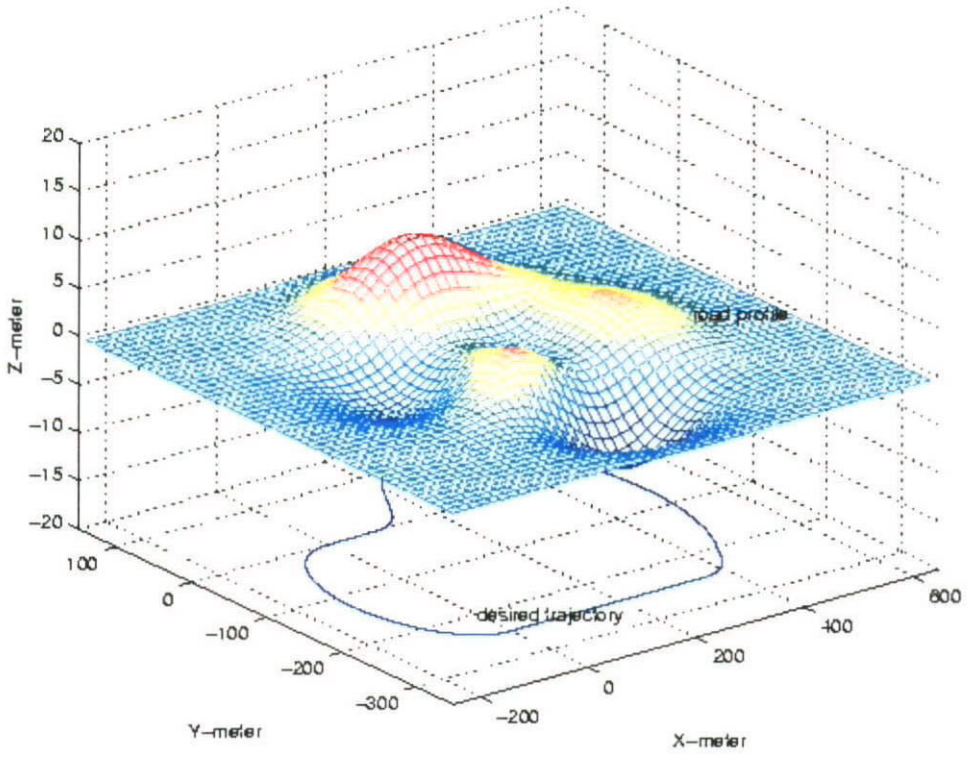

Figure 7.35 3-D Illustration of Road Profile 2

To simulate the vehicle system on these two profiles, the road should be divided into many different landscapes (Figure 4.2.1). Each landscape is a flat slanted surface. By combining all these landscapes, a smooth path along the road profile can be described in the simulations. Figures 7.36 – 7.37 show all the landscapes on the road surfaces. The arrows are pointed to the deepest angle direction on the landscapes. All the parameters about each landscape are described in Tables 7.4 and 7.5. There are two parameters to describe each landscape—road bank angle (deepest angle), T_m, and starting angle, which is made with the rest-most direction (discussed in Chapter 4), St_{pos}.

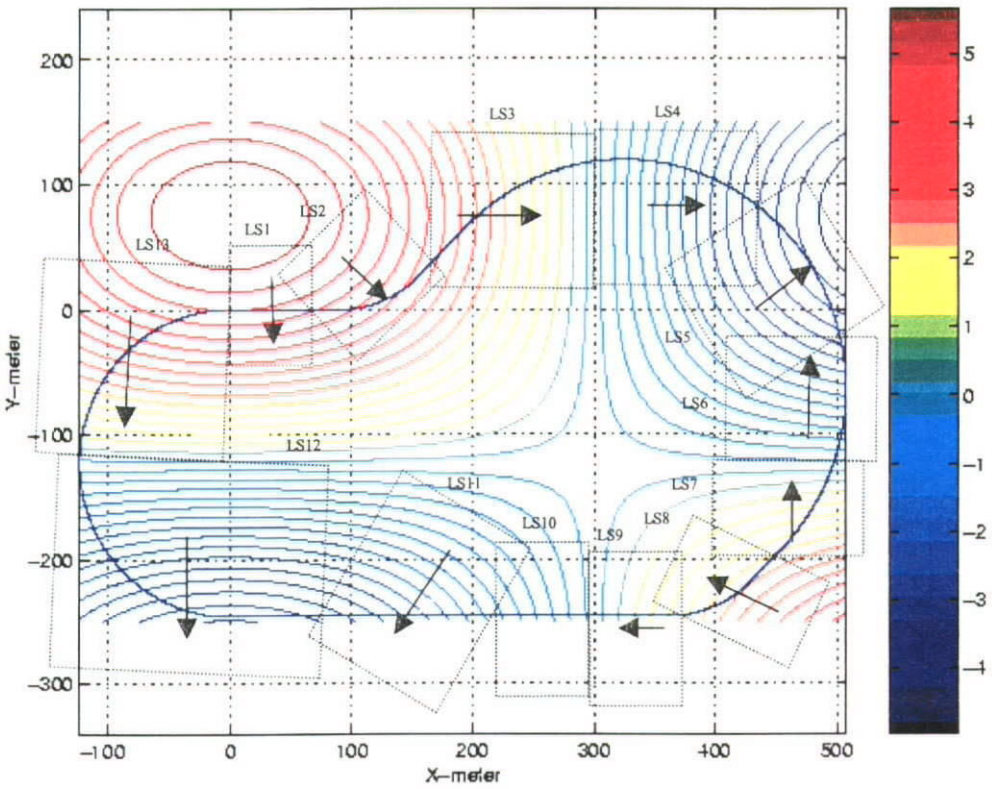

Figure 7.36 Landscape on Road Profile 1

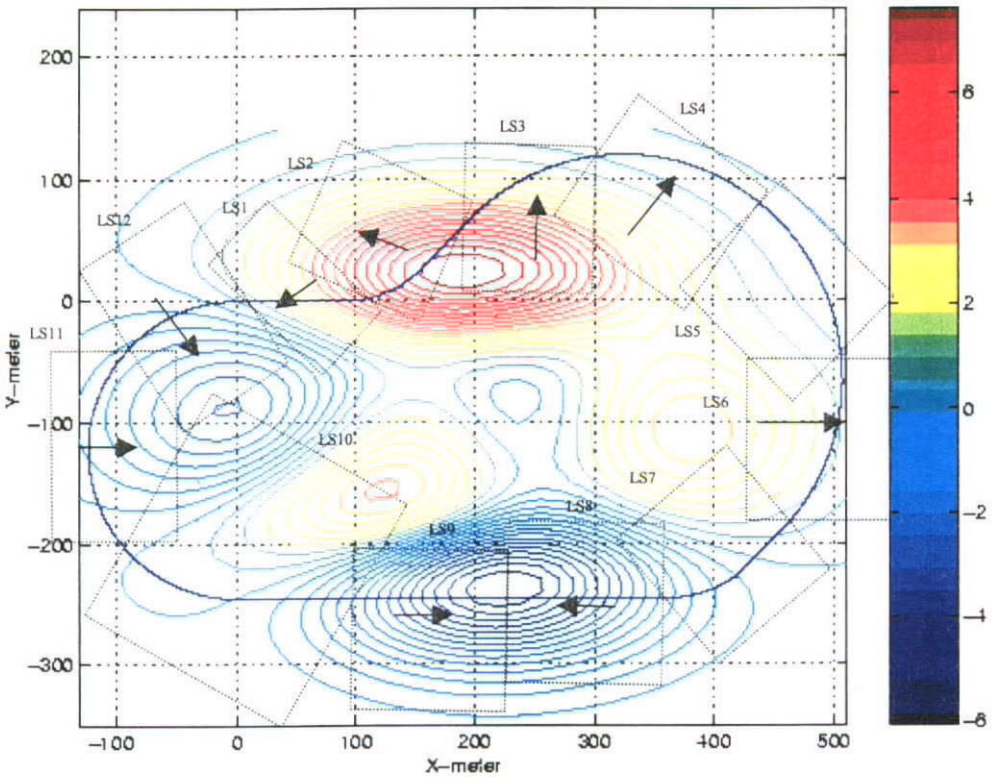

Figure 7.37 Landscape on Road Profile 2

Table 7.4 Parameters of Landscape, LS_i, on Road Profile 1

LS	Road Bank Angle, T_m(rad)	X_{start}(m)	X_{finish}(m)	St_{pos}(rad)
1	0.10	0	70	0
2	0.08	70	165	45
3	0.05	165	300	52
4	0.05	300	430	88
5	0.12	430	501	-8
6	0.15	501	498	85
7	0.08	498	443	-60
8	0.08	443	375	30
9	0.04	375	295	-90
10	0.00	295	218	0
11	0.10	218	76	135
12	0.12	76	-123	188
13	0.10	-123	0	-85

Table 7.5 Parameters of Landscape, LS_i, on Road Profile 2

LS	Road Bank Angle, T_m(rad)	X_{start}(m)	X_{finish}(m)	St_{pos}(rad)
1	0.08	0	115	-45
2	0.14	115	192	-165
3	0.17	192	299	135
4	0.08	299	431	130
5	0.00	431	508	0
6	0.04	508	454	180
7	0.00	454	350	0
8	0.12	350	219	90
9	0.13	219	92	-90
10	0.00	92	-100	0
11	0.07	-100	-97	-15
12	0.09	-97	0	-2

The following table show the trajectory parameters in the simulations and Figure 7.38 shows the trajectory.

Table 7.6 Trajectory Parameters of the Simulation

Path ID	$X_{start}(m)$	$d\theta_s(rad/sec)/\rho(m^{-1})$	Description	Duration(sec)
0	0	0 / 0	go straight toward x_+	5.00
1	91.683	0.2 / 0.01929	turn left for 45 deg	3.94
2	156.383	0 / 0	go straight at 45deg with x_+	3.00
3	195.333	0.1/0.00564	turn right for 180 deg	31.40
4	454.134	0/0	go straight at 45deg with x_-	2
5	428.124	0.2/0.01929	turn right for 45 deg	3.92
6	363.424	0 / 0	go straight toward x_-	19.86
7	0	0.15/0.00809	turn right for 180 deg, back to the starting point	20.88

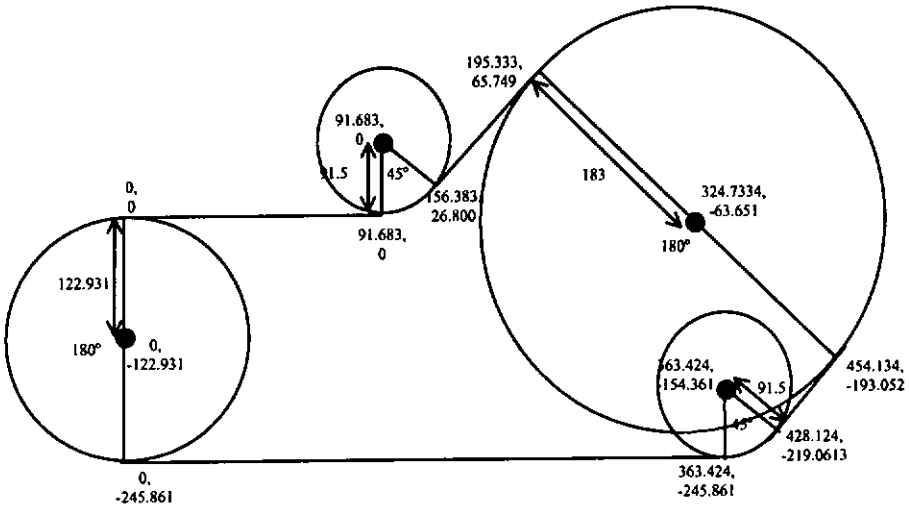

Figure 7.38 Desired Trajectory

Figures 7.39 – 7.41 show the simulation of vehicle on a flat road surface. Figures 7.42 – 7.44 show the simulation of a vehicle on road profile 1. Figures 7.45 – 7.47 show the simulation of a vehicle on road profile 2.

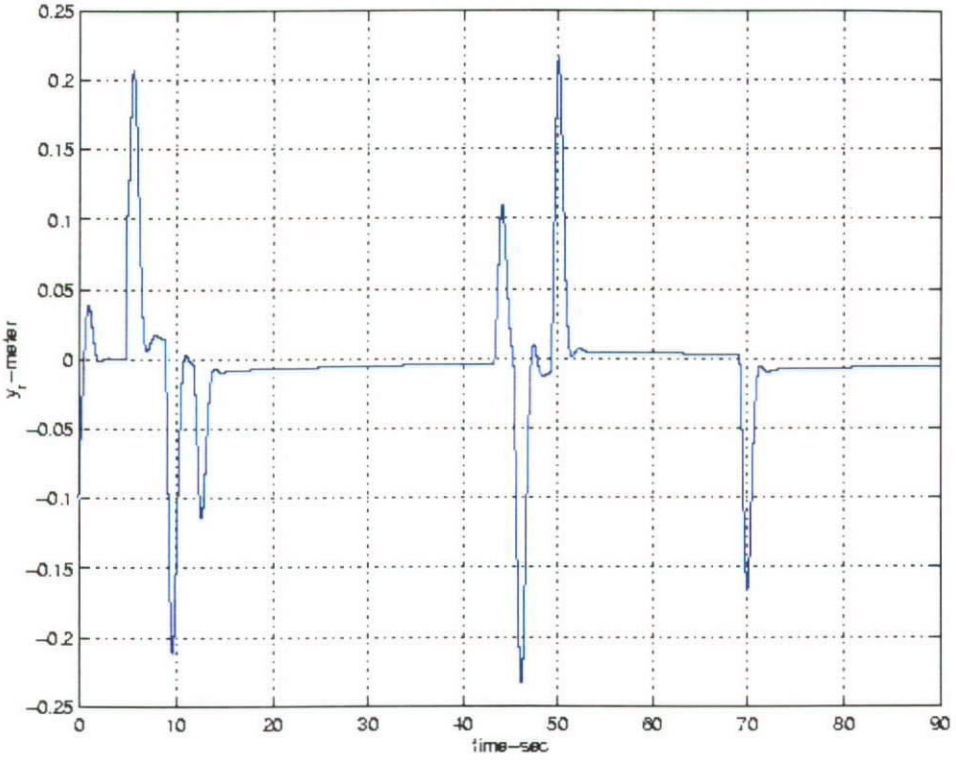

Figure 7.39 System Output y_r in Simulation on Flat Surface

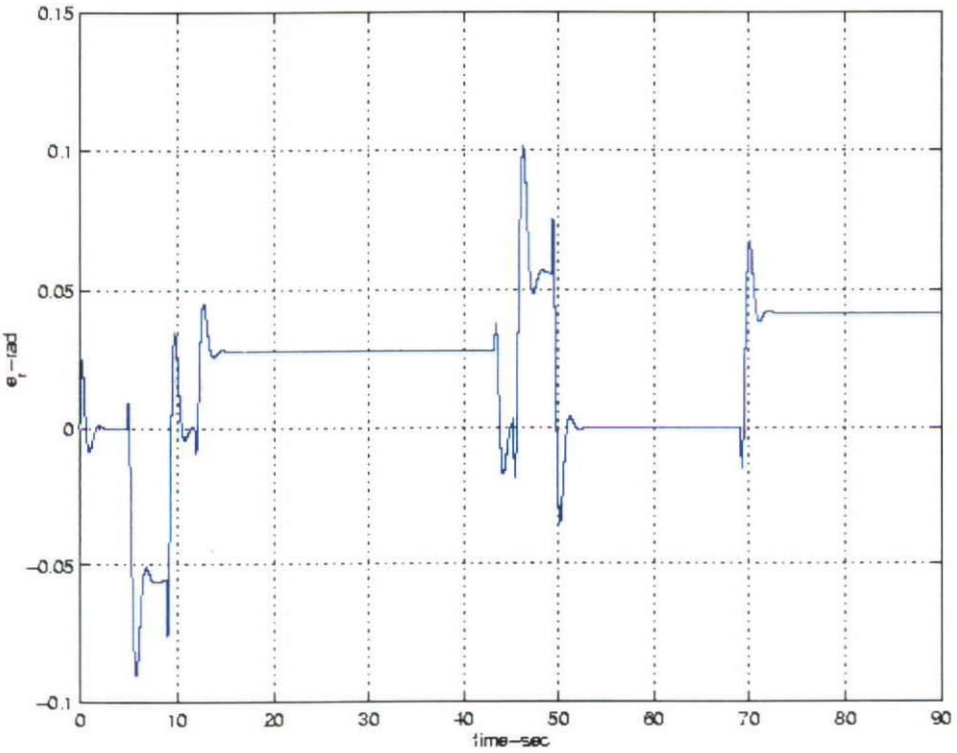

Figure 7.40 System Output ε_r in Simulation on Flat Surface

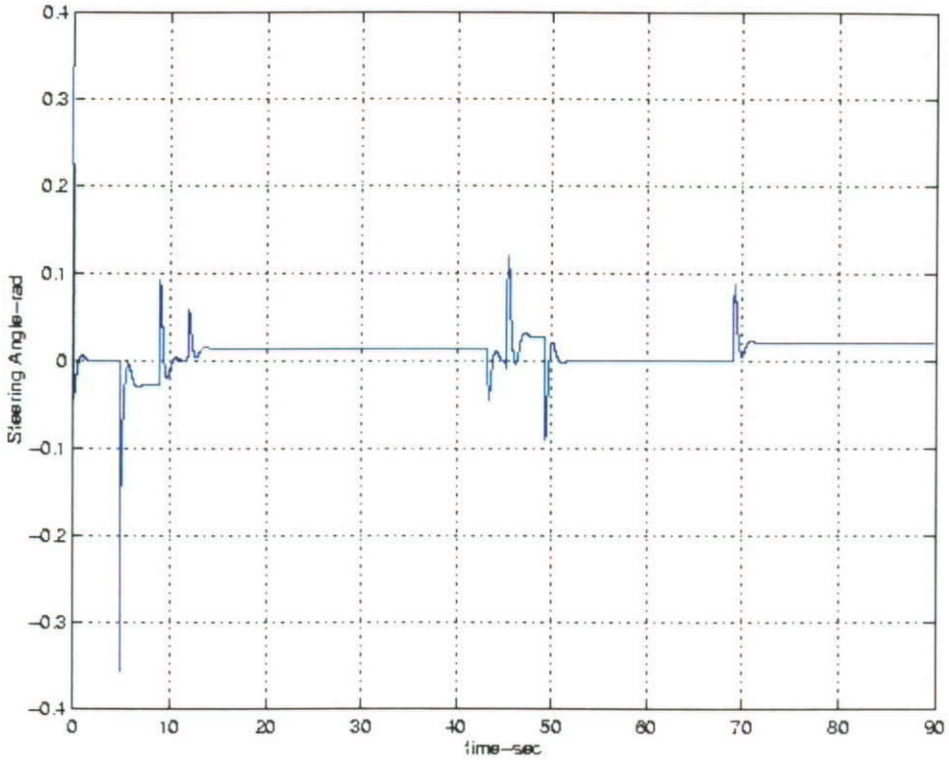

Figure 7.41 Controller Output δ in Simulation on Flat Surface

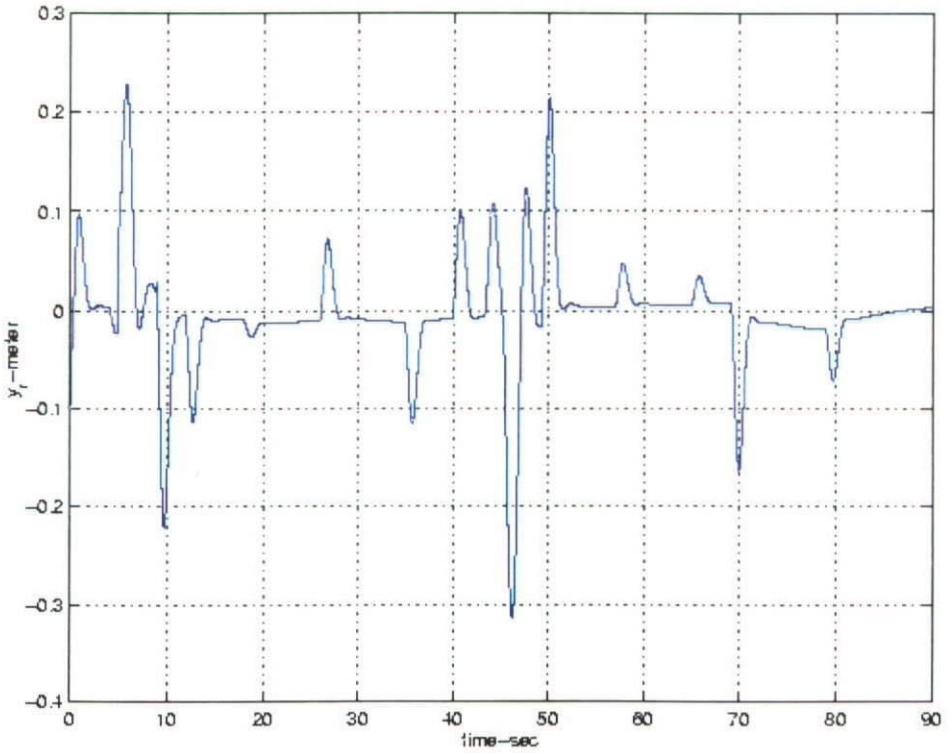

Figure 7.42 System Output y_r in Simulation on Road Profile 1

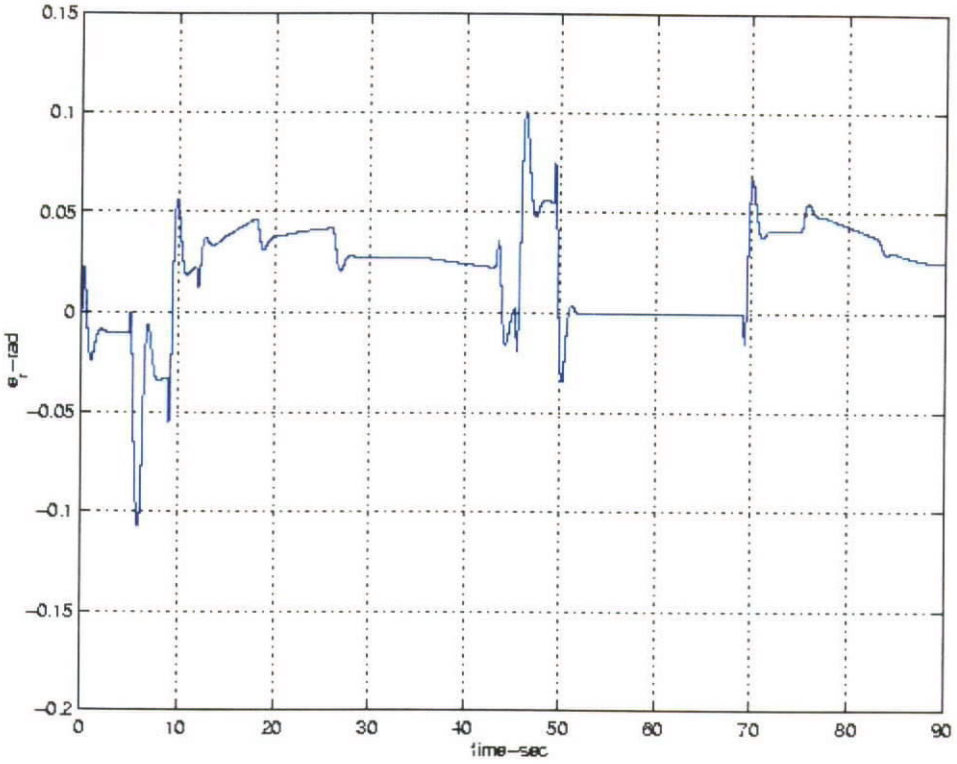

Figure 7.43 System Output ε_r in Simulation on Road Profile 1

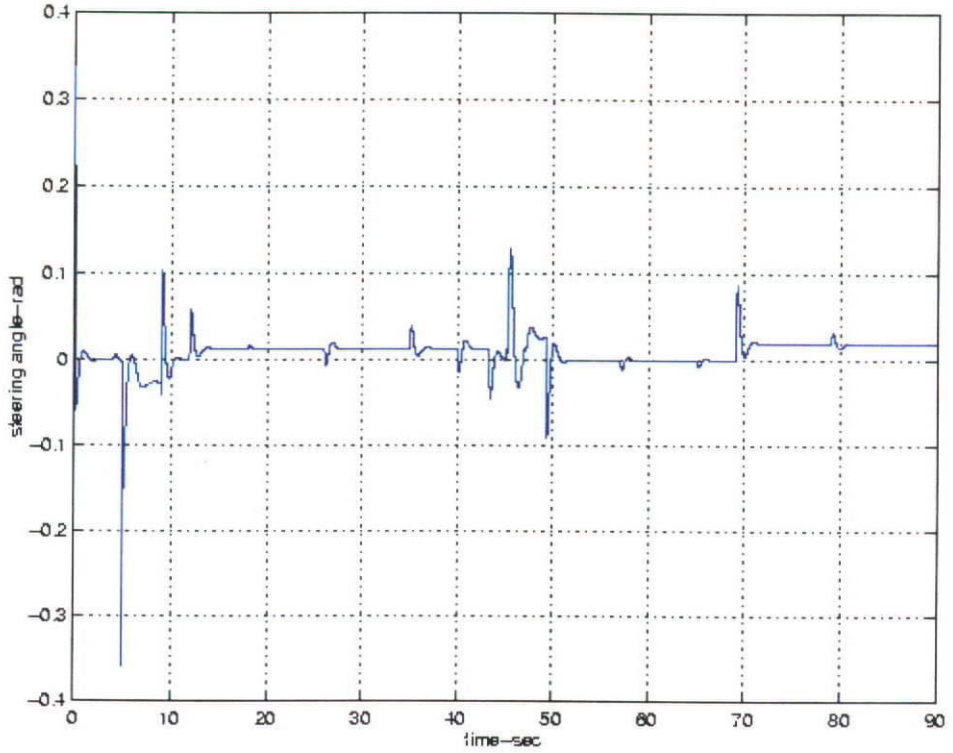

Figure 7.44 System Output δ in Simulation on Road Profile 1

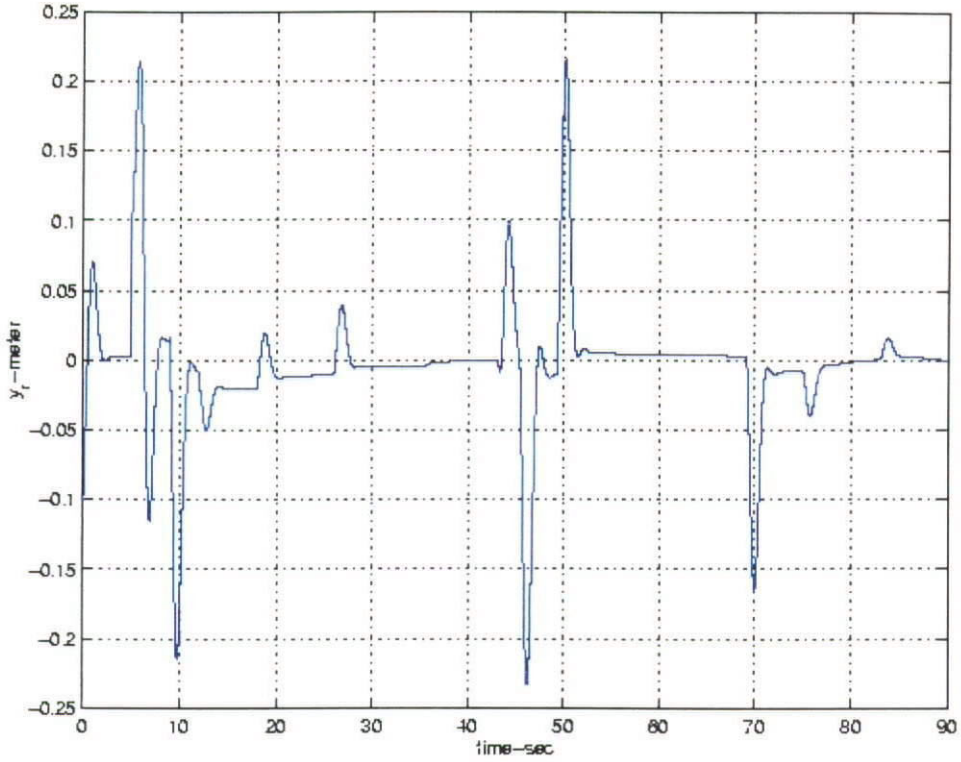

Figure 7.45 System Output y_r in Simulation on Road Profile 2

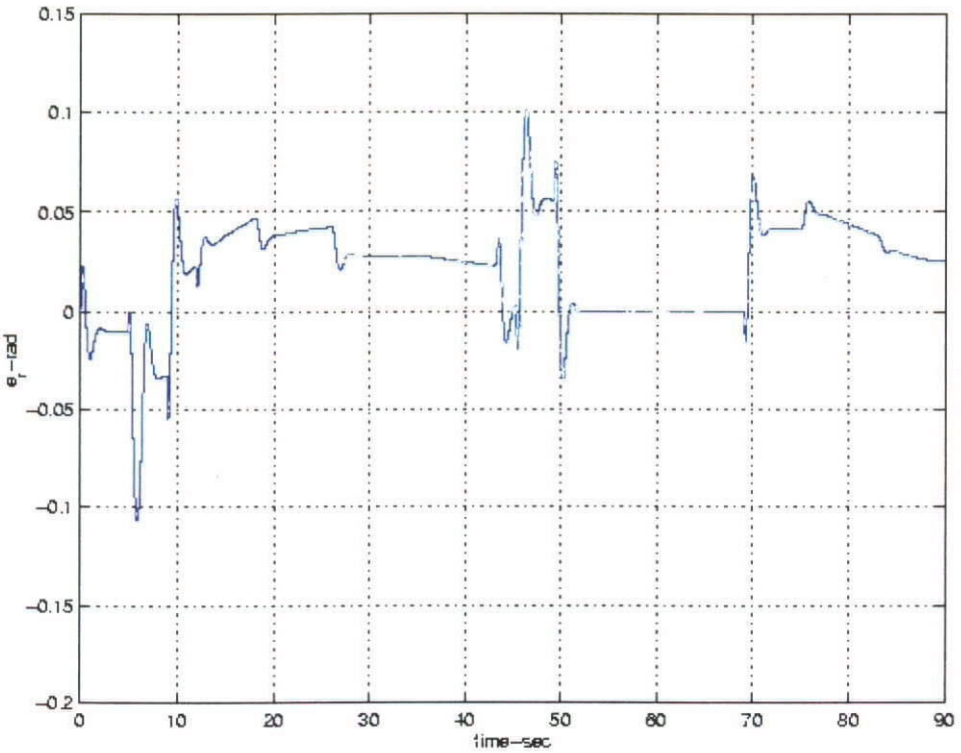

Figure 7.46 System Output ε_r in Simulation on Road Profile 2

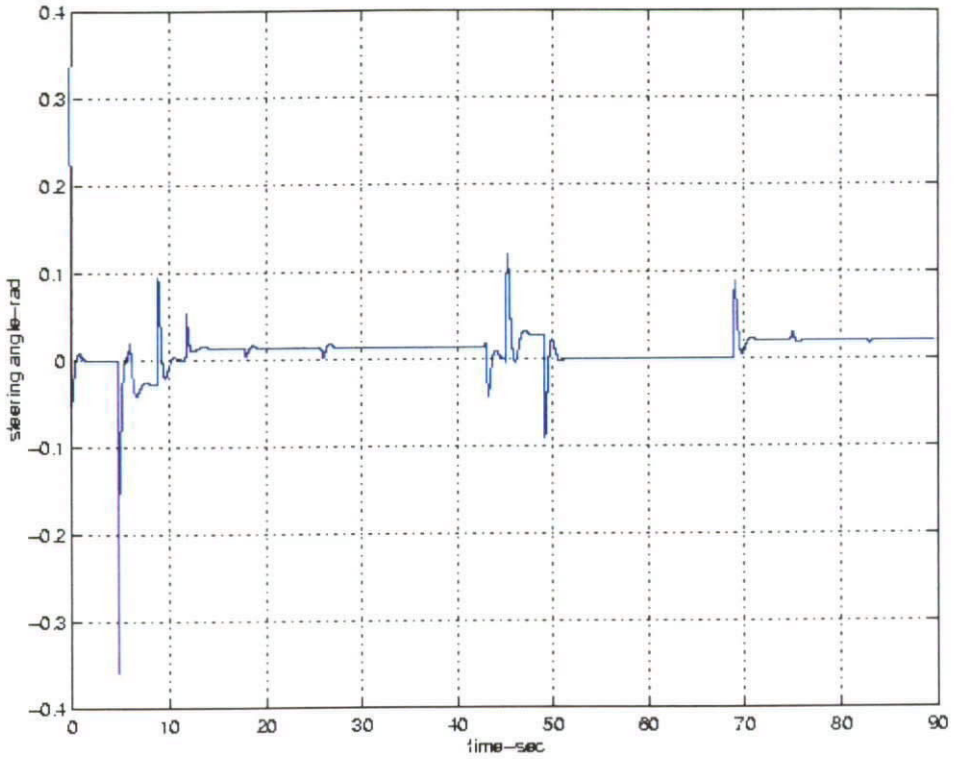

Figure 7.47 System Output δ in Simulation on Road Profile 2

Figures 7.39 and 7.41 show that the simulation of a vehicle running on a road surface with changing geometry is possible by joining all the landscapes together. Besides, the control system shows a good performance in tracking the desired trajectory where y_r is less than 10 cm in most of the simulation time in both simulations and the maximum value of the y_r is less than 23cm. The results obtained in these two simulations are closely match to the control objectives regarding the path tracking.

8. CONCLUSIONS, RECOMMENDATION OF FURTHER STUDIES AND CONTRIBUTION OF THE STUDY

8.1 Conclusions

In this section, all the findings in the study are concluded, including *control system, vehicle model, navigation scheme* and *system analysis*. In this study, H_∞ control method and μ-synthesis methodology are used. A methodology to construct a structured block in μ-formulation from uncertainty system parameters and unmodeled dynamics is developed. The vehicle model is reconstructed from the model found in [88] to include pitch dynamics, vehicle bank angle and vehicle inclination angle. With these three additional system parameters, the vehicle model can be used in the controller design on a 3-dimensional road surface. In addition, the navigation scheme is outlined. Since all the works in this study are done in the simulations, the interconnection between the road surface and the vehicle model becomes more important. On every road surface, the vehicle is assumed to be on a rectangular landscape, which can be on a horizontal plane or a slanted plane surface. By joining all the landscapes together on a road profile, a 'piece-wise' smooth path can be described. Besides, the vehicle model is investigated in great detail in frequency domain. The effects of road bank angle on both lateral velocity and yaw angle rate are explored. The result shows that the effect of road bank angle on the dynamics of lateral velocity is greater than that on the dynamics of yaw angle rate.

8.1.1 Control System

The parameter variations, external disturbances and the unmodeled dynamics are considered in this study. Three H_∞ controllers, K_{nom}, K_{mod} and K_{blk}, are constructed,

where K_{mod} and K_{blk} are built using μ-synthesis. By using K_{nom}, results are obtained to analyze nominal performance, nominal stability, robust performance and robust stability. It shows that the H_∞ controller, K_{nom}, is an effective robust controller on vehicle control, ensuring both robust performance and robust stability. Two structured perturbations of vehicle model, controllers K_{mod} and K_{blk}, are compared. The controllers are structured block μ-formulations expressed from multiplicative input uncertainty and from system parameters uncertainty respectively. The results demonstrate that K_{blk} have better performance, when compare with K_{mod}, in vehicle control on an undulating road surface, where the vehicle simulation model is subjected to parameters variations, external disturbances and unmodelled dynamics.

With Lemma 5.4, general μ-formulation for plant perturbation in parameters is outlined. The system parameter uncertainty can be directly fed into the μ-formulated structured block, which, in turn, can construct a highly robust H_∞ controller using μ. It appears that the structured block formulated by using the methodology developed in this study gives much more physical insight to control engineers, since all the uncertainties in the system parameters are considered separately or together in a structured block rather than making some conservative assumptions of full complex block or full real block on the structure of the perturbation block.

8.1.2 Vehicle Model

The vehicle model is developed in this study. The model is constructed based on [88]. The vehicle model developed is ready for vehicle control system on a 3-dimensional road surface. This is possible since the model includes pitch dynamics, vehicle bank angle and vehicle inclination angle. For the analysis of the effect of road

parameters, say road slanted angles, on vehicle dynamics, the 3-dimensional vehicle model built in this study is the only model available in this area. Although the model is developed based on some assumptions, which make the model development easier, it is accurate enough to demonstrate the importance of involving those road parameters in the design of the vehicle control system. Verifications of vehicle model are also done by comparing this model with that found in [90]. Five types of inputs are used in the verification of the design model. They are sinusoidal, trapezoidal, lane change references, ramp and high frequency sinusoidal input signals. The simulation results show that, with sinusoidal, trapezoidal and lane change references signals, the complex model and the design model are close to each other. However, with ramp and high frequency sinusoidal input signals, the complex model and design models are no longer close to each other. The fact that the design model is not close to the complex model under some typical operation conditions, such as ramp and high frequency sinusoidal input signals, is due to the non-linearity in dynamics of the complex vehicle model. The simulations in Chapter 6 illustrate that the non-linearity is due to the nonlinear functions (Section 3.1) in vehicle tire model. The simulations also show that the effects of the road parameters on the nonlinear functions of the vehicle tire model are quite significant. The simulations also conclude that the road parameters cannot be ignored when designing a vehicle control system that is highly effective and highly robust.

8.1.3 Navigation Scheme

In this study, the navigation scheme on a 3-dimensional road surface is developed. The scheme is useful in the simulation of a vehicle on a 3-dimensional road surface where road parameters are being considered together. The road parameters are road

banking angle (deepest angle) and the rest-most direction. Those vehicle parameters related to the road parameters include vehicle bank angle and vehicle inclination angle. A set of equations (eqs. 4.3 – 4.5) developed in Section 4.2 connects these two sets of parameters. In Section 4.2, Figure 4.2.1 illustrates the attitude of a vehicle on a rectangular landscape. A smooth path on a typical road profile can then be described by joining all the landscapes on a road profile. Two paths on two road profiles (Road Profiles 1 & 2) have been shown in Section 7.5.4, Figures 7.36 – 7.27. The methodology of navigation on a 3-dimensional road surface developed in this study makes the simulation of a vehicle on an undulating road surface possible, where the road surface can be described in any mathematical functions, say $z=f(x,y)$.

8.1.4 System Analysis

In Section 6.3, the vehicle model is investigated in great detail in the frequency domain. The result shows that the lateral forces' effects on the vehicles dynamics are significant. With a possible set of uncertainties in system parameters, the effects of vehicle bank angle on lateral velocity are investigated in the frequency domain. This shows that the vehicle dynamics on lateral velocity are varying to a great extent within a frequency range [8 – 30Hz], when exploring the different sets of uncertainties in the system parameters of the vehicle system. The simulations again show that the lateral tire forces affect the vehicle dynamics to a large extent. The system can vary from a well-posed to a badly-posed system under perturbations. This explains why the linear design model cannot approximate the complex model under some operating conditions. This is also the motivation for control engineers to develop a set of plants which includes a defined set of possible perturbations on the plant. Thus, a H_∞ control system can now be developed using μ-synthesis, where the

μ-formulated structured block captures the set of possible perturbations. This control system has been built in this study.

8.2 Recommendation of Further Studies

The vehicle model is developed under the assumption that the pitch dynamics and the roll dynamics are de-coupled. A more complicated vehicle model can be built by relaxing this assumption. Then, the results obtained in the simulation will come closer to those obtained in the real situation. Another assumption that is used when developing the vehicle model is that the vehicle suspension stretched–spring equations always hold. This assumption is used, because the 3-dimensional free vibration problem on four springs system is difficult to be solved. Actually, normal force on each tire can be directly obtained by equipping a force sensor on each suspension. If those normal forces (or lateral forces) are directly measured, the non-linearity between the normal forces (or lateral forces) and the vehicle system variables can be greatly reduced.

In describing the path on a 3-dimensional road profile, several landscapes are joining together to form a smooth path. In Section 7.5.4, only 13 and 12 landscapes are used to describe the path on road profiles 1 and 2, respectively. A greater number of landscapes can be used in order to obtain a smoother path on the road surface. However, the trade off of using a great number of landscapes is a large computational effort.

In Section 5.2.4.5, general μ-formulation for plant perturbation parameters is developed. With this formulation, the uncertainty in system parameters can be easily

written into a structured block, Δ, and general plant P. However, it is not easy to verify, neither in time domain nor frequency domain, the structured perturbation model using the complex vehicle model. Since the complex vehicle model is highly nonlinear, the system parameters are time-varying. If verification is necessary, the system parameters of the complex vehicle model need to be recorded. The variation in these system parameters should be recalled in the structured perturbation block, and then the time-domain verification can be done.

The simulation has been done by using only the control system, road model and vehicle model. When putting the control system into real practical vehicle control system, some modifications will need to be made. There are two approaches in applying the vehicle control system developed in this study to apply in the real practical vehicle system. The first approach is to record a digital map into the control system, where the desired path can be outlined on the map. The path stores all the information about each turn and direction, similar to paths shown in Figures 7.34 and 7.35. The second approach is to equip sensors, such as video or ultrasonic sensors. These sensors report, in real-time, all the information surrounding the vehicle. When the vehicle needs to go straight ahead, the desired path can be extrapolated from the vehicle local position to a designated direction. When the vehicle needs to turn around or change lane in order to avoid an object ahead, the desired path of arc(s) can be calculated from the vehicle local position to a desired angle.

8.3 Contribution of the Study

In this study, the methodology of navigation of a vehicle on a 3-dimensional road profile is developed. With this methodology, the effect of road parameters on vehicle

dynamics can be investigated in great detail. Also, most of the navigation systems available in the market, such as GPS and INS, do not have a great accuracy in the z-direction. The navigation scheme developed in this study does not need the data on z-direction, which suits any low-cost and effective navigation sensors.

The use (and integration) of different sensors in a vehicle system enhances the performance of the vehicle measurement system and vehicle control system (less than 25cm in lateral off-path distance and 6deg in off-path heading angle). With the control methodology developed in this study, the performance of the vehicle maneuvering is improved, and the accuracy of the vehicle measurement system is increased, from maximum error in GPS of 50cm to less than 25cm in operation in the simulation.

A Lemma 5.4 is written. With this lemma, plant perturbation parameters can be fed into the general μ-formulation directly. Since system parameters are involved, the physical meaning of these perturbations can also be encompassed in the structured block, Δ. With this lemma, both the perturbations in system transfer functions or system matrices can be directly fed into the μ-formulated structured block.

A set of equations (eqs. 4.3 – 4.5) are developed in Section 4.2, which connect road parameters and those vehicle parameters related to the road parameters. Using this sets of equations, the vehicle local sensors are accurate enough to describe the attitude of the vehicle on any road surface,

9. REFERENCES

[1] B. Ulmer, "VITA-an autonomous road vehicle (ARV) for collision avoidance in traffic," *Proceedings of the Intelligent Vehicles '92 Symposium* (Cat. No. 92TH0468-9), 1990, pp.36-41

[2] S. Ozawa, "Image sensors in traffic and vehicle control," *1994 Vehicle Navigation and Information Systems Conference Proceedings* (Cat. No. 94CH35703), 1994, pp.27-34

[3] *Hong Kong Transportation Report*, 1996

[4] J.S. Want and R.R. Knipling, "Single vehicle roadway departure crashes: problem size assessment and statistical description," *National Highway Traffic Safety Administration Technical Report*, DTNH-22-91-C-03121

[5] V.K. Narendran and J.K. Hedrick, "Transition maneuvers in intelligent vehicle highway systems," *Proceedings of the 32nd IEEE Conference on Decision and Control* (Cat. No.93CH3307-6), 1993, pp.1880-1884

[6] B. McQueen, "Smart vehicles and intelligent highways-an integrated system?" *1994 Vehicle Navigation and Information Systems Conference Proceedings* (Cat. No.94CH35703), 1994, pp.A/7

[7] G. Lind, "Test-site-oriented scenario assessment (TOSCA II): IRTE scenarios as a basis for socio-economic evaluation," *1994 Vehicle Navigation and Information Systems Conference Proceedings* (Cat. No.94CH35703), 1994, pp.661-666

[8] M. Nygard and S. Delab, "Reflections on state-of-the-art within RTI/IVHS," *1994 Vehicle Navigation and Information Systems Conference Proceedings* (Cat. No.94CH35703), 1994, pp.519-524

[9] R. C. Luo and M.G. Kay, "Multisensor integration and fusion in intelligent systems," *IEEE Tran. on Systems, Man and Cybernetics*, 1989, pp.901-931

[10] J. Ackermann, J. Guldnet, W. Sienel, R. Steinhauser and V.I. Utkin, "Linear and nonlinear controller design for robust automatic steering," 1995, v.3, pp.132-143

[11] R.E. Fenton and I. Selim, "On the optimal design of an automotive lateral controller," *IEEE Trans. Vehicle Tech.*, 1988, v.37, pp.108-113

[12] T. Ito, M. Furumata, F. Harashima, H. Inaba and S. Matsumoto, "An automatic driving system of automobiles by guidance cables", SAE Paper 790127

[13] B.B. Litkouhi, A.Y. Lee and D.B. Craig, "Estimator and controller design for LaneTrak, a vision-based automatic vehicle steering system," *32nd IEEE Conference On Decision and Control*, 1993, pp.1868-1873

[14] S.M. Liu and A.A. Frank, "On lateral control of highway vehicles guided by a front looking sensor," *ASCE Advanced Transportation Conference*, 1989

[15] U. Ozguner, K.A. Unyelioglu, C. Hatipoglu and F.A. Kautz, "Design of a lateral controller for a cooperative vehicle system," SAE Paper 950474

[16] H. Peng, W. Zhang, S. Shladover and M. Tomizuka, "Magnetic-marker-based lane keeping: a robustness experimental study," SAE Paper 930556

[17] H. Peng and M. Tomizuka, "Vehicle lateral control for highway automation," *Proceedings of the American Control Conference*, 1990, pp.788-794

[18] R.T. O'Brien, P.A. Iglesias and T.J. Urban, "Preview control for vehicle lateral guidance in highway automation," *ASME Journal Dynamic System Measurement Control*, 1993, v.115, pp.679-686

[19] R. Parsons and W.B. Zhang, "Program on advanced technology for the highway-lateral guidance system requirements definition," *Proceedings of the ASCE International Conference on Application of Advanced Technology in Transportation Engineering*, 1989, pp.257-280

[20] R. Fenton, G. Melocik and K. Olson, "On the steering of automated vehicles: theory and experiment," *IEEE Trans. Automat. Control*, 1976, v.AC-21, pp306-315

[21] T. Ito, M. Furumata, F. Harashima, H. Inaba and S. Matsumoto, "An automobile driving system of automobiles by guidance cable," *Soc. Automotive Engineering Tech. Report*, 1973, pp.730127

[22] S. Drakunov and R. DeCarlo, "Sliding mode control design for automated steering via Lyapunov approach," *Proceedings of the 34th IEEE Conference on Decision and Control* (Cat. No. CH350803), 1995, v.4, pp.4086-4088

[23] R. DeCarlo, S. Drakunov, "Sliding mode control design via Lyapunov approach," *Proceedings of the 33rd IEEE Conference on Decision and control* (Cat. No. 94CH3460-3), 1994, v.2, pp.1925-1930

[24] P.A. Shavrin, "Control of independent rear wheel drive vehicle," *Proceedings of the 34th IEEE Conference On Decision and Control* (Cat. No. 95CH35803), 1995, v.4, pp.4380-5

[25] R.T. O'Brien, P.A. Iglesias and T.J. Urban, "Vehicle lateral control for automated highway systems," *IEEE Transactions on Control Systems Technology*, 1996, v.4, issue 3, pp.266-73

[26] J. Gulder, V. Utkin and J. Ackermann, "A sliding mode approach to automatic car steering," *Proceedings of the American Control Conference*, 1994, pp.1969-1973

[27] G. Zames, "Feedback and optimal sensitivity: model reference transformations, multiplicative seminorms, and approximate inverses," *IEEE Trans. Automat. Control*, 1981, v.AC-26, pp.301-320

[28] A. Hemami, "A comparative study of an optimal controller and a fuzzy logic controller for a multi-input multi-output system," *Proceedings of the 4th IEEE Conference on Control Applications* (Cat. No. 95CH35764), 1995, pp.269-274

[29] J.M. Lubin, S. Gilbert, E.C. Huber and A.L. Kornhauser, "Lateral control of an autonomous road vehicle in a simulated highway environment using adaptive resonance neural networks," *Proceedings of the Intelligent Vehicles '92 Symposium* (Cat. No. 92TH0468-9), 1990, pp.85-91

[30] T. Hessburg and M. Tomizuka, "Fuzzy Logic Control for Lateral Vehicle Guidance," *IEEE Control Systems*, 1994, v.4, no.4, pp.55-63

[31] Hussu and Alojz, "Fuzzy Controller," *Journal of Mechanical Engineering*, Ljubljana, 1992, v.38, pp.263-277

[32] C. Altrock and B. Krause, "Fuzzy logic and neurofuzzy technologies in embedded automotive applications," *IFIS '93 The Third International Conference on Industrial Fuzzy Control and Intelligent Systems* (Cat.No.93TH0594-2), 1993, pp.55-59

[33] J.M. Lubin, S. Gilbert, E.C. Huber and A.L. Kornhauser, "Lateral control of an autonomous road vehicle in a simulated highway environment using adaptive resonance neural networks," *Proceedings of the Intelligent Vehicles '92 Symposium* (Cat. No.92TH0468-9), 1990, pp.85-91

[34] E.S. Plumer, "Neural network structure for navigation using potential fields," *IJCNN International Joint Conference on Neural Networks* (Cat. No.92CH3114-6), 1992, v.1, pp.327-32

[35] S. Neusser, J. Nijhuis, L. Spaanenburg, B. Hoefflinger, U. Franke and H. Fritz, "Neurocontrol for lateral vehicle guidance," *IEEE Micro*, 1993, v.13, issue 1, pp.57-66

[36] E. Bass and K.Y. Lee, "System linearization with guaranteed stability using norm-bounded neural networks," *1994 IEEE International Conference on Neural Networks* (Cat. No. 94CH3429-8), 1994, v.4, pp.2355-2360

[37] J. Holgado, A. Ollero and J. Aracil, "Statistical study on stability indices of fuzzy control systems," *Proceedings of the Third IEEE Conference on Fuzzy Systems* (Cat. No. 94CH3430-6), 1994, v.2, pp.936-941

[38] G. Kechriotis and E.S. Manolakos, "A VLSI array architecture for the on-line training of recurrent neural networks," *Conference Record of the 25th Asilomar Conference on Signals, Systems and Computers* (Cat. No.91CH3112-0), 1991, v.1, pp.506-510

[39] J. Nijhuis, B. Hofflinger, S. Neussber, A.Siggelkow and L. Spaanenburg, "A VLSI implementation of a neural car collision avoidance controller," *IJCNN-91-Seattle: International Joint Conference on Neural Networks* (Cat. No.91CH3049-4), 1992, v.1, pp.493-499

[40] K. Shaffer, M.E. Zaghloul and Y. Chen, "Implementation of neural network controller for unknown systems," *Proceedings of the 5th IEEE International Symposium on Intelligent Control 1990* (Cat. No. 90TH0333-5), 1990, v.1, pp.530-535

[41] P.J. McCann and B.L. Kalman, "Parallel training of simple recurrent neural networks," *1994 IEEE International Conference on Neural Networks* (Cat.No.94CH3429-8), 1994, v.1, pp.167-170

[42] S. Shams and J.L. Gaudiot, "Parallel methods for implementations of neural networks," *IJCNN-91-Seattle: International Joint Conference on Neural Networks* (Cat. No.91CH3049-4), 1991, v.2, pp.988

[43] J. Torresen, S. Mori, H. Nakashima, S. Tomita and O. Landsverk, "Exploiting multiple degrees of BP parallelism on the highly parallel computer AP1000," *Fourth International Conference on `Artificial Neural Networks`* (Conference Publication No.409), 1995, pp.483-488

[44] J. Zhang and H. Nagel (to appear), "Texture analysis and model-based road recognition for autonomous driving," *Journal of Computer Vision, Graphics and Image Processing*

[45] U. Kiencke, "Realtime estimation of adhesion characteristic between tyres and road," *Proceedings of the 12th IFAC World Congress*, 1993, v.1, pp.15-18

[46] C. Hatpoglu, "Lateral control of vehicles for highway automation," Master's Thesis, The Ohio State University, Department of Electrical Engineering, 1995

[47] T. Jochem, D. Pomerleau, B, Kumar and J. Armstrong, "PANS: a portable navigation platform," *Proceedings of the Intelligent Vehicles '95. Symposium* (Cat. No. 95TH8132), 1995, pp.107-112

[48] M.J. Hadfield and K.E. Leiser, "Ring Laser Gyros come down to earth: Field Test Results on the RLG Modular Azimuth Position System (MAPS)," *IEEE PLANS*, 1988

[49] K.P. Schwarz, M. Wei and M. Van Gelderen, "Aided versus embedded-a comparison of two approaches to GPS/INS integration," *IEEE, 1994 Position Location and Navigation Symposium* (Cat. No.94CH3358-9), 1994, pp.314-322

[50] D.T. Knight, "Achieving modularity with tightly-coupled GPS/INS," *IEEE PLANS '92: Position Location and Navigation Symposium Record. '500 Years After Columbus - Navigation Challenges of Tomorrow'* (Cat. No.92CH3085-8), 1992, pp.426-432

[51] D.B. Roenblatt, et al., "The impact of Selective Availability on precise relative position with static GPS", *Journal of the Geodesic Society of Japan*, 1992, v.38, no.1, pp.29-44

[52] T. Hunter, W. Kosmalski and P. Truong, "Vehicle navigation using differential GPS," *IEEE PLANS '90: Position Location and Navigation Symposium Record. 'The 1990's - A Decade of Excellence in the Navigation Sciences'* (Cat. No. 90CH2811-8), 1990, pp.392-398

[53] W.C. Collier, "In-vehicle route guidance systems using map-matched dead reckoning," *IEEE PLANS '90: Position Location and Navigation Symposium Record. 'The 1990's - A Decade of Excellence in the Navigation Sciences'* (Cat. No. 90CH2811-8), 1990, pp.359-363

[54] H, Dezert, Y. Bar-Shalom, "Joint probabilistic data association for autonomous navigation," *IEEE Transactions on Aerospace and Electronic Systems*, 1993, v.29, issue 4, pp.1275-1286

[55] R. Jurgen, "The electronic motorist," *IEEE Spectrum*, Mar 1995

[56] F. Morisue and K. Ikeda, "Evaluation of map-matching techniques," *Proceedings of the Vehicle Navigation & Information Systems (VNIS) Conference*, Sept. 1989, pp.23-28

[57] W.C. Collier, "In-vehicle route guidance systems using map matched dead reckoning," *Proceedings of the IEEE Position Location and Navigation Symposium (PLANS)*, Mar. 1990, pp.359-363

[58] J.L. Buxion, S.K. Honey, W.E. Suchowerskyuj and A. Tempelhof, "The Travelpilot: A second-generation automotive navigation system," *IEEE Trans. Vehicle Technology*, Feb. 1991, v.40, pp.41-44

[59] Y. Fuj, T. Nawaoka, and E. Hirohata, "Development of a mapping and guidance database for automobile navigation system," *Proceedings of the IEEE Vehicle Technology Conference*, May 1991, pp.869-874

[60] J.B. Bullock and E.J. Krakiwsky, "Analysis of the use of digital road maps in vehicle," *IEEE 1994 Position Location and Navigation Symposium* (Cat. No. 94CH3358-9), 1994, pp.494-501

[61] K. Watanabe, K. Kobayashi and F. Munekata, "Multiple sensor fusion for navigation systems," *1994 Vehicle Navigation and Information Systems Conference Proceedings* (Cat. No. 94CH35703), 1994, pp.575-578

[62] Y. Konishi, I. Yamamoto and H. Watanabe, "Development of compact-type navigation system," *Japan Car Technology*, 1992, v.46, no.8, pp.45-51

[63] Y. Akazawa and T. Isobe, "Application of optical fiber gyro to vehicle," *Optronics*, 1992, No.9, pp.79-84

[64] R.G. Brown, *Introduction to Random Signal Analysis and Kalman Filtering*, John Wiley and Sons, Inc.

[65] J. Mar and J.H. Leu, "Simulations of the positioning accuracy of integrated vehicular navigation systems," *IEE Proceedings - Radar, Sonar and Navigation*, 1996, v.143, issue 2, pp.121-128

[66] K. Kobayashi, K.C. Cheok, K. Watanabe and F. Munekata, "Accurate Global Position via Fuzzy Logic Kaman Filter-based Sensor Fusion Technique"

[67] U. Ozguner, K.A. Unyelioglu and C. Hatipoglu, "An analytical study of vehicle steering control," *Proceedings of the 4th IEEE Conference on Control Applications* (Cat. No. 95CH35764), 1995, pp.125-130

[68] C.G. Moore, C.J. Harris and E. Rogers, "Utilizing fuzzy models in the design of estimators and predicators: An agile target tracking example," *2nd IEEE International Conference on Fuzzy Systems*, 1993, pp.679-684

[69] R.S. Doyler and C.J. Harris, "Multi-Sensor data fusion for obstacle tracking using neurofuzzy estimation algorithms," *SPIE Optical Engineering in Aerospace Sensing*, Orlando, FL, 1994, pp.2333

[70] H.L. Young, and J.H. Painter, "A fuzzy-tuned adaptive Kalman filter," *IFIS '93: The 3rd International Conference on Industrial Fuzzy Control and Intelligent Systems* (Cat. No. 93TH0594-2), 1993, pp.144-148

[71] R.K. Mehra, "Approaches to Adaptive Filtering," *IEEE Trans. Automatic Control*, 1972, pp.693-698

[72] J. Lalk, "Novel Expert System Strategies for Kalman Filter Adaptation," Ph.D. Thesis, 1994

[73] J.M. Roberts, D.J. Mills, D. Charnley and C.J. Harris, "Improved Kalman filter initialization using neurofuzzy estimation," *4th International Conference on 'Artificial Neural Networks'* (Conf. Publ. No. 409), 1995, pp.329-334

[74] R.M. Rogers, J.S. Wit, Crane III and D.G. Armstrong II, "Integrated INU/DGPS for autonomous vehicle navigation," *IEEE 1996 Position Location and Navigation Symposium* (Cat. NO. 96CH35879), 1996, pp.471-476

[75] R. Paielli, et al, "Carrier phase differential GPS integrated with an inertial navigation system: Flight test evaluation with auto-coupled precision landing guidance," *ION National Technical Meeting*, 1995

[76] K. Kobayashi, F. Munekata and K. Watanabe, "Accurate navigation via differential GPS and vehicle local sensors,"*1994 IEEE International Conference on MFI '94 Multisensor Fusion and Integration for Intelligent Systems* (Cat. No. 94TH06965), 1994, pp.9-16

[77] S. Cooper and H. Durrant-Whyte, "A frequency response method for multi-sensor high-speed navigation systems," *1994 IEEE International Conference on MFI '94* (Cat. No.94TH06965), 1994, pp.1-8

[78] H.F. Durrant-Whyte, "Consistent integration and propagation of disparate sensor observation," *International Journal of Robot. Res.*, 1987, v.6, no.3, pp.3-24

[79] D. Pomerleau, "RALPH: rapidly adoption lateral position handler," *Proceedings of the Intelligent Vehicles '95. Symposium* (Cat. No. 95TH8132), 1995, pp.506-511

[80] K. Tamura, Y. Nakamura, H. Sekine and N. Asanuma, "A study of self-reliant cornering speed control system," *1994 Vehicle Navigation and Information Systems conference Proceedings* (Cat. No. 94CH35703), 1994, pp.441-444

[81] S. Azuma, K. Nishida and S. Hori, "The future of in-vehicle navigation systems," *1994 Vehicle Navigation and Information Systems Conference Proceedings* (Cat. No. 94CH35703), 1994, pp.537-542

[82] R.J. Kelly, "Reducing geometric dilution of precision using ridge regression," *IEEE Tran. on Aerospace and Electronics Systems*, 1990, v.26, issue 1, pp.154-168

[84] S.J. Marshall and R.F. Harrison, "Optimization and training of feed-forward neural networks by genetic algorithms," *2nd International Conference on ANN*, 1992, no.348, pp.39-43

[85] O.M. Omidvar and C.L. Wilson, "An implementation of backpropagation algorithm on massively parallel processor," *Proceedings of the 23rd Southeastern Symposium on System Theory*, 1991, pp.347-352

[86] E.A. Misawa, "Observer-based discrete-time sliding mode control with computational time delay: the linear case," *American Control Conference*, 1995, v.2, pp.1323-1332

[87] J.J. Slotine and S.S. Sastry, "Tracking control of non-linear systems using sliding surfaces, with application to robot manipulators," *International Journal of Control*, 1983, v.38, no.2, pp.465-492

[88] A.B. Will and S.H. Zak, "Modeling and control of an automated vehicle," *Vehicle System Dynamics*, 1997, v.27, pp.131-155

[89] G. Roos, R. Rollet and R.F.C. Kriens, "Numerical simulation of vehicle behavior during straight line keeping on undulating surfaces," *Vehicle System Dynamics*, 1997, v.27, pp.267-283

[90] H. Peng and M. Tomizuka, "Lateral control of front-wheel-steering rubber-tire vehicles," Technical report, JHL/APL, 1990

[91] D.E. Smith and J.M. Starkey, "Effects of model complexity on the performance of automated vehicle steering controllers: model development, validation and comparison," *Vehicle System Dynamics*, 1995, v.24, pp.163-181

[92] P. Lugner, "The influence of the structure of automobile models and tire characteristics on the theoretical results of steady-states and transient vehicle performance," *The Dynamics of Vehicles, Proceeding 5th VSD-2nd IUTAM Symposim*

[93] R.T. O'Brien, T.J. Urban, and P.A. Iglesias, "Lane change maneuver via modern steering control methods," Technical Report TR 94/15, Dept. Elec. & Comp. Eng., Johns Hopkins University, Baltimore, MD, Sept 1994

[94] T.J. Urban, "Stability and control of automated highway vehicles: vehicle dynamics model," Technical Report, JHU/APL, 1994

[95] H. Dugoff, P.S. Fancher and L. Segel, "An analysis of tire traction properties and their influence on vehicle dynamics performance," SAE Transaction, 1970, no.79, SAE Paper No. 700377, pp.341-366

[96] J.C. Doyle and G. Stein, "Multivariable feedback design: concepts for a classical/modern synthesis," *IEEE Trans. Auto. Control*, 1981, v.AC-26, pp.4-16

[97] M.K.H. Fan and A.L. Tits, "Characterization and efficient computation of the structured singular value," *IEEE Trans. Auto. Control*, 1986, v.AC-31, pp.734-743

[98] J. Doyle, A. Packard and K. Zhou, "Review of LFTs, LMIs and μ ," *Proceedings of the 30th IEEE Conference on Decision and Control*, 1991, pp.1227-1232

[99] J.C. Doyle, "Analysis of feedback systems with structured uncertainties," *IEEE Proceedings*, 1982, v.129, Part D, no.6, pp.242-250

[100] P.M. Young, M.P. Newlin and J.C. Doyle, "μ analysis with real parameters uncertainty," *Proceedings of the 30th IEEE Conference on Decision and Control*, 1991, pp.1251-1256

[101] P.M. Young and J.C. Doyle, "Computation of μ with real and complex uncertainties," *Proceedings of the 29th IEEE Conference on Decision and Control*, 1990, pp.1230-1235

[102] Redheffer, "On a certain linear fractional transformation," *Journal of Math. Phys.*, 1960, v.39, pp.269-286

[103] G.J. Balas and A. Packard, "The control handbook: the structure singular value μ framework," pp.671-687

[104]A.M. Holohan, "A tutorial on μ-analysis," *EURACO Networks: Robust and Adoptive Control Tutorial Workshop*, University of Dublin, Trinity College, 1994, Lecture 2.5

[105]J.L. Lin, I. Postlethwaite, and D.W. Gu, "μ-K iteration: a new algorithm for μ-synthesis," *Automatica*, 1993, v.29(1), pp.219-224

[106]R.Y. Chiang and M.G. Safonov, "Real K_m-synthesis via generalized Popov multipliers," *Proceedings of the American Control Conference*, Chicago, IL, Jun 1992

[107]M.A. Rotea and T. Iwasaki, "An alternative to the *D-K* iteration?" *Proceedings of the American Control Conference*, Baltimore, MD, Jun 1994, pp.53-55

[108]S. Toffner-Clausen, P. Andersen, J. Stoustrup, and H.H. Niemann, "A new approach to μ-synthesis for mixed perturbation sets," *Proceedings of the 3rd European Control Conference*, Rome, Italy, 1995, pp.147-152

[109]C.A. Desoer and M. Vidyasagar, *Feedback Systems: Input-Output Properties.* Academic Press, New York, 1975

[110]N.A. Lethomaki, "Practical robustness measures in multivariable control system analysis," Ph.D Thesis, Dept. of Electrical Engineering and Computer Science, Massachusetts Institute of Technology, Cambridge, MA, 1991

PAPER WRITTEN DURING M.PHIL. STUDY

A.F.M. Chan and E.H.K. Fung, "Modeling and control of an electric vehicle on slanted road surface," *IASTED '98*

APPENDIX A

According to the free body diagram in *system A*, it consider the vehicle pitching dynamics.

Concerning the moment balance equation,

$$mgl\sin\theta_p + M_R = I\ddot{\theta}_p - m\ddot{x}l\cos\theta_p \quad \cdots\cdots(A.1)$$

where $M_R = -K_{pitch}\theta_p - B_{pitch}\dot{\theta}_p$, and

$$K_{pitch} = k_{pl} + k_{pr},\ B_{pitch} = \beta_{pl} + \beta_{pr}$$

Concerning the force balance equations,

$$R_i = m\frac{d^2}{dt^2}\{x + \bar{x}\}$$
$$= m\frac{d^2}{dt^2}\{x - l\sin\theta_p\} \quad \cdots\cdots(A.2)$$

$$R_v - mg = -m\frac{d^2}{dt^2}\bar{z}$$
$$= -m\frac{d^2}{dt^2}\{l\cos\theta_p\} \quad \cdots\cdots(A.3)$$

Now, we consider the free body diagram in *system B*,

Concerning the moment balance equation,

$$R_b b + M_R' + m_{uf} ga$$
$$= F_l h_{um} + R_f a + m_{ub} gb \cdots\cdots(A.4)$$

where $M_R' = M_{Rr}' + M_{Rl}'$ and $F_l = f_b + f_f$

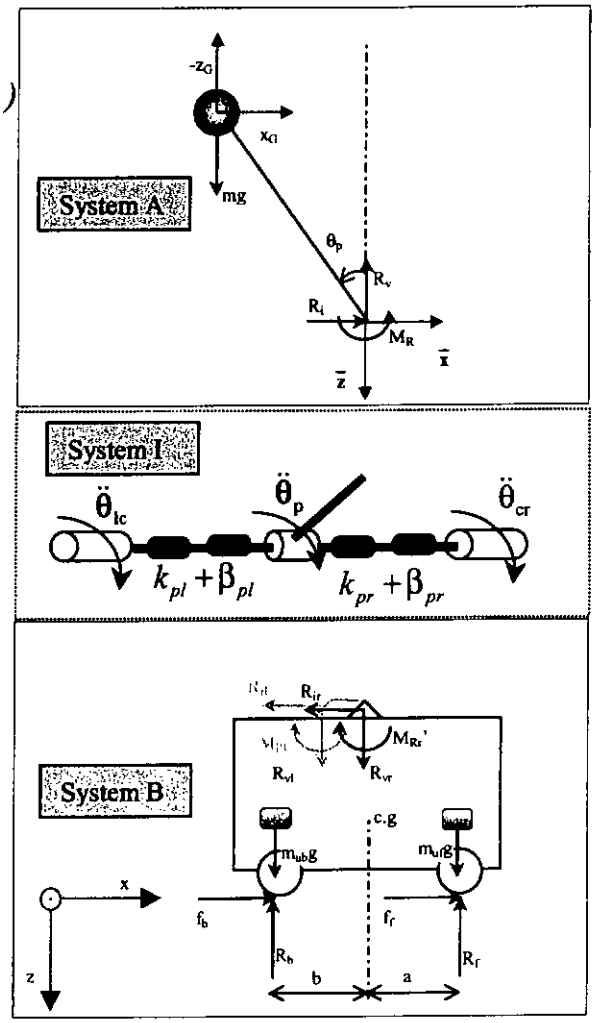

Figure A.1 Vehicle Free Body Diagram (Pitching)

Concerning the force balance equations,

$$F_l = M\ddot{x} + R_i \quad \cdots\cdots(A.5)$$

Now, we consider the free body diagram in *system B*,

Concerning the moment balance equation,

$$R_b b + M_R' + m_{uf} g a = F_l h_{um} + R_f a + m_{ub} g b \cdots\cdots\cdots (A.4)$$

where $M_R' = M_{Rr}' + M_{Rl}'$ and $F_l = f_b + f_f$

Concerning the force balance equations,

$$F_l = M\ddot{x} + R_i \quad \cdots\cdots\cdots (A.5)$$

$$R_f + R_b = Mg + R_v \quad \cdots\cdots\cdots (A.6)$$

Eliminating the interconnection force and moment force,

From equation(A.2)

$$\begin{aligned} R_i &= \bar{m}\{\ddot{x} - l\cos\theta_p \ddot{\theta}_p + l\sin\theta_p \dot{\theta}_p^{\,2}\} \\ &= m\{\ddot{x} - l\ddot{\theta}_p + l\theta_p \dot{\theta}_p^{\,2}\} \quad \text{, assume } \cos\theta_p = 1 \,\&\, \sin\theta_p = \theta_p \text{ when } \theta_p \text{ is smaill} \\ &= m\{\ddot{x} - l\ddot{\theta}_p\} \quad \text{, assume } \theta_p \dot{\theta}_p^{\,2} \approx 0 \text{ when } \theta_p \text{ is small} \cdots\cdots\cdots \text{(A.2a)} \end{aligned}$$

$$\begin{aligned} mg - R_v &= ml\{-\cos\theta_p \dot{\theta}_p^{\,2} - \sin\theta_p \ddot{\theta}_p\} \\ &= ml\{-\dot{\theta}_p^{\,2} - \theta_p \ddot{\theta}_p\} \quad \text{, assume } \cos\theta_p = 1 \,\&\, \sin\theta_p = \theta_p \text{ when } \theta_p \text{ is smaill} \\ &\approx 0 \quad \text{, assume } \dot{\theta}_p^{\,2}, \theta_p \ddot{\theta}_p \approx 0 \text{ when } \theta_p \text{ is small} \cdots\cdots\cdots \text{(A.3a)} \end{aligned}$$

Put equation(A.2a) into equation(A.5),

$$F_l - m\{\ddot{x} - l\ddot{\theta}_p\} = M\ddot{x}$$

$$F_l = (M+m)\ddot{x} - ml\ddot{\theta}_p \quad \cdots\cdots\cdots (A.7)$$

To obtain the M_R', consider the relative rotational motion between the unsprung and the sprung mass,

$$\begin{aligned} M_R' - M_R &= -I\ddot{\theta}_p \\ &\Rightarrow M_R' = M_R - I\ddot{\theta}_p \\ &\Rightarrow M_R' = -m\ddot{x}l\cos\theta_p - mgl\sin\theta_p \quad \cdots\cdots\cdots (A.8) \end{aligned}$$

With equations(A.4) and equations(A.6), solve R_l and R_r

$$\begin{cases} R_b + R_f = (M+m)g \\ bR_b - aR_f = F_l h_{um} + m\ddot{x}l\cos\theta_p + mgl\sin\theta_p + m_{ub}gb - m_{uf}ga \end{cases}$$

$$\Rightarrow \begin{cases} R_b = \frac{1}{a+b}\{a(M+m)g + \{F_l h_{um} + m\ddot{x}l\cos\theta_p + mgl\sin\theta_p + m_{ub}gb - m_{uf}ga\}\} \\ R_f = \frac{1}{a+b}\{b(M+m)g - \{F_l h_{um} + m\ddot{x}l\cos\theta_p + mgl\sin\theta_p + m_{ub}gb - m_{uf}ga\}\} \end{cases}$$

By considering *system B* in Figure A.1, the force and moment on the 3-dimensional free body diagram is obtained in *system B'* shown in Figure A.2.

However, the individual reaction force on each tire is hard to solve. Therefore, the following assumptions are made.

Consider the forces on x-y plane,

Induced the force and moment balance equations

$$\textit{Assumption A.1} \begin{cases} R_{il} = \frac{1}{2}R_i \\ R_{ir} = \frac{1}{2}R_i \end{cases}$$

also, consider the forces and moment on the x-z plane

$$\textit{Assumption A.2} \begin{cases} R_{vl} = \frac{1}{2}R_v \\ R_{vr} = \frac{1}{2}R_v \end{cases}$$

$$K_p\theta_p + B_p\dot{\theta}_p = k_l\theta_p + \beta_l\dot{\theta}_p + k_r\theta_p + \beta_r\dot{\theta}_p$$

and $\frac{K_p}{2}\theta_p = k_l\theta_p = k_r\theta_p$, and

$$\frac{B_p}{2}\theta_p = \beta_l\theta_p = \beta_r\theta_p$$

with $M_R' = M_{Rl}' + M_{Rr}'$

$$\Rightarrow \begin{cases} M_{Rl}' = \frac{1}{2}M_R' \\ M_{Rr}' = \frac{1}{2}M_R' \end{cases} \quad \textit{Assumption A.3}$$

$$\therefore R_3 + R_2 = R_{vr} + \tfrac{1}{2}m_{ub}g + \tfrac{1}{2}m_{uf}g = \tfrac{1}{2}(m + m_{ub} + m_{uf})g$$

$$bR_3 - aR_2 = \{F_{lr}h_{cg} - M_{Rr}' + \tfrac{1}{2}m_{ub}gb - \tfrac{1}{2}m_{uf}ga\}$$

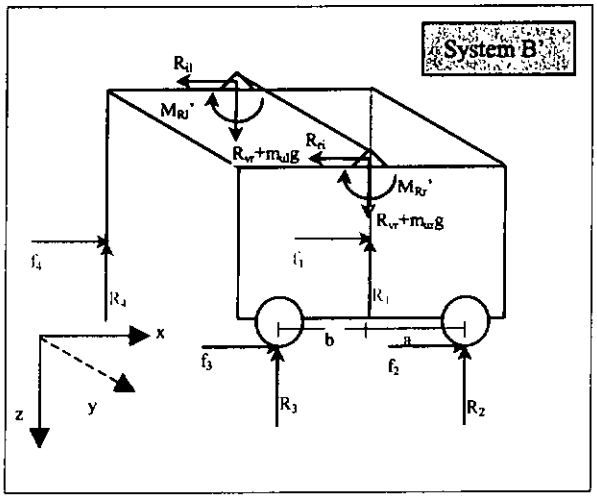

Figure A.2 Vehicle Free Body Diagram, System B' (Pitching)

$$\Rightarrow \begin{cases} R_2 = \frac{1}{a+b}\frac{b}{2}(M+m)g - \frac{1}{a+b}\{F_{lr}h_{cg} - M_{Rr}' + \frac{1}{2}m_{ub}gb - \frac{1}{2}m_{uf}ga\} \\ R_3 = \frac{1}{a+b}\frac{a}{2}(M+m)g + \frac{1}{a+b}\{F_{lr}h_{cg} - M_{Rr}' + \frac{1}{2}m_{ub}gb - \frac{1}{2}m_{uf}ga\} \end{cases}$$

$$\Rightarrow \begin{cases} R_2 = \frac{1}{a+b}\frac{b}{2}\{M+m-m_{ub}+\frac{a}{b}m_{uf}\}g - \frac{1}{a+b}\{F_{lr}h_{cg} - M_{Rr}'\} \\ R_3 = \frac{1}{a+b}\frac{a}{2}\{M+m+\frac{a}{b}m_{ub}-m_{uf}\}g + \frac{1}{a+b}\{F_{lr}h_{cg} - M_{Rr}'\} \end{cases}$$

$$\Rightarrow \begin{cases} R_2 = \frac{1}{a+b}\frac{b}{2}\{m+\frac{a+b}{b}m_{uf}\}g - \frac{1}{a+b}\{F_{lr}h_{cg} - M_{Rr}'\} \\ R_3 = \frac{1}{a+b}\frac{a}{2}\{m+\frac{a+b}{a}m_{ub}\}g + \frac{1}{a+b}\{F_{lr}h_{cg} - M_{Rr}'\} \end{cases}$$

$$\Rightarrow \begin{cases} R_2 = \frac{1}{2}\{\frac{b}{a+b}m+m_{uf}\}g - \frac{1}{a+b}\{F_{lr}h_{cg} - M_{Rr}'\} \\ R_3 = \frac{1}{2}\{\frac{a}{a+b}m+m_{ub}\}g + \frac{1}{a+b}\{F_{lr}h_{cg} - M_{Rr}'\} \end{cases} \cdots (A.10)$$

Similarity,

$$\Rightarrow \begin{cases} R_1 = \frac{1}{2}\{\frac{b}{a+b}m+m_{uf}\}g - \frac{1}{a+b}\{F_{ll}h_{cg} - M_{Rl}'\} \\ R_4 = \frac{1}{2}\{\frac{a}{a+b}m+m_{ub}\}g + \frac{1}{a+b}\{F_{ll}h_{cg} - M_{Rl}'\} \end{cases} \cdots (A.11)$$

Obviously, corresponding to the eqs. A.10 and A.11, R_1+R_2 and R_3+R_4 are equivalent to that in eq A.9, and R_1, R_2, R_3 and R_4 can each be interpreted in a more physical way.

$$\begin{cases} R_1 = \frac{1}{2}\{\frac{b}{a+b}m+m_{uf}\}g - \frac{1}{a+b}\{F_{ll}h_{cg} - M_{Rl}'\} \\ R_2 = \frac{1}{2}\{\frac{b}{a+b}m+m_{uf}\}g - \frac{1}{a+b}\{F_{lr}h_{cg} - M_{Rl}'\} \\ R_3 = \frac{1}{2}\{\frac{a}{a+b}m+m_{ub}\}g + \frac{1}{a+b}\{F_{lr}h_{cg} - M_{Rl}'\} \\ R_4 = \frac{1}{2}\{\frac{a}{a+b}m+m_{ub}\}g + \frac{1}{a+b}\{F_{ll}h_{cg} - M_{Rl}'\} \end{cases}$$

where F_{ll}=F_{lr}=F_l/2

R_i = reaction force on the ith tire resulting from static weight + dynamic force induced by the moment resulting from contact force on the ith tire + dynamic force induced by the pitching moment of the sprung mass on the vehicle base.

$$\begin{cases} R_1 = \frac{1}{2}\{\frac{b}{a+b}m+m_{uf}\}g - \frac{1}{a+b}\frac{1}{2}\{(M+m)\ddot{x}h_{cg} - ml\ddot{\theta}_p h_{cg} + m\ddot{x}l\cos\theta_p + mgl\sin\theta_p\} \\ R_2 = \frac{1}{2}\{\frac{b}{a+b}m+m_{uf}\}g - \frac{1}{a+b}\frac{1}{2}\{(M+m)\ddot{x}h_{cg} - ml\ddot{\theta}_p h_{cg} + m\ddot{x}l\cos\theta_p + mgl\sin\theta_p\} \\ R_3 = \frac{1}{2}\{\frac{a}{a+b}m+m_{ub}\}g + \frac{1}{a+b}\frac{1}{2}\{(M+m)\ddot{x}h_{cg} - ml\ddot{\theta}_p h_{cg} + m\ddot{x}l\cos\theta_p + mgl\sin\theta_p\} \\ R_4 = \frac{1}{2}\{\frac{a}{a+b}m+m_{ub}\}g + \frac{1}{a+b}\frac{1}{2}\{(M+m)\ddot{x}h_{cg} - ml\ddot{\theta}_p h_{cg} + m\ddot{x}l\cos\theta_p + mgl\sin\theta_p\} \end{cases} \cdots (A.12)$$

With the consideration of the small inclination angle of the road, ζ, the dynamic force has an additional term $(\mathrm{M}+\mathrm{m})\sin\zeta$ in F_I, thus

$F_I = (M+m)\ddot{x} - ml\ddot{\theta}_p + (\mathrm{M}+\mathrm{m})\sin\zeta$ and additional parameter,η, absorb in M_R', thus $M_R' = -m\ddot{x}l\cos\theta_p - mgl\sin(\theta_p+\eta)$.. However, the static reaction (normal) forces on each tire are refined with geometric consideration. Also, $\theta_p(t=0)$ is no longer equal to zero.

APPENDIX B

Normed Spaces

Let **H** be a *linear space* over the field **K** where **K** is either the field **C** of complex numbers or the field **R** of real numbers. A *norm* on **H** is a function denoted $\| \cdot \|$ from **H** to **R** having the following properties of

1. $\|f\| \geq 0.$ (B.1)
2. $\|f\| = 0,$ iff $f = 0$ (B.2)
3. $\|\alpha f\| = |\alpha| \, \|f\|.$ (B.3)
4. $\|f + g\| \leq \|f\| + \|g\|,$ (triangle inequality). (B.4)

where $f, g \in \mathbf{H}$ and $\alpha \in \mathbf{K}$. Thus a norm is a single real number measuring the 'size' of an element of **H**. Given a linear space **H** there may be many possible norms on **H**. Given a linear space **H** and a norm $\| \cdot \|$ on **H**, the pair (**H**, $\| \cdot \|$) is denoted a *normed space.*

Vector and Matrix Norms

Let **H** be the space $\mathbf{C}^n$ which is a linear space. Then $x \in \mathbf{C}^n$ means that $x = (x_1, x_2, \ldots, x_n)$ with $x_i \in \mathbf{C}$, $\forall i$. Clearly, $\mathbf{C}^n$ is the space of complex n-dimensional vectors. For $x \in \mathbf{C}^n$ the p-norms are defined by:

$$\|x\|_p = \left(\sum_{i=1}^{n} |x_i|^p\right)^{1/p} \qquad \text{(B.5)}$$

In control theory the 1-, 2- and ∞-norm are most important since they have obvious physical interpretations:

$$\|x\|_1 = \sum_{i=1}^{n} |x_i|, \qquad \text{resource} \qquad \text{(B.6)}$$

$$\|x\|_2 = \sqrt{\sum_{i=1}^{n} |x_i|^2} = \sqrt{x^* x}, \qquad \text{energy} \qquad \text{(B.7)}$$

$$\|x\|_\infty = \max_i |x_i|, \qquad \text{peak} \qquad \text{(B.8)}$$

In (B.7), x^* denotes the complex conjugate transpose of x. Notice that the 2-norm $\| x \|_2$ is the usual Euclidean length of the complex vector x. All norms on $\mathbf{C}^n$ are equivalent norms which means that if $\| \cdot \|_\alpha$ and $\| \cdot \|_\beta$ are norms on $\mathbf{C}^n$, then there exists a pair $c_1, c_2 > 0$ so that

$$c_1 \| x \|_\alpha \le \| x \|_\beta \le c_2 \| x \|_\alpha, \quad \forall x \in \mathbf{C}^n. \qquad \text{(B.9)}$$

In particular, $\forall x \in \mathbf{C}^n$:

$$\| x \|_2 \le \| x \|_1 \le \sqrt{n} \| x \|_2 \qquad \text{(B.10)}$$

$$\| x \|_\infty \le \| x \|_2 \le \sqrt{n} \| x \|_\infty \qquad \text{(B.11)}$$

$$\| x \|_\infty \le \| x \|_1 \le n \| x \|_\infty \qquad \text{(B.12)}$$

Now let us consider the space $\mathbf{H} = \mathbf{C}^{mxn}$, namely the space of m x n complex metrices. $\mathbf{C}^{mxn}$ is also a linear space. Matrix p-norms on $\mathbf{C}^{mxn}$ are defined in terms of the p-norms for vectors on $\mathbf{C}^n$:

$$\|A\|_p = \sup_{x \in C^n, x \neq 0} \frac{\|Ax\|_p}{\|x\|_p}, \qquad \forall A \in \mathbf{C}^{mxn}, \qquad \text{(B.13)}$$

Notice that the matrix p-norms are *induced norms*. They are induced by the corresponding p-norms on vectors. One can think of $\| A \|_p$ as the maximum *gain* of the matrix A measured by the p-norm ratio of vectors before and after multiplication

by A. In general matrix p-norms are difficult to compute. However, for p=1,2, or ∞ there exist simple algorithms to compute $\| A \|_p$ exactly. If $A = [a_{ij}] \in \mathbf{C}^{mxn}$ we have

$$\|A\|_1 = \max_j \sum_{i=1}^{m} |a_{ij}|, \qquad \text{maximum column sum} \qquad \text{(B.14)}$$

$$\|A\|_2 = \bar{\sigma}(A), \qquad \text{maximum singular value} \qquad \text{(B.15)}$$

$$\|A\|_\infty = \max_i \sum_{j=1}^{n} |a_{ij}|, \qquad \text{maximum row sum} \qquad \text{(B.16)}$$

A fourth norm which is important in modern control theory is the F-norm. It is given simply as the root sum of squares of the magnitude of all the matrix elements:

$$\|A\|_F = \sqrt{\sum_{i=1}^{m} \sum_{j=1}^{n} |a_{ij}|^2}, \qquad \forall A \in \mathbf{C}^{mxn} \qquad \text{(B.17)}$$

Notice that the F-norm is not an induced norm.

The F- and p-norms on $\mathbf{C}^{mxn}$ are also equivalent norms. Thus there are upper and lower bounds on the ratio between any two different norms applied to the same matrix. If one type of norm for a given matrix tends towards zero or infinity, so do all other norms. Let $A = [a_{ij}] \in \mathbf{C}^{mxn}$. Then

$$\| A \|_2 \leq \| A \|_F \leq \sqrt{n} \| A \|_2 \qquad \text{(B.18)}$$

$$\max_{i,j} |a_{ij}| \leq \| A \|_2 \leq \sqrt{mn} \max_{i,j} |a_{ij}| \qquad \text{(B.19)}$$

$$\| A \|_2 \leq \sqrt{\| A \|_1 \| A \|_\infty} \qquad \text{(B.20)}$$

$$\sqrt{\tfrac{1}{n}} \| A \|_\infty \leq \| A \|_2 \leq \sqrt{m} \| A \|_\infty \qquad \text{(B.21)}$$

$$\sqrt{\tfrac{1}{n}} \| A \|_1 \leq \| A \|_2 \leq \sqrt{n} \| A \|_1 \qquad \text{(B.22)}$$

The matrix 2-norm and F-norm are invariant under multiplication by unitary or orthogonal matrices. Assume that $Q^*Q = I$ and $Z^*Z = I$ for $Q \in \mathbf{C}^{m \times n}$ and $\mathbf{Z} \in \mathbf{C}^{m \times n}$. Then

$$||QAZ||_F = ||A||_F \tag{B.23}$$

$$||QAZ||_2 = ||A||_2 \tag{B.24}$$

This property is crucial to many proofs in robust control theory.

APPENDIX C

If $\Delta = \{\delta I : \delta \in \mathbf{C}\}$ ($S = 1, F = 0, r_1 = n$), then $\mu_\Delta(M) = \rho(M)$, the spectral radius of M.

Proof: The only Δ's in Δwhich satisfy the $\det(I - M\Delta) = 0$ constraint are reciprocals of nonzero eigenvalues of M. The smallest one of these is associated with the largest (magnitude) eigenvalue, so, $\mu_\Delta(M) = \rho(M)$.

If $\Delta = \mathbf{C}^{n \times n}$ ($S = 0, F = 1, m_1 = n$), then $\mu_\Delta(M) = \bar{\sigma}(M)$

Proof: If $\bar{\sigma}(M) < \frac{1}{\bar{\sigma}(M)}$, then $\bar{\sigma}(M\Delta) < 1$, so $I - M\Delta$ is nonsingular. Applying Definition (5.2) implies $\mu_\Delta(M) \leq \bar{\sigma}(M)$. On the other hand, let u and v be unit vectors satisfying $Mv = \bar{\sigma}(M)u$, and define $\Delta := \frac{1}{\bar{\sigma}(M)} vu^*$. Then $\bar{\sigma}(\Delta) = \frac{1}{\bar{\sigma}(M)}$ and $I - M\Delta$ is obviously singular. Hence, $\mu_\Delta(M) \geq \bar{\sigma}(M)$.

APPENDIX D

$$\mathbf{Q} = \{Q \in \Delta: Q^*Q = I_n\} \tag{D.1}$$

$$\mathbf{D} = \left\{ \begin{matrix} diag[D_1,...,D_s, d_1 I_{m_1},...,d_{F-1} I_{m_{F-1}}, I_{m_F}] : \\ D_i \in C^{n_i \times n_i}, D_i = D_i^* > 0, d_j \in R, d_j > 0 \end{matrix} \right\} \tag{D.2}$$

Note that for any $\Delta \in \mathbf{\Delta}$, $Q \in \mathbf{Q}$, $D \in \mathbf{D}$,

1. $Q^* \in \mathbf{Q}$
2. $Q\Delta \in \mathbf{\Delta}$
3. $\Delta Q \in \mathbf{\Delta}$
4. $\overline{\sigma}(Q\Delta) = \overline{\sigma}(\Delta Q) = \overline{\sigma}(\Delta)$
5. $D\Delta = \Delta D$

Consequently,

Theorem D.1

For all $Q \in \mathbf{Q}$ and $D \in \mathbf{D}$

$$\mu_\Delta(MQ) = \mu_\Delta(QM) = \mu_\Delta(M) = \mu_\Delta(DMD^{-1})$$

Proof: For all $D \in \mathbf{D}$ and $\Delta \in \mathbf{\Delta}$,

$$\det(I - M\Delta) = \det(I - MD^{-1}\Delta D) = \det(I - DMD^{-1}\Delta)$$

since D commutes with Δ. Therefore $\mu_\Delta(M) = \mu_\Delta(DMD^{-1})$. Also, for each $Q \in \mathbf{Q}$, $\det(I - M\Delta) = 0 \Leftrightarrow \det(I - MQQ^*\Delta) = 0$. Since $Q^*\Delta \in \mathbf{\Delta}$ and $\overline{\sigma}(Q^*\Delta) = \overline{\sigma}(\Delta)$, we get $\mu_\Delta(MQ) = \mu_\Delta(M)$ as desired. The argument for QM is the same.

APPENDIX E

Direct programming method

Consider a system defined by:

$$y^n + a_1 y^{n-1} + \ldots + a_{n-1}\dot{y} + a_n y = b_o u^n + b_1 u^{n-1} + \ldots + b_{n-1}\dot{u} + b_n u$$

where u is the input and y is the output. This equation can also be written as:

$$\frac{Y(s)}{U(s)} = \frac{b_o s^n + b_1 s^{n-1} + \ldots + b_{n-1}s + b_n}{s^n + a_1 s^{n-1} + \ldots + a_{n-1}s + a_n} \tag{E.1}$$

Equation (E.1) can be written as:

$$\frac{Y(s)}{U(s)} = b_o + \frac{(b_1 - a_1 b_o)s^{n-1} + \ldots + (b_{n-1} - a_{n-1}b_0)s + (b_n - a_n b_o)}{s^n + a_1 s^{n-1} + \ldots + a_{n-1}s + a_n}$$

which can be modified to:

$$Y(s) = b_o U(s) + \dot{Y}(s) \tag{E.2}$$

where

$$\hat{Y}(s) = \frac{(b_1 - a_1 b_o)s^{n-1} + \ldots + (b_{n-1} - a_{n-1}b_0)s + (b_n - a_n b_o)}{s^n + a_1 s^{n-1} + \ldots + a_{n-1}s + a_n} U(s)$$

Let us rewrite this last equation in the following form:

$$\frac{\hat{Y}(s)}{(b_1 - a_1 b_o)s^{n-1} + \ldots + (b_{n-1} - a_{n-1}b_0)s + (b_n - a_n b_o)}$$

$$= \frac{U(s)}{s^n + a_1 s^{n-1} + \ldots + a_{n-1}s + a_n} = Q(s)$$

From this last equation, the following two equations may be obtained:

$$s^n Q(s) = -a_1 s^{n-1} Q(s) - \ldots - a_{n-1} s Q(s) - a_n Q(s) + U(s) \tag{E.3}$$

$$\hat{Y}(s) = (b_1 - a_1 b_o)s^{n-1} Q(s) + \ldots + (b_{n-1} - a_{n-1}b_0)sQ(s)$$

$$+ (b_n - a_n b_o)Q(s) \tag{E.4}$$

Now define state variables as follows:

$$X_1(s)=Q(s)$$

$$X_2(s)=sQ(s)$$

$$\vdots$$

$$\vdots$$

$$X_{n-1}(s)=s^{n-2}Q(s)$$

$$X_n(s)=s^{n-1}Q(s)$$

Then, clearly

$$sX_1(s)=X_2(s)$$

$$sX_2(s)=X_3(s)$$

$$\vdots$$

$$\vdots$$

$$sX_{n-1}(s)=X_n(s)$$

which may be rewritten as:

$$\dot{x}_1 = x_2$$

$$\dot{x}_2 = x_3$$

$$\vdots$$

$$\vdots$$

$$\dot{x}_{n-1} = x_n$$

Noting that $s^nQ(s) = sX_n(s)$, Equation (E.3) can be rewritten as:

$$sX_n(s) = -a_1X_n - \ldots -a_{n-1}X_2(s) - a_nX_1(s) + U(s)$$

or

$$\dot{x}_n = -a_n x_1 - a_{n-1} x_2 - \ldots - a_1 x_n + u$$

Also, from Equation (E.2) and (E.4) we obtain:

$$\hat{Y}(s) = b_o U(s) + (b_1 - a_1 b_o) s^{n-1} Q(s) + \ldots + (b_{n-1} - a_{n-1} b_0) s Q(s)$$

$$+ (b_n - a_n b_o) Q(s)$$

$$\hat{Y}(s) = b_o U(s) + (b_1 - a_1 b_o) X_n(s) + \ldots + (b_{n-1} - a_{n-1} b_0) X_2(s)$$

$$+ (b_n - a_n b_o) X_1(s)$$

The inverse Laplace transform of this output equation becomes:

$$y = (b_n - a_n b_o) x_1 + (b_{n-1} - a_{n-1} b_0) x_2 + \ldots + (b_1 - a_1 b_o) x_n + b_o u$$

Then the state equation and output equation can be given by:

$$\begin{bmatrix} \dot{x}_1 \\ \dot{x}_2 \\ \vdots \\ \dot{x}_{n-1} \\ \dot{x}_n \end{bmatrix} = \begin{bmatrix} 0 & 1 & 0 & \cdots & 0 \\ 0 & 0 & 1 & \cdots & 0 \\ \vdots & \vdots & \vdots & \ddots & \vdots \\ 0 & 0 & 0 & \cdots & 1 \\ -a_n & -a_{n-1} & -a_{n-2} & \cdots & -a_1 \end{bmatrix} \begin{bmatrix} x_1 \\ x_2 \\ \vdots \\ x_{n-1} \\ x_n \end{bmatrix} + \begin{bmatrix} 0 \\ 0 \\ \vdots \\ 0 \\ 1 \end{bmatrix} u \qquad \text{(E.5)}$$

$$y = [b_n - a_n b_o \mid b_{n-1} - a_{n-1} b_o \mid \cdots \mid b_1 - a_1 b_o] \begin{bmatrix} x_1 \\ x_2 \\ \vdots \\ x_3 \end{bmatrix} + b_o u \qquad \text{(E.6)}$$

APPENDIX F

Lemma 5.4

For the perturbed system with transfer function of $G_r(s) = \sum_{i=0}^{n} \frac{b_i s^{n-i}}{a_i s^{n-i}}$, $a_0 = 1$, *a perturbation model is defined, for each uncertain parameter in* $G_r(s)$, *with the following transfer function matrix:*

$$z_i = \Theta_{z_i w_i}{}^{i}(s) w_i + \Theta_{z_i u_i}{}^{i}(s) u$$
$$y = \Theta_{y_i w_i}{}^{i}(s) w_i + \Theta_{y_i u_i}{}^{i}(s) u \quad , w_i = \delta_i z_i$$

where the superscript i represents the ith uncertain parameter in $G_r(s)$ and $\Theta m_i n_i$ represents the transfer function between m_i *and* n_i.

The perturbation model of $G_r(s)$ is

$$\begin{bmatrix} z_1 \\ \vdots \\ \vdots \\ z_p \end{bmatrix} = \begin{bmatrix} \Theta_{z_1 w_1}{}^{1} & \cdots & \cdots & \Theta_{z_1 w_1}{}^{1} \\ \vdots & \ddots & & \vdots \\ \vdots & & \ddots & \vdots \\ \Theta_{z_p w_p}{}^{p} & \cdots & \cdots & \Theta_{z_p w_p}{}^{p} \end{bmatrix} \begin{bmatrix} w_1 \\ \vdots \\ \vdots \\ w_p \end{bmatrix} + \begin{bmatrix} \Theta_{z_1 u_1}{}^{1} \\ \vdots \\ \vdots \\ \Theta_{z_p u_p}{}^{p} \end{bmatrix} u$$

$$y = \begin{bmatrix} \Theta_{y_1 w_1}{}^{1} & \cdots & \cdots & \Theta_{y_p u_p}{}^{p} \end{bmatrix} \begin{bmatrix} w_1 \\ \vdots \\ \vdots \\ w_p \end{bmatrix} + Gu$$

if the following conditions are fulfilled:

1. $\Theta_{y_1 u_1} = \Theta_{y_2 u_2} = \cdots\cdots = \Theta_{y_p u_p} = G(s)$

2. $\Theta_{y_1 w_1} = \Theta_{y_2 w_2} = \cdots\cdots = \Theta_{y_p w_p} = C(s)$, where $C(s)$ is an abitary transfer function

Proof:

Consider a system with perturbation in system parameters both in denomination and numerator of the transfer function,

$$G_r(s)=\frac{b_0 s^m+\ldots+b_{m-1}\{1+\rho_{n(m-1)}\delta_{n(m-1)}\}s+b_m\{1+\rho_{nm}\delta_{nm}\}}{s^n+\cdots+a_{n-1}\{1-\rho_{d(n-1)}\delta_{d(n-1)}\}s+a_n\{1-\rho_{dn}\delta_{dn}\}},\ \mathrm{m}\le\mathrm{n}$$

$$\Delta_G=G_r-G$$

$$=\frac{b_0 s^m+\ldots+b_{m-1}\{1+\rho_{n(m-1)}\delta_{n(m-1)}\}s+b_m\{1+\rho_{nm}\delta_{nm}\}}{s^n+\cdots+a_{n-1}\{1-\rho_{d(n-1)}\delta_{d(n-1)}\}s+a_n\{1-\rho_{dn}\delta_{dn}\}}-\frac{b_0 s^m+\ldots+b_{m-1}s+b_m}{s^n+\cdots+a_{n-1}s+a_n}$$

$$=\frac{\{s^n+\cdots+a_{n-1}s+a_n\}\{b_0 s^m+\ldots+b_{m-1}\{1+\rho_{n(m-1)}\delta_{n(m-1)}\}s+b_m\{1+\rho_{nm}\delta_{nm}\}\}}{\{s^n+\cdots+a_{n-1}\{1-\rho_{d(n-1)}\delta_{d(n-1)}\}s+a_n\{1-\rho_{dn}\delta_{dn}\}\}\{s^n+\cdots+a_{n-1}s+a_n\}}-$$

$$\frac{\{b_0 s^m+\ldots+b_{m-1}s+b_m\}\{s^n+\cdots+a_{n-1}\{1-\rho_{d(n-1)}\delta_{d(n-1)}\}s+a_n\{1-\rho_{dn}\delta_{dn}\}\}}{\{s^n+\cdots+a_{n-1}\{1-\rho_{d(n-1)}\delta_{d(n-1)}\}s+a_n\{1-\rho_{dn}\delta_{dn}\}\}\{s^n+\cdots+a_{n-1}s+a_n\}}$$

$$=$$

$$\frac{\{s^n+\cdots+a_{n-1}s+a_n\}\{b_0 s^m+\cdots+b_{m-1}s+b_m+(\cdots+\rho_{n(m-1)}\delta_{n(m-1)}s+\rho_{nm}\delta_{nm})\}}{\{s^n+\cdots+a_{n-1}s+a_n\}^2-\{\cdots+a_{n-1}\rho_{d(n-1)}\delta_{d(n-1)}s+a_n\rho_{dn}\delta_{dn}\}\{s^n+\cdots+a_{n-1}s+a_n\}}-$$

$$\frac{\{b_0 s^m+\cdots+b_{m-1}s+b_m\}\{s^n+\cdots+a_{n-1}s+a_n-(\cdots+a_{n-1}\rho_{d(n-1)}\delta_{d(n-1)}s+a_n\rho_{dn}\delta_{dn})\}}{\{s^n+\cdots+a_{n-1}s+a_n\}^2-\{\cdots+a_{n-1}\rho_{d(n-1)}\delta_{d(n-1)}s+a_n\rho_{dn}\delta_{dn}\}\{s^n+\cdots+a_{n-1}s+a_n\}}$$

$$=\frac{\{b_0 s^m+\cdots+b_{m-1}s+b_m\}\{s^n+\cdots+a_{n-1}s+a_n\}}{\{s^n+\cdots+a_{n-1}s+a_n\}^2}\ \mathrm{x}$$

$$\frac{\left\{1+\frac{(\cdots+\rho_{n(m-1)}\delta_{n(m-1)}s+\rho_{nm}\delta_{nm})}{\{b_0 s^m+\cdots+b_{m-1}s+b_m\}}\right\}-\left\{1+\frac{\{\cdots+a_{n-1}\rho_{d(n-1)}\delta_{d(n-1)}s+a_n\rho_{dn}\delta_{dn}\}}{\{s^n+\cdots+a_{n-1}s+a_n\}}\right\}}{1-\frac{\{\cdots+a_{n-1}\rho_{d(n-1)}\delta_{d(n-1)}s+a_n\rho_{dn}\delta_{dn}\}}{\{s^n+\cdots+a_{n-1}s+a_n\}}}$$

$$= \frac{\{b_0 s^m + \cdots + b_{m-1}s + b_m\}}{\{s^n + \cdots + a_{n-1}s + a_n\}} \mathrm{x}$$

$$\frac{(\cdots + \rho_{n(m-1)}\delta_{n(m-1)}s + \rho_{nm}\delta_{nm})}{\{b_0 s^m + \cdots + b_{m-1}s + b_m\}} + \frac{\{\cdots + a_{n-1}\rho_{d(n-1)}\delta_{d(n-1)}s + a_n\rho_{dn}\delta_{dn}\}}{\{s^n + \cdots + a_{n-1}s + a_n\}}$$
$$1 - \frac{\{\cdots + a_{n-1}\rho_{d(n-1)}\delta_{d(n-1)}s + a_n\rho_{dn}\delta_{dn}\}}{\{s^n + \cdots + a_{n-1}s + a_n\}}$$

$$= \frac{\{b_0 s^m + \cdots + b_{m-1}s + b_m\}}{\{s^n + \cdots + a_{n-1}s + a_n\}} \mathrm{x}$$

$$\frac{(\cdots + \rho_{n(m-1)}\delta_{n(m-1)}s + \rho_{nm}\delta_{nm})}{1 - \frac{\{\cdots + a_{n-1}\rho_{d(n-1)}\delta_{d(n-1)}s + a_n\rho_{dn}\delta_{dn}\}}{\{s^n + \cdots + a_{n-1}s + a_n\}}} \frac{1}{\{b_0 s^m + \cdots + b_{m-1}s + b_m\}}$$

$$\frac{\{b_0 s^m + \cdots + b_{m-1}s + b_m\}}{\{s^n + \cdots + a_{n-1}s + a_n\}} \mathrm{x}$$

$$\frac{\{\cdots + a_{n-1}\rho_{d(n-1)}\delta_{d(n-1)}s + a_n\rho_{dn}\delta_{dn}\}}{1 - \frac{\{\cdots + a_{n-1}\rho_{d(n-1)}\delta_{d(n-1)}s + a_n\rho_{dn}\delta_{dn}\}}{\{s^n + \cdots + a_{n-1}s + a_n\}}} \frac{1}{\{s^n + \cdots + a_{n-1}s + a_n\}}$$

$$= \Theta_{21}{}^n(s)\Delta^n(s)\{1 - \Theta_{11}{}^n(s)\Delta^n(s)\}^{-1}\Theta_{12}{}^n(s) +$$

$$\Theta_{21}{}^d(s)\Delta^d(s)\{1 - \Theta_{11}{}^d(s)\Delta^d(s)\}^{-1}\Theta_{12}{}^d(s)$$

where the superscribe n, d represents the perturbation in numerator and denominator respectively.

Therefore,

$$\begin{bmatrix} z_1^n \\ \vdots \\ z_m^n \\ z_1^d \\ \vdots \\ z_n^d \end{bmatrix} = \begin{bmatrix} \Theta_{z_1 w_1}{}^n & \cdots & \cdots & \cdots & \cdots & \Theta_{z_1 w_1}{}^n \\ \vdots & \ddots & & & & \vdots \\ \Theta_{z_m w_m}{}^n & & \ddots & & & \Theta_{z_m w_m}{}^n \\ \Theta_{z_1 w_1}{}^d & & & \ddots & & \Theta_{z_1 w_1}{}^d \\ \vdots & & & & \ddots & \vdots \\ \Theta_{z_n w_n}{}^d & \cdots & \cdots & \cdots & \cdots & \Theta_{z_n w_n}{}^d \end{bmatrix} \begin{bmatrix} w_1^n \\ \vdots \\ w_m^n \\ w_1^d \\ \vdots \\ w_n^d \end{bmatrix} + \begin{bmatrix} \Theta_{z_1 u_1}{}^n \\ \\ \Theta_{z_m u_m}{}^n \\ \Theta_{z_1 u_1}{}^d \\ \\ \Theta_{z_n u_n}{}^d \end{bmatrix} u$$

$$y = \begin{bmatrix} \Theta_{y_1 w_1} & \cdots & \cdots & \Theta_{y_{m+n} w_{m+n}} \end{bmatrix} \begin{bmatrix} w_1 \\ \vdots \\ \vdots \\ w_{m+n} \end{bmatrix} + Gu$$

APPENDIX G

The responses of vehicle running on a slated road surface in open loop simulation are shown here. The road bank angle is 0.15 rad.

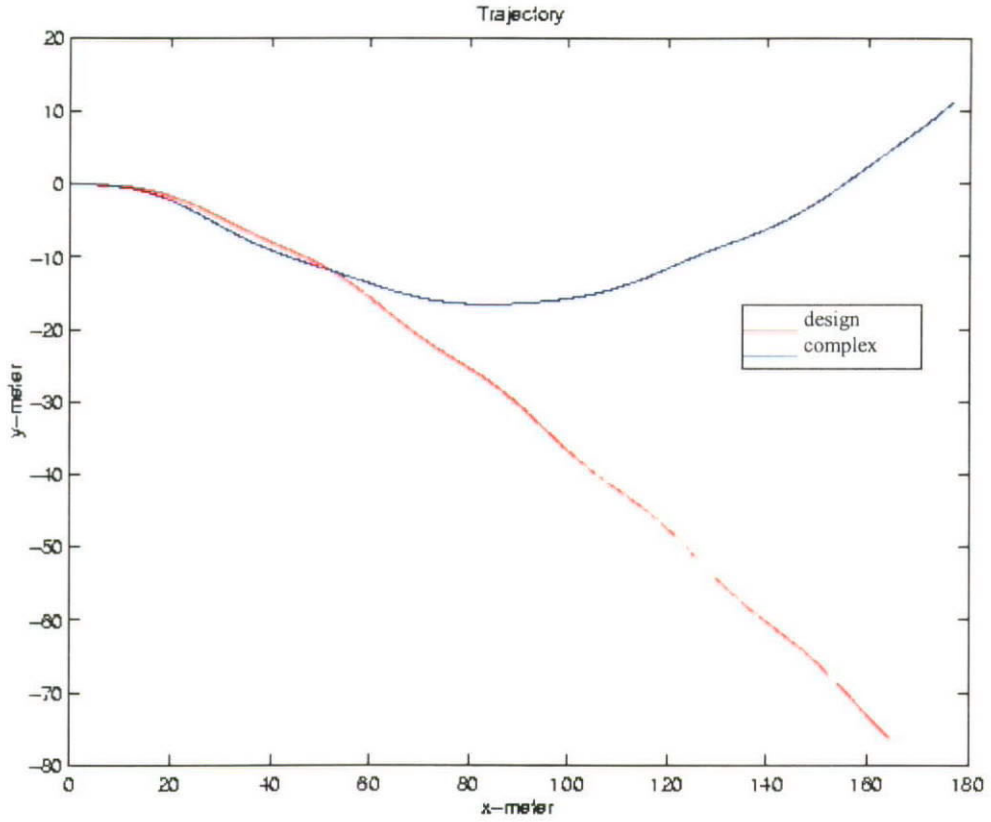

Figure G.1Responses of Vehicle in Open Loop Simulation with Sinsoidal Input

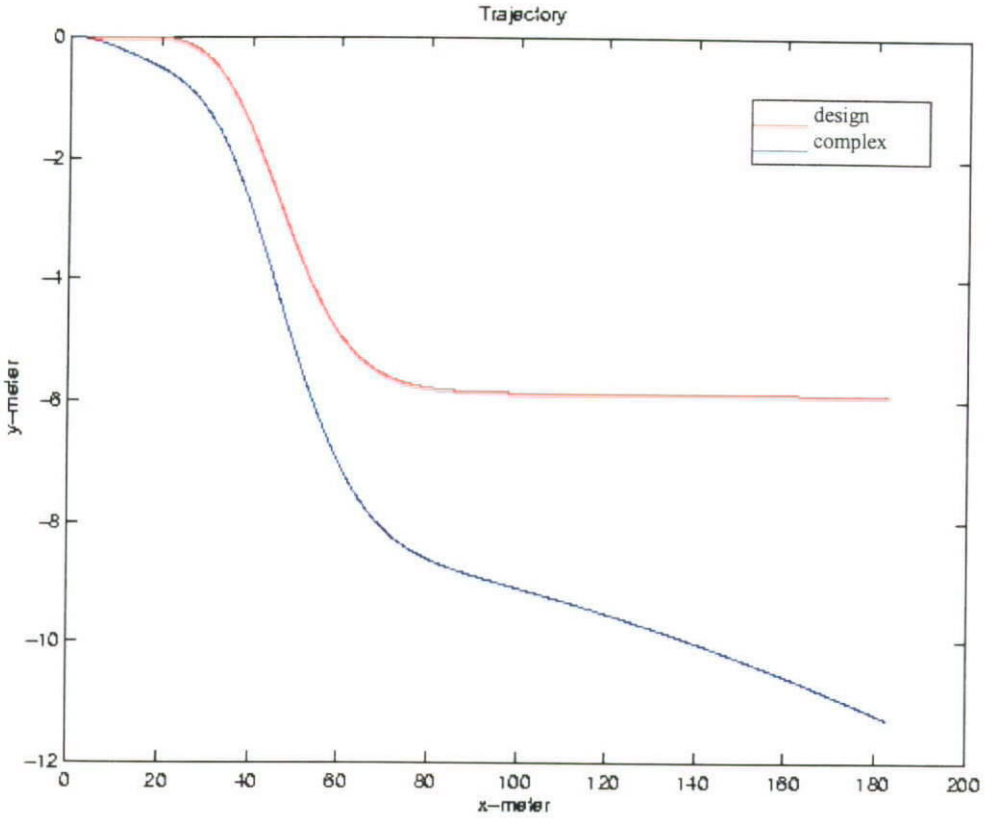

Figure G.2Responses of Vehicle in Open Loop Simulation with Lane Change Reference Input

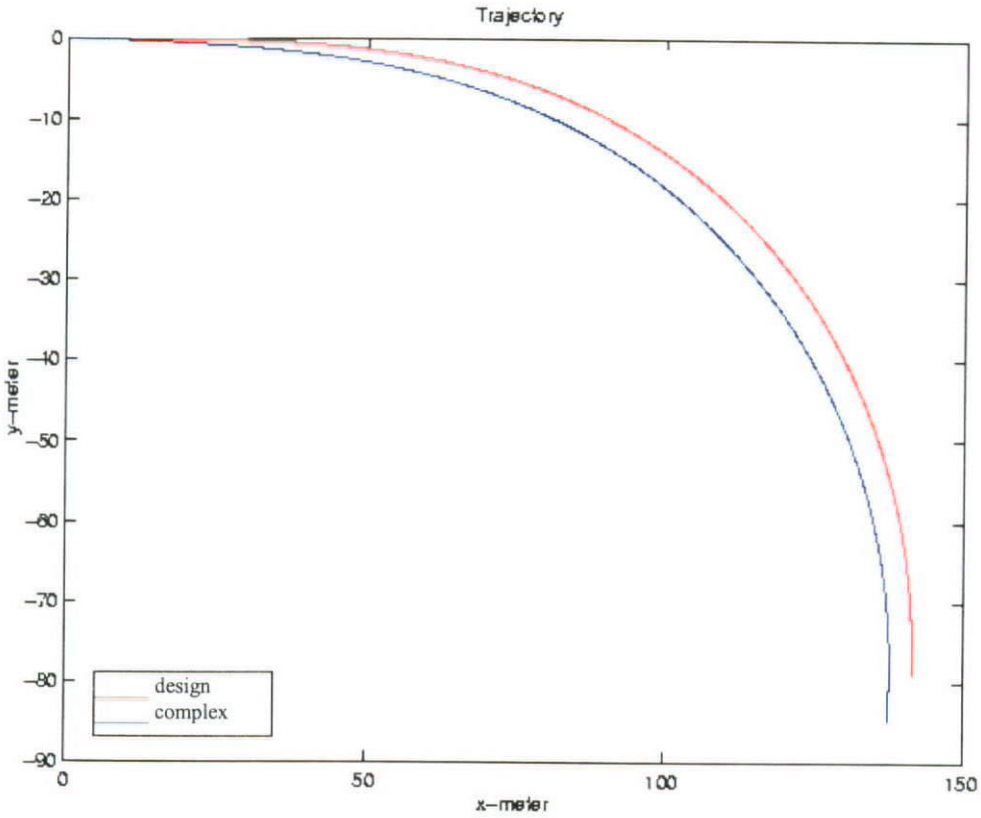

Figure G.3Responses of Vehicle in Open Loop Simulation with Ramp Input

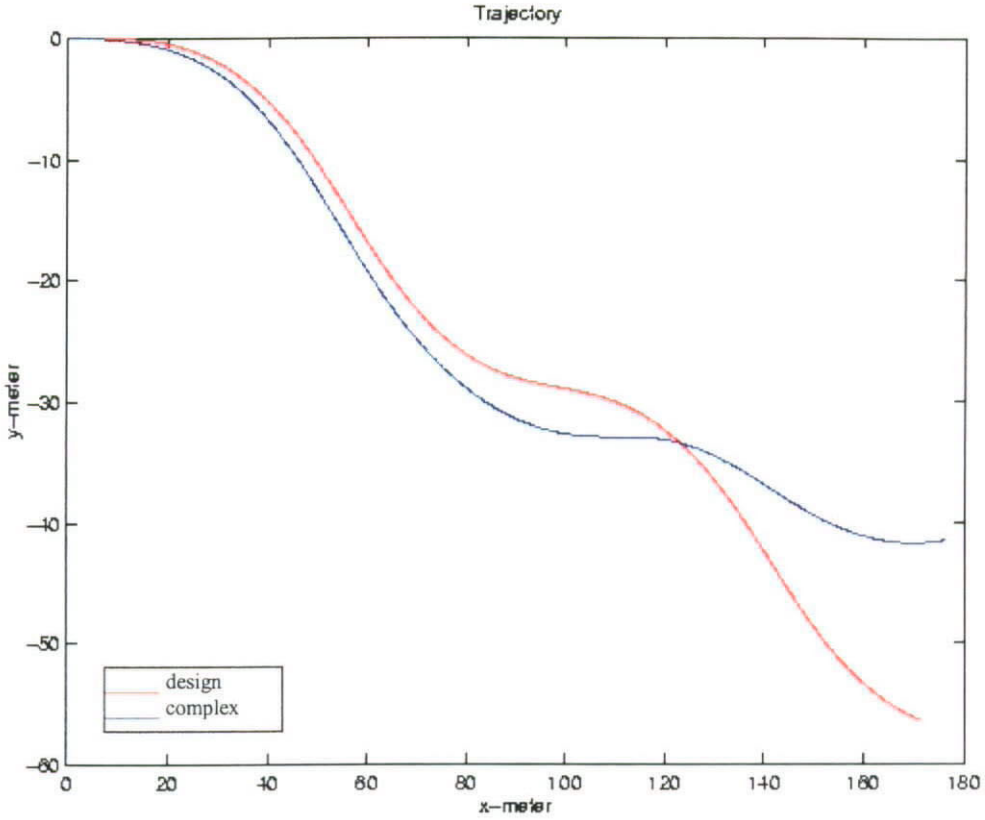

Figure G.4 Responses of Vehicle in Open Loop Simulation with Sinusoidal Input (High Freq.)

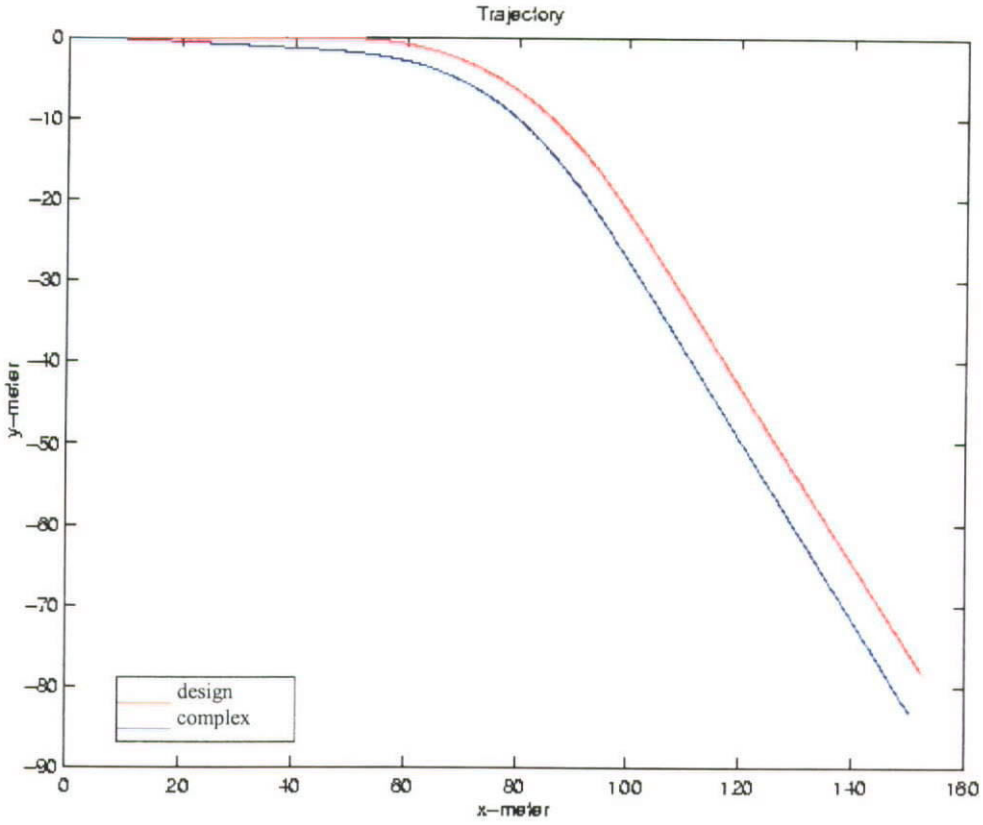

Figure G.5Responses of Vehicle in Open Loop Simulation with trapezoidal Input

PPENDIX H

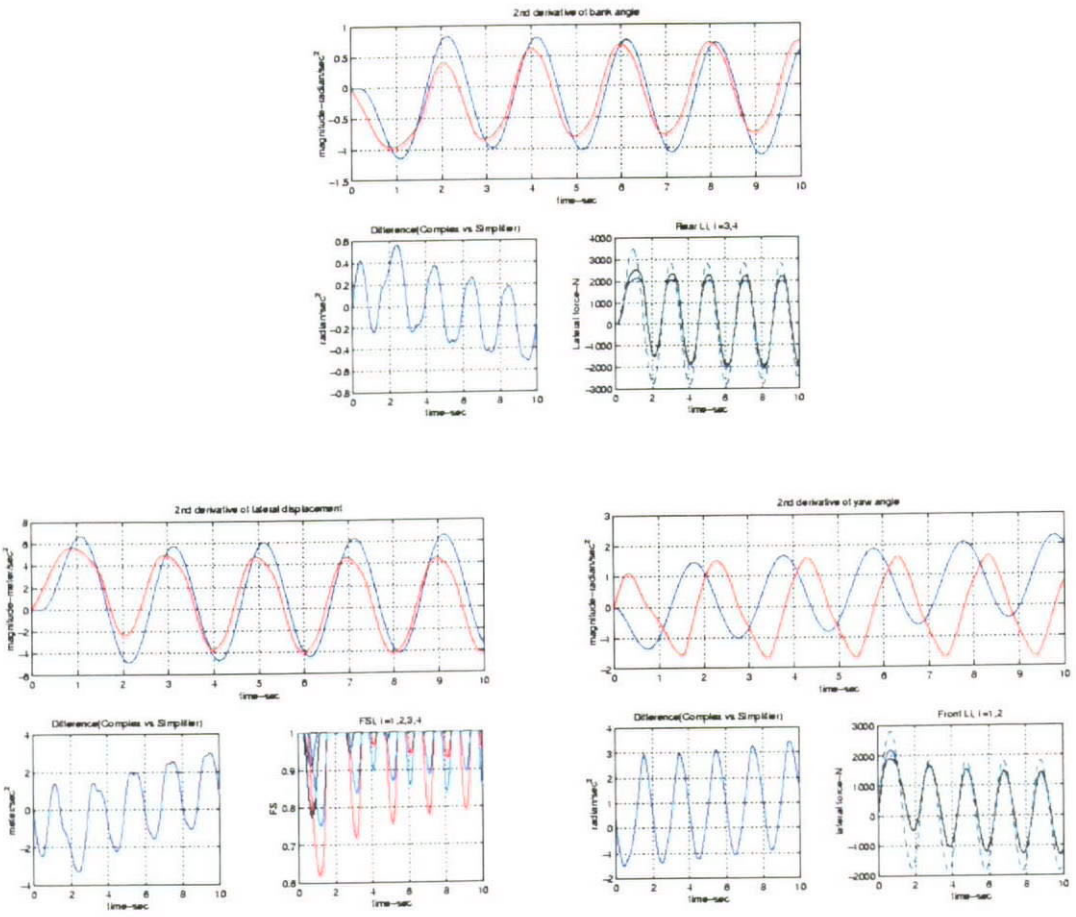

Figure H.1 Comparison of Complex and Design Vehicle Model in Open Loop Simulation with Sinusoidal Input of Steering Angle (0.6rad – 0.5Hz)

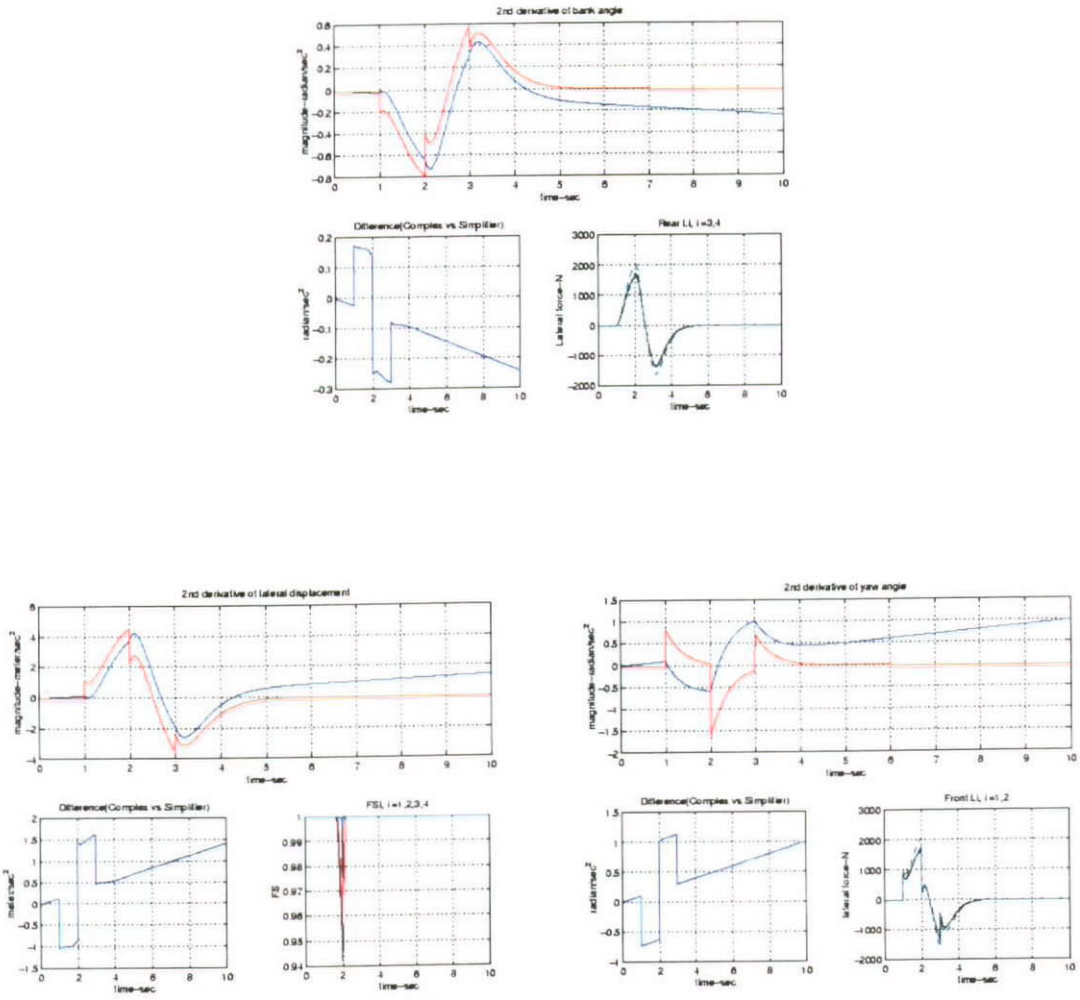

Figure H.2 Comparison of Complex and Design Vehicle Model in Open Loop Simulation with Lane Change Reference Input of Steering Angle

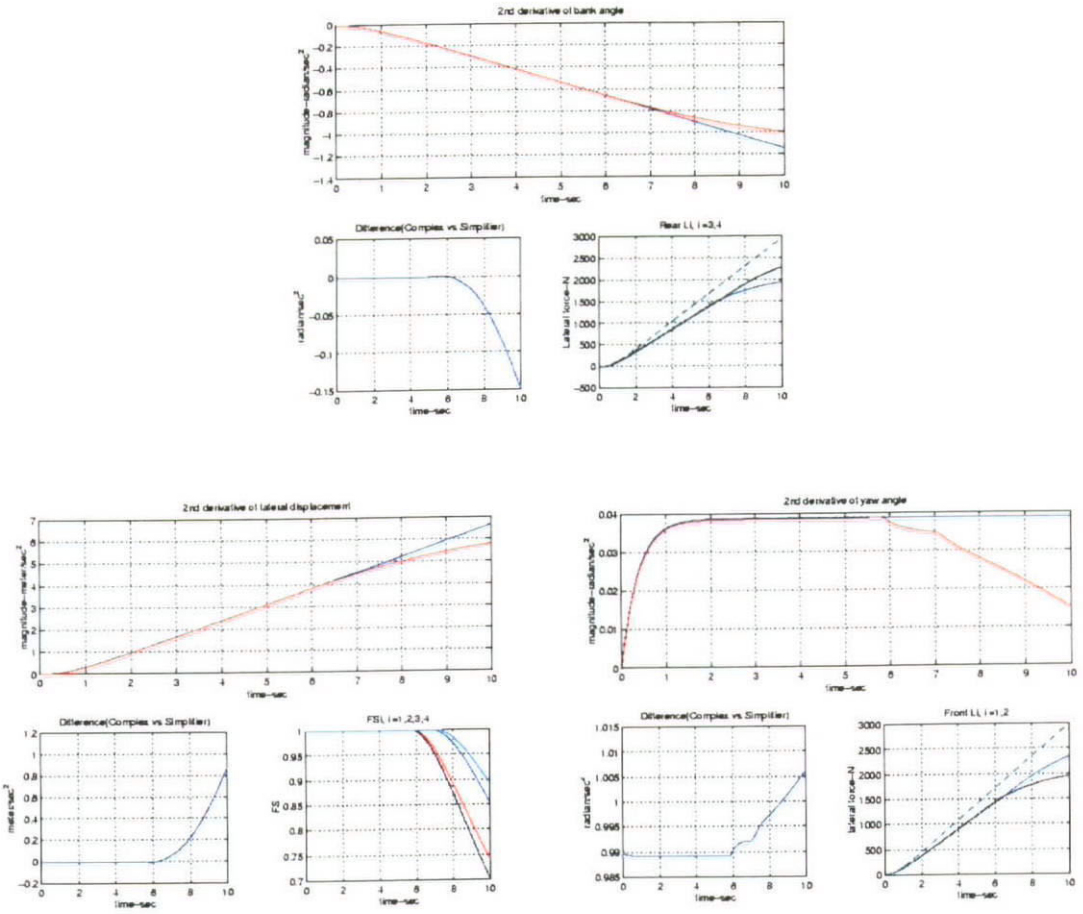

Figure H.3 Comparison of Complex and Design Vehicle Model in Open Loop Simulation with Ramp Input of Steering Angle

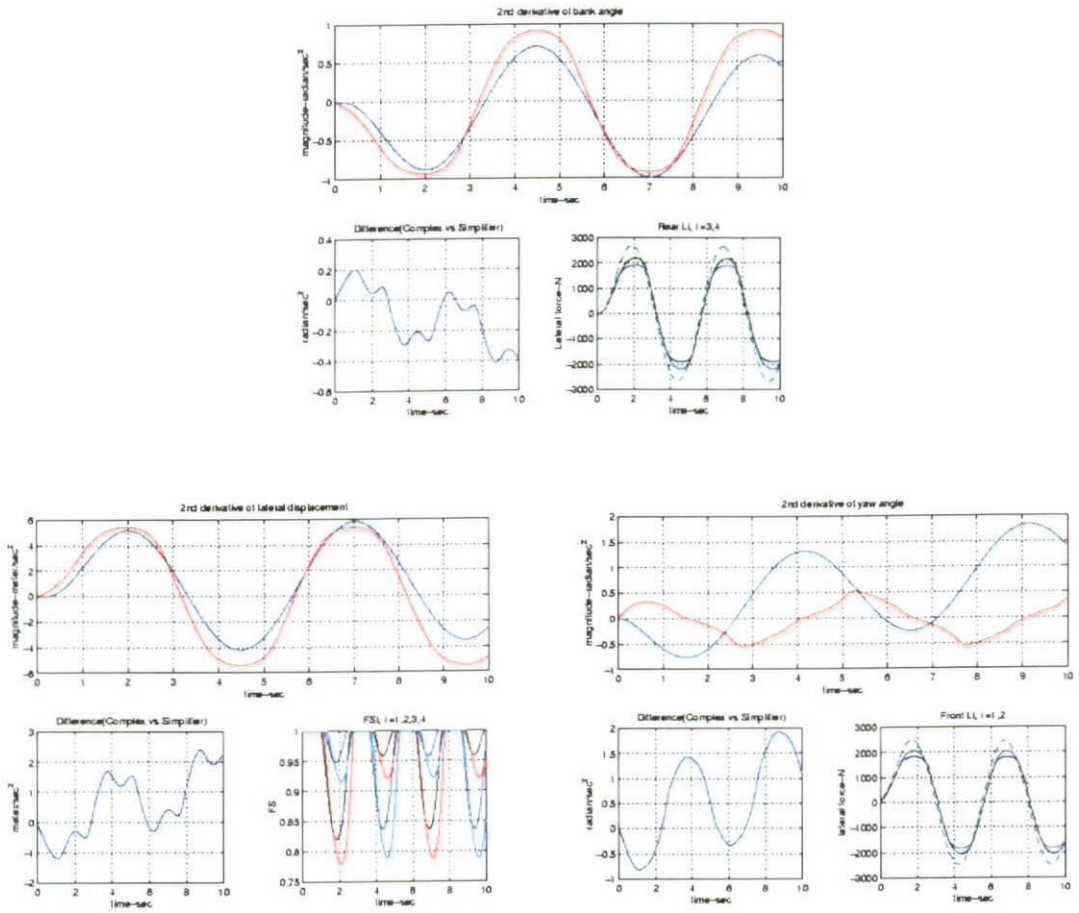

Figure H.4 Comparison of Complex and Design Vehicle Model in Open Loop Simulation with Sinusoidal Input of Steering Angle (0.3rad – 0.2Hz)

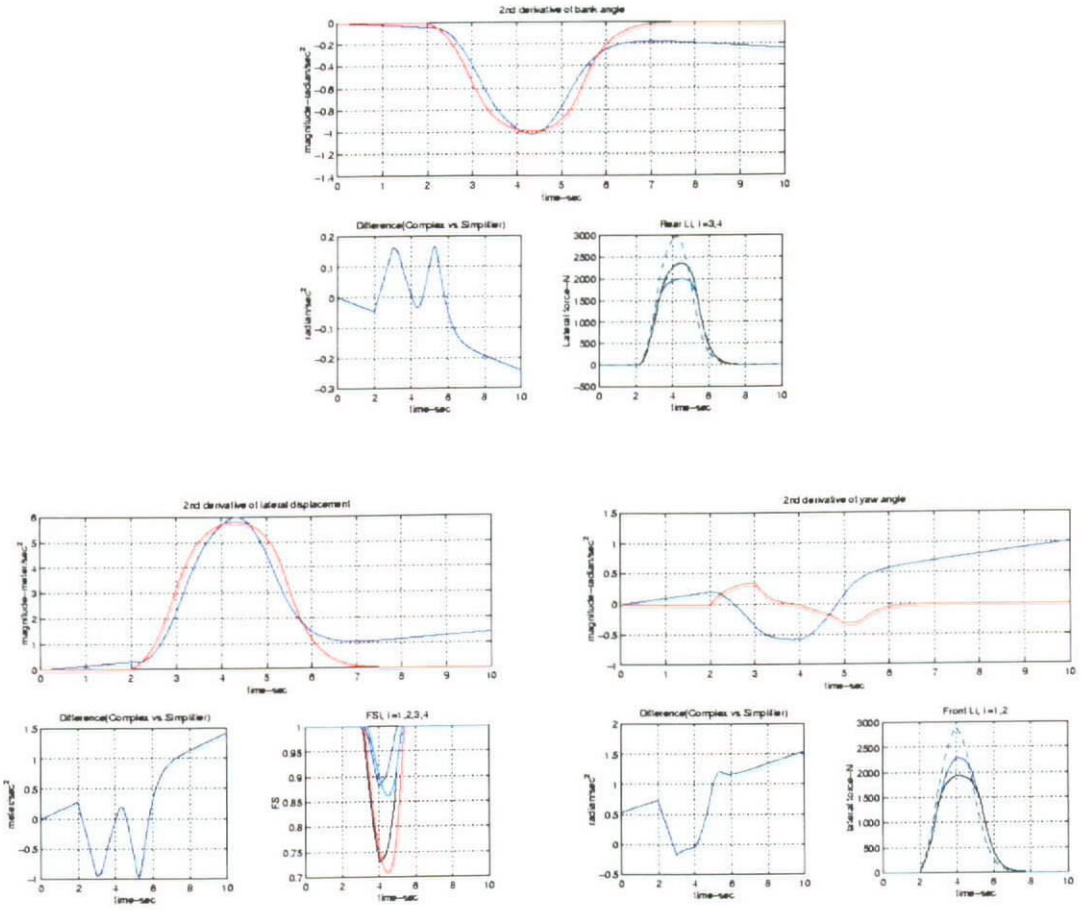

Figure H.5 Comparison of Complex and Design Vehicle Model in Open Loop Simulation with Trapezoidal Input of Steering Angle

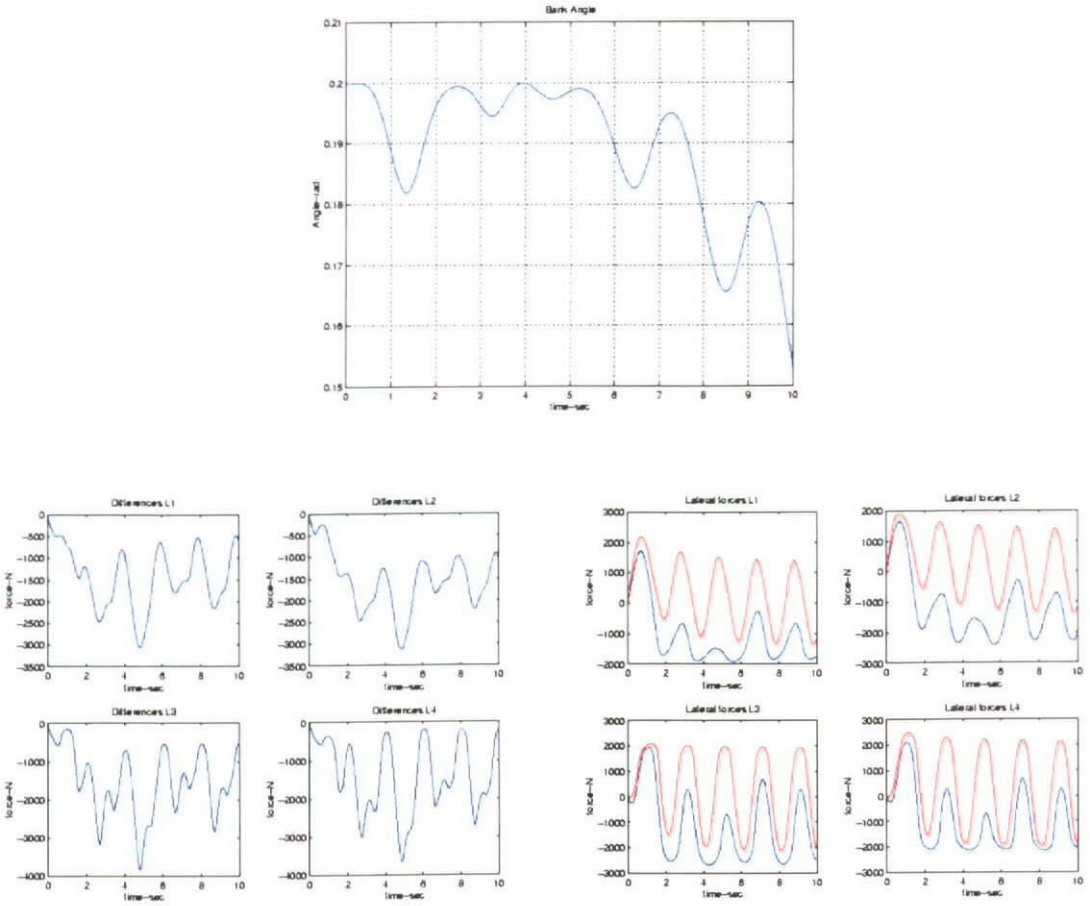

'igure H.6 Distribution of Lateral Forces in Open Loop Simulation with Sinusoidal Input of Steering Angle (0.6rad – 0.5Hz)

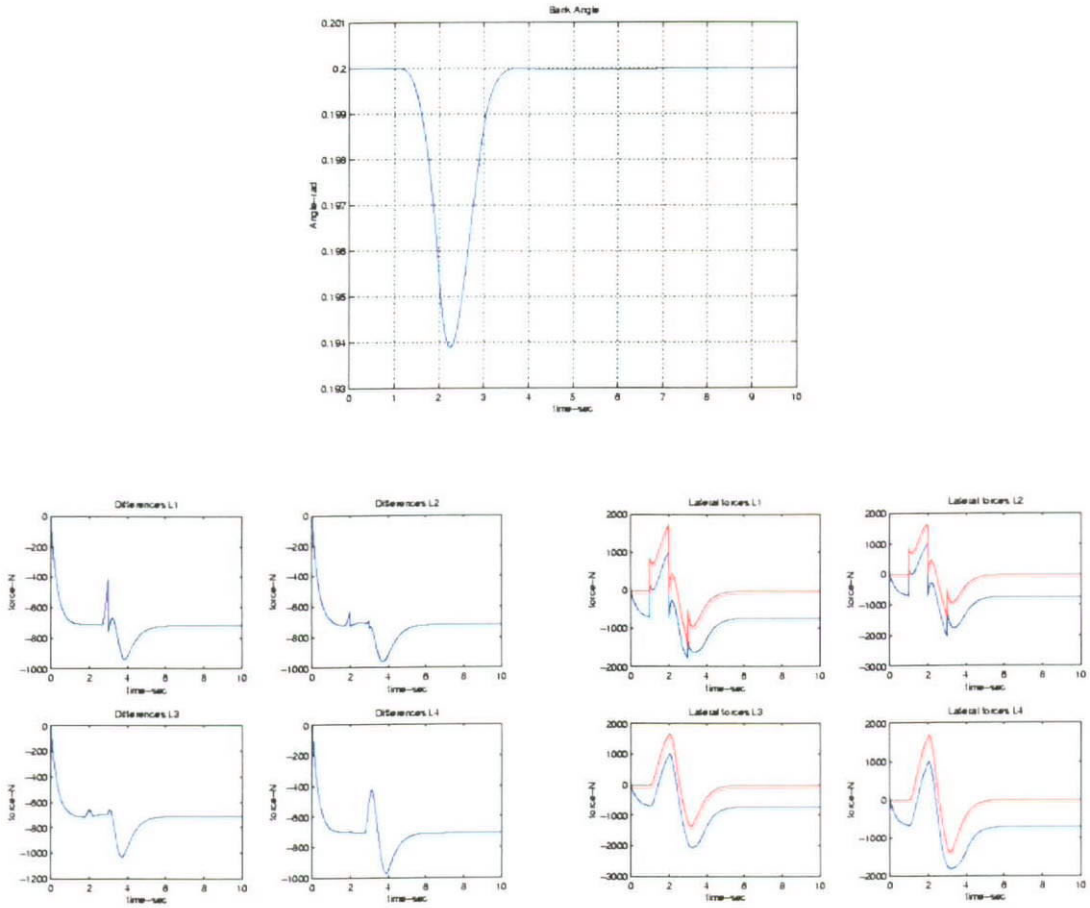

Figure H.7 Distribution of Lateral Forces in Open Loop Simulation with Lane Change Reference Input

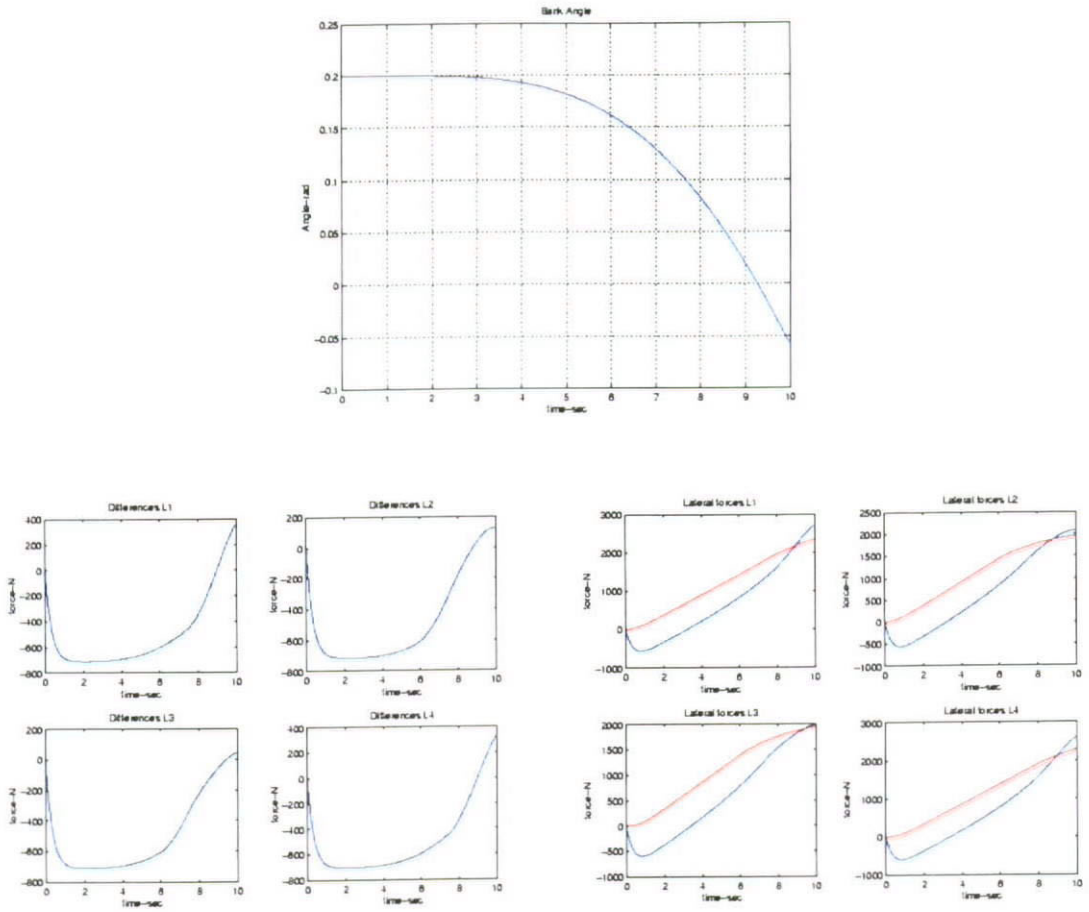

Figure H.8 Distribution of Lateral Forces in Open Loop Simulation with trapezoidal Input of Steering Angle

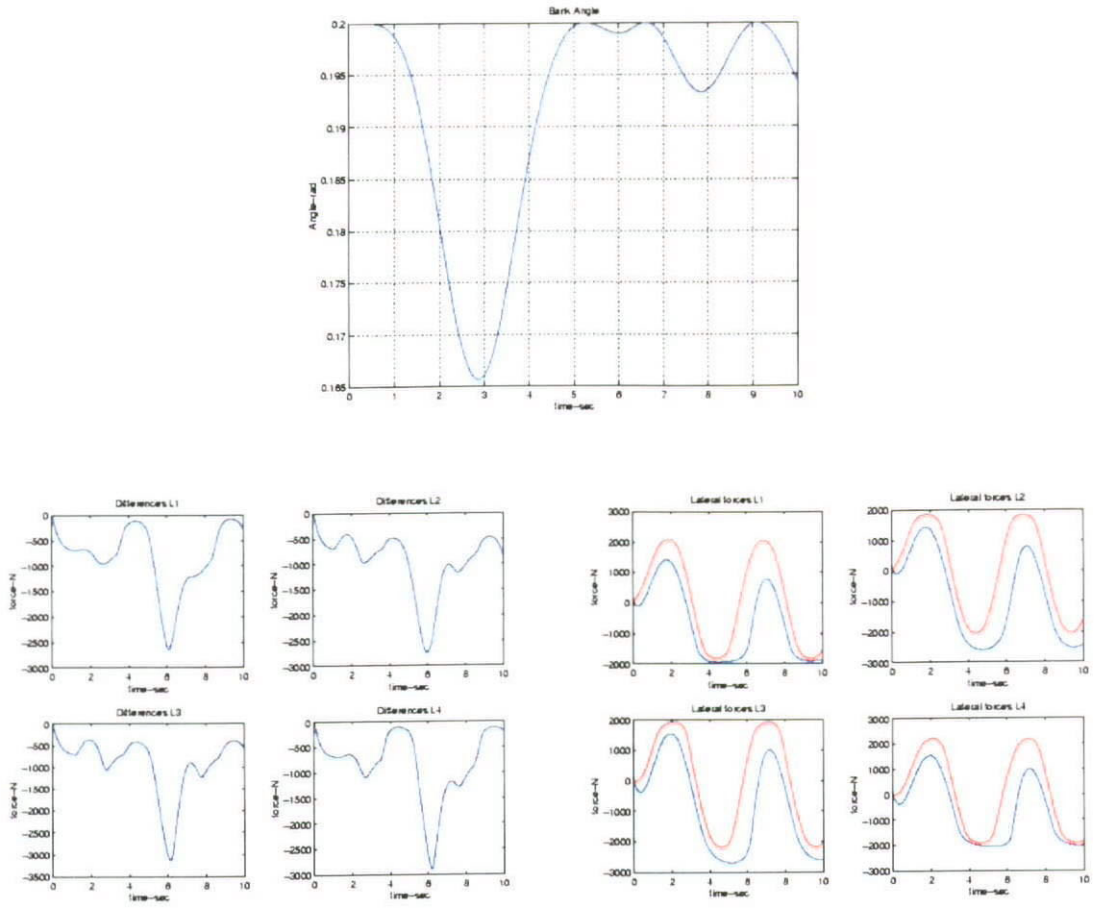

Figure H.9 Distribution of Lateral Forces in Open Loop Simulation with Sinusoidal Input of Steering Angle (0.3rad – 0.2Hz)

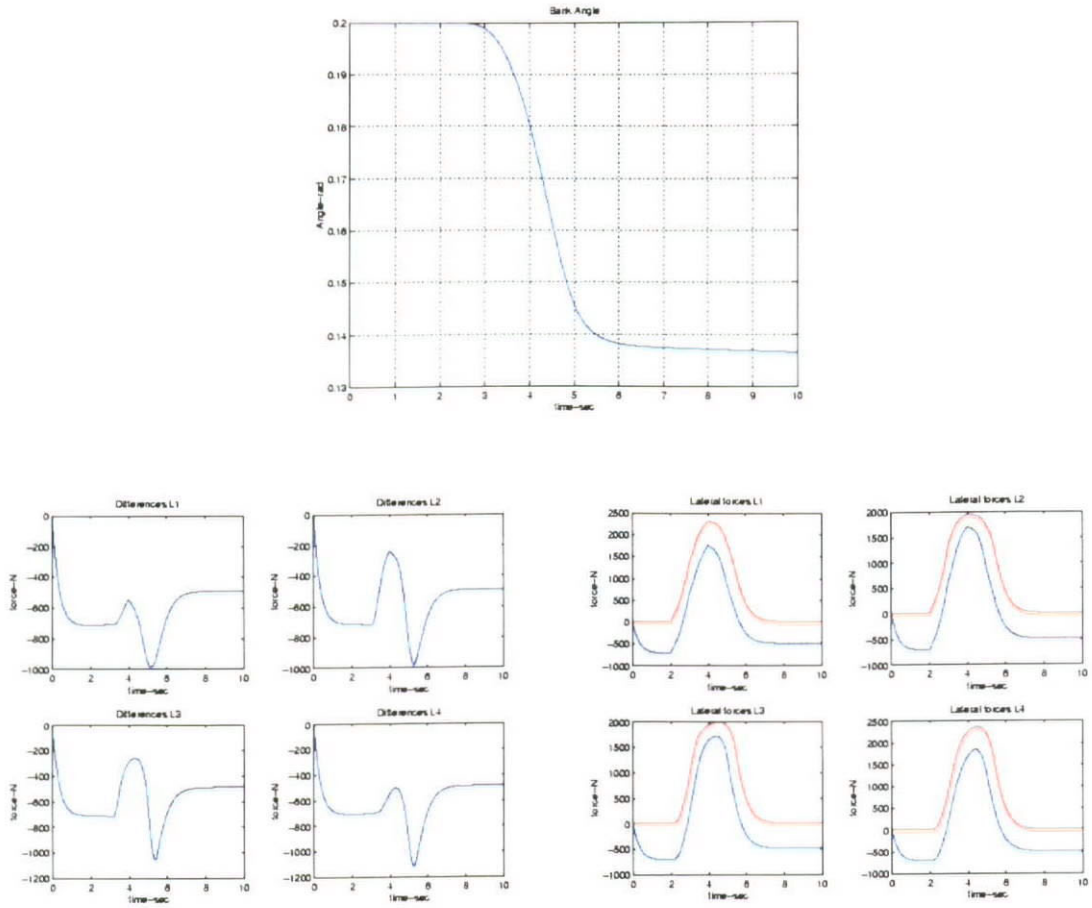

Figure H.10 Distribution of Lateral Forces in Open Loop Simulation with Trapezoidal Input of Steering Angle

APPENDIX I

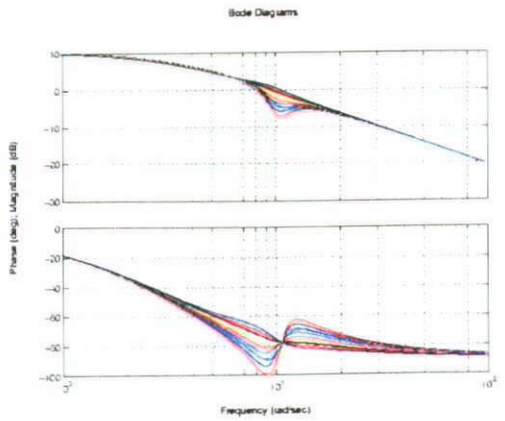

Figure I.1a Vehicle Bank Angle to Lateral Velocity

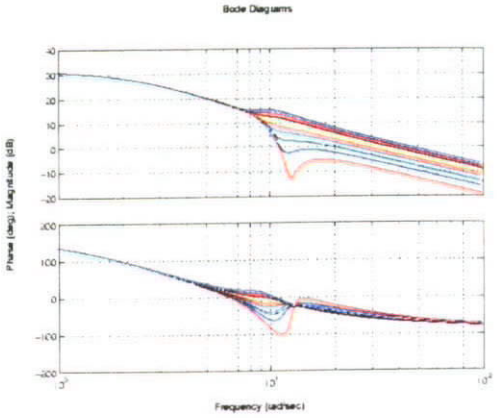

Figure I.1b Steering Angle to Lateral Velocity

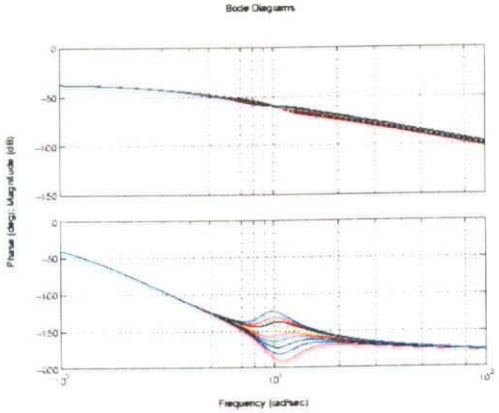

Figure I.1c Vehicle Bank Angle to Yaw Rate

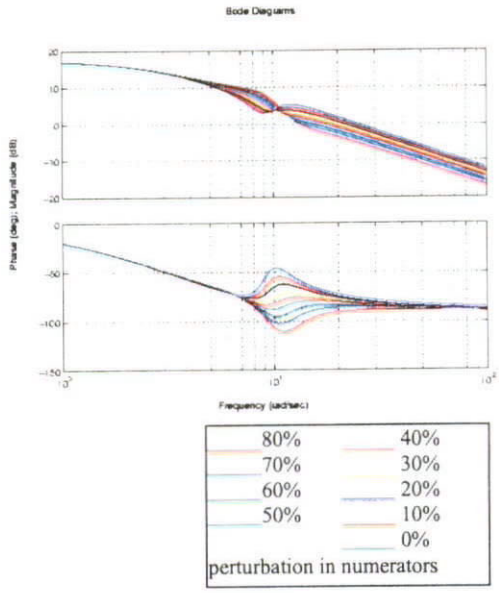

Figure I.1d Steering Angle to Yaw Rate

Figure I.1 Bode Diagrams of the Vehicle System with the Input of Steering Command and Vehicle Bank Angle and Output of Lateral Velocity and Yaw Rate, under Perturbation in System Parameters in Dominator with –10%

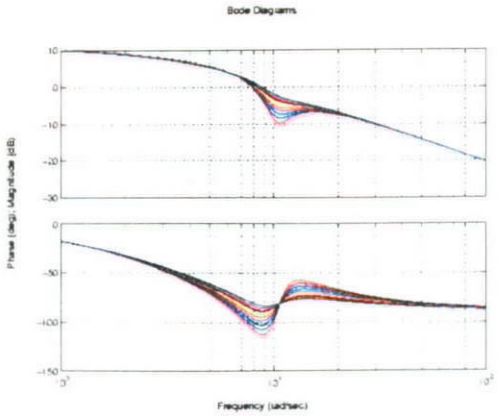

Figure I.2a Vehicle Bank Angle to Lateral Velocity

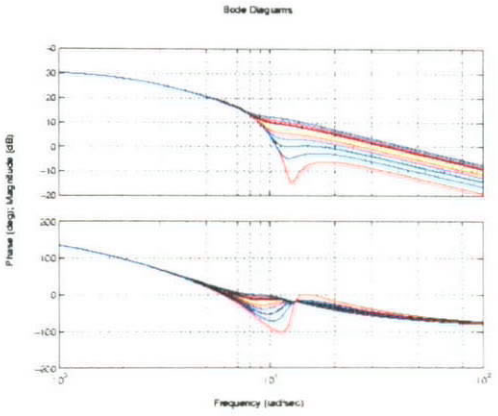

Figure I.2b Steering Angle to Lateral Velocity

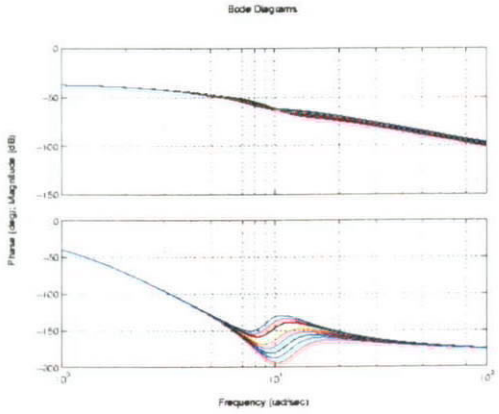

Figure I.2c Vehicle Bank Angle to Yaw Rate

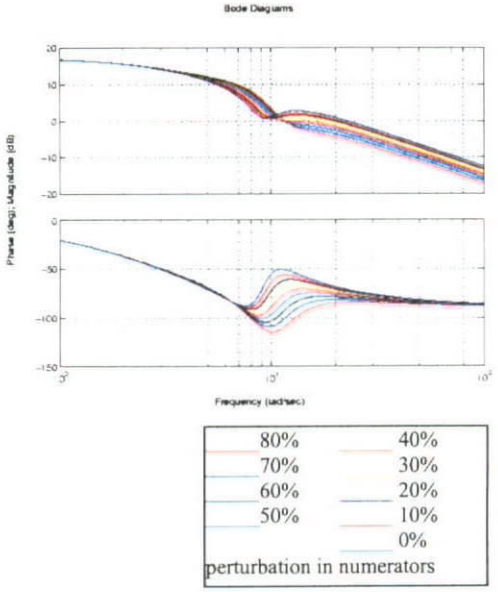

Figure I.2d Steering Angle to Yaw Rate

Figure I.2 Bode Diagrams of the Vehicle System with the Input of Steering Command and Vehicle Bank Angle and Output of Lateral Velocity and Yaw Rate, under Perturbation in System Parameters in Dominator with –30%

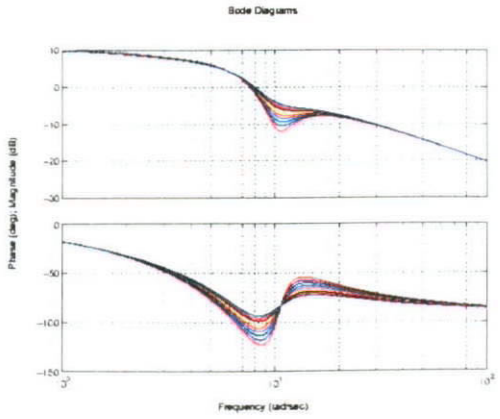

Figure I.3a Vehicle Bank Angle to Lateral Velocity

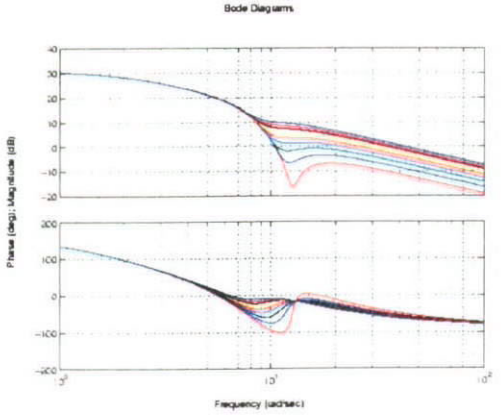

Figure I.3b Steering Angle to Lateral Velocity

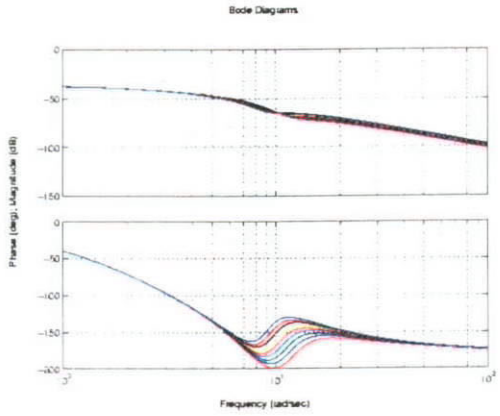

Figure I.3c Vehicle Bank Angle to Yaw Rate

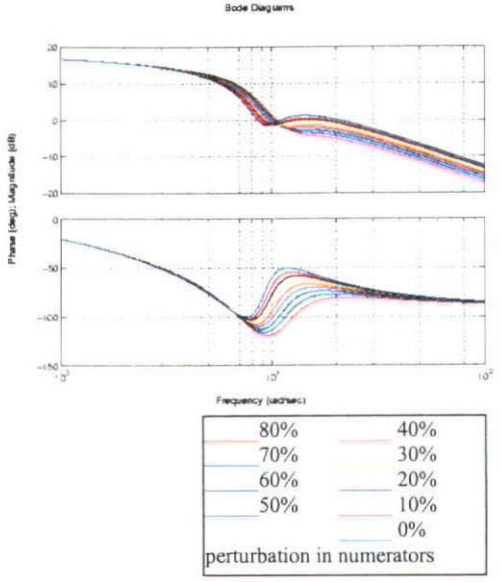

Figure I.3d Steering Angle to Yaw Rate

Figure I.3 Bode Diagrams of the Vehicle System with the Input of Steering Command and Vehicle Bank Angle and Output of Lateral Velocity and Yaw Rate, under Perturbation in System Parameters in Dominator with –50%

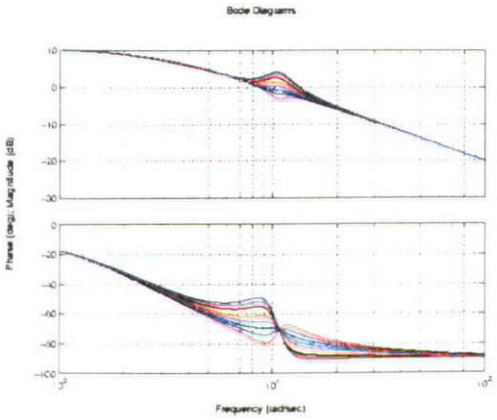

Figure I.4a Vehicle Bank Angle to Lateral Velocity

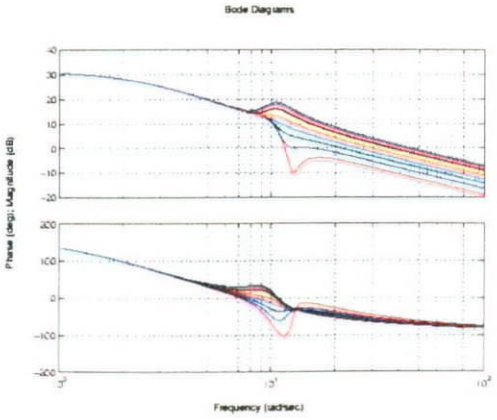

Figure I.4b Steering Angle to Lateral Velocity

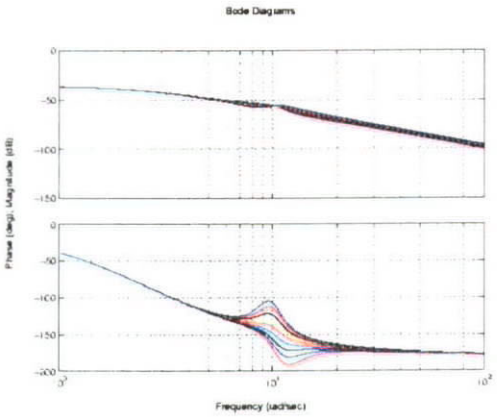

Figure I.4c Vehicle Bank Angle to Yaw Rate

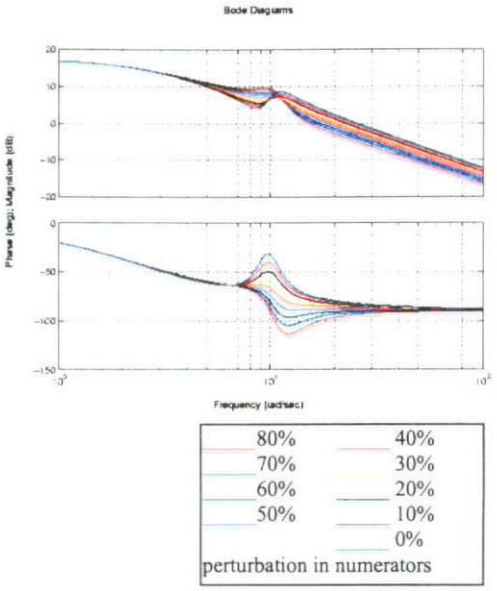

Figure I.4d Steering Angle to Yaw Rate

Figure I.4 Bode Diagrams of the Vehicle System with the Input of Steering Command and Vehicle Bank Angle and Output of Lateral Velocity and Yaw Rate, under Perturbation in System Parameters in Dominator with +10%

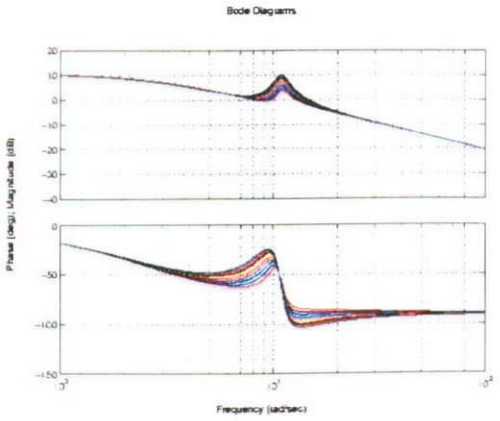

Figure I.5a Vehicle Bank Angle to Lateral Velocity

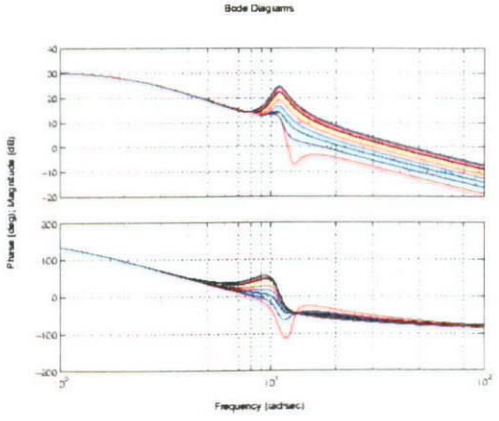

Figure I.5b Steering Angle to Lateral Velocity

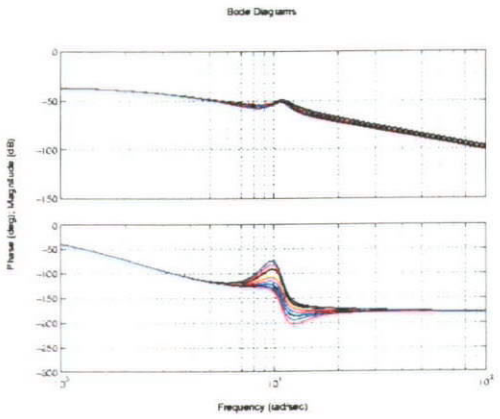

Figure I.5c Vehicle Bank Angle to Yaw Rate

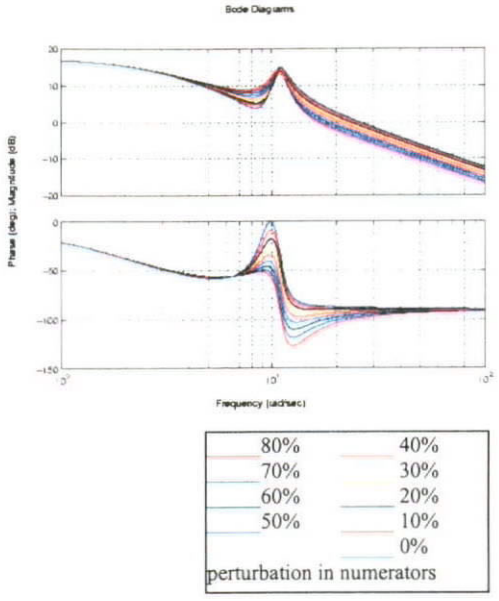

Figure I.5d Steering Angle to Yaw Rate

Figure I.5 Bode Diagrams of the Vehicle System with the Input of Steering Command and Vehicle Bank Angle and Output of Lateral Velocity and Yaw Rate, under Perturbation in System Parameters in Dominator with +30%

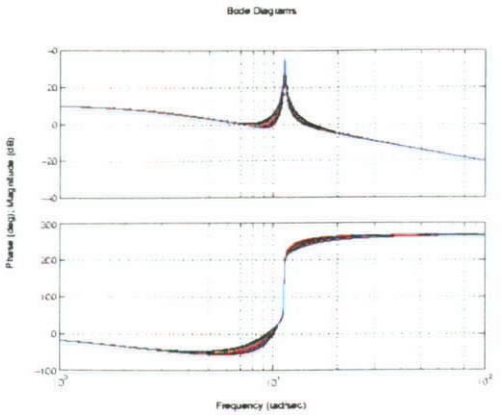

Figure I.6a Vehicle Bank Angle to Lateral Velocity

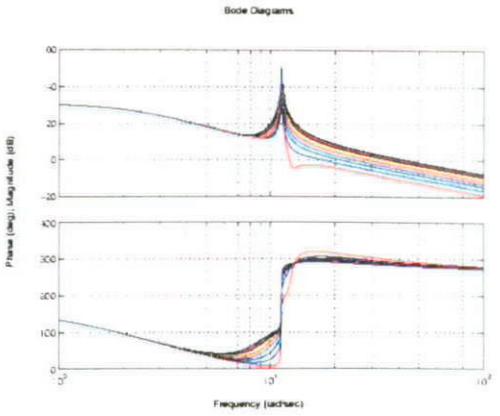

Figure I.6b Steering Angle to Lateral Velocity

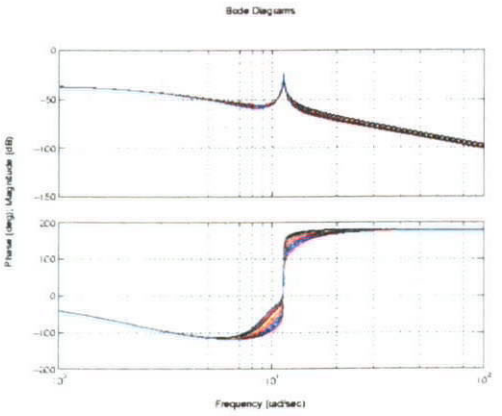

Figure I.6c Vehicle Bank Angle to Yaw Rate

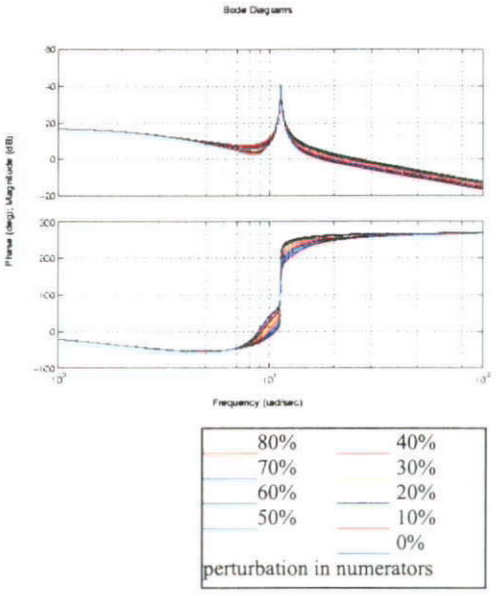

Figure I.6d Steering Angle to Yaw Rate

Figure I.6 Bode Diagrams of the Vehicle System with the Input of Steering Command and Vehicle Bank Angle and Output of Lateral Velocity and Yaw Rate, under Perturbation in System Parameters in Dominator with +50%